UNIVERSITAT DE BARCELONA

Phonons in III-nitride thinfilms, bulk and nanowires: a closer look into InN vibrational properties

Núria Domènech i Amador

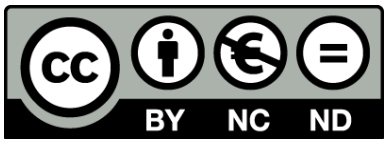

Phonons in III-nitride thin films, bulk and nanowires: a closer look into InN vibrational properties

Núria Domènech i Amador

Tesi presentada per a optar al títol de Doctora en Física

Directors:
Dr. Lluís Artús Surroca
Dr. Ramon Cuscó Cornet
Institut Jaume Almera. Consell Superior d'Investigacions Científiques

Tutor:
Prof. Dr. Albert Cornet Calveras
Departament d'Electrònica. Universitat de Barcelona

Universitat de Barcelona
Programa de Doctorat en Física
Barcelona, Juliol de 2015

Phonons in III-nitride thin films, bulk and nanowires: a closer look into InN vibrational properties

Tesi presentada per per:

Núria Domènech i Amador

per a optar al títol de Doctora en Física per la Universitat de Barcelona

Directors:
Dr. Lluís Artús Surroca
Dr. Ramon Cuscó Cornet
Institut Jaume Almera. Consell Superior d'Investigacions Científiques

Tutor:
Prof. Dr. Albert Cornet Calveras
Departament d'Electrònica. Universitat de Barcelona

Programa de Doctorat en Física
Línia de materials electrònics, sensors i micro- i nanosistemes

This PhD thesis has been developed at the Crystallography and Optical Properties Group from the Institut Jaume Almera (ICTJA-CSIC) under the FPU Program of the Spanish Ministry of Education. The research work has been funded by the project MAT2010-16116.

Acknowledgments

Agraeixo al Dr. Lluís Artús i al Dr. Ramon Cuscó, directors d'aquesta tesi, l'oportunitat de realitzar el doctorat i la seva supervisió i suport durant tots aquests anys. A en Lluís, molt especialment per haver confiat en mi des del primer dia, i per tot el seu esforç i dedicació durant aquest temps. També per la seva tenacitat per a tirar endavant els objectius científics i per la seva perspectiva global de la recerca, que ha sigut clau en la redacció dels articles i d'aquesta memòria. A en Ramon, per tota la física que he après al seu costat i pel seu *savoir faire* meticulós i precís, des del *calibratge* de l'espectròmetre fins la tipografia dels articles. Han estat molts els (eterns!) matins d'aliniament en la foscor del laboratori, i moltes també les explicacions i converses il·luminadores. Tant al Lluís com a en Ramon, vull agrair sincerament les correccions que han fet a aquesta memòria i la seva capacitat didàctica que ha aconseguit encomanarme la passió per la ciència, per la rigorositat i per la feina ben feta.

Agraeixo al Dr. Jordi Ibáñez la seva predisposició permanent a parlar de física i a aclarir dubtes. La seva capacitat de contextualitzar i de donar la importància justa a cada resultat m'ha fet prendre una consciència més realista de la meva feina i del sentit d'aquesta tesi. També per haver-me donat suport en aquests primers passos en el món de la ciència i per compartir la seva experiència i perspectiva sobre el món de la recerca.

Agradezco al Dr. Jesús Zúñiga-Pérez la oportunidad de realizar una estancia doctoral en el laboratorio CRHEA-CNRS. En esta estancia pude descubrir el mundo del crecimiento cristalino, desconocido para mí, y que ha sido fundamental para ampliar mi visión del campo de la física de semiconductores. Je voudrais remercier la Dr. Blandine Alloing, pour avoir été ma guide pendant mon stage au CRHEA et pour m'avoir montré les secrets des nanofils. Je remercie aussi Virginie Brändli et les autres chercheurs du CRHEA pour leur accueil au laboratoire.

Quisiera agradecer al Dr. Rafael Jiménez Riobóo por haberme enseñado las bases de la espectroscopía Brillouin. También al Dr. Germán González-Díaz, a quién debo la implantación iónica de las muestras estudiadas en esta tesis. A ambos, por haberme acogido en sus laboratorios durante sendas estancias.

I would like to thank all the scientific collaborators who have grown the samples studied throughout this thesis, and specially the research groups headed by Prof. Nanishi (Ritsumeikan University), Dr. R. Calarco (Research Center Jülich), Prof. Bensaoula (University of Houston) and Dr. B. Wang (Solid State Scientific Corporation).

Vull agrair també a en Robert Oliva les discussions científiques que hem compartit al llarg d'aquests anys. Teoria de grups, mecanismes de Brillouin, nivell d'estabilització de Fermi. Només els habitants del nostre despatx coneixem la tortura que amaguen les unitats cgs (d'on puc treure un 4π?). També pels cafès matinals, les apostes i les mítiques escapades a la font de la mandra.

Em sembla que aqui s'acaben els agraïments científics. Escrivint-los se m'ha fet tard al Jaume Almera, així que tanco l'ordinador i vaig a buscar l'autobús. En sortir, creuo la terrasseta de bio, *el lloc*. Ho assumeixo: em queden molts agraïments per escriure.

A tota la colla amb qui hem compartit àpats, debats i el *postureo* de la tesi. Al Pol i l'Oleguer, *coach* i *kellog*, per llegir-se aquests agraïments mentre es prenen un cafè-amb-llet-amb-gel (algú brinda perquè aquesta sigui la darrera tesi autonòmica...). A l'Oriol, l'Eloi i en Xavier: pels cafès que són com la vida... llargs, amargs, curts, dolços i fins i tot americans. A en Dani i l'Enric, els tardaners, pels reculls de premsa i les corrents internes. Als *lunchtimers* ocasionals i, com no, als *guiris*, portadors de la complexitat i el multilingüisme als nostres *lunchtimes*.

Arriba l'autobús. Sortim de Barcelona passant per davant de la facultat. Fa exactament deu anys que vaig (vam) entrar-hi per primera vegada. Dinars a l'atri solar, dimenges a la biblio, Tuníssia, Festivals de Primavera. Als *físicspelmón*, per haver compartit aquest camí malgrat saber allò que en Feynman deia de la utilitat de la física, i per seguir-lo compartint des d'arreu.

L'autobús enfila ja l'A2 en sentit Lleida, a l'altre costat del Llobregat hi queda Molins. A la Regina, per la litografia de la maduresa, per les unions túnel autèntiques i sinceres. A l'Anna, per tots els viatges valents i honestos, per tots els destins que val la pena compartir. A la Pilar, pels cultius de somnis i esperances, per tots els miralls. A l'Ana i la Rita, pels principis de *certesa* de Heisemberg. A totes vosaltres, per allò del *all we need is love*.

Això d'escriure els agraïments de la tesi m'està posant molt sentimental, agafo el mòbil per a consultar el twitter. Whatsapp de la Gema! Novedades del CRHEA, fotos de la excursión en bici, nos vemos pronto. A todos los que convirtieron la *côte d'azur* en una segunda casa. A Gema, por la electroluminiscencia del optimismo, por ser cómplice de cafés en la terraza, escapadas al oeste y cenas con botas. À Soumaya, la première habitante de notre *gril's bureau*, parce que il faut aller loin pour voir qu'il n'existe pas de distance. A Maria, asturiana mediterránea, por su energía sin fronteras y por *esos* vinos. À Nico et Florian, les professeurs de français, parce que les bronzés font du ski et les pâles des raquettes. To the lebannese people (*mu mmiha!*) and the rest of people in the lab.

Arribem a Martorell. Casa els avis. A ells i a la resta de família els agraeixo el suport incondicional que m'han donat sempre, i que ha estat tan important en tot aquest temps d'estudi. Menció especial per a l'Andreu, el meu germà(net), per totes les classes de natació, per totes les sessions de submarinisme.

És dimarts i anem a fer el got amb la Neus. Què tal la tesi? Anar fent, recta final! Neus, no ho saps però avui que escric els agraïments i tinc el cervell fet un batut de records i emocions, tinc unes ganes boges de xerrar del *secre* amb tu. A tu, perquè continuem fabricant refugis en aquest aiguabarreig. També a les del *bears*, per totes les croquetes (secretes bombones d'oxigen). A la Gemma, perquè seguim assaborint els detalls del dia a dia, devorant oportunitats, digerint la realitat que ens envolta, recordes el sopar de diumenge al Poble-Sec? A la Mireia, pels brindis casuals de *champions*, pels glops de valentia. A la Roser i la Maria, per creure's el *tant com puc*, per viure *sempre a punt!*

Enfilo la pujada cap a casa. Penso en tots vosaltres i la resta d'amics que heu sigut còmplices d'aquesta ruta. Hem descobert el camí feréstec de les tarteres desdibuixades, la traça invisible de les glaceres, l'esperança d'arribar al coll i descobrir una vall veïna, verda i fèrtil. Hem compartit les decepcions amb nosaltres mateixos, que són les més fosques. Hem agraït les mans amigues en plena pujada. Hem compartit horitzons suaus com carenes, cims retallats sobre el cel impossible. I seguim caminant, seguim obrint la nostra via, seguim.

Els camins no sabem on porten, però tenim molt clar d'on vénen. Un agraïment, el més especial de tots, als qui són l'origen del camí. A quatre grapes, a caminar, a córrer i a aixecar-me. A vosaltres, Maria Josep i Andreu, els qui podeu entendre millor la veritable importància dels fonons en capes primes i nanoestructures de nitrurs.

Barcelona, 22 de juny de 2015

Dedico aquesta tesi
a la Maria Josep i a l'Andreu,
els meus pares.

Contents

1 Introduction **1**

References **9**

2 Properties of the (In,Ga)N system **13**
2.1 The wurtzite crystalline structure 13
2.2 Crystalline growth 17
2.3 Electronic structure 18

References **23**

3 Raman scattering: theoretical background and experimental set-up **25**
3.1 Theory of Raman scattering 26
3.1.1 The Raman effect 26
3.1.2 Semi-classical approach 30
3.1.3 Quantum-mechanical approach 32
3.2 Experimental equipment for Raman spectroscopy 38

References **47**

4 Phonons in wurtzite (In,Ga)N **49**
4.1 Phonon dispersion curves 49
4.2 Optical phonons and Raman spectra 55
4.2.1 First-order Raman spectra 56
4.2.2 Higher order phonons 64
4.2.3 Local vibrational modes 64
4.3 Acoustic phonons and Brillouin spectra 66

References **71**

5 Anharmonic phonon decay in InN **75**
5.1 Framework: Cowley's theory of anharmonic phonon decay 76
5.2 Anharmonic phonon decay in InN epilayers 81
5.3 Anharmonic decay in InN nanowires 92
5.4 Phonon lifetimes of InN thin films and NWs 97
5.5 Anharmonic broadening of LVMs in heavily-doped InN 99

References **105**

6 Resonant Raman scattering in InN and InGaN **107**
6.1 Framework: Resonance effects on the Raman spectra 108
6.1.1 Impurity-induced Fröhlich mechanism 109
6.1.2 Martin's double resonance 111
6.1.3 Cascade multiphonon scattering 112
6.2 Double resonance in InN thin films and NWs 114
6.2.1 Raman spectra with different excitation wavelengths 114
6.2.2 LO frequency dependence on the excitation wavelength . . . 116
6.2.3 LO intensity resonance profile 119
6.3 Multiphonons in He^+-implanted InGaN 122
6.3.1 Ion implantation of the samples 122
6.3.2 Visible Raman spectra of the implanted InGaN thin films . . 125
6.3.3 UV Raman study of the multiphonons in implanted InGaN . 126

References **131**

7 LO-phonon plasmon coupled modes in InN and GaN **135**
7.1 Framework: LOPCMs modelling 137
7.1.1 Classical description of the LOPCMs 138
7.1.2 Lindhard-Mermin model 143
7.1.3 Raman scattering of LOPCMs in *n*-type semiconductors . . . 145
7.2 LOPCMs in bulk *n*-type GaN 150
7.2.1 Raman spectra of the N- and Ga-polar surfaces 152
7.2.2 Charge density gradient along the *z*-axis in the N-polar sector 156
7.3 LOPCMs in undoped, Si-doped and Mg-doped InN nanowires . . . 159
7.3.1 Visible and UV Raman spectra 160
7.3.2 LOPCMs fits 164

References **167**

8 Summary and conclusions **171**

A Future works **177**

B Attributions **179**

C List of publications **181**

D Resum en català **183**

CHAPTER 1

Introduction

The dramatic boost of the research on (In,Ga)N has been propelled by the achievement of light emitting diodes (LEDs) based on gallium nitride (GaN) with indium-gallium nitride (InGaN) as the active layer. Although the interest of the III-nitride system for optoelectronic applications had been highlighted by a number of theoretical works, the initial growth difficulties posed a huge obstacle for the fabrication of GaN-based devices, until Akasaki *et al.* demonstrated the growth of GaN on sapphire substrates with good enough crystal quality [1]. Initial attempts to obtain *p*-type GaN also were unsuccessful until it was shown that a post-growth treatment to activate the Mg-acceptors was needed. Amano *et al.* proposed an electron beam irradiation to activate the acceptors [2], while Nakamura *et al.* demonstrated that acceptor activation could be achieved by a post-growth thermal annealing [3]. A major step forward was done with the invention of the two-flow metalorganic chemical vapour deposition (MOCVD), which allowed a significant improvement of the GaN crystalline quality and scalability using a GaN buffer [4]. These breakthroughs paved the way for the first *pn* junctions in GaN, followed by the double heterostructure that composed the first LEDs with blue emission in the candela scale, reported by Nakamura *et al* [5]. The active region of those LEDs was a Zn-doped InGaN layer, instead of the multi-quantum-well (MQW) active regions used today. Further development allowed the growth of highly efficient GaN-based LEDs with InGaN MQWs as active region, emitting at wavelengths from 365 nm to 530 nm. The combination of those blue LEDs with suitable phosphors (emitting in the yellow range) made possible the fabrication of white-light LEDs, which nowadays are replacing the incandescent bulbs and have enabled a highly efficient lighting technology [6]. For the work leading to the development of these efficient GaN-based LEDs, I. Akasaki, H. Amano and S. Nakamura have been awarded the 2014 Nobel Prize in Physics.

The interest in high efficiency LEDs made GaN the object of huge research efforts in recent years. Surprisingly, even though the active layer of those LEDs is based on InGaN, experimental basic studies on indium nitride (InN) were scarce when those LEDs were obtained, mainly because of the lack of high-quality InN samples. The most paradigmatic example of the little knowledge of InN is that its band gap was overestimated by 1.2 eV until 2002, when the revised value that is

commonly accepted today was given. InN is more difficult to grow than other III-V nitrides such as GaN because its low dissociation temperature (≈ 630°C) and high equilibrium vapour pressure of nitrogen. Due to these difficulties, early InN samples were poorly crystalline and exhibited high free electron concentrations (> 10^{19} cm^{-3}). The optical absorption measurements made with those samples showed a strong absorption edge at 1.9 eV [7], and this was the value commonly accepted for the InN band gap until 2002. The improvement of the growth techniques allowed the growth of higher quality layers. The growth by molecular beam epitaxy (MBE), for instance, enabled obtaining InN thin films with reduced free electron concentrations (< 10^{18} cm^{-3}). New absorption experiments performed in those layers demonstrated that InN has a much smaller band gap than previously reported. In 2002, it was demonstrated that the intrinsic InN band gap at room temperature is 0.64 eV [8].

This smaller band-gap value of InN had a tremendous impact on the interest of the III-nitride system since it extends the emission range of this system from deep-UV (AlN) down to the near-IR region [9]. The relation between the band gaps of the III-nitride semiconductors and their respective lattice parameters are shown in Figure 1.1, in which for comparison we have also plotted other III-V binary semiconductors. It can be seen that only the III-nitrides, and particularly the InGaN system, can cover the whole visible spectrum. We have also plotted the band gaps of cubic III-nitrides, which are very interesting for optoelectronic applications because of the absence of piezoelectric fields along the (001) growth direction. They are nowadays being the focus of strong research efforts in order to improve the quantum efficiency of light emitters.

The band-gap range of the (In,Ga)N system and their remarkable resistance to irradiation by high energy particles make the InGaN an attractive material for outer space solar cells. Another interesting property of this system is the good alignment with the Si band, which facilitates integration with a bond of Si to form a multi-junction cell [9]. In addition, InN exhibits unique transport properties, such as the smallest electron effective mass among the III-nitrides and very high saturation and peak drift velocities [10]. All these properties expand the III-nitrides applications to encompass a wide range of devices such as infra-red emitters, tandem solar cells [11], and high-speed and high-frequency electronic devices [12].

In recent years, strong research efforts have been devoted to developing growth techniques in order to improve the quality of the III-nitride samples, to reduce the defect density and to advance in the doping control. Due to the lack of native substrates, III-nitride thin films are usually grown on sapphire (Al_2O_3), silicon (Si) or silicon carbide (SiC) substrates. The existence of a considerable lattice mismatch and the different thermal expansion coefficients give rise to a

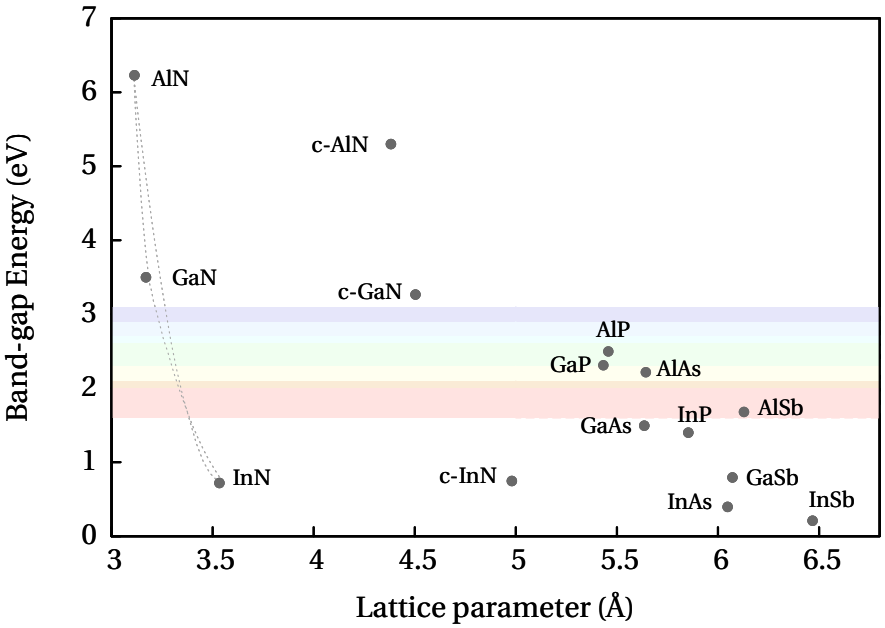

Figure 1.1: *Band-gap energy of representative III-V binary semiconductors vs. lattice parameter. Lines show the band-gap dependence for the wurtzite III-nitride ternary alloys, as reported in Ref. [9].*

sizeable built-in strain in the III-nitride thin films, as well as to a high density of defects such as threading dislocations. In the case of InGaN alloys, the crystal quality is also affected by the difficulties in the In incorporation and the fluctuations in composition that may exist, making it challenging to obtain high quality crystals for intermediate compositions [9]. Another approach to obtain better-quality III-nitrides is provided by bulk growth techniques. In the case of GaN, growth methods such as the ammonothermal technique have attracted much interest as a route to large-scale synthesis of crystals. It has been demonstrated that large GaN crystals exhibiting good crystalline quality and a reduced defect density can be obtained by the ammonothermal growth method [13]. In addition to the improvement of the growth techniques for epitaxial and bulk material, the growth of nitride nanostructures has also driven the research in group-III nitrides. These structures are interesting both for their structural properties and for their promising applications, such as infra-red emitters [14, 15] or sensing devices [16]. Concerning their lattice properties, nanostructures offer important advantages because they usually exhibit reduced built-in strains and better crystalline quality than thin films due to lateral strain relaxation. For instance, it has been shown that single crystal InN NWs have lower defect concentration

and less strain than InN thin films [17].

Although the present and future applications of the (In,Ga)N system materials are very promising, a large amount of research is required for a full development of their capabilities. Further work is needed to acquire a better understanding of the mechanisms underlying the basic physical properties of III-nitrides, to improve the growth techniques and to optimize device performance.

The vibrational properties are among the most fundamental characteristics of the materials. Moreover, the lattice dynamics and phonon vibrations are closely related to other basic properties of the materials such as the electronic structure. Raman spectroscopy is a well-suited technique to study the vibrational properties of semiconductor compounds and structures [18, 19]. Raman scattering is primarily applied to the study of the phonon vibrations in crystalline structures, and from the analysis of the phonon spectrum, it yields information about the crystal quality and the strain state of the lattice [20, 21]. It can be used to gain a better understanding of the lattice dynamics, the phonon lifetimes and their anharmonic interactions [22, 23]. In samples with a significant impurity concentration, Raman measurements can detect local vibrational modes related to the impurities [24, 25]. Besides, in doped samples the free carrier oscillations couple with the polar modes and give rise to LO-phonon-plasmon coupled modes (LOPCMs) which can be detected by means of Raman spectroscopy and can be used as an optical probe of electrical properties [26, 27].

During the last decades, an important effort has been devoted to the study of the vibrational properties of nitrides. However, the advancements have been made at different pace: much more work has been devoted to GaN than to InN. Concerning Raman studies on GaN, the main phonon modes were identified in the early works [28, 29]. Subsequently, Azuhatat *et al.* reported the measurement of all the Raman active modes on the same sample [30]. The increasing quality of the GaN thin films allowed Davydov *et al.* to perform a complete study of Raman scattering on GaN, including accurate measurements of the second-order Raman spectra [31]. In that study, *ab-initio* calculations of the GaN phonon dispersion curves and phonon density of states were also given. A study of the phonon lifetimes on the basis of Raman measurements was presented in Ref. [32]. The main results concerning Raman scattering of GaN were compiled in a comprehensive review by Harima in Ref. [33].

In contrast, studies on InN and In-rich InGaN lattice dynamics are more scarce. This is because, apart from the mentioned difficulties to obtain high quality samples, InN has a weak Raman signal. Early Raman studies of InN were reported in 1996 by Kwon *et al.* [34] using backscattering geometry and different polarization configurations, and unambiguous identification of the main phonon modes was given. Later, Davydov *et al.* [31] carried out a Raman scat-

tering study of InN in a variety of geometries, which allowed them to identify all the Raman active modes from their selection rules and to give a determination of the strain-free phonon frequencies. In that work they also presented the phonon dispersion curves and phonon density of states obtained using a phenomenological model. Their results are consistent with those obtained later using first-principles calculations [35].

Several controversies arose on the origin and behaviour of the InN longitudinal optical phonons measured in Raman experiments. It was experimentally measured that the frequency of these modes changes significantly when the Raman spectra is obtained using different excitation wavelengths. In thin films, Davydov *et al.* showed that the scattering mechanism mediating in the LO phonon scattering is Martin's double-resonance. The occurrence of this mechanism relies on the electronic structure of InN and the presence of native charged defects.

InN is not only difficult to grow with high crystalline quality, but is also difficult to *p*-dope. In fact, there is a strong tendency for as-grown InN to be *n*-type, and it usually displays a high free electron density [9]. The origin of this *n*-type conductivity is related to its electronic band structure, which favours the creation of donor-like defects. The ionization of surface states gives rise to an extremely high free electron density close to the sample surface, where InN exhibits an electron accumulation layer [9]. This is in contrast with most semiconductor compounds, which usually present a surface depletion layer. The existence of an electron accumulation layer makes the assessment of the free charge density in InN layers particularly problematic by regular Hall measurements, and it has to be taken into account in the interpretation of the Raman spectra of doped samples.

Scope of the thesis

This thesis is devoted to the study of phonon interactions in wurtzite III-nitrides, making special emphasis on those aspects that remain less studied. Since the vibrational properties of GaN have been widely studied, we mainly focus on the still controversial InN and other closely related materials. To this purpose, we present a series of Raman scattering studies on different kinds of samples (from layers to nanostructures, from undoped to heavily-doped or implanted samples, from InN to InGaN or GaN) in order to give a global overview of the phonon dynamics in those materials. We study how phonons interact with other phonons through anharmonic interactions leading to their decay. In general, the interactions of polar phonons with charged impurities play a key role in the resonant Raman scattering measurements. Here we study the Raman scattering resonances in the (In,Ga)N system and the influence of the impurity density on the

resonance efficiency. Finally, we study the polar phonon coupling with the free-charge plasmons in doped samples in order to probe the free electron density locally using Raman spectroscopy.

To facilitate the reading of this thesis and to provide a solid groundwork for the interpretation of the results, Chapter 2 introduces the fundamentals of the crystal and electronic structure of the (In,Ga)N system, making special emphasis on those aspects related to the vibrational properties and the Raman measurements.

The main experimental technique used throughout this thesis is Raman spectroscopy. The theory underlying this technique is presented in Chapter 3, giving both a classical and a quantum-mechanical approach to the Raman effect. Then, the experimental equipment used to carry out the measurements presented in this thesis is described. A framework to analyse the Raman scattering of phonons in the wurtzite (In,Ga)N system is given in Chapter 4. We present theoretical calculations of the phonon dynamics in both GaN and InN. We describe the first-order Raman spectra of the (In,Ga)N system and present a discussion of the scattering of phonon modes. We also introduce the Brillouin scattering of acoustic phonons and present a study of the InN elastic constants based on Brillouin spectroscopy measurements.

The main results of this thesis are described throughout the following chapters. They have been classified according to the physical phenomena they are concerned with. Each chapter contains first the theoretical framework of the physical phenomena, followed by the experimental results obtained. The studies related to the anharmonic phonon interactions are described in Chapter 5. This chapter first presents the theory of the anharmonic processes and the model used to deduce the decay channels. Following this model, a detailed study of the decay channels for each lattice phonon mode in InN layers is presented. The decay channels are also studied for the phonons in InN NWs, and the results are compared with those of thin films. Finally, the decay of high-frequency local vibrational modes of H complexes is dealt with.

Chapter 6 addresses the resonance effects on the Raman spectra of InN. It presents a study of the double resonance in InN nanowires by means of excitation wavelength-dependent Raman measurements. The results are compared with those obtained from InN thin films and the role of impurities is discussed. In this chapter we also study the cascade-like resonance mechanism underlying the multiphonon scattering. We study the multiphonon resonance in InGaN layers with different In concentrations. To investigate the role of impurities and defects in the cascade-like resonance, we perform Raman scattering experiments on He^+-implanted samples.

Finally, in Chapter 7 the coupling effects of the LO phonons with the free charge oscillations are studied in both GaN and InN. A bulk ammonothermally-

grown GaN is studied, and the differences between the Ga- and the N-polar face are presented. The LOPCMs are also studied in a series of Si-doped, Mg-doped and undoped InN NWs, and their analysis is used to extract the NWs free charge density. The benefit of Raman spectroscopy as a technique for a local assessment of the free charge density is emphasised by these results.

References

[1] I. Akasaki, H. Amano, Y. Koide, K. Hiramatsu, and N. Sawaki. *J. Cryst. Growth*, 98:209 – 219, 1989.

[2] H. Amano, I. Akasaki, T. Kozawa, K. Hiramatsu, N. Sawaki, K. Ikeda, and Y. Ishii. *Journal of Luminescence*, 40:121122, 1988.

[3] S. Nakamura, T. Mukai, M. Senoh, and N. Iwasa. *Jpn. J. Appl. Phys.*, 31:L139, 1992.

[4] S. Nakamura. *Jpn. J. Appl. Phys.*, 30:L1705, 1991.

[5] S. Nakamura, T. Mukai, and M. Senoh. *Appl. Phys. Lett.*, 64:1687–1689, 1994.

[6] S. Pimputkar, J. S. Speck, S. P. DenBaars, and S. Nakamura. *Nature Photonics*, 3:180–182, 2009.

[7] T. L. Tansley and C. P. Foley. *J. Appl. Phys.*, 59:3241, 1986.

[8] J. Wu, W. Walukiewicz, K. M. Yu, J. W. Ager III, E. E. Haller, H. Lu, W. J. Schaff, Y. Saito, and Y. Nanishi. *Appl. Phys. Lett.*, 80:3967–3969, 2002.

[9] J. Wu. *J. Appl. Phys.*, 106:011101, 2009.

[10] B. E. Foutz, S. K. O'Leary, M. S. Shur, and L. F. Eastman. *J. Appl. Phys.*, 85:11, 1999.

[11] A. Yamamoto, Md. R. Islam, T-T. Kang, and A. Hashimoto. *Phys. Status Solidi C*, 7:1307, 2010.

[12] G. D. Chern, E. D. Readinger, H. Shen, M. Wraback, C. S. Gallinat, G. Koblmüller, and J. S. Speck. *Appl. Phys. Lett.*, 89:141115, 2006.

[13] B. Wang, D. Bliss, M. Suscavage, S. Swider, R. Lancto, C. Lynch, D. Weyburne, T. Li, and F. A. Ponce. *J. Cryst. Growth*, 318:1030–1033, 2011.

[14] T. Stoica, R. J. Meijers, R. Calarco, T. Richter, E. Sutter, and H. Luth. *Nano Lett.*, 6:1541, 2006.

[15] C.-H. Shen, H.-Y. Chen, H.-W. Lin, S. Gwo, A. A. Klochikhin, and V. Yu. Davydov. *Appl. Phys. Lett.*, 88:253104, 2006.

[16] J. S. Wright, W. Lim, D. P. Norton, S. J. Pearton, F. Ren, J. L. Johnson, and A. Ural. *Semicond. Sci. Technol.*, 25:024002, 2010.

[17] Y.-L. Chang, Z. Mi, and F. Li. *Adv. Funct. Mater.*, 20:4146–4151, 2010.

[18] M. Cardona. *Light scattering in Solids I.* Springer-Verlag, 1975.

[19] M. Cardona and G. Güntherodt. *Light scattering in Solids IV.* Springer-Verlag, 1984.

[20] N. Hasuike, H. Fukumura, H. Harima, K. Kisoda, H. Matsui, H. Saeki, and H. Tabata. *J. Phys. Condens. Matter*, 16:S5807, 2004.

[21] T. M. G. Mohiuddin, A. Lombardo, R. R. Nair, A. Bonetti, G. Savini, R. Jalil, N. Bonini, D. M. Basko, C. Galiotis, N. Marzari, K. S. Novoselov, A. K. Geim, and A. C. Ferrari. *Phys. Rev. B*, 79:205433, 2009.

[22] J. Menéndez and M. Cardona. *Phys. Rev. B*, 29:2051, 1984.

[23] R. Cuscó, E. Alarcón-Lladó, J. Ibáñez, L. Artús, J. Jiménez, B. Wang, and M. J. Callahan. *Phys. Rev. B*, 75:165202, 2007.

[24] A. Kaschner, U. Haboeck, M. Strassburg, M. Strassburg, G. Kaczmarczyk, A. Hoffmann, C. Thomsen, A. Zeuner, H. R. Alves, D. M. Hofmann, et al. *Appl. Phys. Lett.*, 80:1909–1911, 2002.

[25] M. S. Brandt, J. W. Ager III, W. Götz, N. M. Johnson, J. S. Harris Jr, R. J. Molnar, and T. D. Moustakas. *Phys. Rev. B*, 49:14758, 1994.

[26] L. Artús, R. Cuscó, J. Ibáñez, N. Blanco, and G. González-Díaz. *Phys. Rev. B*, 60:5456, 1999.

[27] R. Cuscó, J. Ibáñez, E. Alarcón-Lladó, L. Artús, T. Yamaguchi, and Y. Nanishi. *Phys. Rev. B*, 79:155210, 2009.

[28] G. Burns, F. Dacol, J. C. Marinace, B. A. Scott, and El. Burstein. *Appl. Phys. Lett.*, 22:356–357, 1973.

[29] P. Perlin, C. Jauberthie-Carillon, J. P. Itie, A. San Miguel, I. Grzegory, and A. Polian. *Phys. Rev. B*, 45:83, 1992.

[30] T. Azuhata, T. Sota, K. Suzuki, and S. Nakamura. *J. Phys. Condens. Matter*, 7:L129, 1995.

[31] V. Yu. Davydov, V. V. Emtsev, I. N. Goncharuk, A. N. Smirnov, V. D. Petrikov, V. V. Mamutin, V. A. Vekshin, S. V. Ivanov, M. B. Smirnov, and T. Inushima. *Appl. Phys. Lett.*, 75:3297, 1999.

[32] L. Bergman, D. Alexson, P. L. Murphy, R. J. Nemanich, M. Dutta, M. A. Stroscio, C. Balkas, H. Shin, and R. F. Davis. *Phys. Rev. B*, 59:12977–12982, 1999.

[33] H. Harima. *J. Phys. Condens. Matter*, 14:R967, 2002.

[34] H-J Kwon, Y-H Lee, O. Miki, H. Yamano, and A. Yoshida. *Appl. Phys. Lett.*, 69:7, 1996.

[35] C. Bungaro, K. Rapcewicz, and J. Bernholc. *Phys. Rev. B*, 61:6720, 2000.

CHAPTER 2

Properties of the (In,Ga)N system

The (In,Ga)N system is very interesting from the point of view of the present and the potential applications. Apart from its potential for optoelectronic devices such as solid state lighting and photovoltaics, the (In,Ga)N system is interesting for chemical sensing and fast electronics, as well as for the integration with fibre optics technology (due to the proximity between the 1.55 μm and the InN band gap energy) [1]. Some of these applications are still not fully developed due to the growth difficulties of the nitrides, which result in samples with high defect concentration, lattice strain and high free electron density. These sample characteristics diminish the electron mobility, increase the internal fields and reduce device efficiency.

This chapter presents the main physical properties of the (In,Ga)N system, making special emphasis on those properties that have an impact on the phonon dynamics and that are relevant for the applications. We first describe the wurtzite crystalline structure and its symmetries. Next, the main growth techniques used to obtain III-nitride samples are explained. Finally, we present the basic electronic properties of the (In,Ga)N system. We introduce the Fermi stabilization energy and we relate it to the residual free electron density and the surface electrical properties.

2.1 The wurtzite crystalline structure

(In,Ga)N system compounds are usually grown in the wurtzite structure. The relatively small size of nitrogen atoms determines this structure to be thermodynamically stable under ambient conditions, but also rocksalt and zinc-blende structures can be obtained. Zinc-blende GaN and InN have been achieved by epitaxial growth on certain cubic substrates such as GaAs, although wurtzite structure domains are likely to be present at the extended defect sites [2]. The rocksalt structure is stable at high pressures [3].

Since this thesis is devoted to the study of phonons in wurtzite InN and GaN, we address now the analysis of this crystalline structure and its symmetries. The wurtzite structure is an hexagonal non-centrosymmetric crystalline structure. Figure 2.1(a) shows a scheme of the conventional cell of wurtzite, in which the primitive cell is depicted with bold lines. The wurtzite structure is formed by two

hexagonal closed packed sub-lattices displaced by the vector $\vec{u} = [(2\vec{a}_1 + \vec{a}_2)/3 + \vec{a}_3/2]$, one of which is formed by the cations of the material and the other one by the anions. Its primitive cell is defined by the vectors

$$\vec{a}_1 = \frac{a_0}{2}(1, -\sqrt{3}, 0), \quad \vec{a}_2 = \frac{a_0}{2}(1, \sqrt{3}, 0), \quad \vec{a}_3 = c_0(0, 0, 1).$$

From the crystalline lattice, we can define the reciprocal space, which is the space of all the wave vectors that result in planar waves with the same periodicity of the real space. This is the vectorial space usually employed to study the behaviour of phonons and electrons in crystals [4]. The primitive cell of the reciprocal space (first Brillouin zone) is given by the primitive vectors of the reciprocal lattice, which for the wurtzite structure are

$$\vec{b}_1 = \frac{2\pi}{\sqrt{3}a_0}(\sqrt{3}, -1, 0), \quad \vec{b}_2 = \frac{2\pi}{\sqrt{3}a_0}(-\sqrt{3}, 1, 0), \quad \vec{b}_3 = \frac{2\pi}{c_0}(0, 0, 1).$$

Figure 2.1(b) shows the first Brillouin zone of the wurtzite structure and its high-symmetry points and directions. The Γ point is the highest-symmetry point of the reciprocal space and corresponds to $\vec{k} = 0$. The Bloch waves with $\vec{k} = 0$ represent the ionic vibrations with infinite wavelength. Furthermore, the point symmetry operations of this symmetry point correspond to those of the direct space.

The wurtzite structure belongs to the space group C_{6v}^4 ($P6_3mc$) and is homomorphic to the point symmetry group C_{6v} ($6mm$). The symmetry operations for the wurtzite structure at the Γ point are (Ref. [5]):

- $\{E|0\}$: The identity
- $\{C_2|\vec{c}/2\}$: One binary axis along the z direction with an additional translation by $c/2$

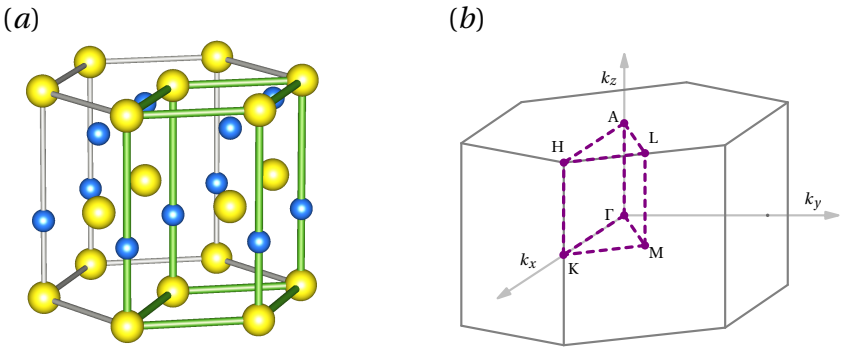

Figure 2.1: *(a) Conventional cell of the wurtzite structure. (b) First Brillouin zone of the wurtzite structure with the high-symmetry points.*

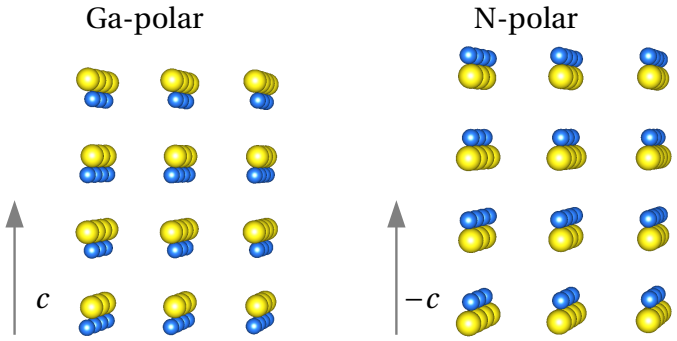

Figure 2.2: *Scheme of the GaN crystalline structure in the Ga-polar and N-polar orientations. Ga atoms are represented in yellow and N atoms in blue. In both cases the c axis direction is indicated in the figure and the structure is represented in the (10-10) plane with a slight perspective, in order to show the atomic bilayers.*

- $\{C_3|0\}$ and $\{C_3^{-1}|0\}$: A ternary axis along the z direction
- $\{C_6|\vec{c}/2\}$ and $\{C_6^{-1}|\vec{c}/2\}$: A six-fold rotation followed by a $\vec{c}/2 = (0,0,c_0/2)$ translation
- $\{\sigma_{d1}|\vec{c}/2\}$,$\{\sigma_{d2}|\vec{c}/2\}$ and $\{\sigma_{d3}|\vec{c}/2\}$: Three symmetry planes perpendicular to $\vec{a}_1$, $\vec{a}_2$ and $\vec{a}_1+\vec{a}_2$, respectively, with a $\vec{c}/2$ translation
- $\{\sigma_{v1}|0\}$,$\{\sigma_{v2}|0\}$ and $\{\sigma_{v3}|0\}$: Three symmetry planes perpendicular to σ_d planes

These symmetry operations can be described by matrices and they impose restrictions on the atomic motions of the vibrational modes. In fact, as is described in Sec. 4.2, from the analysis of these symmetry operations the atomic displacements involved in the phonon modes can be derived, and also the Raman or infra-red activity of each phonon can be deduced.

Polarity and crystalline orientations

A crystal is called polar when a crystallographic direction cannot be reversed by any combination of symmetry operations of the associated point group. This is the case of the wurtzite structure, in which $+c$ and $-c$ directions are not equivalent. In the growth directions normal to the (0001) basal plane, the atoms are arranged in bilayers consisting in two close-packed hexagonal layers. When the nitrogen atoms are on the top of the 0001 bilayer, the growth direction is the [000-1] and the crystal orientation is called *N-face* or *N-polar*. When the atoms in the top bilayer are the cations (In or Ga), the growth direction is the [0001]

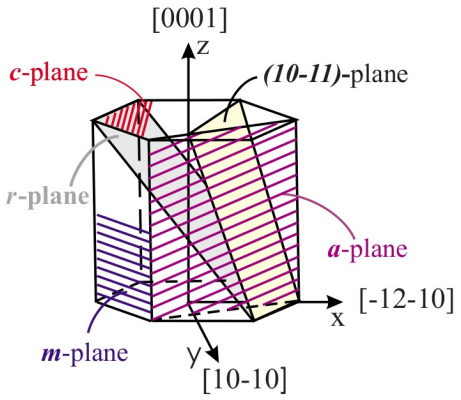

Figure 2.3: *Conventional cell of the wurtzite structure and the most used crystallographic planes. Figure extracted from Ref. [11]*

and the growth face is called *In/Ga-face* or *In/Ga-polar*. The polarity does not determine the surface termination of the crystal, but the bilayer orientation, as schematically shown for GaN in Fig.2.2.

The polarity of the crystal determines the surface morphology, and therefore it has important consequences on its growth rates, defect density and impurity incorporation [6, 7]. For the case of GaN, the N-polarity surface is much more chemically reactive than the Ga-polarity surface. It has been extensively studied that the polarity of the crystal determines the crystal quality. In particular, the Ga-polar face exhibits a columnar growth that leads to a reduced crystalline quality [8, 9].

The polar surfaces have both an spontaneous and a piezoelectric components of the polarisation. This results in the quantum confined Stark effect (QCSE). In quantum well LED structures, the polarisation fields separate the electron and hole wave functions in the active zone, which causes a reduction of the LED internal quantum efficiency. In the case of InGaN-based LEDs, the lattice mismatch between the substrate and the active layers adds piezoelectric polarisation fields that are greater for higher indium concentrations, which results in a further reduction of the emission efficiency for intermediate compositions [10].

Recently, nitride materials with nonpolar or semipolar surface orientations have attracted attention because the possibility to reduce the defect concentration and to avoid or minimise built-in electric fields. Some of the most studied nonpolar orientations are the *m*-plane (1-100) and the *a*-plane (11-20) (see scheme in Fig. 2.3).

2.2 Crystalline growth

Nitride thin films are usually grown heteroepitaxially by either molecular beam epitaxy (MBE) or metalorganic chemical vapour deposition (MOCVD). In the case of the GaN, huge research efforts have led to high-quality samples obtained by both techniques. One of the most challenging issues was to obtain p-doped GaN layers by MOCVD. This was achieved by performing post-growth annealing process to activate the acceptors [12].

The growth of the InN is more difficult, because the growth temperature is limited to 600°C due to the In-N bond weakness, which prevents the use of growth techniques requiring high temperatures. Therefore, InN encounters difficulties in MOCVD growth since this temperature restriction weakens the ability to decompose the residual impurities such as hydrogen and oxygen [13]. One of the most suitable solutions is the growth using plasma-assisted molecular beam epitaxy (PAMBE), which can be performed at lower temperatures. This technique significantly prevents the incorporation of impurities and makes post-growth annealing processes unnecessary. PAMBE consists of a regular well-known MBE growth in which a radio frequency plasma source is used to activate atomic nitrogen flux. As in MBE, the flux of the metal atoms is controlled by the temperature of each effusion cell [14].

The most commonly used substrates for the heteroepitaxial growth of nitrides are sapphire (Al_2O_3), silicon carbide (SiC) or silicon (Si). Due to the differences in lattice parameters, thermal expansion coefficients, surface symmetries and chemical composition, defects are formed in the substrate/layer interface and propagate into the thin film. Moreover, the resulting thin films usually present a sizeable built-in strain.

The interest for achieving high-quality large-scale synthesis of nitride crystals is driving the development of different new growth approaches to overcome the difficulties associated with heteroepitaxy. Among those, we highlight epitaxial lateral overgrowth (ELO), nanostructured growth and bulk growth methods such as the ammonothermal technique. Epitaxial lateral overgrowth techniques are mainly used to obtain semipolar crystalline orientations with reduced defect density, but they require several growth steps and have a low scalability [10, 11]. The growth of nanostructured nitrides is interesting for their potential applications and also for their structural properties. Nanostructures have been shown to present structural defects only near the interface with the substrate, because in the upper parts the strain induced by the lattice mismatch is reduced by lateral strain relaxation [15, 16]. The ammonothermal growth is a solvothermal method to grow III-nitrides, similar to the hydrothermal processes used to grow α-quartz, but using an alkaline ammonia solution. In this growth technique, the material grows around a highly crystalline template seed [17]. Several studies on

Table 2.1: *Basic physical parameters of wurtzite GaN and InN. Ref. [1]*

Parameter	GaN	InN
Lattice constant a (nm) ($T = 300$ K)	0.3189	0.3533
Lattice constant c (nm) ($T = 300$ K)	0.5185	0.5693
Density (g/cm^{-3})	6.15	6.81
Band gap E_g (eV) ($T = 0$ K)	3.51	0.69
Band gap E_g (eV) ($T = 300$ K)	3.43	0.64
Electron effective mass at band edge m_e^*/m_0	0.20	0.07
High-frequency dielectric constant $\varepsilon_\infty/\varepsilon_0$	5.4	6.7

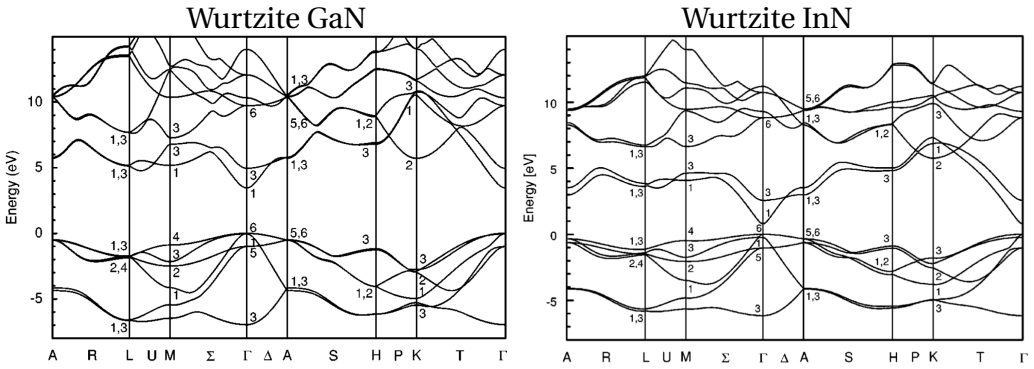

Figure 2.4: *First-principle calculation of the electronic band structure of wurtzite GaN (left, Ref. [20]) and InN (right, Ref. [21]) in the entire Brillouin zone.*

ammonothermal growth showed that the defect density can be greatly reduced and high quality samples can be obtained [18, 19].

2.3 Electronic structure

As described in the Introduction, early studies on InN electronic structure were misleading because, due to poor material quality, the experimental measurements systematically overestimated the band-gap value. After the InN band-gap revision in 2002, it is accepted that GaN and InN are direct band-gap semiconductors, whose band-gap energies at room temperature are 3.43 eV and 0.64 eV, respectively. The basic structural and electrical parameters of InN and GaN are plotted in Table 2.1, which are the commonly accepted values for a relaxed lattice. For heteroepitaxially grown thin films, the lattice mismatch and the differential thermal expansion with the substrate may lead to a lattice strain that alters the lattice parameters and the electronic structure.

The calculated full electronic band structures of wurtzite GaN and InN are

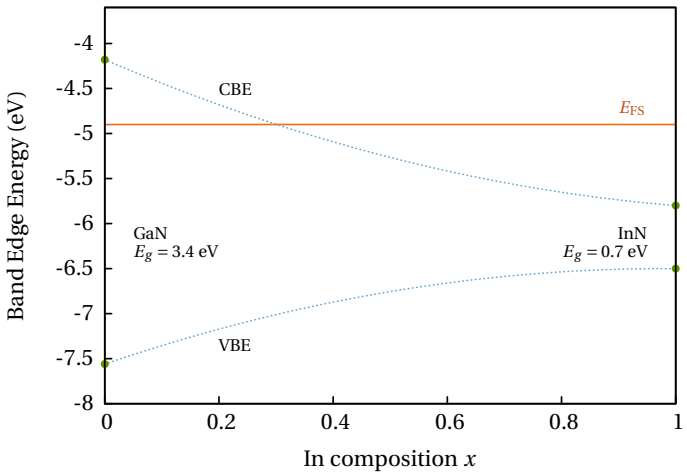

Figure 2.5: *Energy of the conduction band edge (CBE) and the valence band edge (VBE) relative to the vacuum level for the InGaN system. The Fermi stabilization energy* $E_{FS} = -4.9$ *eV is also plotted.*

plotted in Fig. 2.4. The comparison between their respective electronic structures makes evident the narrowness of the InN band gap. An important consequence of the narrow gap of InN is the strong non-parabolicity of the lowest conduction band. This has already been reported for other narrow-gap semiconductors such as InSb and InAs [22]. Another consequence of the InN narrow band gap is the tendency of InN to be electrically n-type, as will be discussed below.

The $In_{1-x}Ga_xN$ ternary alloy exhibits a band-gap bowing that is described by the following standard equation:

$$E_g^{In_xGa_{1-x}N}(x) = E_g^{InN}(1-x) + E_g^{GaN}x - bx(1-x) \tag{2.1}$$

The band-gap bowing is usually accepted to be $b = 1.4 \pm 0.1$ eV [23], which agrees with experimental results [24] and theoretical calculations [25]. On the other hand, InGaN lattice parameters are usually assumed to depend linearly on the composition following Vegard's law [1, 24].

Fermi stabilization level

InN has a strong tendency to present unintentional n-type doping. The origin of this behaviour lies in the position of the Fermi stabilization level (E_{FS}) and in the amphoteric behaviour of the native defects. In Ref. [26], it was shown that the introduction of very large concentration of native defects always lead to the

same position of the Fermi energy, which was defined as the E_{FS}.

Following the amphoteric model developed by Walukiewicz *et al.* in Refs. [26, 27], the relative position of the E_{FS} and the Fermi level determines the donor or acceptor behaviour of the intrinsic defects. In most semiconductors, the E_{FS} lies in the energy band gap and, consequently, the native defects have the same tendency to be donors or acceptors. This is the case of GaN, as can be seen in Fig. 2.5.

In the case of InN, however, the E_{FS} is well above the conduction band edge (see Fig. 2.5), and therefore for undoped InN, E_{FS} is higher than E_F. In this case, the intrinsic defects will be donor-like, increasing the free electron density, and pushing the Fermi energy towards E_{FS} until $E_{FS} = E_F$. This explains the fact that the InN samples, which usually have a remarkable defect density, present an unitentional n-type doping.

The nature of the native defects that generate the high free electron density in InN is still matter of study. First-principle calculations show that nitrogen vacancies (V_N) are the lowest energy native defects, and some experimental results support it. Other kind of native defects such as indium vacancies (V_{In}) may also play a role. The high background electron density can be also caused by the interplay of local complexes formed by impurities and native defects. The most studied impurity is hydrogen, which has been found to play a different role depending on its position in the InN lattice. It is considered to be a single donor when it is interstitial, and to act as a double donor when it is substitutional [1].

The high unintentional n-doping of InN makes it difficult to obtain p-type doping. The most studied acceptor dopant is Mg, and evidence of p-type doping was first reported by Jones *et al.* in Ref. [28]. In that work, a net concentration of ionized acceptors in the bulk was demonstrated by means of capacitance-voltage measurements made on highly-doped Mg:InN, but those samples exhibited n-type behaviour in the Hall effect measurements. This behaviour is due to the existence of a surface electron accumulation layer in InN.

The Fermi stabilization energy in the InGaN alloy

As shown in Fig. 2.5, the E_{FS} is above the band gap for InN, whereas it is below in in the case of GaN. For the case of InGaN, taking into account the commonly accepted band-gap bowing, $E_{FS} > E_{CBM}$ for [In]> 0.34, as demonstrated by Li *et al.* in Ref. [27]. In that paper they showed that the introduction of point defects in a crystalline lattice through high particle irradiation leads to an increase of the free electron density only for [In]> 0.34.

We have investigated the amphoteric behaviour of defects in InGaN as a function of [In]. To this purpose, we have performed photoluminescence (PL) and absorption measurements on InGaN layers with different In compositions,

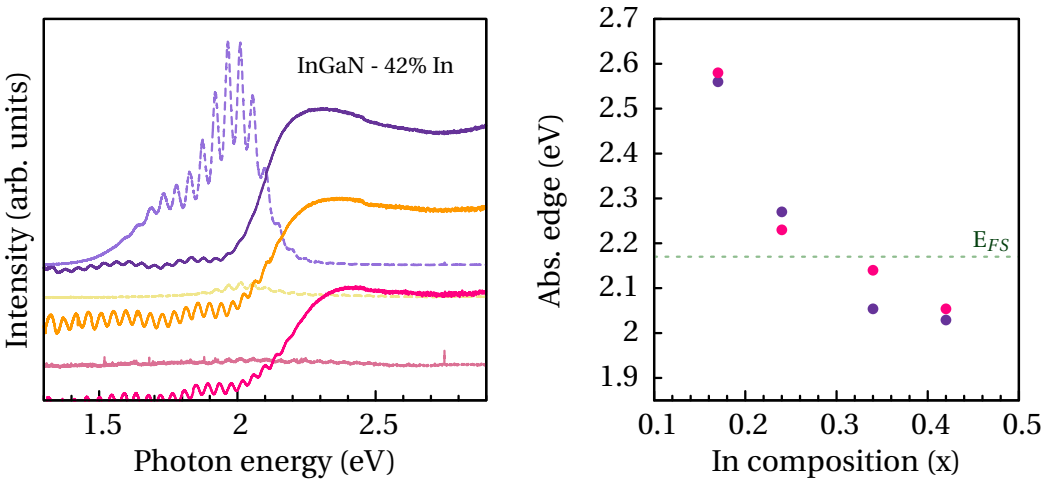

Figure 2.6: *Left: PL and absorption spectra of unimplanted and implanted InGaN layers with [In]=0.42. Results from the unimplanted layer (A) are plotted in blue, while those from the less implanted layer (A') are plotted in yellow and those from the most heavily implanted layer (A") in magenta. Description of the implantation conditions is given in Table 6.1. The right panel shows the energy of the absorption edge of the unimplanted specimen (blue) and of the most heavily implanted specimen (magenta) as a function of the indium composition. The* E_{FS} *relative to the valence band maximum is also plotted.*

ranging from 0.17 to 0.42. For each sample, we have three specimens, two of which have been implanted with high-energy He^+-ions. A description of the growth and implantation of the samples is given in Sec. 6.3. In Fig. 2.6(a) we plot the absorption coefficients and the PL spectra of the sample with [In]=0.42. It can be seen that the implantation completely quenches the PL signal, and therefore we have analysed the absorption spectra, which exhibit a slight band-gap upshift with increasing implantation. The band-gap values extracted from the absorption experiments on the as-grown and the most-implanted samples are shown in Fig. 2.6(b) with respect to the E_{FS}. This plot shows that, for the InGaN samples with the lowest indium content the implantation results in a reduction of the absorption edge, while the samples with higher indium content exhibit an upshift of the absorption edge in the implanted samples with respect to the as-grown layers. This measurements corroborate the predictions of the amphoteric model.

Surface properties

The surface of crystals generally contains a higher defect density than the bulk. In InN, due to the position of the Fermi stabilization energy above the conduc-

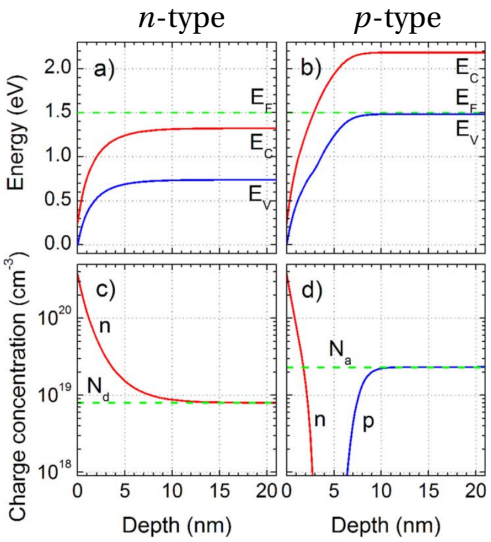

Figure 2.7: *Band bending (a and b) and free charge distribution (c and d) near the surface of a n-type (a and c) and p-type (b and d) polar InN film. The bulk doping in each case is* $N_d = 8\times10^{18}$ cm^{-3} *and* $N_a = 2.3\times10^{19}$ cm^{-3}. *Figure extracted from Ref. [1].*

tion band edge, the surface native defects are preferentially donors. Therefore, there will exist a high density of ionised donors close to the surface which induce an electric field that bends downwards the electronic bands. This is illustrated in Fig. 2.7 for both a n-doped (a) and p-doped (b) polar InN. As a consequence, an extremely high electron density is confined near the surface, as plotted in Fig. 2.7 for n-doped (c) and p-doped (d) InN.

The presence of the electron accumulation layer in nonpolar surfaces is still matter of debate. While some authors reported the universality of the electron accumulation layer in all InN surfaces, regardless their polarity [29]; others showed evidence of absence of electron accumulation layer in nonpolar InN surfaces [30].

This surface electron accumulation of InN strongly affects its basic electrical characterization through Hall effect because it acts as a parallel conduction layer which affects the detection of the free carrier density in the bulk. Capacitance-voltage (CV) measurements can be used to probe the net charge concentration as a function of depth [1]. As will be discussed in Chapter 7, Raman scattering can also probe the free electron density in an accurate, local and non-destructive way.

References

[1] J. Wu. *J. Appl. Phys.*, 106:011101, 2009.

[2] M. Cardona and G. Güntherodt. *Handbook of Nitride Semiconductors and Devices. Vol. 1.* Wiley-VCH, 2008.

[3] J. Ibáñez, R. Oliva, F. J. Manjón, A. Segura, T. Yamaguchi, Y. Nanishi, R. Cuscó, and L. Artús. *Phys. Rev. B*, 88(11):115202, 2013.

[4] N. W. Ashcroft and N. D. Mermin. *Solid State Physics*. Harcourt College Publishers, 1976.

[5] P. Y. Yu and M. Cardona. *Fundamentals of Semiconductors. Physics and materials properties.* Springer-Verlag, 1996.

[6] M. Sumiya, K. Yoshimura, K. Ohtsuka, and S. Fuke. *Appl. Phys. Lett.*, 76(15):2098–2100, 2000.

[7] F. Tuomisto, T. Suski, H. Teisseyre, M. Krysko, M. Leszczynski, B. Lucznik, I. Grzegory, S. Porowski, D. Wasik, A. Witowski, W. Gebicki, P. Hageman, and K. Saarinen. *Phys. Status Solidi B*, 240(2):289–292, 2003.

[8] M. Seelmann-Eggebert, J. L. Weyher, H. Obloh, H. Zimmermann, A. Rar, and S. Porowski. *Appl. Phys. Lett.*, 71(18):2635–2637, 1997.

[9] A. R Arehart, T. Homan, M. H. Wong, C. Poblenz, J. S. Speck, and S. A. Ringel. *Appl. Phys. Lett.*, 96:242112, 2010.

[10] F. Scholz. *Semicond. Sci. Technol.*, 27:024002, 2012.

[11] V. Darakchieva, M.-Y. Xie, N. Franco, F. Giuliani, B. Nunes, E. Alves, C. L. Hsiao, L. C. Chen, T. Yamaguchi, Y. Takagi, et al. *J. Appl. Phys.*, 108:073529–073529, 2010.

[12] S. Nakamura, T. Mukai, M. Senoh, and N. Iwasa. *Jpn. J. Appl. Phys.*, 31:L139, 1992.

[13] S. Ruffenach, M. Moret, O. Briot, and B. Gil. *Phys. Status Solidi A*, 207:9–18, 2010.

[14] T. Stoica, E. Sutter, and R. Calarco. *GaN and InN Nanowires: Growth and Optoelectronic Properties.* Engineering Materials. Springer Berlin Heidelberg, 2010.

[15] B. Alloing, E. Beraudo, Y. Cordier, F. Semond, S. Sergent, O. Totterau, P. Vennéguès, S. Vézian, and J. Zúñiga-Pérez. *Int. J. Nanotechnol.*, 9:412427, 2012.

[16] M. A. Sánchez-Carcía, J. Grandal, E. Calleja, S. Lazic, J. M. Calleja, and A. Trampert. *Phys. Status Solidi B*, 243:1490, 2006.

[17] B. Wang, D. Bliss, M. Suscavage, S. Swider, R. Lancto, C. Lynch, D. Weyburne, T. Li, and F. A. Ponce. *J. Cryst. Growth*, 318:1030–1033, 2011.

[18] T. Hashimoto, F. Wu, J. S. Speck, and S. Nakamura. *Nature Materials*, 6:568, 2007.

[19] D. Ehrentraut, R. T. Pakalapati, D. S. Kamber, W. Jiang, D. W. Pocius, B. C. Downey, M. McLaurin, and M. P. D'Evelyn. *Jpn. J. Appl. Phys.*, 52:08JA01, 2013.

[20] D. Fritsch, H. Schmidt, and M. Grundmann. *Phys. Rev. B*, 67:235205, 2003.

[21] D. Fritsch, H. Schmidt, and M. Grundmann. *Phys. Rev. B*, 69:165204, 2004.

[22] E. O. Kane. *J. Phys. Chem. Solids*, 1:249, 1957.

[23] J. Wu, W. Walukiewicz, K. M. Yu, J. W. Ager III, E. E. Haller, H. Lu, and W. J. Schaff. *Appl. Phys. Lett*, 80:4741–4743, 2002.

[24] R. Oliva. *Optical emission and Raman scattering in InGaN thin films grown by molecular beam epitaxy*. Master Thesis, Universitat de Barcelona, 2010.

[25] B. Lee and L. W. Wang. *J. Appl. Phys.*, 100:093717, 2006.

[26] W. Walukiewicz. *Appl. Phys. Lett.*, 54:2094, 1989.

[27] S. X. Li, K. M. Yu, J. Wu, R. E. Jones, W. Walukiewick, J. W. Ager, W. Shan, E. E. Haller, H. Lu, and W. J. Schaff. *Phys. Rev. B*, 71:161201, 2005.

[28] R. E. Jones, K. M. Yu, S. X. Li, W. Walukiewick, J. W. Ager, S. X. Li, E. E. Haller, H. Lu, and W. J. Schaff. *Phys. Rev. Lett.*, 96:125505, 2006.

[29] P. D. King, T. D. Veal, C. F. McConville, F. Fuchs, J. Furthmüller, F. Bechstedt, P. Schley, R. Goldhahn, J. Schörmann, D J. As, et al. *Appl. Phys. Lett.*, 91:092101, 2007.

[30] C.-L. Wu, H.-M. Lee, C.-T. Kuo, C.-H. Chen, and S. Gwo. *Phys. Rev. Lett.*, 101:106803, 2008.

CHAPTER 3

Raman scattering: theoretical background and experimental set-up

By focusing sunlight on a liquid and filtering both the incident and the scattered light, Prof. C. V. Raman and K. S. Krishnan observed in 1928 that a small fraction of the scattered light underwent a wavelength change. They repeated the same experiment on sixty different liquids and studied the polarisation of that scattered light to rule out the fluorescence as a responsible of the observations. Their experimental discovery was published in a paper entitled "A new type of secondary radiation" (Ref. [1]). The same year, and independently, Prof. G. S. Landsberg and Prof. L. I. Mandelstam observed the experimental evidence of what they called the *inelastic combinatorial scattering of light* in crystals [2]. The effect observed by both Raman and Krishnan in liquids, and Mandelstam and Landsberg in crystals was, in fact, the same: an inelastic scattering of light occurring due to the excitation of collective excitations in the material. This effect had been theoretically predicted by Smekal in 1923 [3]. For that discovery Prof. C. V. Raman was awarded the Nobel prize in Physics in 1930, *"for his work on the scattering of light and for the discovery of the effect named after him"*, the Raman effect.

The early Raman experiments were extremely difficult due to the inherent weak efficiency of the effect and the lack of powerful light sources. The first Raman spectra were of molecular liquids like benzene, and were excited using a mercury lamp and recorded using a spectrograph [4]. The evolution of the Raman experiments was linked to the availability of more powerful and monochromatic light sources. The advent of the laser in 1960 and the main developments in laser technology had a crucial role in the consolidation of Raman scattering as a research technique for chemistry, physics and materials science. During the second half of the past century, the first-order Raman spectra of a wide variety of materials were studied, including organic and inorganic molecules, polymers, minerals, semiconductors and superconductors [5]. During the last few decades, the advances in digital data acquisition and the development of compact equipments have enabled the use of Raman spectroscopy as a more conventional characterization technique for most physics and chemistry laboratories and companies. Furthermore, the emergence of Surface-Enhanced Raman

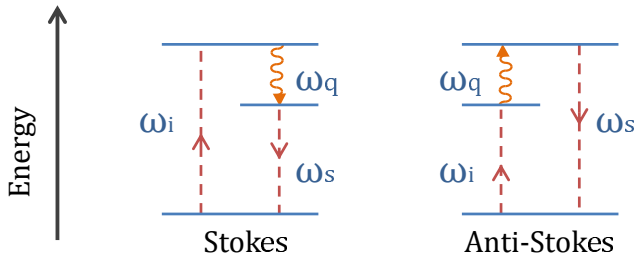

Figure 3.1: *Energy scheme of the Stokes and anti-Stokes Raman processes, where ω_i is the frequency of the incident photon, ω_q is the frequency of the scattered phonon and ω_s is the frequency of the scattered photon.*

Scattering and Tip-Enhanced Raman Scattering has expanded the applications of Raman scattering which now include biology, pharmacy and medicine.

In this chapter we give a global theoretical framework of the physics underlying Raman scattering and a description of the experimental equipment used in this thesis.

3.1 Theory of Raman scattering

In this section we describe the physics of the Raman scattering process from different approaches. First, we give a phenomenological outline of the Raman effect. Then, we describe it using a semi-classical approach and finally we present the quantum-mechanical description of the process.

3.1.1 The Raman effect

When electromagnetic radiation strikes a material surface, it can be reflected, absorbed, scattered or transmitted. Among the scattered radiation, the biggest part is elastically scattered (Rayleigh scattering), while a small part is inelastically scattered (Raman and Brillouin scattering). In the Raman or Brillouin light scattering in solids, the light interacts with the lattice system by creating or annihilating elementary excitations. In the case of Brillouin scattering, these elementary excitations correspond to acoustic phonons. For Raman scattering processes, these quanta of energy can correspond to optical phonons, free-electron plasmons, local vibrational modes or spin waves, among others. In this thesis we are mainly focused on the Raman scattering by lattice phonons. Therefore, for simplicity, throughout this chapter we describe the Raman scattering taking into account lattice phonons as the elementary excitations involved in the

scattering process. Particularities of the Raman scattering by phonon-plasmon coupled modes are addressed in Chapter 7.

Kinematics of the Raman effect

The quantum mechanical mechanisms underlying the interaction of the photons with the lattice system are complex and, as will be presented throughout the next sections, they involve interaction with the electron-hole pairs. However, an intuitive picture of the Raman effect can be obtained from the kinematics of the scattering process.

The kinematics of inelastic light scattering is determined by the conservation of the energy and momentum in the overall process. We consider the incident photon (with frequency ω_i and wave vector $\mathbf{k}_i$), an elementary excitation such as a phonon (with frequency ω_q and wave vector $\mathbf{q}$) and the scattered photon (with frequency ω_s and wave vector $\mathbf{k}_s$). The conservation of energy and momentum of this interaction can be written as [6]

$$\hbar\omega_i = \hbar\omega_s \pm \hbar\omega_q \tag{3.1}$$

$$\hbar\mathbf{k}_i = \hbar\mathbf{k}_s \pm \hbar\mathbf{q}. \tag{3.2}$$

These equations correspond to a first-order Raman process, and the positive signs correspond to scattering processes in which a phonon is created (Stokes component), while the negative correspond to phonon absorption (anti-Stokes). A scheme illustrating the energy conservation in these Raman processes is shown in Fig. 3.1.

The conservation of the wave vector in the scattering processes imposes important restrictions on the phonons that can be detected through the light scattering experiments. The magnitude of the phonon wave vector $\mathbf{q}$ is determined by the scattering geometry, i. e. the angle θ between the incident and the scattered radiation. The minimum value of $|\mathbf{q}|$ is obtained in forward-scattering ($\theta = 0°$), while the maximum value is obtained in backscattering ($\theta = 180°$). However, in all scattering geometries the range of scattering wave vectors that can be probed with inelastic light scattering is determined by the excitation light used [7]. Since $|\mathbf{k}_i| = 2\pi/\lambda$, for typical light scattering experiments (near the visible range), the range of scattering wave vectors is

$$0 \leq |\mathbf{q}| \lesssim 1 \times 10^6 \mathrm{cm}^{-1}. \tag{3.3}$$

This implies that first-order Raman scattering only allows one to study the excitations near the center of the Brillouin zone. In higher-order processes, in which two or more elementary excitations participate in the scattering process,

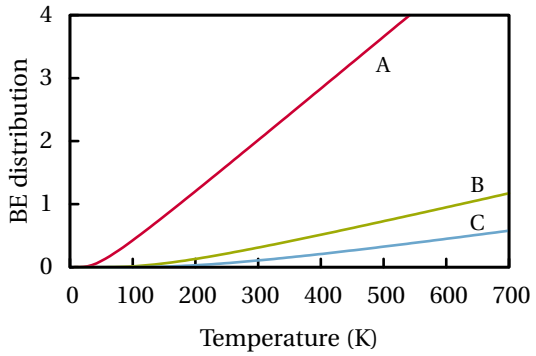

Figure 3.2: *Bose-Einstein occupation factors as a function of the temperature for phonons with a frequency of 84 cm^{-1} (A), 300 cm^{-1} (B) and 488 cm^{-1} (C).*

the individual wave vectors of the excitations $\mathbf{q}_i$ can range from zero to a reciprocal lattice wave vector corresponding to the edge of the first Brillouin zone. In this case it is the total scattered wave vector $\mathbf{q}_N$, defined as

$$\mathbf{q}_N = \sum_i^n \mathbf{q}_i, \tag{3.4}$$

that satisfies the wave vector conservation given in Eq. (3.2).

As mentioned above, in the case of the Brillouin scattering, the elementary excitations involved are acoustic phonons. Just like in the case of Raman scattering, the fulfilment of the wave vector conservation rule given by Eq. (3.2) implies that only phonons close to the zone-center can be detected. Since acoustic phonons with wave vectors close to the zone-center have very small energies, the scattered light in Brillouin experiments has frequencies that are extremely close to the elastically scattered light. Thus, the experimental set-up for the Brillouin scattering consists of a interferometric system, while Raman scattering can be measured by a dispersive spectrometer.

Stokes and anti-Stokes scattering

The Stokes scattering is the component of the Raman scattering that refers to phonon excitation, while the anti-Stokes scattering corresponds to phonon annihilation. Since for the anti-Stokes process a phonon must exist before the interaction, the probability of the process depends on the phonon population. In Figure 3.2 we can see the population of three different phonons as a function of the temperature, which is given by the Bose-Einstein distribution. The phonon frequencies used in this figure have been chosen to illustrate the Bose-Einstein distribution behaviour and correspond to the InN E_2^{low} phonon mode (A), a Si second-order peak (B) and InN E_2^{high} (C).

The probability of the anti-Stokes scattering increases with the temperature,

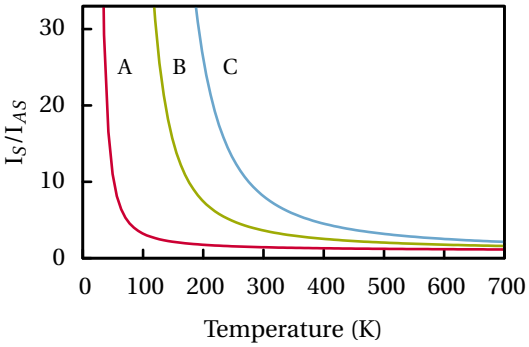

Figure 3.3: *Intensity ratio between the Stokes and the anti-Stokes scattering for phonons with frequencies of 84 cm^{-1} (A), 300 cm^{-1} (B) and 488 cm^{-1} (C).*

while the probability of the Stokes scattering is fairly independent of temperature. In Fig. 3.3 we have plotted the ratio between the Stokes intensity (I_S) and the anti-Stokes intensity (I_{AS}) for a non-resonant scattering by a phonon with frequency ω_q, which is given by

$$\frac{I_S}{I_{AS}} = \frac{(\omega_i - \omega_q)^4}{(\omega_i + \omega_q)^4} \times \exp\left(\frac{\hbar\omega_q}{k_B T}\right). \tag{3.5}$$

Figure 3.4 shows both the Stokes and the anti-Stokes spectrum of the low-frequency phonons of an InN NWs sample taken at room temperature. The spectra have been obtained with very low excitation power in order to minimize heating effects. These spectra exhibit three modes: the E_2^{low} phonon mode of InN (84 cm^{-1}), a large-wavevector longitudinal acoustical phonon (LA) of InN (150 cm^{-1}), and a second-order mode arising from the silicon substrate (300 cm^{-1}). In fact, calculations A and B plotted in Fig. 3.2 and Fig. 3.3 have been obtained using the frequencies of the E_2^{low} and the Si second order mode mode shown in the spectra of Fig. 3.4. As expected, the intensity ratio between the Stokes and anti-Stokes signal plotted in Fig. 3.4 depends on the energy of the modes. The lowest-energy mode (E_2^{low}) is visibly more intense in the Stokes than in the anti-Stokes spectra, but the difference in intensity is more pronounced for the higher energy modes. This is because at room temperature the occupation factor for the E_2^{low} phonon mode is greater than for the higher energy modes. In general, Eq. (3.5) can be used to extract the actual temperature of the samples from the analysis of the Stokes to Anti-Stokes intensity ratio. In the spectra shown in Fig. 3.4 the only phonon mode arising from NWs is the low-energy E_2^{low}. As can be seen in Fig. 3.3, the Stokes to Anti-Stokes intensity ratio of these mode (corresponding to A) is almost constant in the temperature range of interest. Therefore, a reliable determination of the NWs temperature cannot be extracted from the Anti-Stokes and Stokes spectra comparison in this case. All

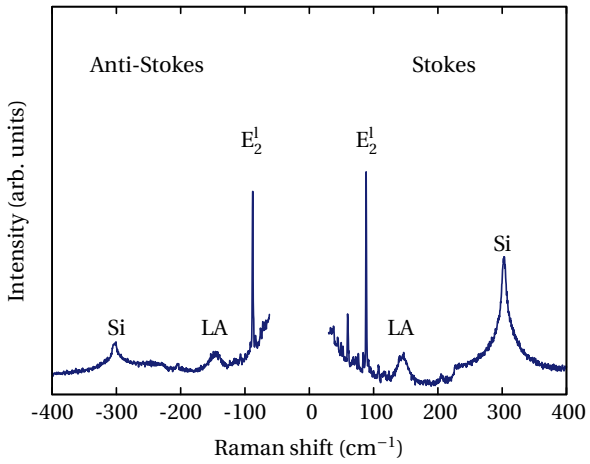

Figure 3.4: *Raman spectrum of InN NWs grown on silicon substrate. Low-frequency ranges of both Stokes and anti-Stokes signal are shown.*

the Raman spectra presented in this thesis correspond to Stokes spectra, since they are significantly more intense at the measurement temperatures.

3.1.2 Semi-classical approach

In the framework of a semi-classical approach, the light-matter interaction can be understood taking into account the description of matter as an ensemble of dipoles. In this framework, the response of the material to an electromagnetic perturbation is governed by its electric susceptibility χ [8]. Although χ is in general a second rank tensor, we assume an isotropic medium and then the susceptibility becomes an scalar. A perturbation in the material, such as an atom displacement pattern, results in changes of its electric susceptibility.

The atomic displacements in a crystalline material are quantised into phonons with frequency ω_q and wave vector q, and can be expressed as plane waves,

$$\mathbf{Q}(\mathbf{r},t) = \mathbf{Q}(\mathbf{q},\omega_q)\cos(\mathbf{qr} - \omega_q t). \tag{3.6}$$

As these phonon excitations have frequencies much smaller than those corresponding to the electronic transitions, the electric susceptibility can be written in terms of $\mathbf{Q}$ within the quasi-static approximation. Given that the vibration amplitudes are small compared to the lattice constant, the susceptibility can be expanded as a Taylor series in the atomic displacements as

$$\chi(\mathbf{k}_i,\omega_i,\mathbf{Q}) = \chi_0(\mathbf{k}_i,\omega_i) + \left(\frac{\partial\chi}{\partial\mathbf{Q}}\right)_0 \mathbf{Q}(\mathbf{r},t) + ..., \tag{3.7}$$

where χ_0 corresponds to the electric susceptibility of the unperturbed medium.

Taking into account this description of the electric susceptibility modulation by the phonon excitation, we can evaluate the response of the medium to an electromagnetic wave. We consider a sinusoidal plane electromagnetic field described by

$$\mathbf{E}(\mathbf{r},t) = \mathbf{E}_i(\mathbf{k}_i,\omega_i)\cos(\mathbf{k}_i\mathbf{r}-\omega_i t), \tag{3.8}$$

which induces a polarisation in the medium given by [8]

$$\mathbf{P}(\mathbf{r},t) = \chi(\mathbf{k}_i,\omega_i)\mathbf{E}(\mathbf{r},t) = \chi(\mathbf{k}_i,\omega_i)\mathbf{E}(\mathbf{k}_i,\omega_i)\cos(\mathbf{k}_i\mathbf{r}-\omega_i t). \tag{3.9}$$

If we take into account the dependence of the susceptibility on the atomic displacements given in Eq. (3.7), the polarisation can be written as

$$\mathbf{P}(\mathbf{r},t,Q) = \mathbf{P}_0(\mathbf{r},t) + \mathbf{P}_{\text{ind}}(\mathbf{r},t,\mathbf{Q}) \tag{3.10}$$

where $\mathbf{P}_0$ accounts for the polarisation vibrating in phase with the incident vibration and $\mathbf{P}_{\text{ind}}$ is the polarisation induced by the atomic oscillations,

$$\mathbf{P}_0(\mathbf{r},t) = \chi_0(\mathbf{k}_i,\omega_i)\mathbf{E}_i(\mathbf{k}_i,\omega_i)\cos(\mathbf{k}_i\mathbf{r}-\omega_i t) \tag{3.11}$$

and

$$\mathbf{P}_{\text{ind}}(\mathbf{r},t,\mathbf{Q}) = \left(\frac{\partial\chi}{\partial\mathbf{Q}}\right)_0 \mathbf{Q}(\mathbf{r},t)\mathbf{E}_i(\mathbf{k}_i,\omega_i)\cos(\mathbf{k}_i\mathbf{r}-\omega_i t). \tag{3.12}$$

The induced polarisation can be written in terms of the phonon frequency and wave vector as

$$\begin{aligned}\mathbf{P}_{\text{ind}}(\mathbf{r},t,\mathbf{Q}) &= \left(\frac{\partial\chi}{\partial\mathbf{Q}}\right)_0 \mathbf{Q}(\mathbf{q},\omega_q)\cos(\mathbf{q}\mathbf{r}-\omega_q t)\times\mathbf{E}_i(\mathbf{k}_i,\omega_i)\cos(\mathbf{k}_i\mathbf{r}-\omega_i t)\\ &= \frac{1}{2}\left(\frac{\partial\chi}{\partial\mathbf{Q}}\right)_0 \mathbf{Q}(\mathbf{q},\omega_q)\mathbf{E}_i(\mathbf{k}_i,\omega_i t)\times\Big\{\cos\left[(\mathbf{k}_i+\mathbf{q})\mathbf{r}-(\omega_i+\omega_q)t\right]\\ &\quad+\cos\left[(\mathbf{k}_i-\mathbf{q})\mathbf{r}-(\omega_i-\omega_q)t\right]\Big\}.\end{aligned} \tag{3.13}$$

This expression describes the modulation of the dipole due to changes in the polarisability caused by the atomic oscillations (i.e., phonons). When the partial derivative of the susceptibility is non-zero, this term accounts for the radiation which is scattered with a frequency corresponding to the sum or the difference of the incident light frequency (ω_i) and the vibrational mode frequency (ω_q). Therefore, this term accounts for the Raman scattering processes which, depending on the frequency of the scattered light, are known as Stokes process (sum frequency) or an anti-Stokes process (difference frequency). From this equation, it can be deduced that within the semi-classical approximation, the

Raman scattering takes place when the atomic oscillations induced by the interaction of the crystal with the radiation result in a change of the crystal susceptibility. This depends on the crystal symmetry and on its relative orientation with respect the propagation and the polarisation of the incident and scattered light.

By calculating the time-averaged power radiated by the induced polarisations $\mathbf{P}_{\text{ind}}$ into the solid angle, the intensity of the Stokes scattered radiation can be expressed as [8]

$$I_s \propto \left| \mathbf{e}_i \cdot \left(\frac{\partial \chi}{\partial \mathbf{Q}} \right)_0 \mathbf{Q}(\omega_q) \cdot \mathbf{e}_s \right|^2, \tag{3.14}$$

where $\mathbf{e}_i$ and $\mathbf{e}_s$ correspond to the polarisation of the incident and scattered light, respectively. The partial derivatives of the susceptibility with respect to the atomic displacements of a given phonon are, in general, the elements of a second-rank tensor called Raman tensor $\overleftrightarrow{R}$,

$$\overleftrightarrow{R} = \left(\frac{\partial \chi}{\partial \mathbf{Q}} \right)_0 \hat{\mathbf{Q}}(\omega_q). \tag{3.15}$$

Each phonon mode is described by one Raman tensor that transforms like the irreducible representation to which it belongs. The irreducible representations and Raman tensors for phonons in wurtzite crystals will be given in Chapter 4. The expression given in Eq. (3.14) can therefore be rewritten in terms of the Raman tensor as

$$I_s \propto \left| \mathbf{e}_i \cdot \overleftrightarrow{R} \cdot \mathbf{e}_s \right|^2. \tag{3.16}$$

Eq. (3.16) gives the selection rules of the first-order phonon Raman scattering. Since this expression has been derived from the semi-classical approximation, it does not account for all the possible Raman interactions but it describes well those occurring via the so-called *dipole-allowed* mechanisms that will be discussed in the next section.

3.1.3 Quantum-mechanical approach

Within the semi-classical approach we have described the Raman effect taking into account the interaction between the electromagnetic radiation and the atomic displacements. Although that framework provides an intuitive picture of the phenomenon, it is necessary to use quantum mechanics to fully describe the inelastic light scattering process.

We recall the approach to the Raman scattering by phonons given at the beginning of this chapter, that is, we consider an incident photon (with frequency ω_i and wave vector $\mathbf{k}_i$) which is scattered by a phonon (with frequency ω_q and wave vector $\mathbf{q}$) and a photon is emitted (ω_s and $\mathbf{k}_s$). Regarding this semiclassical

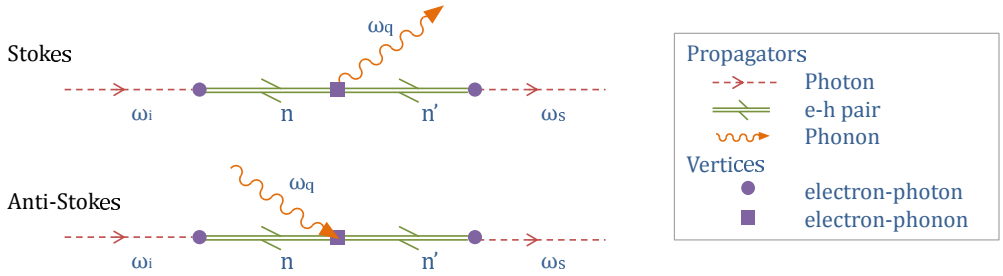

Figure 3.5: *Feynman diagrams of the most likely Stokes and anti-Stokes processes. The rules for drawing the Feynman diagrams are given in Ref. [8], and can be summarised as: excitations are represented by lines (propagators) and interaction between excitation is prepresented by vertices; arrows in propagators indicate creation (pointing away from the vertex) or anihilation (pointing towards the vertex) of the excitation.*

picture, it might appear that electrons are not involved in the scattering process, which could therefore be described by the photon-phonon Hamiltonian. However, the strength of the photon-phonon interaction is very weak due to the big difference existing between their respective energies, while electron-phonon coupling is much stronger. Therefore, Raman scattering by phonons in a semiconductor occurs through the creation of an electron-hole pair in the system [8]. Therefore, although the electrons remain unchanged after the process, they play a key role in the scattering by phonons.

All the possible interactions involved in a scattering process can be represented systematically with Feynman diagrams. We plot in Fig. 3.5 the Feynman diagrams of the most likely process involved in a one-phonon Stokes or anti-Stokes scattering. We can describe the first diagram in Fig. 3.5, as a three-step process:

1. The incident photon (ω_i, $\mathbf{k}_i$) excites the lattice system by creating an electron-hole pair (real or virtual), denoted by n.

2. The electron-hole pair is scattered to another state (denoted by n') via the creation/annihilation of a phonon (ω_q, $\mathbf{q}$).

3. The electron-hole pair recombines radiatively and emits the scattered photon (ω_s, $\mathbf{k}_s$)

There are in total six possible diagrams for the Stokes as well as for the anti-Stokes process. They correspond to permutations of the time order of the three vertices of the diagrams shown in Fig. 3.5, and can be found in Ref. [8]. Taking into account the interactions shown by each of these diagrams, we can derive

the scattering probability. To this purpose, we calculate the scattering rate for the interaction at each vertex. As shown in Ref. [8], the scattering rate $P(k,k')$ of a scattering process described with a generic Hamiltonian H_{sc} can be calculated using the Fermi Golden Rule,

$$P(k,k') = \frac{2\pi}{\hbar}\left|\langle k|H_{\text{sc}}|k'\rangle\right|^2 \rho_f, \tag{3.17}$$

where ρ_f is the density of final states k' that conserve both the energy and the wave vector.

Then, for the Raman scattering process, the total scattering rate can be obtained by the product of the scattering rates associated with each vertex of the Feynman diagram. This results in a long expression whose denominator can be simplified assuming the energy conservation condition. For the Stokes scattering process depicted in Fig. 3.5, the scattering probability will be given by

$$P_{\text{ph}}(\omega_s) = \frac{2\pi}{\hbar}\left|\sum_{n,n'}\frac{\langle i|H_{\text{eR}}(\omega_s)|n'\rangle\langle n'|H_{\text{ep}}|n\rangle\langle n|H_{\text{eR}}(\omega_i)|i\rangle}{\left[\hbar\omega_i-(E_n-E_i)\right]\left[\hbar\omega_i-\hbar\omega_q-(E_{n'}-E_i)\right]}\right|^2 \delta\left(\hbar\omega_i-\hbar\omega_q-\hbar\omega_s\right). \tag{3.18}$$

In this equation, H_{eR} and H_{ep} are the electron-radiation and the electron-phonon interaction hamiltonians, respectively. Due to the large number of unknown parameters, Eq. (3.18) is not too useful for a quantitative calculation of Raman efficiencies. However, the inspection of the Hamiltonians describing the electron-radiation and electron-phonon interactions gives insight on the mechanisms underlying the scattering process.

3.1.3.1 H_{eR}: Electron - photon interaction

The first and the last terms of Eq. (3.18) account for the interaction between electrons and photons. This interaction has an electromagnetic nature and its Hamiltonian can be written as

$$H_{\text{eR}} = \frac{e}{mc}\mathbf{A}\cdot\mathbf{p}, \tag{3.19}$$

where $\mathbf{A}$ is the vector potential of the electromagnetic field and $\mathbf{p}$ is the quasi-momentum of the electron or hole involved in the scattering process.

The electron-photon scattering rate increases dramatically when the incident or scattered light have the same energy as a real electronic transition. To illustrate this point, we take into account the first vertex of the diagram shown in Fig. 3.5. The term that this vertex adds to the total scattering probability is of the form

$$\sum_n \frac{\langle n|H_{\mathrm{eR}}(\omega_i)|i\rangle}{[\hbar\omega_i - (E_n - E_i)]}, \tag{3.20}$$

where $|i\rangle$ and $|n\rangle$ are the initial and the intermediate electronic states, respectively, whose energies are E_i and E_n. If we consider that the initial state is the fundamental state ($|0\rangle$, $E_i = 0$) and the intermediate state is a real state ($|g\rangle$, E_g), then Eq. (3.20) can be written as

$$\frac{\langle 0|H_{\mathrm{eR}}(\omega_i)|g\rangle}{\left(\hbar\omega_i - E_g\right)}. \tag{3.21}$$

Therefore, when the energy of the incident light equals the band-gap energy ($\hbar\omega_i = E_g$), the term of the scattering probability described in Eq. (3.21) is enhanced and the total scattering probability is much higher. This leads to an incoming resonance in the Raman scattering cross-section. Similarly, an outgoing resonance occurs when it is the scattered photon that has the same energy as the real electronic transition.

3.1.3.2 H_{ep}: Electron - phonon interaction

As a general rule, the electron-phonon interaction occurs when there is a change in the bond polarisability that alters the energy of the electronic bands. Optical phonons can cause these changes essentially through two mechanisms. The first one is by altering the bond lengths and/or angles, and is referred to as *deformation potential* interaction. The second mechanism is the *Fröhlich* interaction, which takes place only in polar crystals. In these crystals, the lattice phonons that involve a net charge displacement in the unit cell give rise to a macroscopic electric field that alters the energy of the electronic bands.

As stated above, the deformation potential entails a change in the electronic energies is due to changes in bond angles or interatomic lengths. The Hamiltonian that describes this scattering mechanism can be written as a function of the electronic energy E and the atomic displacement coordinates $\mathbf{Q}$ as

$$H_{\mathrm{ep}}^{\mathrm{DP}} \propto \frac{\partial E}{\partial \mathbf{Q}}\mathbf{Q} \tag{3.22}$$

The expansion of this Hamiltonian is equivalent to the expansion of the susceptibility tensor. Therefore, the Raman tensors and selection rules that can be derived from the semi-classical approximation are conceptually equivalent to those derived taking into account the deformation potential mechanism in the quantum mechanical approach.

The other mechanism accounting for electron-phonon interaction is the Fröhlich mechanism, which is specific to polar crystals. In these materials, the

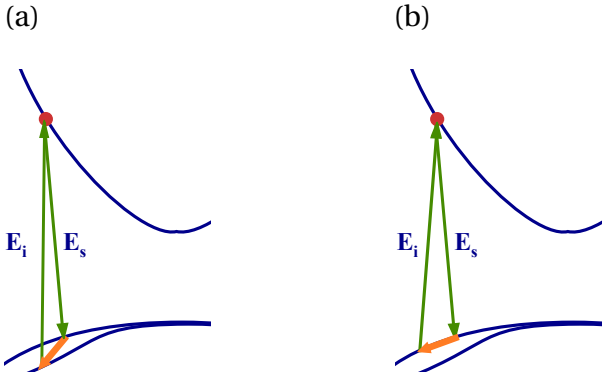

Figure 3.6: *Scheme of the inter-band electro-optic scattering (a) and the intra-band Fröhlich scattering (b).*

atomic displacements related to the longitudinal optical (LO) phonon modes give rise to macroscopic electric fields that interact with the electronic energies through a long-range Coulomb interaction. This mechanism is described by the Hamiltonian

$$H_{\mathrm{ep}}^{F} = -\frac{iC_F}{q^2 V^{1/2}}(\mathbf{q}\cdot\hat{\mathbf{e}}_{\mathrm{LO}})\left(a_{-\mathbf{q}}^{\dagger} + a_{\mathbf{q}}\right) \times \exp\left(i\mathbf{q}\cdot\mathbf{r}\right), \tag{3.23}$$

where C_F is the Fröhlich constant, $V^{1/2}$ is the crystal volume, and $a_{-\mathbf{q}}^{\dagger}$ and $a_{-\mathbf{q}}$ are the phonon creation and annihilation operators. The Fröhlich constant can be written as a function of the frequency of the phonon ω_q and the high-frequency and low-frequency dielectric constants as follows

$$C_F = e\left[2\pi\hbar\omega_q\left(\frac{1}{\varepsilon_\infty} - \frac{1}{\varepsilon_0}\right)\right]^{\frac{1}{2}}. \tag{3.24}$$

There exist two kinds of Fröhlich mechanisms, which arise from the number of electronic bands involved in the interaction process. When the initial and the final electronic states correspond to the same electonic band, the process is *intra-band* and is known as the generic Fröhlich interaction. Figure 3.6(b) shows a schematic representation of this interaction. If the initial and the final electronic bands are different, the process is *inter-band* and the interaction mechanism is the *electro-optic* [see Fig. 3.6(a)]. Although being described by the same Hamiltonian, both processes have different Raman tensor symmetry, which implies that their selection rules are also different [8].

The inter-band electro-optic interaction is described by a Raman tensor with the same symmetry as the deformation potential mechanism, and therefore it is

detected in the same scattering configurations. In fact, both the deformation potential and the electro-optic interaction are called *dipole-allowed* mechanisms, since they can be derived from the semi-classical approach that considers the matter as an ensemble of dipoles.

The intra-band Fröhlich interaction is described by a diagonal Raman tensor, which implies that this mechanism takes place when the polarisation of the incident and the scattered light have components in the same direction. Since its Raman tensor symmetry is in general different from that of the *dipole-allowed* mechanisms, this mechanism allows the detection of phonons in *dipole-forbidden* configurations, as will be presented in the next Chapter.

Due to its electromagnetic origin, the intra-band Fröhlich scattering mechanism is strongly enhanced near electronic resonances or by the presence of external electric fields. One example is the *impurity-induced Fröhlich* interaction, in which the scattering rate is enhanced by the Coulomb interaction with charged impurities. In this process the intermediate electron or hole undergoes two scattering processes (with an impurity and with a phonon). Since the wave vector selection rule [Eq. (3.2)] has to be fulfilled by the total scattered wave vector $\mathbf{q}_N$ [Eq. (3.4)], non-zone-center phonons can participate in the scattering process. The participation of non-zone-center phonons results in wider Raman peaks, since phonons with different frequencies participate on the scattering [7].

This and other resonance mechanisms are described in Chapter 6, that is entirely devoted to resonant Raman scattering.

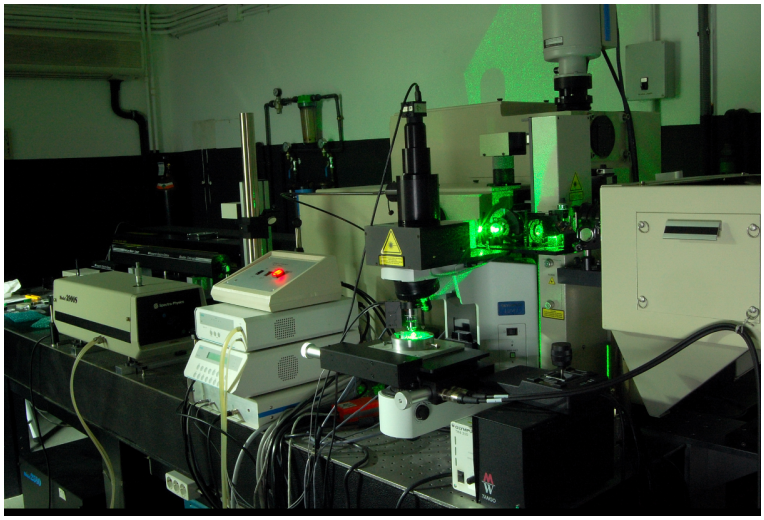

Figure 3.7: *Image of the spectrometer Jobin-Yvon T-64000 installed in the Raman laboratory of the Institute Jaume Almera (ICTJA-CSIC).*

3.2 Experimental equipment for Raman spectroscopy

In the previous section we have addressed the theoretical basis of the Raman scattering. In this section we describe the experimental equipment used in this thesis to perform the Raman scattering measurements.

To obtain Raman spectra, a monochromatic light source is focused on the sample and the scattered light is collected and analysed by an spectrometer. The spectrometer eliminates the strong signal arising from the elastic scattering and separate all the components of the inelastically scattered light before focusing it on the detector. The resulting Raman spectrum displays the intensity of the inelastically scattered light as a function of the Raman shift, which is defined as the difference between the incident and scattered spectroscopic wave numbers,

$$\text{Raman shift} = \frac{1}{\lambda_i} - \frac{1}{\lambda_s} \tag{3.25}$$

and is usually given in cm^{-1} units. Since on account of Planck's equation ($E = \hbar\omega = hc/\lambda$) the photon wave number is proportional to the photon energy (and hence to the photon frequency), energy conservation implies that the Raman shift is proportional to the energy (or frequency) of the created or absorbed elementary excitation [6].

The Raman scattering studies presented in this thesis have been carried out

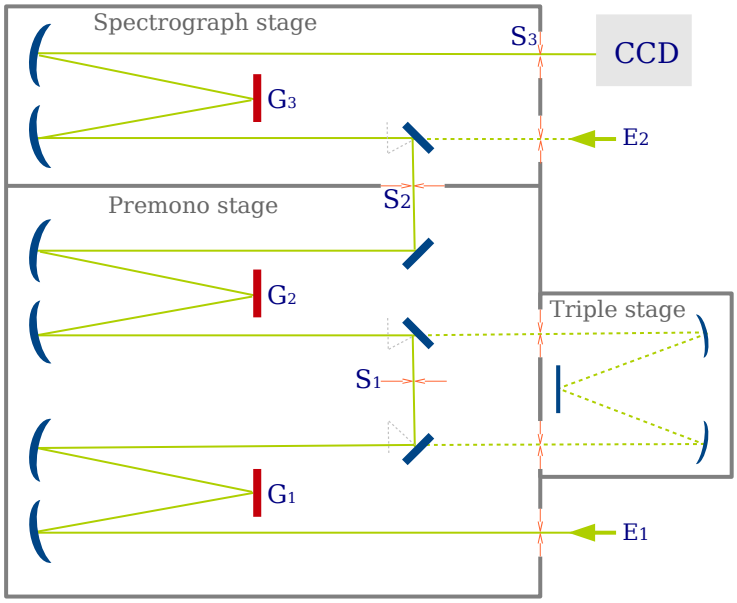

Figure 3.8: *Scheme of the T-64000 spectrometer. The three stages of the equipment are depicted with its main optical elements (blue elements represent mirrors, G = diffraction gratings, E = entrance slits, S = intermediate slits. Green line indicates the optical path of the light inside the spectrometer.*

in the Raman laboratory of the Institute Jaume Almera (ICTJA-CSIC). In this section we describe the experimental equipment used to perform the optical measurements.

The T-64000 Raman spectrometer

The Raman spectrometer used in this thesis is a Jobin-Yvon T-64000, a high resolution Raman spectrometer with high sensitivity and stray-light rejection capabilities. Fig. 3.7 shows an image of the spectrometer as it is installed in our laboratory. It can be operated in different configurations due to its versatile design. An scheme of the spectrometer is shown in Fig. 3.8. In our present set-up, the T-64000 can operate in two configurations and in three different modes. The two configurations differ in how the light is focused on the sample: either through a microscope (*micro-Raman*) or through converging lenses (*macrocamera* configuration). The three modes of operation differ in the optical path of the scattered light inside the spectrometer, and in the configuration of the diffraction gratings, mirrors and slits.

In order to describe all of them, we first outline the optical elements of the spectrometer, referring to the scheme presented in Fig. 3.8. As can be seen in

Table 3.1: *Characteristics of the diffraction gratings*

Lines/mm	Blaze λ (nm)	Characteristics
2400	400	High-resolution UV spectra
1800	500	High-resolution visible and IR spectra
1200	330	Wide-range UV spectra
600	500	Wide-range visible and IR spectra

the figure, we consider essentially three parts of the spectrometer. The *premono* stage is used to eliminate the elastically scattered light. When the scattered light enters the premono stage it is dispersed at G_1 and can go through the intermediate slit S_1 (which eliminates the elastically scattered light) or through the *triple* stage (to increase the spectral resolution). The second diffraction grating (G_2) can recombine or disperse again the beam, depending on the spectrometer mode of operation. After the premono stage, the beam is focused on the intermediate slit (S_2), which is the image of the entrance slit E_1. Next, the beam passes through the *spectrograph* stage, where it is dispersed before reaching the LN_2-cooled charge-coupled device (CCD) detector.

The diffraction gratings of the spectrograph stage can be changed in order to optimise the scattering efficiency for a certain excitation wavelength and to choose between highly-dispersive and low-dispersive scattering performance. A list of the diffraction gratings used in this thesis with their specifications is given in Table 3.1.

Among all the available diffraction gratings, the most commonly used in this thesis has been the one with 1800 lines/mm, which is a highly dispersive diffraction grating (25.9 cm^{-1}/mm at 514.5 nm) and has its maximum performance at the visible light range.

As mentioned above, the spectrometer set up can collect the scattered light in two different configurations, *micro-Raman* and *macrocamera*.

In the case of *micro-Raman* measurements, the excitation light reaches the sample through a microscope system, and therefore it provides local probing of the Raman spectra with high spatial resolution (the laser spot diameter on the sample is $\approx 1\mu$m). This configuration is useful to assess the homogeneity of a sample and to have spatially-resolved measurements. Furthermore, using the confocal pinhole allows us to have in-depth resolution (the confocal set-up is explained below). On the other hand, the concentration of light in a small area can lead to heating effects in opaque samples. To avoid these effects, very low excitation powers are usually employed in the micro-Raman configuration.

In the *macrocamera* configuration, the excitation light reaches the sample

through converging lenses. The laser spot on the sample has a diameter of ≈ 250μm, which is much greater than that of the micro-Raman, and therefore the collected spectra arise from a bigger area. It is useful for homogeneous samples and it avoids heating effects on the sample.

Depending on the optical path and the stages used, three spectrometer modes exist, which are:

- Triple additive - In the triple additive mode, the scattered light enters the spectrometer through the E_1 entrance slit, and passes through the pre-mono and the triple stage before entering the spectrograph stage. This is the highest-resolution mode because the three diffraction gratings scatter the light successively and the focal length is maximum.

- Triple subtractive - In this mode, the scattered light enters the spectrometer through the E_1 entrance slit but does not pass through the triple stage. In this optical configuration the first grating scatters the light and the second one recombines it once that the elastically scattered light has been blocked in S_1. This configuration allows one to measure low-frequency Raman spectra. Because the wavelength separation achieved by a single spectrograph grating is lower than the one achieved by the three gratings in the triple additive configuration, the triple subtractive configuration has a somewhat lower resolution. However, since for a given peak the photons are distributed over a smaller number of pixels, the Raman peak intensity is higher. Because of the favourable tradeoff between signal level and resolution, the triple subtractive is the mode most widely used in this thesis.

- Single - In single mode the scattered light enters the spectrograph stage directly through the E_2 entrance slit. This requires the use of a notch filter to remove the elastically scattered light before entering the spectrometer. This is the mode with highest signal, since the scattered light only interacts with one diffraction grating. However, the use of the notch filter limits the low-frequency measurements to ≈ 180 cm^{-1}.

Spectral resolution

Each of the spectrometer modes leads to spectra with different intensity, spectral range and spectral resolution. In addition to the scattering mode, the entrance slit width also plays a crucial role in determining the spectral resolution of the measurements. To characterise the spectral resolution of the spectrometer, we have measured the emission line of an Hg lamp in the most commonly used spectrometer modes. The obtained spectra for different slit widths are shown in Fig. 3.9. In this figure it can be seen that, as explained above, the linewidth

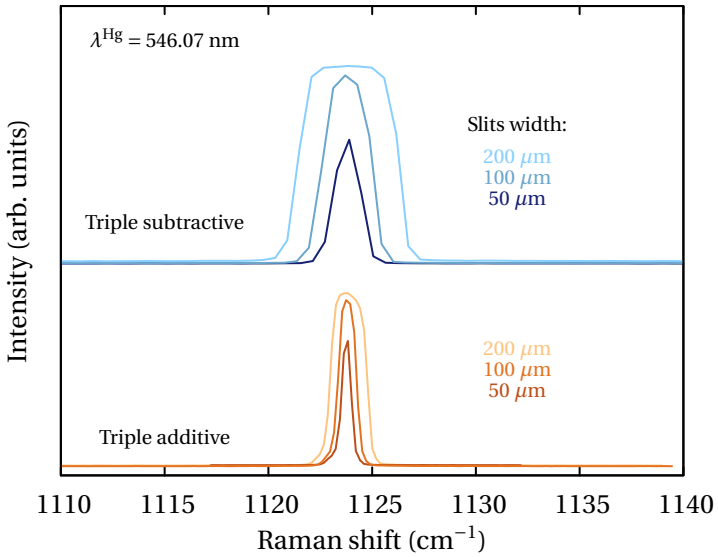

Figure 3.9: *Spectra of the Hg emission line obtained with different spectrometer configurations and entrance slit widths. The spectrometer was centered at* λ = 514.5 *nm.*

Table 3.2: *Spectral width for different entrance slit widths in the triple subtractive and additive spectrometer modes, respectively. Values of the spectral width correspond to the full width at half maximum of a Gaussian fit to the spectra of the 546.07-nm emission line of a Hg lamp (shown in Fig. 3.9).*

Spectrometer mode	Slit width (μm)	Spectral width (cm^{-1})
Triple subtractive	200	4.8
	100	2.2
	50	1.4
Triple additive	200	1.7
	100	0.9
	50	0.5

of the emission line is about three times higher in the case of the triple subtractive mode for the same slit width. To evaluate the spectral resolution in each scattering mode, we have fitted a Gaussian line shape to the spectra shown in Fig. 3.9. The values of the full width at half maximum (FWHM) of these Gaussian fits correspond to the spectral band width of each operation mode, and are summarised in Table 3.2.

The *standard spectrometer mode* used in this thesis is the triple subtractive, with a slit width of 100 μm. This mode has a spectral width of 2.2 cm^{-1}, which is much smaller than the linewidth of most of the studied phonon modes. However, in order to measure the linewidth of very narrow peaks, high-resolution triple additive mode with a slit width of 50μm has also been used (we refer to it as *high-resolution* mode).

The Raman line shape measured in the experiments is the convolution of the natural Lorentzian line shape of the phonons with the Gaussian instrument broadening function. In order to separate both contributions and to know the intrinsic linewidth of the phonon modes, the actual phonon linewidths can be evaluated from the Raman spectra using the Voigt profile approximation. According to this approximation, the measured peak linewidth (Γ) is related to the intrinsic phonon mode linewidth (Γ_L) and the spectral bandwidth (Γ_G) through the following expression [9]:

$$\Gamma \approx 0.5346\Gamma_L + \sqrt{0.2166\Gamma_L^2 + \Gamma_G^2}. \tag{3.26}$$

In Fig. 3.10 we have plotted the measured linewidth as a function of the intrinsic phonon linewidth for the standard and the high-resolution scattering modes. It can be seen that in the high-resolution scattering mode the spectrometer response has a negligible effect on the measured linewidth, while in the standard triple subtractive scattering mode the spectrometer response results in a small increase of the measured linewidth with respect the intrinsic one. The effect of the spectrometer response has been taken into account throughout all this thesis by using the expression given in Eq. (3.26).

The laser excitation sources

The excitation wavelength used in most studies presented here is the 514.5-nm line of an Ar^+ laser. However, other excitation wavelengths have been used to perform some specific experiments such as the studies related to the resonance effects (which are presented in Chapter 6). An Argon ion laser, a He-Ne gas laser, a He-Cd laser, a Ti:sapphire solid state pumped laser and a frequency-doubled Nd:YAG solid-state laser diode were used as excitation sources. The wavelengths used are listed in Table 3.3 for the different excitation lasers. The selection of a

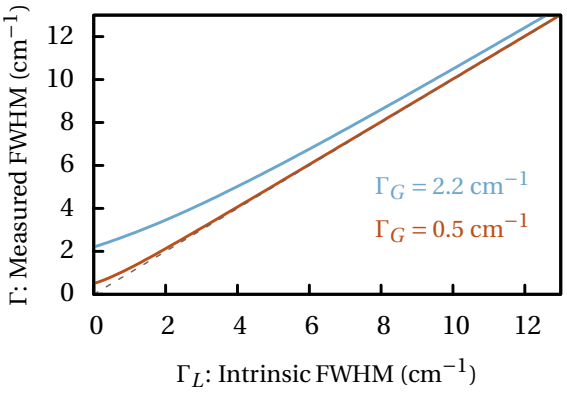

Figure 3.10: *Measured linewidth vs. intrinsic linewidth, obtained from Eq. (3.26.)*

specific excitation energy was required in some of the experiments to achieve suitable resonant or optical absorption conditions.

Table 3.3: *Excitation sources and wavelengths of the excitation lines used in this thesis*

Laser	Wavelengths (nm)
Ar^+	514, 488
He-Ne	633
He-Cd	325
Ti:sapphire	710, 780, 820
Nd:YAG diode	532

The excitation light is focused on the sample through a converging lens system. The experiments presented in this thesis have been performed in backscattering geometry, and therefore the scattered light has been collected through the same lens system before being focused on the spectrometer entrance slit.

Since the efficiency of the diffraction gratings strongly depends on the light polarisation direction, the control of the polarisation of the scattered light is important to maximise the intensity of the Raman signal. We have used polarisers and polarisation rotators to control the polarisation of the incident and scattered light, and therefore to select the scattering configuration of each measurement.

The T-dependent measurements

To perform low-temperature measurements, the samples have been cooled using the liquid-nitrogen cryostat that is shown in Figure 3.11(a). It can be attached to the macrocamera stage of the T-64000 spectrometer and it is able to vary the

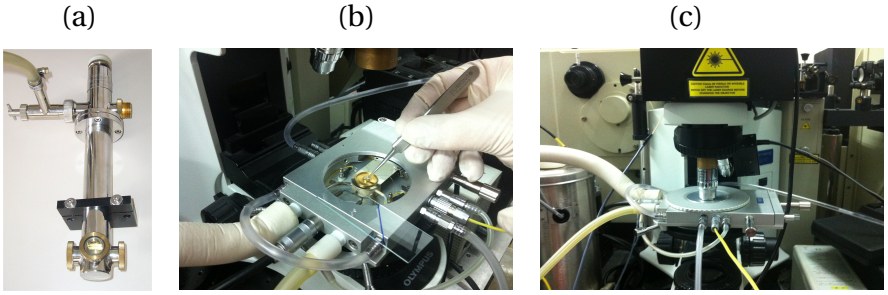

Figure 3.11: *LN_2 cryostat used to perform low-temperature measurements (a). The Linkam stage used for the high-temperature measurements with lid open (b) and in the operating mode (c)*

sample temperature from 80 to 390 K. To extend the temperature range up to 660 K, a Linkam high-temperature stage has been used (see pictures in Figure 3.11(b)(c)). This stage can be attached to the microscope used for the micro-Raman, and the measurements are performed with a long working-distance ×80 objective. A thermocouple is attached to the sample holder in close proximity to the sample in order to monitor its actual temperature, and very low excitation power is used to minimise local heating effects. An indium droplet is used to ensure a good thermal contact between the sample and the gold-plated copper sample holder.

The confocal measurements

In order to perform spatially-resolved Raman measurements, confocal Raman measurements have been used. In confocal Raman measurements, a point-like light source is focused onto the sample through a microscope, and the image of this spot enters the spectrometer through a small pinhole, as can be seen in the scheme shown in Fig. 3.12. As the pinhole is located in the image focal plane of the microscope, it is *confocal* with the illuminated spot. Only the light arising from a small area around the focal point reaches the detector [10]. Therefore, confocal micro-Raman allows one to select the probing depth of the measurements and to perform spatially-resolved experiments.

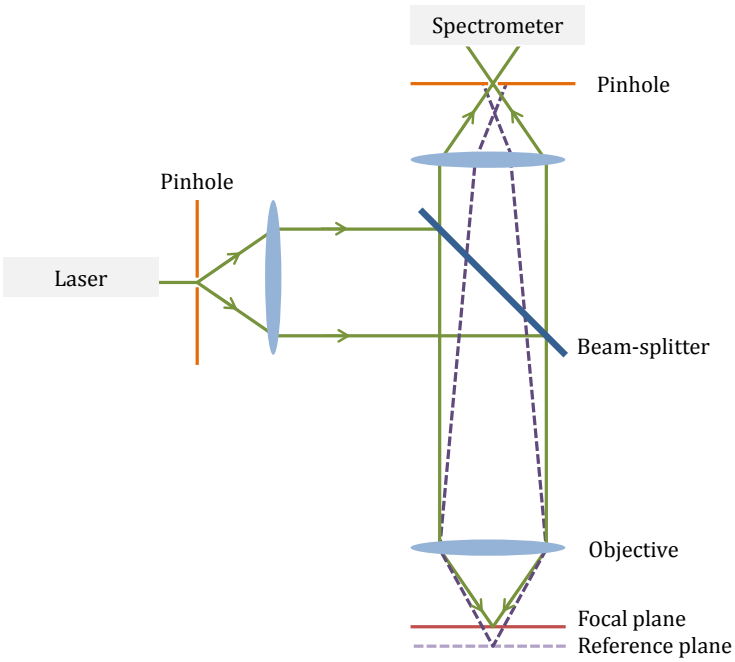

Figure 3.12: *Optical scheme of the confocal microscope. Green lines show the optical path of the focused plane. Dashed violet line show the optical path of a reference plane, different from the focal plane.*

References

[1] C. V. Raman and K. S. Krishnan. *Nature*, 121:501–502, 1928.

[2] G. S. Landsberg and L. I. Mandelstam. *Journal of the Russian Physico-Chemical Society, Physics Section*, 60:335, 1928.

[3] A. Smekal. *Naturwissenchaften*, 11:873–875, 1923.

[4] D. J. Gardiner and P. R. Graves. *Practical Raman Spectroscopy*. Springer-Verlag, 1989.

[5] W. H. Weber and R. Merlin. *Raman Scattering in Materials Science*. Springer-Verlag, 2000.

[6] J. Ibáñez and R. Cuscó. *Raman spectroscopy of compound semiconductors*. Semiconductor Research. Experimental Techniques. Editors: A. Patanè and N. Balkan. Springer-Verlag, 2012.

[7] M. Cardona. *Light scattering in Solids I*. Springer-Verlag, 1975.

[8] P. Y. Yu and M. Cardona. *Fundamentals of Semiconductors. Physics and materials properties*. Springer-Verlag, 1996.

[9] J. J. Olivero and R. L. Longbolhum. *Jour. of Quant. Spectr. and Rad. Transfer*, 17:233, 1977.

[10] T. Dieing, O. Hollricher, and J. Toporski. *Confocal Raman Microscopy*. Springer-Verlag, 2010.

CHAPTER 4

Phonons in wurtzite (In,Ga)N

In 1907, Einstein postulated the quantized nature of the atomic vibrations in a crystalline lattice in order to explain the temperature dependence of the molar specific heat capacity of a crystal [1]. He argued that the heat capacity of insulators was due to the vibrations of uncoupled atomic harmonic oscillators. Several years later, Debye postulated the coupling of the neighbouring oscillators [2]; and Born and von Kármán developed the classical theory of vibrations in a crystal lattice. Within this framework, the atomic vibrations can be represented by a collection of independent harmonic oscillators whose frequencies depend on the wave vector [3]. The quantization of these wave-particles are called *phonons* after Tamm in 1930 [4], and a decade later they became accepted as bosonic quasi-particles. Nowadays, all the physics textbooks define phonons as quanta of excitation of a normal vibrational mode [5].

This Chapter is devoted to describe the phonon modes in wurtzite InN and GaN. We first present some basic phonon theory such as the derivation of the phonon modes from the crystal Hamiltonian and the phonon dispersion curves of both InN and GaN (Sec. 4.1). In Sec. 4.2 we present the wurtzite Raman-active modes, and several experimental examples are given. Finally, in Sec. 4.3 we introduce the Brillouin scattering measurement of acoustic phonons in nitrides.

4.1 Phonon dispersion curves

The description of the crystalline lattice vibrations in terms of atomic displacements is complex, but the problem is simplified by the formulation of normal modes, which are combinations of atomic displacements that diagonalize the lattice Hamiltonian up to second order [5]. Here we present the main steps in the derivation of the normal modes, as well as their wave vector dependence. To this purpose, we consider the terms of the crystal Hamiltonian that involve ionic motion, which are given by Ref. [6],

$$H_{\text{ion}}(\mathbf{R}_1,...,\mathbf{R}_n) = \sum_j \frac{P_j^2}{2M_j} + \sum_{j,j'(j\neq j')} \frac{1}{2}\frac{Z_j Z_{j'} e^2}{4\pi\varepsilon_0|\mathbf{R}_j-\mathbf{R}_{j'}|} - \sum_{i,j}\frac{Z_j e^2}{4\pi\varepsilon_0|\mathbf{r}_i-\mathbf{R}_j|}, \quad (4.1)$$

where $\mathbf{r}_i$ are the electron positions and $\mathbf{R}_j$, $\mathbf{P}_j$, Z_j and M_j are nuclear position, momentum, charge and mass, respectively. By assuming that the electrons

follow the ionic motion adiabatically (Born-Oppenheimer approximation), the electronic and the ionic motion can be decoupled and the Hamiltonian for the ions reads

$$H_{\text{ion}} = \sum_j \frac{P_j^2}{2M_j} + E_e(\mathbf{R}_j - \mathbf{R}_{j'}). \tag{4.2}$$

Here E_e represents the total energy of the valence electrons with ions held at the positions $\mathbf{R}_1, ..., \mathbf{R}_n$. To qualitatively describe the lattice dynamics and give a picture of the phonon physical meaning, a phenomenological approach can be used. Within this approach we define the static Hamiltonian (H_0), which contains the terms depending on the equilibrium positions ($\mathbf{R}_{j0}$); and the displacement Hamiltonian (H'), which contains the terms depending on the atomic displacements ($\delta\mathbf{R}_{j0}$),

$$H_{\text{ion}} = H_0(\mathbf{R}_{10}, ..., \mathbf{R}_{n0}) + H'(\delta\mathbf{R}_{10}, ..., \delta\mathbf{R}_{n0}). \tag{4.3}$$

A further approximation is to consider only the second order terms in the displacement Hamiltonian (H'), so that the ionic displacements are described as harmonic oscillators. This approach is known as the *harmonic approximation*, and within this approach H' is given by

$$H'(\mathbf{u}_{kl}) = \frac{1}{2} M_k \left(\frac{d\mathbf{u}_{kl}}{dt}\right)^2 + \frac{1}{2} \sum_{k'l'} \mathbf{u}_{kl} \cdot \phi(kl, k'l') \cdot \mathbf{u}_{k'l'}, \tag{4.4}$$

where $\mathbf{u}_{kl}$ are the displacements from the equilibrium of the ion k in the unit cell l and $\phi(lk, k'l')$ accounts for the force constants that describe the interaction between the kl ion and the $k'l'$ ion. The harmonic approximation is useful to provide a simple approach to the lattice dynamics and phonon frequencies. In this approximation, phonon modes are eigenstates of the lattice system, i. e. they have an infinite lifetime and do not interact. However, in real lattices phonons have finite lifetimes and do interact with other phonons and defects in the lattice. These phonon interactions, which are described by higher order terms in the lattice Hamiltonian are called *anharmonic phonon effects*, and will be presented and studied in Chapter 5.

Following with the harmonic approximation, since $\phi(lk, k'l')$ has translational symmetry, Eq. (4.4) can be solved by plane waves similar to the Bloch functions that describe the electron dynamics in a crystal. These plane waves will have the form

$$\mathbf{u}_{kl}(\mathbf{q}, \omega) = \mathbf{u}_{k0} \exp\left[i(\mathbf{q} \cdot \mathbf{R}_l - \omega t)\right], \tag{4.5}$$

where $\mathbf{q}$ and ω are the wave vector and frequency of the wave, and $\mathbf{u}_{k0}$ corresponds to the displacement of the ion k at the unit cell 0. The representation

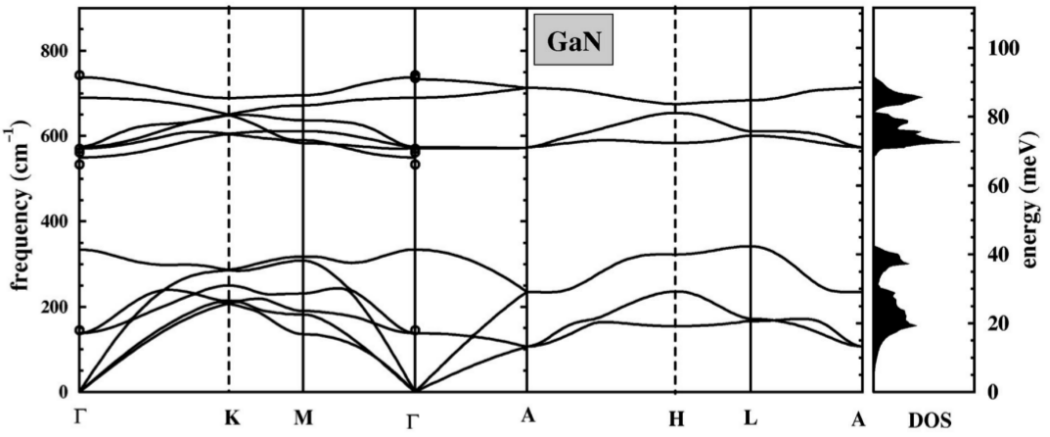

Figure 4.1: *Phonon-dispersion relation of wurtzite GaN and phonon density of states, extracted from Ref. [7]. The dispersion curves are the result of ab-initio calculations and filled circles are from Raman scattering data.*

of the phonon frequencies versus wave vector along representative directions in the first Brillouin zone are the phonon dispersion curves. The precise dependence of the phonon frequencies on wave vector can be measured experimentally (usually by means of neutron scattering) or obtained from model calculations.

The phonon dispersion curves of a crystal formed by n atoms in the primitive cell (being $n \geq 2$) will consist on $3n$ phonon branches, 3 of which correspond to the acoustic phonons and the rest correspond to optical phonons (phonon branches can be degenerate for some wave vectors). Thus, for a wurtzite material such as InN or GaN, we expect twelve phononic branches [5].

The acoustic phonons are characterized because all the ions move in phase. The frequency of the acoustic phonons is zero at the center of the Brillouin zone and it exhibits a linear dependence on the wave vector for small wave vectors. In fact, the denomination *acoustic* is related to the fact that the proportionality constant is the sound velocity of the material [8]. These phonons cannot be detected by Raman scattering and are usually measured using Brillouin spectroscopy, as will be presented in Sec. 4.3.

Beside the acoustic phonons, the crystals that have more than one atom in the unit cell have additional phonon branches whose frequency at $k = 0$ is non-zero: the optical phonons. The atomic displacements related with optical phonons are out-of-phase. As will be discussed in the next section, some optical phonons can be detected by means of optical techniques such as IR absorption or Raman scattering [8]. The optical phonons can have a transversal or a longitudinal nature, depending on the direction of propagation with respect to the

atomic displacement. In polar semiconductors, a macroscopic electric field is induced by the longitudinal optical phonons, which causes their frequencies to be different from those of the transversal optical modes. This phenomenon is called *LO-TO splitting* and will be explained in Sec. 4.2.

An example of the phonon dispersion curves is given in Fig. 4.1, which corresponds to wurtzite GaN. Since GaN has four atoms in the primitive cell, there will be twelve phonon branches, some of which may be degenerate along certain high-symmetry directions in the reciprocal space. The three less energetic branches correspond to the acoustic phonons whose frequency at zone centre is zero. The other branches correspond to the optical phonons, which exhibit a flatter dispersion than the acoustic phonons. In the 350-500 cm^{-1} frequency range there are no phonon states, and we call this range the *phononic gap*. This is an important concept because it implies that no phonon states within this frequency range are availible in the lattice. The width of the phononic gap may have important consequences on the way the optical phonons decay into less energetic modes.

Calculation of the phonon dispersion curves of wurtzite InN

InN has the same crystalline structure as GaN, but In ions are heavier than Ga ions. As a consequence, we expect all the phonon modes in InN to have smaller frequencies than the counterpart phonons in GaN, and specially those modes which involve In motion. This results in InN having a wider phononic gap. To evaluate these effects, we have calculated the phonon dispersion curves of the wurtzite InN using the ABINIT code package [9]. These *ab-initio* calculations are carried out using a plane-wave pseudo-potential approach to density functional theory (DFT). The calculations were performed in the local density approximation (LDA) using the Teter parametrization of the exchange-correlation [10] and Troullier-Martins pseudo-potentials [11]. For the In pseudo-potential the $4d$ electrons were included as valence states. A $8 \times 8 \times 4$ Monkhorst-Pack k-point sampling and a plane-wave basis set with a cut-off energy of 65 Ha were used in the calculations.

In Fig. 4.2, we display the calculated phonon dispersion curves for wurtzite InN, as well as the phonon density of states (PDOS) and the two-phonon density of states (2-PDOS) for sums (ρ^+) and differences (ρ^-) of phonons with opposite wave vectors. The dispersion of the modes [Fig. 4.2(a)] is similar to that of GaN, since they arise from the same crystalline structure. However, the phonons have smaller frequencies for InN than for GaN, because the In ions are heavier than the Ga ones. The phononic gap of InN spans from 220 to 445 cm^{-1} and is smaller than that of GaN. The limitations of the ABINIT code yield a E_1(LO) frequency which exhibits a spurious dispersion in the $\Gamma - M$ direction. This anomalous

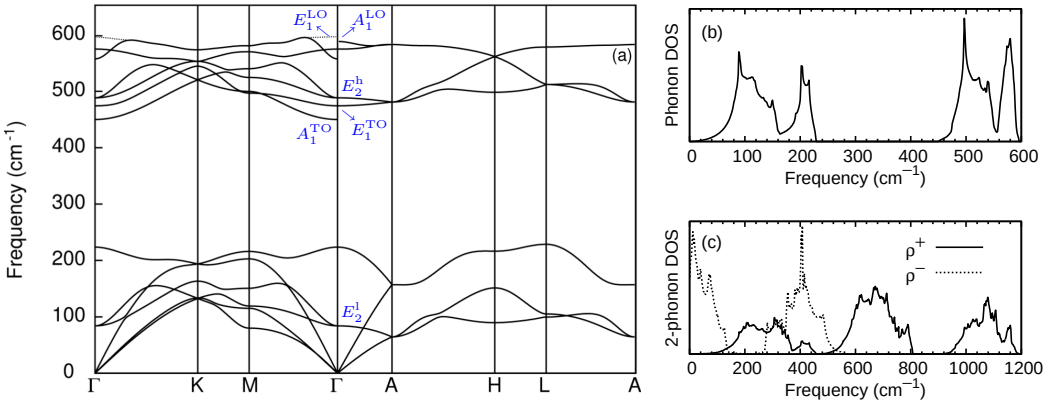

Figure 4.2: *(a) Phonon dispersion curves of wurtzite InN. Dotted lines for the E_1(LO) mode correspond to data taken from Ref. [7]. (b) Phonon density of states. (c) Two-phonon density of states for sums (ρ^+) and differences (ρ^-) of opposite wave-vector phonons.*

dispersion results in the ordering of the E_1(LO) and the A_1(LO) frequencies at zone-center that differ from the experimental observations. We have considered for this branch the E_1(LO) dispersion calculated by Bungaro *et al.* [7], which is represented in Fig. 4.2(a) using dotted lines. This correction does not have any noticeable effect on the calculated phonon DOS, which agrees very well with the one reported in Ref. [7]

The calculated PDOS is displayed in Fig. 4.2(b). In the acoustic mode region, there are two sharp PDOS maxima at 90 cm^{-1}, corresponding to transverse acoustic (TA) branches, and at 204 cm^{-1}, associated with longitudinal acoustic (LA) branches. In the optical mode region, the sharp peak at 498 cm^{-1} corresponds to transverse optical (TO) modes, while the maxima at 523 cm^{-1} and 541 cm^{-1} are due to TO modes. The two-phonon density of states (2-PDOS) for sums (ρ^+) and differences (ρ^-) of phonons with opposite wave vector are shown in Fig. 4.2(c). Their relevant features will be commented in the Section 5.2, in the framework of the study of the 2-PDOS implications on the effective decay mechanism of the phonon modes.

For obtaining the phonon dispersion curves, the lattice parameters of the relaxed lattice were calculated, and were found to be $a = 3.520$ Å and $c = 5.691$ Å. These values are in good agreement with reported high-resolution X-ray diffraction values [12]. The frequencies of the zone-center phonons are displayed in Table 4.1. A good agreement between the experiments and the *ab-initio* calculations is achieved for all the phonon frequencies except for the longitudinal optical ones. The deviations of the longitudinal modes calculated frequencies were previously reported for other compounds and may arise from a problem in the LDA gap in obtaining the dielectric constants [13].

Table 4.1: *Zone-center phonon frequencies and mode Grüneisen parameters for wurtzite InN calculated using the ABINIT code.*

	E_2^{low}	B_1^{low}	A_1(TO)	E_1(TO)	E_2^{high}	B_1^{high}	A_1(LO)	E_1(LO)
ω	84.0	223.7	450.2	474.5	488.6	575.1	588.6	557.7
γ	-1.01	1.10	1.74	1.70	1.76	1.47	1.39	1.78

The *ab-initio* calculations allow us to calculate relevant magnitudes related with the lattice dynamics, such as the bulk modulus or the Grüneisen parameters, that are useful to analyse the measurements presented in this thesis. The Grüneisen parameters describe the frequency variation of each phonon mode when the volume of the unit cell changes, and are defined as

$$\gamma = \frac{B}{\omega}\frac{\partial \omega}{\partial P}, \tag{4.6}$$

where B is the bulk modulus, defined as

$$B = -V\frac{\partial P}{\partial V}. \tag{4.7}$$

The volume changes of the unit cell can be due to the hydrostatic pressure or to the thermal expansion. The Grüneisen parameters will therefore be useful to evaluate the contribution of the thermal expansion to the overall temperature dependence of the phonon frequencies. We have determined the phonon frequencies and the Grüneisen parameters for InN using the ABINIT code. From our calculations we obtain B = 163 GPa and the frequency values and Grüneisen parameters are listed in Table 4.1. It is worth mentioning that the E_2^{low} has a negative Grüneisen parameter, i. e. it is a *soft mode*. This fact is related to some structural instability of the mode and leads to an anomalous frequency decrease of this mode under hydrostatic pressure or upon thermal cooling.

Table 4.2: *Character table for the point group C_{6v} at Γ, extracted from Ref. [14]*

	E	C_2	$2C_3$	$2C_6$	$3\sigma_d$	$3\sigma_v$	Basis	Optical act.
A_1	1	1	1	1	1	1	z, x^2+y^2, z^2	IR, Raman
A_2	1	1	1	1	-1	-1	R_z	
B_1	1	-1	1	-1	-1	1	x^3-3xy^2	Silent
B_2	1	-1	1	-1	1	-1	y^3-3yx^2	Silent
E_1	2	-2	-1	1	0	0	$(R_x, R_y), (xz, yz), (x, y)$	IR, Raman
E_2	2	2	-1	-1	0	0	(x^2-y^2, xy)	Raman

4.2 Optical phonons and Raman spectra

The phonons of a crystalline lattice can be deduced from the study of the lattice symmetry. The symmetry operations $\{g_i\}$ can be grouped in classes, which are formed by all the conjugate operations of the form $g_j = xg_ix^{-1}$, where x are elements of the symmetry group. The wurtzite crystalline structure belongs to the symmetry point group C_{6v}, and we have described its symmetry operations in Sec. 2.1. These symmetry operations are grouped in six different classes: E, C_2, $2C_3$, $2C_6$, $3\sigma_d$, $3\sigma_v$.

In general, each symmetry operation can be represented by a matrix, and the set of matrices for all the symmetry operations constitute a representation of the symmetry group. All the matrices that belong to a given class have the same trace. An irreducible representation consists of matrices that cannot be reduced to block-diagonal matrices with smaller block dimensions by a similarity transformation. Although a group may have an infinite number of representations, the number of inequivalent, irreducible representations is equal to the number of classes [6].

Therefore, the wurtzite symmetry point group C_{6v} contains six irreducible representations, which are A_1, A_2, E_1, E_2, B_1 and B_2. Each of these irreducible representations is characterized by the set of characters associated with the different classes of the symmetry group. The character table for the irreducible representations of the C_{6v} group is given in Table 4.2. Basis functions which transform according to each representation are also given. Since each phonon of the lattice can be associated with a certain representation, the inspection of the basis functions indicates the phonon optical activity. The phonons whose representations have linear basis functions can be detected via infrared absorption, and representations with quadratic basis functions can be measured by means of Raman scattering.

As described in Sec. 2.1, wurtzite-type III-nitrides belong to the space group C_{6v}^4 with two formula units in the primitive cell, and therefore the total representation at zone-center is formed by twelve normal modes. According to the

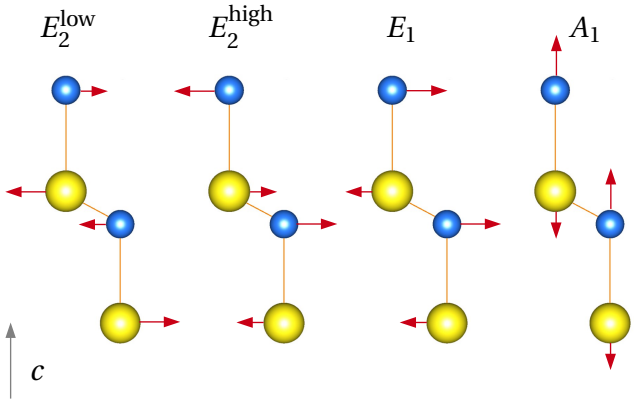

Figure 4.3: *Atomic diplacements of the wurtzite Raman active modes. Big yellow spheres represent cations (Ga/In) while small blue spheres represent the anions (N).*

factor group analysis, the total representation can be decomposed as $\Gamma_{total} = 2A_1 + 2B_1 + 2E_1^{(2)} + 2E_2^{(2)}$, where the superscript indicates the mode degeneracy. From these irreducible representation decomposition, one set of A_1 and $E_1^{(2)}$ correspond to acoustic phonons. Therefore, the representation of the optical phonons at the zone-center is $\Gamma_{opt} = A_1 + 2B_1 + E_1^{(2)} + 2E_2^{(2)}$. Taking into account their respective basis (shown in Table 4.2), the representation of the Raman-active phonons is $\Gamma_{Raman} = A_1 + E_1^{(2)} + 2E_2^{(2)}$, and A_1 and E_1 are also IR active.

In the following sections we present the Raman active modes in wurtzite III-nitrides. First, we introduce the Raman tensors, discuss the Raman selection rules and show several first-order Raman spectra of the compounds studied in this thesis. Then, we introduce the Raman scattering by higher order modes and local vibrational modes. Finally, we describe the fundamentals of the Brillouin scattering by acoustic phonons.

4.2.1 First-order Raman spectra

The atomic displacements involved in each Raman active mode are shown in Figure 4.3. It can be seen that the Raman active modes belonging to the unidimensional representation A, correspond to atomic vibrations along the c axis, whereas those belonging to the E_1 and E_2 two-dimensional representations correspond to atomic vibrations in the plane normal to c. The subindex (2) is used for modes in which the atomic oscillation of both cations (anions) of the primitive cell separate during the vibration, and therefore the resulting electric dipole is zero. In the E_2^{low} mode the heavier ions have a bigger ionic displacement amplitude than the lighter ions, while in the E_2^{high} mode the lighter ions are those undergoing the bigger displacement. In the modes A_1 and E_1 the ions of op-

posite sign separate during the vibration, which gives rise to an electric dipole. These modes are called polar and can propagate along the vibration direction (longitudinal optical, LO) or perpendicular to the vibrations (transversal optical, TO). In the case of LO phonons, the long-range Coulomb interaction of the net dipole moments results in a macroscopic electric field. This causes the LO phonons to have a higher energy than their TO counterparts (*LO-TO splitting*). The Lyddane-Sachs-Teller relation gives the magnitude of the LO-TO splitting as a function of the low and high frequency dielectric constants of the material,

$$\frac{\varepsilon_0}{\varepsilon_\infty} = \frac{\omega_{\mathrm{LO}}^2}{\omega_{\mathrm{TO}}^2}. \tag{4.8}$$

The longitudinal optical modes couple with the free electron density excitations via their macroscopic electric fields. As a result of this coupling, LO phonon-plasmon coupled modes (LOPCMs) appear. These modes have a phonon/plasmon mixed nature and their line shape and frequency strongly depend on the free charge density of the sample and on its electronic properties. All the theory concerning LOPCM Raman scattering will be presented in Chapter 7.

The selection rules for the Raman scattering follow from the Raman tensor according to Eq. (3.16). Therefore, the Raman scattering of a phonon described by a Raman tensor $\overleftrightarrow{R}$ will be *dipole-allowed* when

$$I_s \propto |\, \mathbf{e}_i \cdot \overleftrightarrow{R} \cdot \mathbf{e}_s \,|^2 \neq 0, \tag{4.9}$$

where $\mathbf{e}_i$ and $\mathbf{e}_s$ correspond to the polarization of the incident and scattered light, respectively.

The Raman tensors for the phonon modes are 3×3 matrices in a Cartesian basis. For the wurtzite structure, the Raman tensors of the optical active modes are:

$$E_1(x) = \begin{pmatrix} 0 & 0 & c \\ 0 & 0 & 0 \\ c & 0 & 0 \end{pmatrix}, \qquad E_1(y) = \begin{pmatrix} 0 & 0 & 0 \\ 0 & 0 & c \\ 0 & c & 0 \end{pmatrix}, \qquad A_1(z) = \begin{pmatrix} a' & 0 & 0 \\ 0 & a' & 0 \\ 0 & 0 & b \end{pmatrix},$$

$$E_2^{(1)} = \begin{pmatrix} d & 0 & 0 \\ 0 & -d & 0 \\ 0 & 0 & 0 \end{pmatrix}, \qquad E_2^{(2)} = \begin{pmatrix} 0 & d & 0 \\ d & 0 & 0 \\ 0 & 0 & 0 \end{pmatrix}$$

For polar modes, the coordinate in parentheses denotes the direction of phonon polarization, i. e. the direction of the atomic displacements. As stated above, the propagation direction of these polar phonon modes can be perpendicular or parallel to the atomic motion leading to TO or LO phonon modes.

Table 4.3 shows the selection rules for the Raman scattering under non-resonant conditions for the configurations used in this work. The scattering configurations are given in the Porto notation, that consist in four coordinates corresponding to (1) the incident light propagation direction, (2) the incident light polarization direction, (3) the scattered light polarization direction and (4) the scattered light propagation direction. As can be seen in Table 4.3, all the Raman active modes can be observed in backscattering geometry except the E_1(LO) mode. This mode is only dipole-allowed in the $x(yz)y$ configuration, a scattering configuration that can be difficult to realize in materials with strong optical absorption (such as InN for $\lambda_{exc} = 514$ nm). However, the E_1(LO) phonon mode is usually observed under near-resonant condition in the symmetry-forbidden $x(zz)\bar{x}$ configuration due to intra-band Fröhlich interaction [15]. In the following sections we present the first-order Raman spectra of wurtzite InN and GaN and discuss the observed modes in the studied scattering configurations.

Table 4.3: *Symmetry-allowed Raman modes of the wurtzite structure for different scattering configurations.*

Scattering	Raman active modes					
configurations	E_2^{low}	A_1(TO)	E_1(TO)	E_2^{high}	A_1(LO)	E_1(LO)
$z(xx)\bar{z}$	✓			✓	✓	
$z(xy)\bar{z}$	✓			✓		
$x(yy)\bar{x}$	✓	✓		✓		
$x(yz)\bar{x}$			✓			
$x(zz)\bar{x}$		✓				
$x(yz)y$			✓			✓
$x(yy)x$	✓	✓		✓		
$x(yy)z$	✓	✓		✓		

4.2.1.1 Raman spectra of wurtzite InN

Figure 4.4 shows first-order InN Raman spectra recorded using the macrocamera and the standard spectrometer mode. The excitation wavelength is 514-nm and the spectra have been recorded in several backscattering configurations on InN thin films. While the $z(--)\bar{z}$ configuration was obtained from a c-face InN sample, the $x(zz)\bar{x}$ and $x(yz)\bar{x}$ geometries were recorded from a m-face layer. The samples description can be found in Sec. 5.2.

The $z(--)\bar{z}$ spectrum exhibits three sharp peaks at 87, 494 and 584 cm^{-1}, corresponding to the E_2^{low}, E_2^{high} and A_1(LO) modes, respectively. In addition to these modes there is a weak, broad feature around 180 cm^{-1} which does not

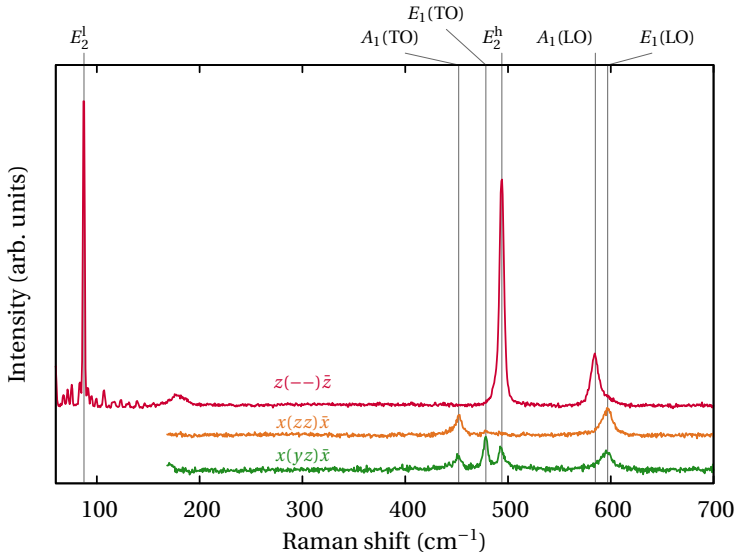

Figure 4.4: *Room temperature first-order Raman spectra of InN thin films obtained with* $\lambda_{exc} = 514$ *nm.*

Table 4.4: *Frequencies of the Raman active phonons of wurtzite InN (in cm*$^{-1}$*).* * *The theoretical frequency of the* E_1 *(LO) has been extracted from Ref. [7].*

	E_2^{low}	A_1(TO)	E_1(TO)	E_2^{high}	A_1(LO)	E_1(LO)
InN calc. (this thesis)	87	450.1	474.5	488.6	588.6	595*
InN exp. (this thesis)	87	447	476	488	586	593

correspond to any Raman active mode. A peak in this region has been previously reported by different authors [16–19], but its origin remains unclear. Pu *et al.* [16] assigned it to the silent mode B_1^{low}, but according to the theoretical calculations presented in Sec. 4.1, the expected frequency for the B_1^{low} mode is 224 cm^{-1}, which is significantly higher than that of the Raman feature measured in the spectra. Kaczmarczyk *et al.* [18] attributed this feature to acoustic phonons around the A point. On the other hand, another study reports a similar peak around 170 cm^{-1} and assigns it to large-wave-vector longitudinal acoustic phonons selectively excited by resonant Raman scattering [19].

The $x(zz)\bar{x}$ and $x(yz)\bar{x}$ Raman spectra were recorded in backscattering geometry on an m-face sample. As can be seen in Table 4.3, the dipole allowed Raman modes in these configurations are the A_1(TO) and E_1(TO) modes, respectively. The $x(zz)\bar{x}$ spectrum displays two peaks at 452 and 597 cm^{-1} that can be clearly assigned to the A_1(TO) and to the symmetry-forbidden E_1(LO) phonon modes. As mentioned above, the latter is detected in forbidden backscatter-

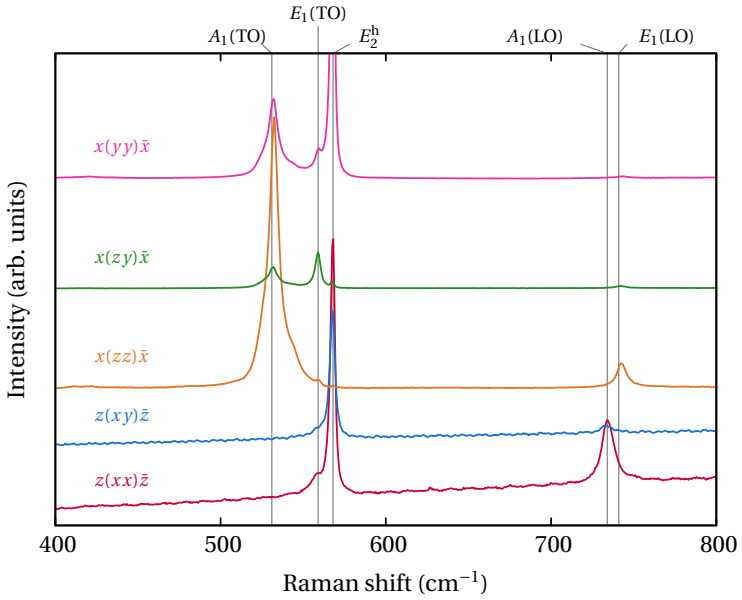

Figure 4.5: *Room temperature first-order Raman spectra of wurtzite GaN obtained with* $\lambda_{exc} = 514$*-nm.*

ing geometries on the *m*-face due to intra-band Fröhlich interaction [17]. The E_1(TO) phonon mode is detected at 478 cm^{-1} in the $x(yz)\bar{x}$ configuration. In this geometry we also observe residual Raman peaks related to A_1(TO), E_2^{high} and E_1(LO) phonon modes, which may arise from the relaxation of the selection rules in the lower quality *m*-face samples or from sample misalignment. By performing these Raman measurements we have obtained an experimental determination of the frequencies of all the phonon modes. The values are displayed in Table 4.4 in comparison with the phonon frequencies resulting from the *ab-initio* calculations presented previously. The experimental and calculated phonon frequencies exhibit very good agreement.

4.2.1.2 Raman spectra of wurtzite GaN

Here we present the first-order spectra of wurtzite GaN obtained in different scattering geometries. The spectra were measured from the Ga-face of an ammonothermally-grown GaN sample (details on growth and sample structure can be found in Sec. 7.2). To perform these measurements we have used micro-Raman in the standard spectrometer mode, and an excitation wavelength of 514 nm. The Raman spectra are shown in Fig. 4.5, and it can be seen that Raman selection rules hold strictly for the displayed spectra, except for a small leakage of the A_1(TO) mode in the $x(zy)\bar{x}$ spectrum. As mentioned above, the observation

Table 4.5: *Frequencies of the Raman active phonons of wurtzite GaN (in cm^{-1}).*

	E_2^{low}	A_1(TO)	E_1(TO)	E_2^{high}	A_1(LO)	E_1(LO)
GaN calc. [7]	138	550	572	574	733	737
GaN exp. (this thesis)	144	531	559	568	734	741

of a weak E_1(LO) peak in the $x(zz)\bar{x}$ spectrum is due to impurity-induced Fröhlich intra-band interaction. The phonon frequencies measured experimentally and those obtained from theoretical calculations are shown in Table 4.5.

4.2.1.3 Raman spectra of InGaN

Raman scattering studies of ternary alloys can be used to characterize the strain and the composition of the alloy samples. In some ternary alloys, phonon frequencies exhibit a composition dependence between the corresponding phonon frequencies of the binary extremes (*one-mode behaviour*). Other ternary alloys exhibit two sets of phonons whose frequencies change upon composition from those of one end-member binary to the impurity mode in the other end-member binary (*two-mode behaviour*). In the case of InGaN, early experimental studies by Alexson *et al.* suggested that the A_1(LO) mode follows a one-mode behavior, while the E_2 mode follows a two-mode behaviour [20]. Theoretical calculations [21] and later experimental studies [22, 23] demonstrated one-mode behaviour for both modes.

In Fig. 4.6 we present Raman spectra of InGaN layers with different In/Ga relative composition, as well as the spectra of GaN and InN for comparison purposes. The InGaN samples were grown by PAMBE and will be described in Sec. 6.3.1. The spectra have been obtained using the 514-nm excitation light, in backscattering configuration and standard spectrometer mode. The used excitation energy (2.4 eV) matches to the band-gap energy of the InGaN alloy for intermediate compositions, and therefore some samples are under near-resonant conditions. In fact, only the spectra corresponding to the sample with [In]=0.17 is out-of-resonance and exhibit all the phonon modes. The other spectra, which correspond to samples with higher [In], exhibit an intense PL signal that masks the phonon modes signal, and only a broad peak corresponding to the LO phonon mode can be measured due to Fröhlich resonance.

The choice of more energetic excitation in the UV range allows one to measure the InGaN Raman spectra under out-of-resonance conditions for all the compositions. UV spectra of InGaN layers will be displayed and studied in Chapter 6, which is devoted to resonances in the Raman spectra of the (In,Ga)N system.

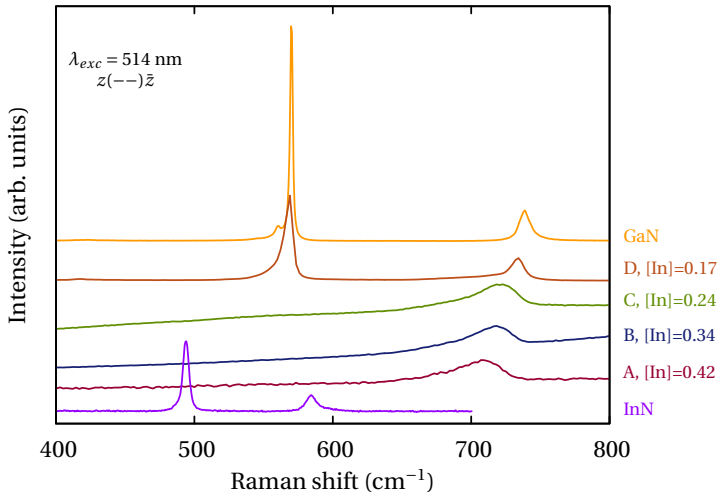

Figure 4.6: *Room temperature first-order Raman spectra of wurtzite InGaN. The overall intensity of the spectra from samples A, B and C has been reduced in order to fit in the Figure.*

4.2.1.4 Raman spectra of nanowires: effective light scattering

The measurement of the Raman spectra of semiconductor nanowires has an additional difficulty in comparison to the Raman experiments on thin films. Due to their reduced size and characteristic shape, it can be difficult to select a well-defined scattering configuration, and therefore collected light may arise from a mix of scattering configurations. In addition, in uni-axial polar crystals like wurtzite, for phonon propagation directions out of the optical axis a mix of different symmetry polar modes occurs, giving rise to quasi-LO and quasi-TO modes with angular dispersion. As a consequence, the analysis of the Raman spectra is not straightforward.

Here we present the first-order Raman spectra of the InN NWs studied in this thesis, which were grown catalyst-free by plasma assisted molecular beam epitaxy under N-rich conditions on Si (111) substrates (details on the growth conditions are given in Sec. 5.3). The nanowires have a diameter between 30 and 110 nm and a length up to 1μm. The c axis is parallel to the wire, but the nanowires exhibit a small tilt relative to the substrate normal. In these samples, due to the NWs orientation and the large lateral-to-top surface ratio, most of the excitation light enters the nanowires through the lateral faces. Given the high refractive index of InN, the propagation direction of the light in the NWs is close to perpendicular to the c-axis, as can be seen in the scheme of Fig. 4.7.

The Raman spectra of InN NWs have been obtained by using near-backscattering geometry on the as-grown samples. The spectra have been ex-

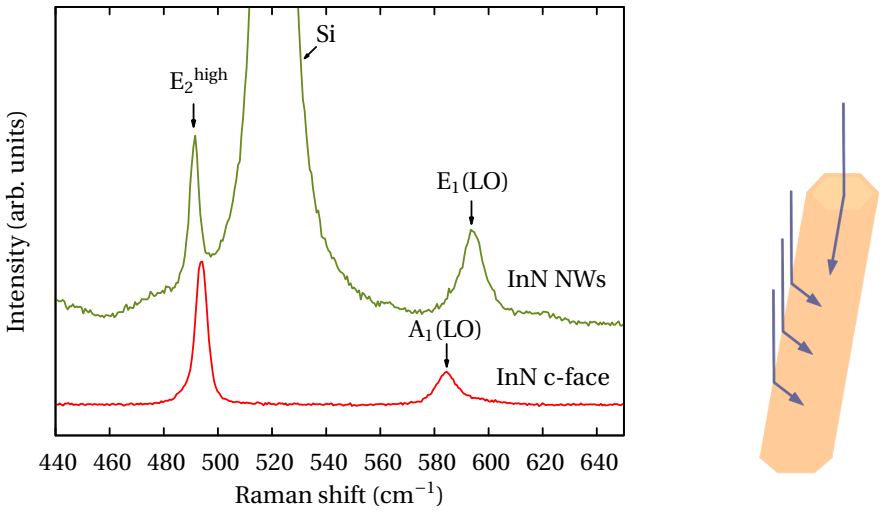

Figure 4.7: *Backscattering Raman spectrum of InN NWs compared to that of InN c-face epilayers, measured with* $\lambda_{exc} = 514$ *nm. At right we show an scheme of the light entrance in the NWs grown along the c-axis.*

cited using micro-Raman with λ_{exc} = 514-nm light and the scattered light has been analysed in the standard spectrometer mode. In Fig. 4.7 the Raman spectrum of InN NWs is compared to the spectra obtained from a *c*-face InN thin film in backscattering geometry. The nanowire spectrum presents two peaks, corresponding to the E_2^{high} and the quasi-LO phonon modes, superimposed to the strong Si substrate signal. As discussed in previous sections, LO phonon modes can be detected in backscattering configuration due to Fröhlich interaction. When the measurements are performed on the *c*-face thin film, the A_1(LO) phonon is detected, whereas E_1(LO) phonon is detected for measurements performed in backscattering in a direction perpendicular to the *c*-axis of the crystal. The measurement of the E_1(LO) mode can be understood in terms of the effective scattering configurations that occur in the case of NWs. As discussed previously, the detected quasi-LO modes contain a dominant component of the E_1(LO) mode, which is observed in the $x(zz)\bar{x}$ scattering configuration. The dominant role of this scattering configuration in the NWs may also be favoured by the fact that the internal field polarized perpendicular to the *c*-axis is attenuated inside the NWs [24, 25]. It should be noted high that the E_2 mode is forbidden in the $x(zz)\bar{x}$ configuration and therefore the E_2 Raman peak observed in the NWs spectra arises from other polarization configurations such as $x(yy)\bar{x}$ or $z(yy)\bar{z}$.

4.2.2 Higher order phonons

When more than one phonon take part in the scattering process, the wave-vector conservation rule [given by Eq. (3.2)] is satisfied by the total scattered wave-vector $\mathbf{q}_N$. This fact allows non-zone-centre phonons to participate in the scattering process in combinations so that wave-vector conservation holds.

In the case of the second-order Raman spectrum, the two phonons that take part in the scattering process have approximately opposite wave vectors. Because of the large number of phonon combinations that verify this condition cause the second-order Raman spectra generally consist of broad structures.

In the particular case of multiple scattering by the same phonon, the resulting Raman peak is called *overtone* or *multiphonon* [6]. While the number of combination modes is much larger than that of overtones, the contribution of overtones is usually enhanced by the optical matrix elements [26]. For certain electronic structures and experimental conditions, high-order multiphonons can be detected through the so-called *cascade mechanism*. In Chapter 6, which is devoted to Resonant Raman scattering, the resonant multiphonon cascade mechanism is described and studied.

4.2.3 Local vibrational modes

The incorporation of substitutional impurities in the crystalline structure induces atomic oscillations around the impurities, which are known as *local vibrational modes* (LVM) [27]. If impurity atoms are lighter than the host-lattice atoms, the LVM frequencies are within the phononic gap or above the optical branches and may show up in the Raman spectra as sharp peaks. Apart from substitutional impurities, LVM can also originate from other point defects such as vacancies or impurity complexes, which can also be detected by means of Raman scattering. In fact, since excitons are likely to be strongly localized at the impurities, LVMs can have a significant Raman signal despite their local nature. The study of the LVM Raman signal can provide information about the type of impurities and the microscopic structure of complex defects [6].

The most studied LVMs in nitrides are related to acceptors and to acceptor-hydrogen complexes that can be formed in p-doped samples. The nitride samples grown by MOCVD typically contain hydrogen and carbon impurities because of the use of organic reactants. After thermal annealing, hydrogen impurities related to acceptors are dissociated, which is linked with the p-dopant activation.

Concerning the acceptor-hydrogen complexes, they have been studied in several III-V semiconductors such as GaAs, GaP, ZnSe, and GaN [28]. In the case of Mg:GaN, Raman peaks observed around 2200 cm^{-1} have been attributed to

Mg-H complexes. In the case of InN, Davydov *et al.* reported Raman studies of Mg-doped InN that revealed peaks associated with Mg-H complexes for very high doping concentrations in the $10^{19} - 10^{21}$ cm^{-3} range [29, 30]. In Sec. 5.5 of the following chapter, a study of LVM of Mg-H complexes in Mg:InN will be presented, and the anharmonic decay of these modes will be studied.

4.3 Acoustic phonons and Brillouin spectra

Brillouin spectroscopy is used to study the acoustic phonons, which have very small frequencies near the center of the first Brillouin zone. In Brillouin scattering experiments, one analyses the light inelastically scattered by the material by means of an interferometric system, which allows the study of light with frequencies extremely close to the elastically scattered light.

The Brillouin scattering of the acoustic phonon modes allows one to study the elastic properties of small samples in a contactless way, under various temperature or pressure conditions. There are two main mechanisms contributing to the inelastic light scattering by acoustic phonons: the *elasto-optical* mechanism and the *surface-ripple* mechanism [31]. In transparent materials, the dominant scattering mechanism is the *elasto-optical* scattering mechanism, in which the incident photon is scattered by the the fluctuations of the dielectric constant caused by the dynamic fluctuations in the strain field.

In the case of opaque materials, the high optical absorption limits the scattering to a volume close to the sample surface and only the wave-vector component of the incident light parallel to the surface is conserved. In this case, the dominant mechanism is the *surface-ripple* mechanism, in which the surface phonon vibrations make the surface to appear as a moving grating without any modulation of the dielectric constant in the interior of the crystal. In this case, only surface acoustic waves (SAW) can be excited. By varying the incident angle (sagittal angle α), it is possible to control the length of the SAW wave vector (k), whereas rotation of the sample around its normal (azimuthal angle, φ) permits one to select the direction of the SAW wave vector in the sample plane.

A scheme of the backscattering configuration used in the Brillouin scattering measurements on opaque samples is shown in Fig. 4.8. Under these conditions, the component along the surface of the acoustic scattering wave vector(k), is given by

$$k = \frac{4\pi \sin(\alpha)}{\lambda_{\text{exc}}}. \tag{4.10}$$

SAW velocities in thin films depend on the respective elastic properties of the film and the substrate. When the sound velocity is lower in the film than in the substrate, as it is the case for the samples studied here, the first-order SAW (Rayleigh mode) may be accompanied by higher order modes (Sezawa modes). The Rayleigh mode frequency varies between the one corresponding to the substrate and that of the film material, depending on the film thickness h. The Sezawa surface wave velocities are higher than for the Rayleigh mode and lie between those of the shear modes in the film and those of the substrate [32]. The v_{SAW} can be determined from Brillouin spectra using

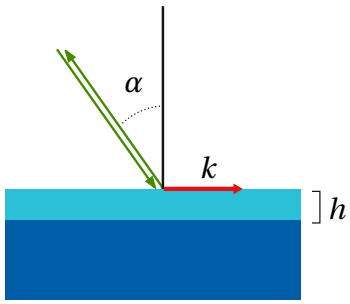

Figure 4.8: *Scheme of the backscattering configuration used to perform sagittal-dependent HRBS measurements.*

$$v_{\mathrm{SAW}} = \frac{\nu \lambda_{\mathrm{exc}}}{2\sin(\alpha)}, \tag{4.11}$$

where ν is the mode frequency.

The analysis of scattered light in High Resolution Brillouin Spectroscopy (HRBS) experiments allows obtaining information about the elastic properties of both transparent [33] and opaque materials [31, 34], albeit the nature of the measured acoustic waves and the information extracted is different in both cases. The knowledge of the elastic properties is fundamental to describe the dynamics of a crystalline structure and can provide information about the characteristics of the crystal lattice. For instance, in GaN layers the elastic constants have been found to be very sensitive to residual strain [35]. In the case of InN, although several theoretical studies of the InN elastic constants have been carried out using different approaches [36–43], no experimental study had been previously reported by means of Brillouin scattering.

Brillouin spectra of InN thin films

We have performed a study of the elastic constants of InN based on from the Brillouin spectroscopy measurements, in collaboration with the Brillouin spectroscopy laboratory of the *Instituto de Ciencia de Materiales de Madrid (ICMM-CSIC)*. The studied samples were grown along *c* and *m*-face crystallographic orientations. Samples C1, C2 and C3 are *c*-face thin films grown on GaN/sapphire with thicknesses of 0.25, 0.55 and 1.0 μm, respectively. Sample M is an InN *m*-face thin film grown on γ-$LiAlO_2(100)$ with a thickness of 0.8 μm. Details of the samples are given in Sec. 5.1. The experimental measurements were performed in backscattering geometry using the $\lambda_{\mathrm{exc}} = 514$ nm of an Ar^+ laser, and therefore the Brillouin experiments are performed in the absorption regime, and only surface acoustic waves (SAW) can be detected. The experimental set-up is reported elsewhere [44, 45].

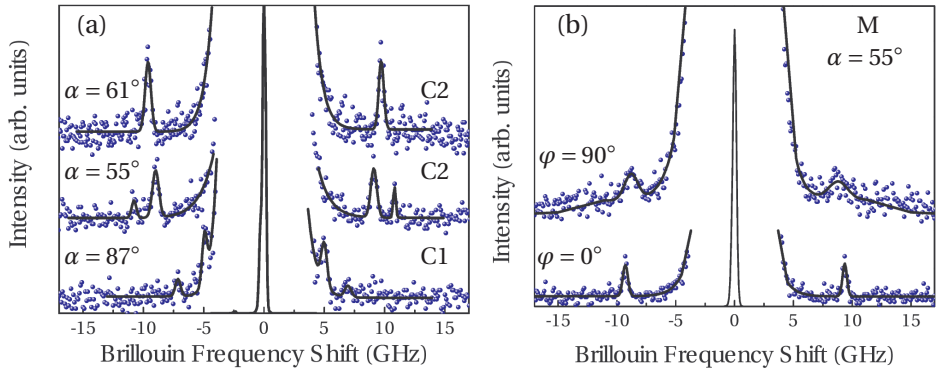

Figure 4.9: *HRBS spectra obtained from c-face (a) and m-face (b) InN thin films. Sample specimen, sagittal angle (α) and azimuthal angle (φ) are indicated in the figure.*

Figure 4.9 shows representative HRBS spectra obtained from the studied InN thin films. In Fig. 4.9(a) the plotted spectra were obtained from *c*-face samples for different sagittal angles. All these spectra exhibit a sharp peak corresponding to the Rayleigh mode. Two of the spectra also exhibit the first-order Sezawa mode, which is less intense than the Rayleigh peak, and it also undergoes a change in its frequency shift. Figure 4.9(b) displays HRBS measured from the *m*-face thin film, for different azimuthal angles, in which the Rayleigh mode is detected.

The crystallographic orientation of the sample determines the dependence of the v_{SAW} on the azimuthal axis. In the case of *c*-face wurtzite samples, the axis contained in the surface are equivalent and therefore v_{SAW} is expected to be independent of the azimuthal angle. In contrast, the v_{SAW} is strongly dependent of the azimuthal angle in the case of the *m*-face sample, since this is an anisotropic surface.

From the sagittal angle-dependent spectra performed on InN thin films, we extract the v_{SAW} dependence on kh, where k is the component along the surface of the acoustic scattering wave vector defined in Eq. (4.10) and h is the thickness of the sample. The results are plotted in Fig. 4.10(a). In the same figure we show the results of simulations of the v_{SAW} dependence on kh for InN thin films grown on GaN/Sapphire, using the method introduced by Zhang *et al.* [46]. This method gives the scattered light intensity due to the interaction of the incident light with surface ripples using a Green's function formalism. For these simulations, a density of 6.81 g/cm^3 for InN films and the set of elastic constants given by Ref. [37] have been used (see Table 4.6). The resulting simulations show good agreement with experimental results. It can be seen that, for kh values greater than 10, the v_{SAW} of the Rayleigh wave keeps almost constant. Thus, this is ap-

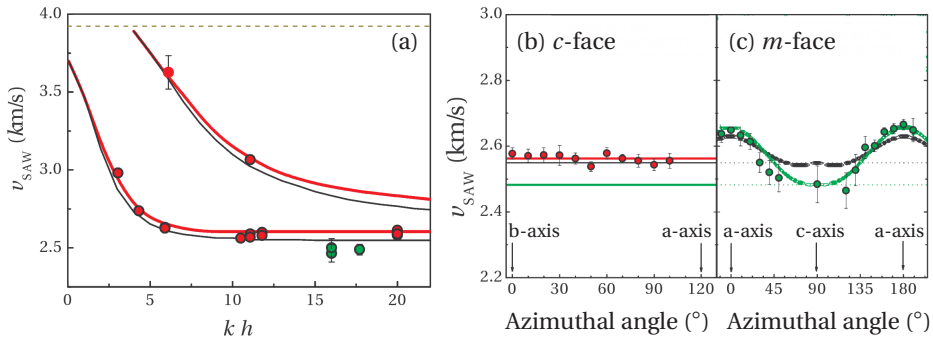

Figure 4.10: v_{SAW} *extracted from HRBS measurements as a function of* kh *(a) and the azimuthal angle (b,c). Red circles correspond to the measurements from the* c*-face samples (specimen C2), while green circles refer to the* m*-face sample. Solid lines are the results of simulations described in the text. The green and red curves were obtained using the elastic constants determined in this work for* $m-$ *and* $c-$ *face films respectively (see Table 4.6), whereas the black curves were calculated using the elastic constants of Ref. [37].*

proximately the critical thickness from which the elastic constants of the thin film are almost independent than those of the substrate.

Figure 4.10(b) shows the azimuthal dependence of the v_{SAW} in a c-face sample in comparison with the results obtained from calculations. As expected, in the c-face thin film the v_{SAW} keeps constant for different azimuthal angles, and its value is well reproduced by the calculations performed using the elastic constants given by Ref. [37] (see Table 4.6). The azimuthal dependence of the v_{SAW} in the m-face is plotted in Fig. 4.10(c). For symmetry reasons, the SAWs propagating on the m-face along the c-axis should have the same velocity as the SAWs on the c-face. The comparison of Fig. 4.10(b) and (c) indicates however that this is not fulfilled by our experimental data. This indicates that the elastic constants are different in the m-face sample.

We have calculated a new set of elastic constants for the m-face sample in order to fit its azimuthal v_{SAW} dependence. In the m-face, phonons propagating along the a-axis are strongly dependent on c_{66} and phonons propagating along the c-axis are primarily determined by c_{44}. Taking into consideration all these facts as well as elastic constants values reported at the literature, we propose two consistent sets of elastic constants for the InN c-face and m-face thin films, respectively (given in Table 4.6). These sets of elastic constants for InN are the first obtained from HRBS experiments in combination with numerical simulations of the SAW propagation velocity. The calculations performed with these revised elastic constants are shown in Fig. 4.10 for both sagittal and azimuthal dependences, and accurately adjust the experimental results. The differences

Table 4.6: *InN elastic constants reported in the literature and the proposed values for m- and c-face films in this work (note that $c_{66}{}^* = (c_{11} - c_{12})/2$ in hexagonal symmetry crystals).*

	c_{11} (GPa)	c_{12} (GPa)	c_{13} (GPa)	c_{33} (GPa)	c_{44} (GPa)	$c_{66}{}^*$ (GPa)
Ref. [37]	223	115	92	224	48	54
This thesis (m-face)	222.7	112.1	107.5	258	44.9	55.3
This thesis (c-face)	222.7	112.1	107.5	258	48.5	55.3

in the elastic constants between c- and m-face samples may be related to the growth difficulties or structural defect anisotropy of InN nonpolar surfaces.

By performing a HRBS study on InN samples with different crystalline orientations, and combining the experimental data with numerical simulations of the SAW propagation velocity, a reliable set of elastic constants for InN is obtained. This study demonstrates the power of the Brillouin spectroscopy as a technique for determining important structural parameters such as the elastic constants.

References

[1] A. Einstein. *Ann. Phys. (Leipzig)*, 22:180, 1907.

[2] P. Debye. *Ann. Phys. (Leipzig)*, 39:789, 1912.

[3] M. Born and von Kármán. *Phys. Z*, 13:297, 1912.

[4] F. Seitz. *Imperfections in nearly perfect crystals*, J. Wiley, New York, 1952.

[5] G. Burns. *Solid state physics.* Academic Press, 1990.

[6] P. Y. Yu and M. Cardona. *Fundamentals of Semiconductors. Physics and materials properties.* Springer-Verlag, 1996.

[7] C. Bungaro, K. Rapcewicz, and J. Bernholc. *Phys. Rev. B*, 61:6720, 2000.

[8] U. Rössler. *Solid State Theory.* Springer-Verlag, 2009.

[9] X. Gonze, J.-M. Beuken, R. Caracas, F. Detraux, M. Fuchs, G.-M. Rignanese, L. Sindic, M. Verstraete, G. Zerah, F. Jollet, and *et al. Comput. Mater. Sci.*, 25:478, 2002.

[10] S. Goedecker, M. Teter, and J. Hütter. *Phys. Rev. B*, 54:1703, 1996.

[11] N. Trouiller and J. L. Martins. *Phys. Rev. B*, 43:1993, 1991.

[12] M. F. Wu, S. Q. Zhou, A. Vantomme, Y. Huang, H. Wang, and H. Yang. *J. Vac. Sci. Technol. A*, 24:275, 2006.

[13] J. Serrano, A. H. Romero, F. J. Manjón, R. Lauck, M. Cardona, and A. Rubio. *Phys. Rev. B*, 69:094306, 2004.

[14] L. C. Lew Yan Voon, M. Willatzen, M. Cardona, and N. E. Christensen. *Phys. Rev. B*, 53:10703, 1996.

[15] J. M. Calleja and M. Cardona. *Phys. Rev. B*, 16:3753, 1977.

[16] X. D. Pu, J. Chen, W. Z. Shen, H. Ogawa, and Q. X. Guo. *J. Appl. Phys.*, 98:033527, 2005.

[17] V. Yu. Davydov, V. V. Emtsev, I. N. Goncharuk, A. N. Smirnov, V. D. Petrikov, V. V. Mamutin, V. A. Vekshin, S. V. Ivanov, M. B. Smirnov, and T. Inushima. *Appl. Phys. Lett.*, 75:3297, 1999.

[18] G. Kaczmarczyk, A. Kaschner, S. Reigh, A. Hoffmann, C. Thomson, D. J. As, A. P. Lima, D. Schikora, K. Lischka, R. Averbeck, and H. Riechert. *Appl. Phys. Lett.*, 76:2122, 2000.

[19] V. Y. Davydov, A. A. Klochikhin, A. N. Smirnov, I. Y. Strashkova, A. S. Krylov, H. Lu, W. J. Schaff, H.-M. Lee, Y.-L. Hong, and S. Gwo. *Phys. Rev. B*, 80:081204, 2009.

[20] D. Alexson, L. Bergman, R. J. Nemanich, M. Dutta, M. A Stroscio, C. A. Parker, S. M. Bedair, N. A. El-Masry, and F. Adar. *J. Appl. Phys.*, 89:798–800, 2001.

[21] C. J. Deatcher, C. Liu, S. Pereira, M. Lada, A. G. Cullis, Y. J. Sun, O. Brandt, and I. M. Watson. *Semicond. Sci. Technol.*, 18:212, 2003.

[22] S. Hernández, R. Cuscó, D. Pastor, L. Artús, K. P. O'Donnell, R. W. Martin, I. M. Watson, Y. Nanishi, E. Calleja, et al. *J. Appl. Phys.*, 98:013511, 2005.

[23] R. Oliva. *Optical emission and Raman scattering in InGaN thin films grown by molecular beam epitaxy.* Master Thesis, Universitat de Barcelona, 2010.

[24] J. Wang, M. S. Gudiksen, X Duan, Y. Cui, and C. M. Lieber. *Science*, 293:1445, 2001.

[25] E. O. Shäffer-Nolte, T. Stoica, T. Gotschke, F. Limbach, E. Sutter, and R. Calarco. *Appl. Phys. Lett.*, 96:091907, 2010.

[26] M. Cardona. *Light scattering in Solids II.* Springer-Verlag, 1982.

[27] H. Harima. *J. Phys. Condens. Matter*, 14:R967, 2002.

[28] M. D. McCluskey and N. M. Johnson. *J. Vac. Sci. Technol. A*, 17:2188, 1999.

[29] V. Y. Davydov, A. A. Klochikhin, M. B. Smirnov, A. N. Smirnov, I. N. Goncharuk, D. A. Kurdykov, H. Lu, W. J. Schaff, H.-M. Lee, H.-W. Lin, and S. Gwo. *Appl. Phys. Lett.*, 91:111917, 2007.

[30] V. Y. Davydov, A. A. Klochikhin, M. B. Smirnov, Y. E. Kitaev, A. N. Smirnov, E. Y. Lundina, H. Lu, W. J. Schaff, H.-M. Lee, H.-W. Lin, Y.-L. Hong, and S. Gwo. *Phys. Status Solidi C*, 5:1648, 2008.

[31] J. R. Sandercock. *Brillouin Spectroscopy and its application to Polymers.* Light Scattering in Solids III. Springer-Verlag, 1982.

[32] N. L. Rowell and G. I. Stegeman. *Phys. Rev. Lett.*, 41:970–973, 1978.

[33] J. K. Krüger. *Brillouin Spectroscopy and its application to Polymers.* Optical techniques to characterize polymer systems. Elsevier, 1989.

[34] P. Mutti, C. E. Bottani, G. Ghislotti, M. Beghi, G. A. D. Briggs, and J. R. Sandercock. volume 1 of *Adv. Acoustic Microscopy.* Plenum Press, 1995.

[35] T. Deguchi, D. Ichiryu, K. Toshikawa, K. Sekiguchi, T. Sota, R. Matsuo, T. Azuhata, M. Yamaguchi, T. Yagi, S. Chichibu, and S. Nakamura. *J. Appl. Phys.*, 86:1860–1866, 1999.

[36] K. Kim, W. R. L. Lambrecht, and B. Segall. *Phys. Rev. B*, 53:16310–16326, 1996.

[37] A. F. Wright. *J. Appl. Phys.*, 82:2833–2839, 1997.

[38] A. A. Marmalyuk, R. K. Akchurin, and V. A. Gorbylev. *Inorg. Mat.*, 34:691–694, 1998.

[39] J. A. Chisholm, D. W. Lewis, and P. D. Bristowe. *J. Phys. Cond. Mat.*, 11:L235–L239, 1999.

[40] V. Yu. Davydov, A. A. Klochikhin, V. V. Emtsev, D. A. Kurdyukov, S. V. Ivanov, V. A. Vekshin, F. Bechstedt, J. Furthmüller, J. Aderhold, J. Graul, A. V. Mudryu, H. Harima, A. Hashimoto, A. Yamamoto, and E. E. Haller. *Phys. Status Solidi B*, 234:787, 2002.

[41] S. P. Lepkowski, J. A. Majewski, and G. Jurczak. *Phys. Rev. B*, 72:245201, 2005.

[42] Feng Peng, Yunxia Han, Hongzhi Fu, and Xiangdong Yang. *J. Alloys and Compounds*, 475:885–888, 2009.

[43] Kanoknan Sarasamak, Sukit Limpijumnong, and Walter R. L. Lambrecht. *Phys. Rev. B*, 82:035201, 2010.

[44] E. Salas, R. J. Jiménez-Riobóo, C. Prieto, and A. G. Every. *J. Appl. Phys.*, 110:023503, 2011.

[45] R. J. Jiménez-Riobóo, M. García-Hernández, C. Prieto, J. J. Fuentes-Gallego, E. Blanco, and M. Ramírez del Solar. *J. Appl. Phys.*, 81:7739–7745, 1997.

[46] X. Zhang, J. D. Comins, A. G. Every, P. R. Stoddart, W. Pang, and T. E. Derry. *Phys. Rev. B*, 58:13677–13685, 1998.

CHAPTER 5

Anharmonic phonon decay in InN

The harmonic approximation of the crystal Hamiltonian assumes a perfect, infinite crystal without any kind of impurities or defects in which phonons do not interact. Within this simplified framework, we expect phonons to be eigenstates of the crystal Hamiltonian, with fixed frequency and infinite lifetime.

However, real crystals are not perfect nor infinite, and a number of crystalline defects exist even in the highest quality samples. Therefore, phonons in real crystals interact with other phonons and with crystalline defects, and have a finite lifetime. All the interactions that are not accounted for in the harmonic description of the crystal are called *anharmonic interactions*. The processes through which phonons interact among them and disappear are known as *anharmonic decay* processes. The knowledge of this phonon anharmonic interactions and decay processes is fundamental in order to achieve a good understanding of the vibrational properties and phonon interactions with the free carriers in a material, both of which have great impact on optoelectronic device performance.

The anharmonic interactions of phonons result in changes in the phonon frequencies and linewidths of their Raman peaks. Furthermore, since the phonon decay is a temperature-dependent process, the study of the temperature dependence of the Raman peaks gives insight into the anharmonic interactions and decay channels of phonons. In fact, Raman scattering measurements have been extensively used to obtain information about phonon lifetimes [1–3]. The temperature dependence of phonons in wurtzite AlN and GaN has been widely studied by means of Raman scattering [4]. Concerning InN, Raman scattering studies of the phonon temperature dependence were reported by Pomeroy *et al.* [5] and Pu *et al.* [6], both of them focusing on the E_2^{high} and $A_1(\text{LO})$ phonon modes. Using a simplified model which assumes a constant PDOS, those articles concluded that the $A_1(\text{LO})$ mode decays asymmetrically into a high energy and a low energy phonon, while the the E_2^{high} mainly decays through a 4-phonon process, but the identification of the decay channels was not addressed.

Phonon dynamics in InN NWs have been scarcely studied in comparison with other semiconductor NWs. The only Raman study of the phonon temperature dependence of InN NWs was made by Song *at al.* [7] and the studied samples, grown by *in situ* nitridation of indium metal in ammonia flux, presented

low crystalline quality. That work presented a study of the temperature dependence of the E_2^{high} and A_1(LO) phonon modes, and the found temperature behaviour was similar to that of the InN thin films.

In this chapter we present a detailed study of the anharmonic interactions in InN. To this end, we carry out a temperature dependence study of all the Raman modes in InN thin films. Based on the *ab-initio* calculations of the phonon dispersion and density of states presented in Chapter 4, the temperature dependence of the phonon linewidths and frequencies is discussed in terms of third- and fourth-order anharmonic decay, and the lifetimes and decay channels of the phonon modes are derived. We also measure the temperature dependences of phonons in InN NWs to compare them with the data obtained from thin films. Finally, the anharmonic interactions of local vibrational modes in heavily-doped InN are studied.

5.1 Framework: Cowley's theory of anharmonic phonon decay

As stated above, in the harmonic approximation the lattice potential is expanded up to quadratic terms in the atomic displacements. This approximation assumes small oscillations of the ions and no phonon-phonon interactions. The eigenstates of the harmonic Hamiltonian are phonons with a fixed frequency and infinite lifetime. However, in real crystals phonons interact with other phonons and have finite lifetimes. The anharmonic terms in the lattice Hamiltonian account for phonon processes in which certain phonons disappear (*decay*) and others are created. The cubic anharmonic term considers the three-phonon processes (one phonon decays into two phonons, or two phonons decay into one phonon) and the quartic term accounts for the four-phonon processes (one phonon decays into three, three merge into one, or two are replaced by other two). All these processes conserve the energy and the total wave vector. A schematic representation of these cubic and quartic interactions is shown in Fig. 5.1.

The anharmonic coupling was described in the perturbation theory framework by Cowley in Ref. [8]. This theory has been successfully used to describe the anharmonic interactions in several semiconductors such as Si, Ge [9], AlAs [10], and ZnO [3] by analysing their temperature-dependent Raman spectra. In Cowley's theory, a complex phonon self-energy is defined to evaluate the anharmonic renormalization of the phonon frequencies and lifetimes. The real part of the self-energy is related to the anharmonic frequency shift, while the imaginary part is related to the phonon linewidth. The formalism used to model these contributions and their evaluation from the phonon line shape is described in

the following sections.

Phonon self-energy

Taking into account the interaction between the harmonic eigenstates results in a renormalization of the *bare* phonon energies and lifetimes that can be described by the complex phonon self-energy

$$\Sigma(\omega) = \Delta(\omega) - i\Gamma(\omega). \tag{5.1}$$

Taking into account the cubic and quartic anharmonic terms, the imaginary part of the self-energy can be written as

$$\Gamma(\omega) = \Gamma_0 + \Gamma^{(3)}(\omega) + \Gamma^{(4)}(\omega), \tag{5.2}$$

where Γ_0 is an additive contribution due to background defect scattering. This defect-related contribution has no temperature dependence, and is expected to be greater in the samples with poor crystalline quality.

The cubic term takes into account the decay processes through interactions with two other phonons, and is given by [8, 9]

$$\begin{aligned}\Gamma^{(3)}(\omega) &= \frac{18\pi}{\hbar^2}\sum_{\mathbf{q}j_1j_2}|V_3(\mathbf{q}j_1,-\mathbf{q}j_2)|^2 \\ &\times\Big\{[n(\omega_1)+n(\omega_2)+1]\,\delta(\omega_1+\omega_2-\omega) \\ &+[n(\omega_2)-n(\omega_1)]\,\delta(\omega_1-\omega_2-\omega)\Big\}.\end{aligned} \tag{5.3}$$

Here, $V_3(\mathbf{q}j_1,-\mathbf{q}j_2)$ is the third-order coefficient in the expansion of the lattice potential in normal coordinates, $n(\omega)$ is the Bose-Einstein occupation factor, and ω_1 and ω_2 are the frequencies of the other phonons taking part of the process. If we assume that the V_3 coefficients and the Bose-Einstein factors are constant over the small energy range considered, this contribution to imaginary part of the self-energy can be written as

$$\begin{aligned}\Gamma^{(3)}(\omega) &= |V_3^+|^2\left[1+n(\omega_1^+)+n(\omega_2^+)\right]\rho^+(\omega) \\ &+|V_3^-|^2\left[n(\omega_2^-)-n(\omega_1^-)\right]\rho^-(\omega),\end{aligned} \tag{5.4}$$

where $\rho^+(\omega)$ and $\rho^-(\omega)$ are, respectively, the two-phonon density of states (2-PDOS) for phonon sums and differences. The V_3^+ and V_3^- are the effective third-order anharmonic constants for decay into phonon sums (processes like the depicted in Fig. 5.1a) and decay through up-conversion processes (scheme shown in Fig. 5.1b).

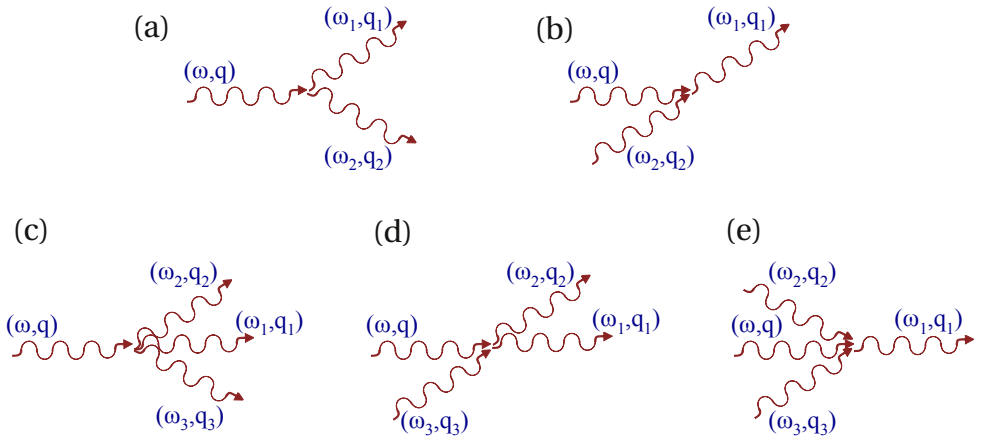

Figure 5.1: *Scheme of the possible phonon decay processes throguh three and four phonon interactions. (a) Cubic: one phonon decays into two phonons; (b) Cubic: two phonons merge into one (up-conversion process); (c) Quartic: One phonon decays into three phonons; (d) Quartic: two phonons turn into other two phonons; (e) Quartic: three phonons merge into one phonon (triple up-conversion).*

Some previous Raman scattering studies have assumed a constant two-phonon DOS to analyse the temperature dependence of the the optical phonon linewidths, and then the imaginary part of the self-energy is simply proportional to the Bose-Einstein factors [3, 4, 11–14]. In the expression given in Eq. (5.4), the contribution of the Bose-Einstein factors to the imaginary part of the self-energy is weighted by the 2-PDOS [$\rho^+(\omega)$ and $\rho^-(\omega)$]. It is worth noting that the temperature dependence is given by the Bose-Einstein factors. For high temperatures, as the occupation factors are bigger, there are more anharmonic interactions and the self-energy corrections are greater.

The contribution of quartic anharmonicity terms in the Hamiltonian was calculated by Balkanski *et al.* [12]. Unfortunately, the sums over wave vectors of the three phonons involved are mathematically intractable and the expressions given in Ref. [12] are difficult to evaluate explicitly. However, we can estimate the effect of the quartic anharmonicity term on the phonon self-energy by considering that the most likely decay channels involve the decay into a zone-center phonon and a pair of opposite wave-vector phonons at the zone edges or at critical points of the phonon dispersion, where the phonon DOS is maximum. Also for the sake of simplicity, we neglect the triple up-conversion (Fig.5.1e) because it is highly unlikely, and we only take into account the decay into three phonons (corresponding to the scheme in Fig. 5.1c) and the process in which two phonons decay into other two phonons (diagram in Fig. 5.1d).

The specific phonon combinations for phonon decay are selected for each

phonon mode on the basis of the calculated DOS. The assumed simplification, together with the assumption of constant fourth-order anharmonic coefficients, reduces the quartic anharmonicity contribution to a term proportional to the two-phonon DOS,

$$\begin{aligned}\Gamma^{(4)}(\omega) &\approx |\tilde{V}_4^+|^2\Big\{\left[n(\omega_1^+)+1\right]\left[n(\omega_2^+)+1\right]\left[n(\omega_3^+)+1\right]\\ &- n(\omega_1^+)n(\omega_2^+)n(\omega_3^+)\Big\}\rho^+(\omega-\omega_1^+)\\ &+ |\tilde{V}_4^-|^2\Big\{\left[n(\omega_1^-)+1\right]\left[n(\omega_2^-)+1\right]n(\omega_3^-)\\ &- n(\omega_1^-)n(\omega_2^-)\left[n(\omega_3^-)+1\right]\Big\}\rho^-(\omega-\omega_1^-). \qquad (5.5)\end{aligned}$$

In Eq. (5.5), ω_1 is the frequency of the zone-center mode considered and ω_2, ω_3 are the frequencies of opposite wave-vector phonon modes satisfying energy conservation. It should be emphasized that $\tilde{V_4}^+$, $\tilde{V_4}^-$ are *effective* anharmonic constants for the channel considered which include a PDOS weight factor for the zone-center mode involved. In the present analysis, $\tilde{V_4}^+$, $\tilde{V_4}^-$ should be considered as empirical adjustable parameters whose direct comparison with V_3^+, V_3^- is not straightforward.

Since real and imaginary parts of the phonon self-energy are related by a Kramers-Kronig transformation, the corresponding real part of the self energy, $\Delta(\omega)$, can be evaluated as

$$\Delta(\omega) = -\frac{2}{\pi}\mathscr{P}\int_0^\infty \frac{\omega'}{\omega'^2-\omega^2}\Gamma(\omega')d\omega', \qquad (5.6)$$

which yields a frequency-dependent renormalization of the phonon energy.

Phonon line shape

The phonon line shape is determined by both the real and imaginary terms of the self-energy. For small self-energy corrections, the Raman peak is described by a Lorentzian-like line shape, given by [9]

$$I(\omega) \propto \frac{\Gamma(\omega)}{[\omega_0+\Delta_0+\Delta(\omega)-\omega]^2+\Gamma(\omega)^2}. \qquad (5.7)$$

The inspection of this expression shows that the real part of the self-energy introduces a frequency shift, while the imaginary term leads to a peak broadening. In the case of a frequency-independent self-energy, the phonon line shape is a Lorentzian, with a full width at half maximum (FWHM) equal to two times the imaginary part of the self-energy. If the self-energy depends on the frequency, the line shape can deviate from a Lorentzian line shape.

Besides the real and imaginary parts of the self-energy, Eq. (5.7) also takes into account the shift in frequency due to the thermal expansion of the lattice, Δ_0. This contribution can be written as [15]

$$\Delta_0 = -\omega_0 \gamma \int_0^T [\alpha_c(T') + 2\alpha_a(T')] dT', \tag{5.8}$$

where α_c and α_a are the linear thermal expansion coefficients along directions parallel and perpendicular to the c axis, respectively [16], and γ is the Grüneisen parameter of the phonon mode. Note that this expression only accounts for the frequency shift caused by a thermal expansion of the lattice of the studied material. There exist other contributions to the frequency shift, such as native strain of the lattice or strain caused by differential thermal expansion of the substrate/film, but these are not accounted for in Eq. (5.8).

Since the temperature dependence of the phonon frequencies may be affected by contributions which are difficult to calculate, throughout this chapter we study the anharmonic decay by fitting the temperature dependence of the phonon mode linewidths. The fitting procedure is as follows. First, we evaluate the phonon frequencies and FWHM as a function of temperature by direct determination on the line shapes numerically calculated from Eq. (5.7). The most likely decay channels are deduced by inspection of the phonon dispersion curves and 2-PDOS and they are taken into account to adjust the temperature dependence of the phonon intrinsic linewidth using Eq. (5.2), (5.4) and (5.5). Next, we take into account the instrument broadening of the peaks described in Sec. 3.2 in order to extract the intrinsic linewidth of the phonon mode from the measured Raman spectra and we fit the theoretical temperature dependence to the experimental data. The fitting parameters we consider in this model are V_3^+, V_3^-, $\tilde{V_4}^+$, $\tilde{V_4}^-$ and Γ_0.

From the linewidth fitting, we obtain the values of the anharmonic potentials, which are used to calculate the contribution to the frequency shift that arises from the anharmonic interactions. This calculation is useful to discuss other contributions to the frequency shift, such as biaxial strain.

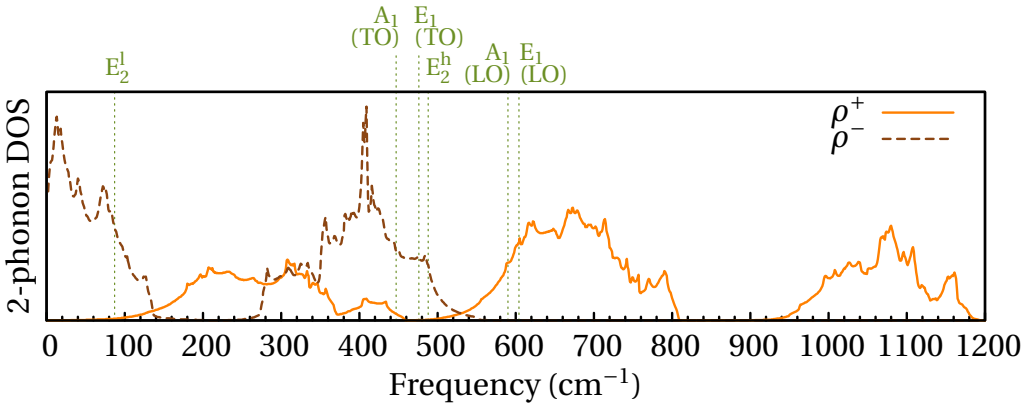

Figure 5.2: *Two-phonon density of states for sums (ρ^+) and differences (ρ^-) of opposite wave-vector phonons.*

5.2 Anharmonic phonon decay in InN epilayers

In this section a complete study of the phonon decay in InN thin films is presented. Temperature-dependent Raman measurements are carried out on both *c*- and *m*-faces and their phonon temperature dependences are studied on the basis of the model described in Sec. 5.1.

The characteristic phonon energies of InN have a bearing on the anharmonic interactions of phonons in this material. As presented in Section 4.1, the large mass difference between the indium and the nitrogen ions results in a phonon dispersion with a large energy gap between the upper-lying and lower-lying optical branches. This phononic structure severely limits the possible phonon interactions and, for instance, certain optical phonons cannot decay into a sum of phonons.

In order to discuss the possible decay channels for each phonon mode, we have plotted in Fig. 5.2 the two-phonon DOS for sums (ρ^+) and differences (ρ^-) of phonons with opposite wave vectors. This is the same result presented previously in Sec. 4.1, but here we have labelled in the same figure the frequencies corresponding to the optical phonon modes of InN. The inspection of this figure gives insight into the possible 3-phonon decay channel mechanisms for each phonon mode. The only phonons that are likely to decay through the creation of a pair of phonons are the LO modes, since for their frequencies the 2-phonon DOS for sums (ρ^+) is high. Figure 5.2 shows that at the frequencies of all the other phonon modes, the 2-PDOS of sums is very low, and therefore the main 3-phonon mechanisms for the decay of such phonons are up-conversion processes. As it has been previously explained, the up-conversion decay is less likely than the decay into sums because in that mechanism an existing phonon is needed. As a consequence, if a phonon decays only through up-conversion pro-

cesses, it is expected to show very small anharmonic frequency shift and broadening.

Besides the 3-phonon mechanisms, we also consider 4-phonon mechanisms as a decay channels. In general, 4-phonon mechanisms have an intrinsic lower probability than 3-phonon mechanisms, but their role can be specially relevant in the case of those phonons whose 3-phonon decay mechanisms are restricted to up-conversion processes.

In this section we present Raman spectra of all the phonon modes of InN taken at different temperatures from thin films. The temperature behaviour of the peak linewidths is studied with the model presented in Sec. 5.1 and the decay channels are deduced. The anharmonic contribution to the frequency shift is subsequently calculated and other possible contributions to the frequency shift are discussed in each case.

InN *c*-face and *m*-face epilayers

This chapter presents Raman measurements performed on *c* and *m* faces of high quality InN epilayers. The samples were grown at 500 °C by plasma-assisted molecular beam epitaxy (PAMBE).

The *c*-face sample was grown on a sapphire substrate, and the thickness of the film is 550 nm. The in-plane thermal expansion coefficient at 300 K of the InN is $\alpha_a = 3.6 \times 10^{-6}$ K^{-1} [17], which is a similar value to that corresponding to sapphire $\alpha_a = 4.3 \times 10^{-6}$ K^{-1} [18]. Thus, the biaxial strain arising from differential thermal expansion is expected to be small in this sample.

The *m*-face sample was grown on (100) γ-$LiAlO_2$, and the film thickness is 800 nm. The in-plane thermal expansion coefficient of this substrate at 300 K is $\alpha_c = 14.9 \times 10^{-6}$ K^{-1} [19], which is considerably higher than the thermal expansion coefficient found in InN for a similar temperature: $\alpha_c = 2.6 \times 10^{-6}$ K^{-1} [17]. Then, in this sample the temperature dependence of the phonon frequencies may be significantly affected by the differential thermal expansion of the substrate.

Electrical characterization of the samples was performed by standard Hall measurements, which showed that both samples display *n*-type conductivity. A free-electron density of 2.3×10^{18} cm^{-3} and a Hall mobility of μ_{Hall}=1440 cm^{2}V^{-1}s^{-1} was measured in the *c*-face sample, while the *m*-face sample showed higher free electron density (5×10^{19} cm^{-3}) and lower mobility (μ_{Hall}=160 cm^{2}V^{-1}s^{-1}). Due to the difficulties in the growth of non-polar faces, the density of dislocations and defects is usually higher in such samples [20], which results in an increment of electron density and a lower electron mobility.

The Raman temperature-dependent measurements

Measurements in several scattering configurations were performed using backscattering geometry on samples differently oriented. The m-face sample was used to perform measurements in the $x(zz)\bar{x}$ and the $x(zy)\bar{x}$ scattering configurations, while the c-face sample was used to measure the Raman spectra in the $z(--)\bar{z}$ configuration. The excitation wavelength was the 514-nm line of an Ar^+ laser and the scattered light was analysed with the experimental system described in Sec. 3.2.

Raman spectra were obtained in the standard spectrometer mode, corresponding to a spectral slit width of ≈ 2.2 cm^{-1} (see Table 3.2). The triple additive configuration with 50 μm slit was used to obtain high-resolution spectra of the E_2^{low} mode. To minimize Rayleigh stray light, the intermediate slits of the spectrometer were set to 100 μm to allow only a narrow window of ≈ 30 cm^{-1} around the E_2^{low} frequency to reach the detector. The Raman linewidhts were studied taking into account the Voigt profile approximation [Eq. (3.26)] and the instrument broadening corresponding to each spectrometer configuration ($\Gamma_G = 2.2$ cm^{-1} for the triple subtractive and $\Gamma_G = 0.5$ cm^{-1} in the high-resolution triple additive configuration).

To vary the temperature of the samples a LN_2 cryostat and a Linkam high-temperature stage described in Sec. 3.2 were used. Both sets of measurements yield consistent results in the overlapping temperature range between 290 and 390 K.

The E_2^{low} mode

The full Raman spectrum of the c-face InN thin film obtained at room temperature is displayed in Fig. 4.4. In that figure it can be seen that the E_2^{low} is the phonon mode with the smallest frequency and the narrowest linewidth. This mode exhibits a singular anharmonic behaviour because, due to its low frequency, it cannot decay into lower-energy phonons. To study the anharmonic decay of the E_2^{low} mode we have performed temperature-dependent measurements of the E_2^{low} Raman peak in the high-resolution triple additive configuration of the spectrometer. Figure 5.3(a) shows representative Raman spectra of the E_2^{low} mode measured from the c-face thin film in the range of temperatures studied. The intensity of the E_2^{low} Raman peak increases with temperature as expected from the increase in the occupation factor of such a low-energy phonon. Only a small frequency shift of about 1 cm^{-1} over the whole temperature range is apparent from these spectra.

By inspection of the 2-PDOS (Fig. 5.2), it can be seen that the two-phonon sum DOS is very low at frequencies below 150 cm^{-1}. Therefore, the E_2^{low} phonon mode cannot decay into lower energy phonons. Since the 2-PDOS for phonon

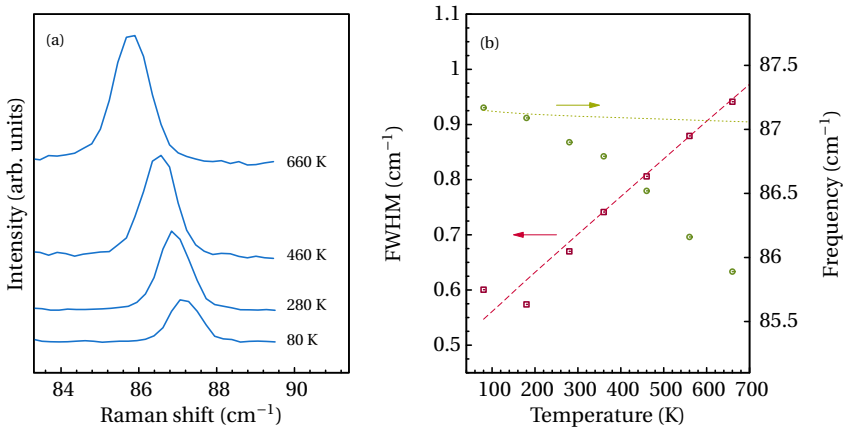

Figure 5.3: *Temperature dependence of the E_2^{low} phonon mode in InN. (a) Representative Raman spectra for temperatures in the 80-660 K range measured from c-face thin film. (b) Temperature dependence of the linewidth (squares, left axis) and the frequency (circles, right axis). The dashed line is a fit of the model discussed to the linewidth data. The dotted line shows the temperature dependence of the frequency given by the model for the same set of parameters.*

differences is relatively high at the E_2^{low} frequency, *up-conversion* processes are the most likely decay channels for the E_2^{low} anharmonic decay. These processes are 3-phonon interactions in which two phonons are annihilated and a higher energy phonon is created. By inspection of the phonon dispersion curves [Fig. 4.2(a)] and the phonon DOS [Fig. 4.2(b)], we identify the most likely up-conversion channel as

$$E_2^{low} \rightarrow \mathrm{LA}(M)-\mathrm{TA}(M) \quad [\omega(\mathrm{TA}) = 118\ \mathrm{cm}^{-1}, \omega(\mathrm{LA}) = 202\ \mathrm{cm}^{-1}]$$

Another possible channel that would match the E_2^{low} frequency would be $E_2^{low} \rightarrow \mathrm{LO}(M)-\mathrm{TO}(M)$, where $\omega(\mathrm{TO}) = 498\ \mathrm{cm}^{-1}$ and $\omega(\mathrm{LO}) = 579\ \mathrm{cm}^{-1}$. However, because of the high energies involved relative to $k_B T$, the Bose-Einstein factors for this channel are very small, and the channel can be neglected.

In Fig. 5.3(b) we plot the frequency and the FWHM after correcting for instrumental broadening of the E_2^{low} Raman peak as a function of temperature. To analyse the FWHM temperature dependence we have used the anharmonic decay model described in Sec. 5.1 taking into account only the difference term in Eq. (5.4). By fitting Γ_0 and V_3^- to the experimental data we obtain $\Gamma_0 = 0.5\ \mathrm{cm}^{-1}$ and $|V_3^-|^2 = 56\ \mathrm{cm}^{-2}$. As can be seen in Fig. 5.3(b), the model predicts a linear increase of the FWHM with increasing temperature that fits very well the experimental data.

Using the anharmonic coupling parameter V_3^- obtained from the FWHM fit,

the anharmonic contribution to the temperature dependence of the E_2^{low} frequency has been calculated and it is also plotted in Fig. 5.3(b). It is worth noting that the calculations do not predict any measurable frequency shift as the temperature is increased. As already discussed in Sec. 4.1, the InN E_2^{low} mode has a negative Grüneisen parameter (see Table 4.1). In this soft mode, the lattice thermal expansion induces an upward frequency shift which nearly compensates the downward shift that results from the cubic anharmonicity. The experimental data actually show a small frequency downshift (about 1 cm^{-1} over the whole temperature range studied) that can be attributed to a small temperature dependent biaxial strain induced by differential thermal expansion of the lattice with respect to the substrate.

The E_2^{high} mode

In previous studies of the E_2^{high} temperature dependence [5, 6], the experimental data were analysed using a simplified anharmonic model in which only the variation of the Bose-Einstein coefficients was taken into account. According to the analysis based on that model, it was concluded that the E_2^{high} phonon mode decays through a generic, symmetric 4-phonon process and no specific decay channels were identified [5, 6]. Here we study the E_2^{high} phonon decay using the general model described in Sec. 5.1, which yields a more accurate description of the E_2^{high} decay processes and gives insight into the most likely decay channels involved.

As can be seen in Fig. 5.2, both the two-phonon sum and difference DOS are very low in the region corresponding to the E_2^{high} frequency (489 cm^{-1}). This suggests that higher order processes may take place in order to mediate in the E_2^{high} decay.

Representative E_2^{high} spectra measured from c-face thin film in the temperature range studied are displayed in Fig. 5.4(a). The E_2^{high} Raman peak shows a considerable broadening and downward frequency shift with increasing temperature. As discussed above, this remarkable broadening cannot be accounted for by 3-phonon interactions because of the low 2-PDOS at the E_2^{high} frequency. Therefore, we consider also the quartic contribution in the model that fits the linewidth temperature dependence. By inspection of the phonon dispersion

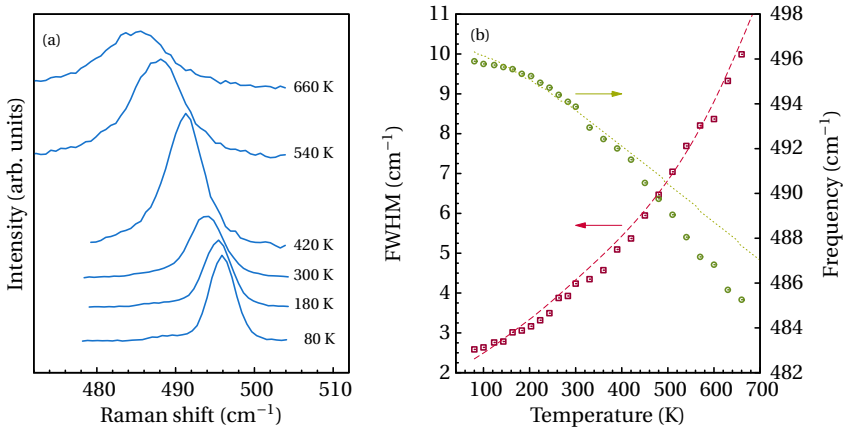

Figure 5.4: *Temperature dependence of the E_2^{high} phonon mode in InN. (a) Measured Raman spectra on c-face thin film for temperatures ranging from 80 to 660 K. (b) Temperature dependence of the linewidth (squares, left axis) and the frequency (circles, right axis). The dashed line is a fit of the model discussed to the linewidth data. The dotted line shows the temperature dependence of the frequency given by the model for the same set of parameters.*

curves and DOS two such decay channels can be identified:

$$\begin{aligned}
&\textit{(i)}\ E_2^{\text{high}} \rightarrow E_2^{\text{low}}(\Gamma) + 2\text{TO}(\Gamma - K, M - \Gamma) && [\omega(E_2^{\text{low}}) = 84\ \text{cm}^{-1},\\
&&& \omega(\text{TO}) = 202\ \text{cm}^{-1}]\\
&\textit{(ii)}\ E_2^{\text{high}} \rightarrow E_2^{\text{low}}(\Gamma) + \text{TO}(A - H) - \text{TA}(A - H) && [\omega(E_2^{\text{low}}) = 84\ \text{cm}^{-1},\\
&&& \omega(\text{TO}) = 495\ \text{cm}^{-1},\\
&&& \omega(\text{TA}) = 91\ \text{cm}^{-1}]
\end{aligned}$$

By fitting $\Gamma(\omega) = \Gamma_0 + \Gamma^{(3)}(\omega) + \Gamma^{(4)}(\omega)$ to the experimental data points we find that the observed temperature dependence of E_2^{high} FWHM is closely matched and we obtain $|V_3^+|^2 = 50\ \text{cm}^{-2}$, $|\tilde{V}_4^+|^2 = 170\ \text{cm}^{-2}$, $|\tilde{V}_4^-|^2 = 34\ \text{cm}^{-2}$ and $\Gamma_0 = 1.9$ cm^{-1}. As can be seen in Fig. 5.4(b) a very good fit to the experimental linewidths is obtained over the whole temperature range.

The anharmonic re-normalization of the E_2^{high} frequency was calculated with the parameters determined above and the resulting temperature dependence is also plotted in Fig. 5.4(b). A good agreement is found with the experimental E_2^{high} frequencies obtained from the Raman measurements at low temperature, but a deviation of about 2 cm^{-1} is observed for higher temperatures. As for the E_2^{low} mode, we attribute this deviation to the temperature dependent biaxial strain induced by differential thermal expansion of the substrate.

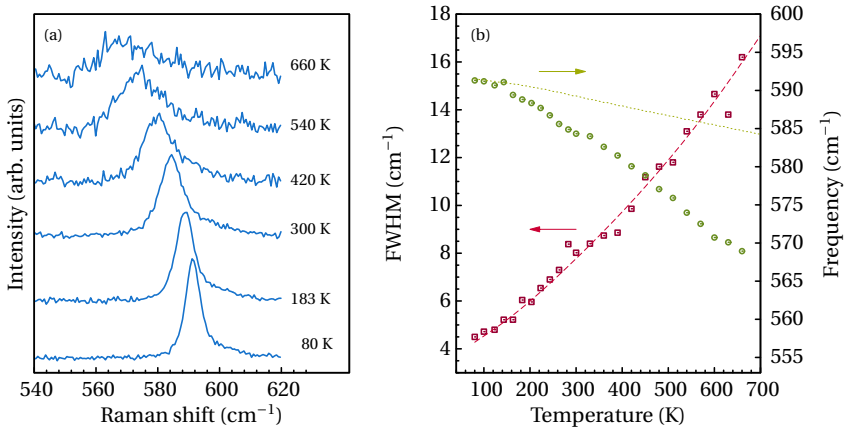

Figure 5.5: *Temperature dependence of the A_1 (LO) phonon mode in InN. (a) Measured Raman spectra for temperatures in the 80-660 K range from c-face thin film. (b) Temperature dependence of the linewidth (squares, left axis) and the frequency (circles, right axis). The dashed line is a fit of the model discussed to the linewidth data. The dotted line shows the temperature dependence of the frequency given by the model for the same set of parameters.*

The A_1(LO) and E_1(LO) modes

Figures 5.5(a) and 5.6(a) show, respectively, Raman spectra of the A_1(LO) and E_1(LO) phonon modes recorded at different temperatures. The A_1(LO) peak is studied from measurements performed on *c*-face thin film, while the E_1(LO) is measured on the *m*-face sample. Both modes display the strongest downshift and broadening of all Raman active modes of InN. That strong temperature dependence are indicative of strong anharmonic interactions of both modes.

In order to fit the FWHM *vs T* data obtained from the Raman measurements we consider the cubic anharmonicity contribution corresponding to phonon sums, and also the quartic contribution. According to the calculated phonon dispersion curves and 2-phonon DOS (Fig. 4.2), the most likely 3-phonon and 4-phonon channels for the A_1(LO) can be identified as :

$$A_1(\mathrm{LO}) \rightarrow \mathrm{TO}(A-H)+\mathrm{TA}(A-H) \qquad [\omega(\mathrm{TO}) = 500\ \mathrm{cm}^{-1}, \omega(\mathrm{TA}) = 89\ \mathrm{cm}^{-1}]$$
$$A_1(\mathrm{LO}) \rightarrow E_2^{\mathrm{high}}(\Gamma)+\mathrm{LA}(M)-\mathrm{TA}(M) \qquad [\omega(E_2^{\mathrm{high}}) = 488.6\ \mathrm{cm}^{-1}, \omega(\mathrm{LA}) = 218\ \mathrm{cm}^{-1}, \omega(\mathrm{TA}) = 118\ \mathrm{cm}^{-1}]$$

The model has been fitted taking into account this channels, and the obtained parameters are $|V_3^+|^2 = 600\mathrm{cm}^{-2}$, $|\tilde{V}_4^-|^2 = 120\ \mathrm{cm}^{-2}$ and $\Gamma_0 = 2\ \mathrm{cm}^{-1}$.

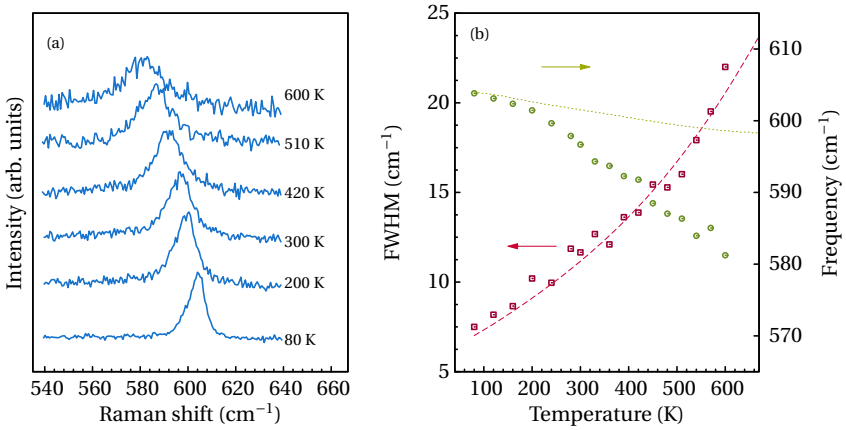

Figure 5.6: *Temperature dependence of the E_1(LO) phonon mode in InN. (a) Measured Raman spectra for temperatures in the 80-600 K range from m-face thin film. (b) Temperature dependence of the linewidth (squares, left axis) and the frequency (circles, right axis). The dashed line is a fit of the model discussed to the linewidth data. The dotted line shows the temperature dependence of the frequency given by the model for the same set of parameters.*

Similarly, the decay channels for the E_1(LO) can be identified to be:

$E_1(\mathrm{LO}) \rightarrow \mathrm{TO}(L)+\mathrm{TA}(L)$	$[\omega(\mathrm{TO}) = 505\ \mathrm{cm}^{-1}, \omega(\mathrm{TA}) = 96\ \mathrm{cm}^{-1}]$
$E_1(\mathrm{LO}) \rightarrow E_2^{\mathrm{high}}(\Gamma)+\mathrm{LA'}(M)-\mathrm{TA'}(M)$	$[\omega(E_2^{\mathrm{high}}) = 488.6\ \mathrm{cm}^{-1}, \omega(\mathrm{LA'}) = 202\ \mathrm{cm}^{-1}, \omega(\mathrm{TA'}) = 85\ \mathrm{cm}^{-1}]$

In this case, the obtained parameters are $|V_3^+|^2$=450 cm^{-2}, $|\tilde{V}_4^-|^2$=200 cm^{-2} and Γ_0=4.5 cm^{-1} for the E_1(LO) mode.

The curves corresponding to the results of the FWHM fits are plotted in Fig. 5.5(b) and Fig. 5.6(b), and show very good agreement with the experimental points. The obtained parameters indicate that the A_1(LO) and E_1(LO) phonon modes mainly decay through 3-phonon mechanisms, but 4-phonon interactions have also to be considered to properly describe the linewidth temperature dependence. This is in contrast with previous studies in which, based on a simplified anharmonic model, it was concluded that the A_1(LO) phonon mode decays asymmetrically through a 3-phonon process into a high energy and a low energy phonon [5, 6].

Concerning the frequency dependence on the temperature, the measured downshift is much larger than the calculated shift taking into account the anharmonic and lattice expansion contributions [see Figures 5.5(b) and 5.6(b)]. As in the case of the E_2 modes, we suggest that the phonon frequency may be affected by the biaxial strain. In the case of the E_1(LO) mode (which has been measured

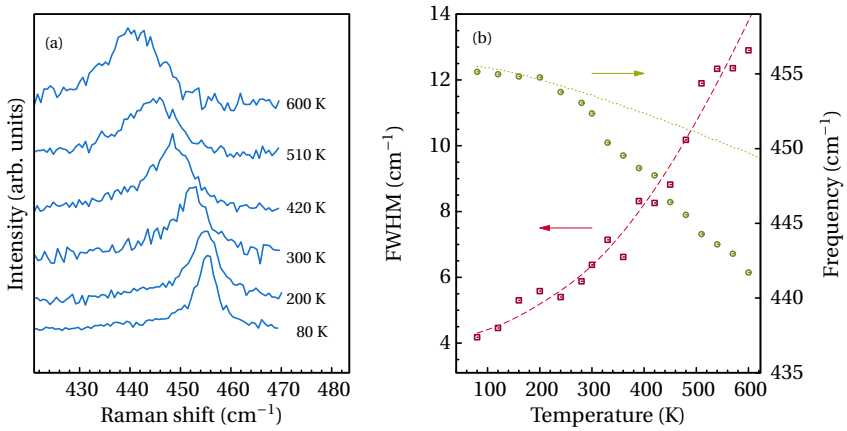

Figure 5.7: *Temperature dependence of the A_1(TO) phonon mode. (a) Raman peak for temperatures in the 80-600 K range under $x(zz)\bar{x}$ configuration, measured from the m-face sample. (b) Temperature dependence of the linewidth (squares, left axis) and the frequency (circles, right axis). The dashed line is a fit of the model discussed to the linewidth data. The dotted line shows the temperature dependence of the frequency given by the model for the same set of parameters.*

on the *m*-face sample), this contribution is expected to be higher than in the modes measured on the *c*-face since, as discussed before, the substrate of the *m*-face sample has much higher thermal expansion coefficients than InN.

The strong frequency downshift exhibited by the experimental data suggests that additional temperature-dependent mechanisms may be affecting the phonon frequencies. The temperature dependence of the dielectric constant ε_∞ and of the effective transverse charge e_T^*, which results in a temperature dependent LO-TO splitting, may also contribute to the large deviation of the measured LO frequencies to the calculated anharmonic shifts.

The A_1(TO) and E_1(TO) modes

The transversal optical modes have been measured from the *m*-face thin film using different scattering geometries. Their temperature-dependent spectra are plotted in Fig. 5.7(a) and Fig. 5.8(a) for the A_1(TO) and the E_1(TO), respectively. In these figures it can be seen that both phonon peaks exhibit a significant broadening and downward frequency shift. Due to the weak signal obtained from the *m*-face sample at high temperature, the maximum temperature considered for the anharmonicity study is lower than for the other phonon modes.

Both the frequencies of the A_1(TO) and E_1(TO) phonon modes of InN and their temperature dependence are very similar, which indicates that similar an-

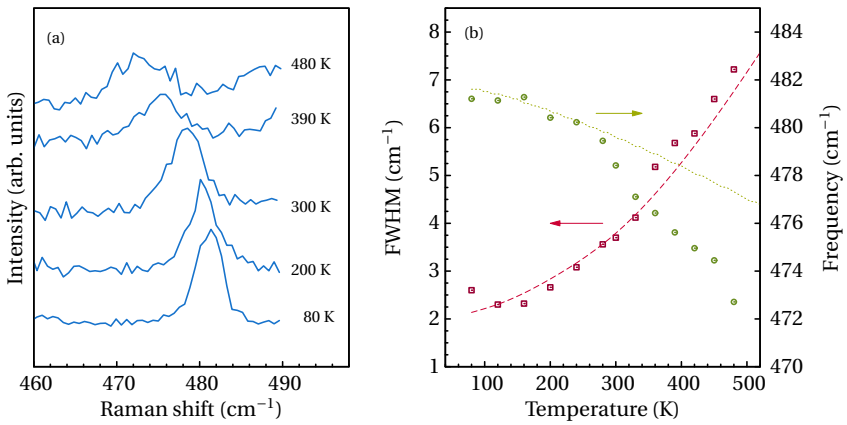

Figure 5.8: *Temperature dependence of the E_1(TO) phonon mode. (a) Measured Raman spectra for temperatures in the 80-480 K range under $x(zy)\bar{x}$ configuration from the m-face sample. (b) Temperature dependence of the linewidth (squares, left axis) and the frequency (circles, right axis). The dashed line is a fit of the model discussed to the linewidth data. The dotted line shows the temperature dependence of the frequency given by the model for the same set of parameters.*

harmonic interactions take place for both phonon modes. In fact, both the A_1(TO) and the E_1(TO) frequencies lie in a two-phonon difference DOS plateau, whereas the two-phonon sum DOS is almost zero in the same region (Fig. 5.2). This indicates that *up-conversion* processes are the only 3-phonon mechanisms which can take place in the decay of these modes. However, the temperature dependence of the linewidth of both the A_1(TO) and E_1(TO) phonon modes exhibits a strong non-linear behaviour, which indicates that higher order processes may take place. Therefore, we have taken into account the cubic difference term and also a quartic term in the modelling of the linewidth temperature dependence. The inspection of the phonon dispersion curves and DOS (Fig. 4.2) allows us to identify the most likely channels. For the A_1(TO) we consider:

$A_1(\mathrm{TO}) \rightarrow \mathrm{TO}(M)-\mathrm{TA}(M)$	$[\omega(\mathrm{TO}) = 523\ \mathrm{cm}^{-1}, \omega(\mathrm{TA}) = 80\ \mathrm{cm}^{-1}]$
(i) $A_1(\mathrm{TO}) \rightarrow E_2^{\mathrm{low}}(\Gamma)+\mathrm{LO}(M)-\mathrm{LA}(M)$	$[\omega(E_2^{\mathrm{low}}) = 84\ \mathrm{cm}^{-1}, \omega(\mathrm{LO}) = 570\ \mathrm{cm}^{-1},$ $\omega(\mathrm{LA}) = 204\ \mathrm{cm}^{-1}]$
(ii) $A_1(\mathrm{TO}) \rightarrow B^{\mathrm{low}}(\Gamma) + 2\mathrm{TA}(M)$	$[\omega(B^{\mathrm{low}}) = 224\ \mathrm{cm}^{-1}, \omega(\mathrm{TA}) = 113\ \mathrm{cm}^{-1}]$

The parameters obtained from the fit are $|V_3^-|^2 = 100\ \mathrm{cm}^{-2}$, $|\tilde{V}_4^{-,(i)}|^2 = 100\ \mathrm{cm}^{-2}$, $|\tilde{V}_4^{+,(ii)}|^2 = 50\ \mathrm{cm}^{-2}$ and $\Gamma_0 = 4\ \mathrm{cm}^{-1}$.

For the E_1(TO) phonon mode, the examination of the phonon DOS indicates

that the most suitable 4-phonon processes are:

$E_1(\mathrm{TO}) \rightarrow \mathrm{LO}(L)-\mathrm{TA}(L)$	$[\omega(\mathrm{LO}) = 581\ \mathrm{cm}^{-1}, \omega(\mathrm{TA}) = 106\ \mathrm{cm}^{-1}]$
(i) $E_1(\mathrm{TO}) \rightarrow E_2^{\mathrm{low}}(\Gamma)+\mathrm{TO}(M)-\mathrm{TA}(M)$	$[\omega(E_2^{\mathrm{low}}) = 84\ \mathrm{cm}^{-1}, \omega(\mathrm{TO}) = 541\ \mathrm{cm}^{-1}, \omega(\mathrm{TA}) = 150\ \mathrm{cm}^{-1}]$
(ii) $E_1(\mathrm{TO}) \rightarrow B^{\mathrm{low}}(\Gamma) + 2\mathrm{TA}(K-M)$	$[\omega(B^{\mathrm{low}}) = 224\ \mathrm{cm}^{-1}, \omega(\mathrm{TA}) = 126\ \mathrm{cm}^{-1}]$

The parameters obtained by the fit are $|V_3^-|^2 = 20\ \mathrm{cm}^{-2}$, $|\tilde{V}_4^{-,(i)}|^2 = 39\ \mathrm{cm}^{-2}$, $|\tilde{V}_4^{+,(ii)}|^2 = 60\ \mathrm{cm}^{-2}$ and $\Gamma_0 = 1.9\ \mathrm{cm}^{-1}$. Fig. 5.7(b) and Fig. 5.8(b) show the curves resulting from the fits of the $A_1(\mathrm{TO})$ and the $E_1(\mathrm{TO})$ FWHM, respectively. As can be seen in these figures, the calculated linewidth temperature dependences exhibit very good agreement with the experimental data.

The temperature frequency shift of the $A_1(\mathrm{TO})$ and $E_1(\mathrm{TO})$ modes corresponding to the anharmonic coupling parameters determined from the FWHM fits are also plotted in Fig. 5.7(b) and Fig. 5.8(b), respectively. In both cases, when the temperature increases, the experimental data show a higher frequency shift than that expected from the anharmonicity calculations. As for previous modes, we suggest differential thermal expansion of the substrate as the reason for this deviation. Both the $A_1(\mathrm{TO})$ and the $E_1(\mathrm{TO})$ Raman spectra were obtained from the m-face sample grown on (100) γ-$LiAlO_2$. As the thermal expansion coefficient of the substrate is much higher than that of the InN, an additional temperature-dependent frequency downshift is expected because of the tensile biaxial strain induced by the differential thermal expansion, which may explain the discrepancy between the calculated and the measured frequency shift in the m-face samples.

Throughout this section, the temperature dependence of the InN phonon linewidths has been studied using an anharmonic model which considers the contribution of 3-phonon and 4-phonon processes. This model gives an accurate description of the temperature dependence of the phonon linewidth for all the modes. From the anharmonic coupling parameters, determined from the model fits to the FWHM, we have calculated the the anharmonic contribution to the frequency downshift. We have seen that the measured frequency downshift in the case of the E_2 modes is well accounted for by the anharmonic frequency renormalization. For the other modes, the measured frequencies show a frequency downshift much higher than that predicted by the anharmonic calculation. In the case of the modes measured from the m-face sample, this difference may be due to the biaxial strain arising from the thermal mismatch between the lattice and the substrate. For the LO modes, an additional temperature dependence of the LO-TO splitting may contribute to the frequency downshift.

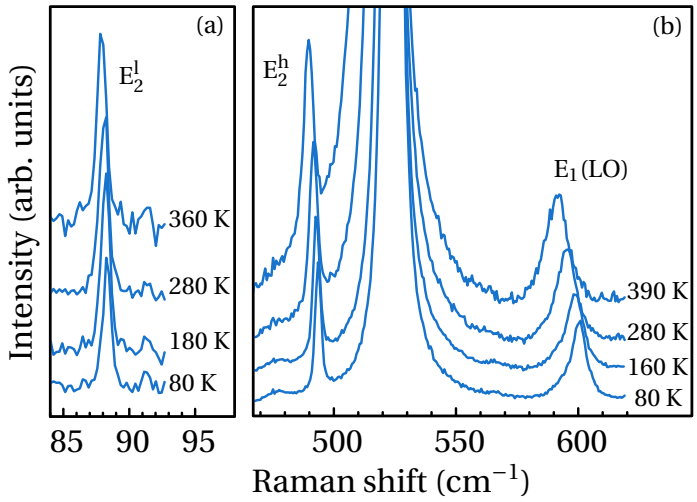

Figure 5.9: *Raman spectra of InN NWs taken at different temperatures. Note that the axis scale is different for (a) and (b). Experimental conditions are detailed in the text.*

5.3 Anharmonic decay in InN nanowires

In the previous section the phonon anharmonic decay in InN thin films has been analysed. In this section we address the phonon anharmonic decay in InN NWs, whose crystalline structure is expected to present a reduced defect density and less strain than heteroepitaxially-grown thin films. As described in Sec. 4.2.1.4, a difficulty in studying nanostructures with Raman spectroscopy is that a well-defined scattering configuration cannot be selected and then Raman selection rules cannot be used to separate the different phonon modes. In addition, in uniaxial polar crystals, for phonon propagation directions out of the optical axis a mixing of different symmetry modes occurs, giving rise to quasi-LO and quasi-TO modes which display an angular dispersion of their frequencies.

InN NWs

The studied InN NWs were catalyst-free grown by plasma-assisted MBE (PAMBE) under N-rich conditions on Si (111) substrates [21]. They have diameters between 30 and 110 nm and lengths up to 1μm. The nanowires are single crystalline with the *c*-axis parallel to the wire and the point defects and stacking faults are mainly at the base of the wires. They exhibit a small tilt of the wire axis relative to the surface normal of the substrate.

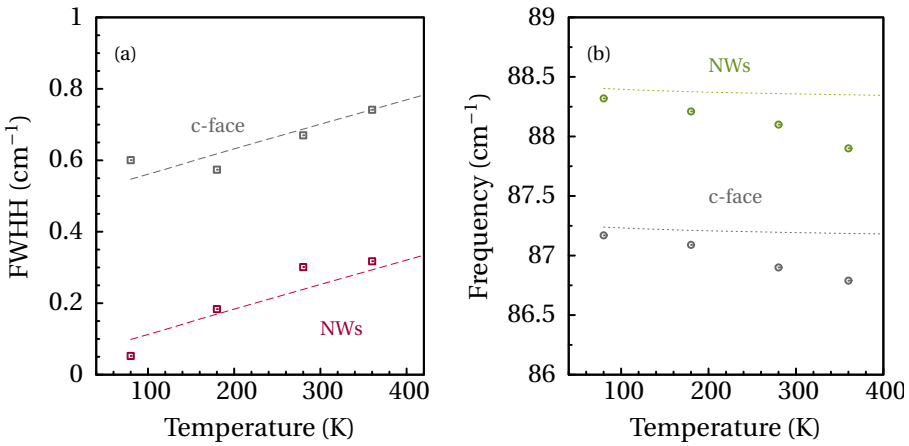

Figure 5.10: *Temperature dependence of the E_2^{low}. Phonon mode linewidth (a) and frequency (b) measured in InN nanowires and thin films are compared. The lines are the fits to the linewidth data and the frequency shift predicted by the model.*

Temperature-dependent measurements

The Raman spectra were obtained in near-backscattering geometry on the as-grown samples and are shown in Fig. 5.9. The slit widths and spectrometer configurations were the same as for thin films.

The spectra exhibit three InN peaks, corresponding to the E_2^{low}, E_2^{high} and E_1(LO) phonon modes, superimposed to the Si substrate signal. It is worth noting that the E_2^{low} frequency remains nearly constant with increasing temperature, while the E_2^{high} and the E_1(LO) phonon modes exhibit a considerable frequency shift and peak broadening.

The temperature dependence of each phonon mode is studied here following the same scheme as for InN thin films. For each mode, we compare the temperature dependence of the phonon linewidth with that obtained from thin films in order to contrast the similar decay channels in both structures. We also compare the frequency temperature dependences measured from NWs with those of thin films.

Linewidth temperature dependence and decay channels

The temperature dependence of the E_2^{low}, E_2^{high} and E_1(LO) phonon modes are shown in Fig. 5.10(a), Fig. 5.11(a) and Fig. 5.12(a), respectively, in comparison with the data obtained from thin films. It can be seen that for all the phonon modes the linewidths measured from nanowires are significantly lower than those obtained from thin films, but the dependence that they exhibit with in-

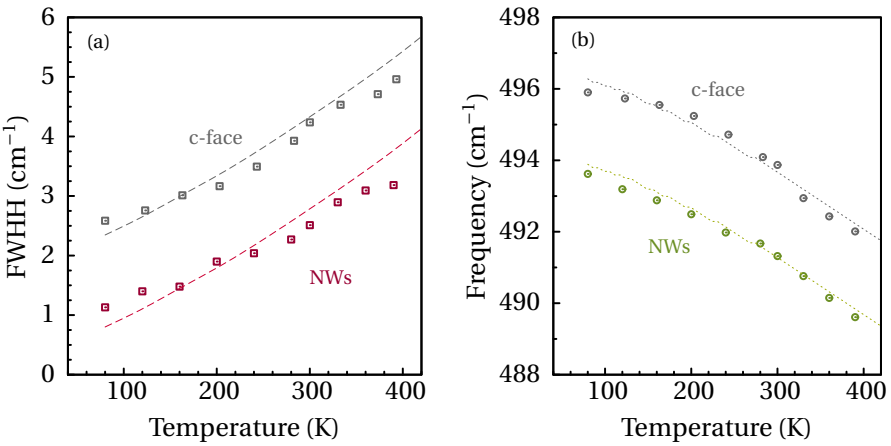

Figure 5.11: *Temperature dependence of the E_2^{high}. Phonon mode linewidth (a) and frequency (b) measured in InN nanowires and thin films are compared. The lines are the fits to the linewidth data and the frequency shift predicted by the model.*

Table 5.1: *Background impurity broadening parameter (Γ_0) used to fit the FWHH temperature dependence and phonon linewidths (Γ) of the E_2 and E_1(LO) modes in InN NWs at 80 K in comparison with those of InN thin films. All the values are given in cm^{-1} units.*

	Γ NWs	Γ Thin films.	Γ_0 NWs	Γ_0 Thin films
E_2^{low}	0.053	0.6	0.05	0.5
E_2^{high}	1.13	2.6	0.35	1.9
E_1(LO)	5.81	7.5	2.95	4.5

creasing temperature is very similar. Indeed, by changing the constant parameter Γ_0, the temperature-dependence of the phonon linewidth measured from NWs can be adjusted with the anharmonic parameters derived from the analysis performed on the thin films phonon modes. This indicates that the phonon decay channels deduced in the case of InN thin films are also valid for InN NWs.

The temperature-independent Γ_0 parameter accounts for the background impurity contribution to the phonon broadening. The values used to fit the data from nanowires are much lower than those used to fit the thin-film data (see Table 5.1). Since this term is related with defects and impurities of the lattice structure, the lower value of Γ_0 in all the phonon modes confirms that the studied nanowires have lower defect concentration and better crystalline structure than the *c*-face and *m*-face thin films.

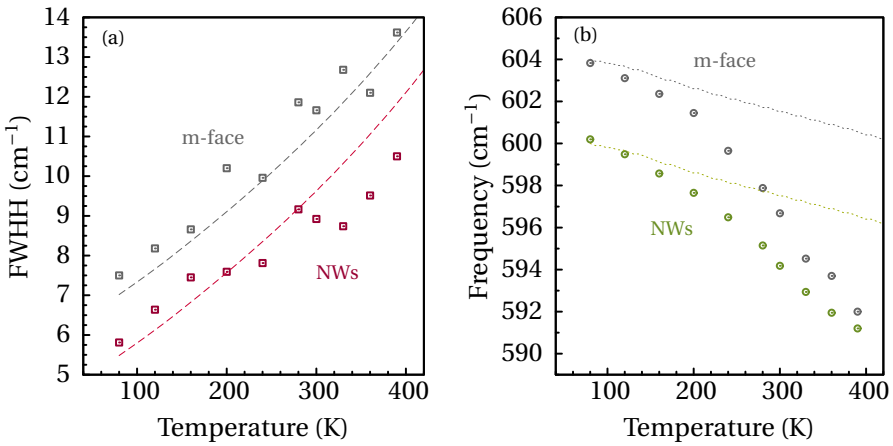

Figure 5.12: *Temperature dependence of the E_1 (LO) phonon mode linewidth (a) and frequency (b) measured in InN nanowires and thin films. The lines are the fits to the linewidth data and the frequency shift predicted by the model.*

Frequency temperature dependence: NWs *vs.* thin films

The frequency temperature dependence of the E_2^{low} is plotted in Fig. 5.10(b) in comparison with that measured from thin films. It can be seen that in both cases the E_2^{low} frequency changes very little within the studied temperature range. As discussed in the previous section, this is a consequence of the soft-mode nature of the E_2^{low} mode, as the frequency shift associated with the thermal expansion of the lattice has an opposite sign and nearly compensates the anharmonic shift.

From the comparison between both datasets, and considering the NWs to be nearly strain-free, we can extract information about the strain in the thin film sample. Since the c-face thin film is biaxially strained, the E_2^{low} frequency in the thin film is lower than in the NWs. Following the analysis of Ref. [22], from the observed frequency shift $\Delta\omega = [2a - bv/(1-v)]\varepsilon_a$ and the hydrostatic linear pressure coefficient $\partial\omega/\partial P = -2a(S_{11} + S_{12} + S_{13} + b(2S_{13} + S_{33}))$ we can derive the deformation potentials a, b for the E_2^{low} mode. Using the hydrostatic linear pressure coefficient $\partial\omega/\partial P = -0.44$ cm^{-1} GPa^{-1} [23], the Poisson ratio $v = 0.21$ and the compliance tensor components given in Ref. [24], we find $a = -711$ cm^{-1} and $b = 387$ cm^{-1}.

Fig. 5.11(b) shows the temperature dependence of the E_2^{high} frequency in comparison with that measured for thin films. The E_2^{high} frequency measured in the NWs at room temperature is close to the strain-free frequency estimated in Ref. [25] and about 2.5 cm^{-1} lower than the frequency shown by the same phonon mode measured in the c-face sample at the same temperature. This

shift is constant over all the temperature range, and indicates the presence of residual strain in the thin films.

The agreement between the calculated curves and the measured data is less satisfactory in the case of the E_1(LO) mode frequency. Figure 5.12(b) shows the temperature dependence of the E_1(LO) frequency measured in nanowires and in an m-face epilayer grown on a γ-$LiAlO_2$ substrate. In the previous section, the strong frequency downshift with increasing temperature measured in the m-face thin film was tentatively attributed to the combined effect of a temperature-dependent biaxial strain induced by the large thermal mismatch with the substrate and of a possible decrease of the dielectric constant, and hence of the LO-TO splitting, with increasing temperature. Here we see that, although the E_1(LO) frequency downshift observed in the NWs is still higher than predicted by the calculations, it is less pronounced than in the m-face epilayer. From this result, we can extract two conclusions. First, this indicates that effectively the LO-TO splitting temperature dependence may have a significant impact on the observed frequency shift. Second, this result corroborates that the temperature-dependent biaxial strain plays a significant role in the E_1(LO) frequency downshift observed in the m-face epilayer. This suggests that the reduction of the LO-TO splitting with increasing temperature may indeed play a major role in the large frequency downshift observed in the relatively unstrained NWs, and confirms that in the case of thin films the additional contribution of the differential thermal expansion must be taken into account.

These results confirm that the phonon dynamics are not substantially changed in the studied NWs, but the reduced defect density affects the phonon linewidths and frequencies.

5.4 Phonon lifetimes of InN thin films and NWs

The phonon lifetime τ can be evaluated from the Raman linewidth via the energy-time uncertainty relation [2],

$$\frac{1}{\tau} = \frac{\Gamma}{\hbar}, \tag{5.9}$$

where Γ is the intrinsic phonon linewidth (after correcting for the spectrometer broadening) and $\hbar$ is the Planck's constant. As shown throughout this chapter, the Raman peaks measured in NWs are narrower than their counterparts in thin films and therefore the phonon lifetimes of all the studied modes are longer in NWs than in thin films. Since we have found the same temperature-dependent phonon anharmonic decay both in NWs and thin films, the lifetime difference must be accounted for by another limiting mechanism.

There are mainly two mechanisms which limit phonon lifetime: *(i)* anharmonic decay of the phonon, with a characteristic decay time τ_A, and *(ii)* perturbation of the translational symmetry of the crystal by the presence of impurities and defects, with a characteristic decay time τ_I. The phonon lifetime deduced from our Raman measurements can be decomposed as

$$\frac{1}{\tau} = \frac{1}{\tau_A} + \frac{1}{\tau_I}. \tag{5.10}$$

It is difficult to separate the contribution of both mechanisms, but we can obtain an estimation of the characteristic decay time associated with impurities from the values of the Γ_0 parameter provided by the temperature dependence FWHM fits,

$$\frac{1}{\tau_I} = \frac{\Gamma_0}{\hbar}. \tag{5.11}$$

In Table 5.2 we list the lifetimes for the InN phonons at 80 K and room temperature, as well as the estimated impurity-related contribution for both thin films and NWs. The E_2^{low} phonon mode exhibits a remarkably high lifetime (8.8 ps at 80 K). This value is however still one order of magnitude lower than that reported for the E_2^{low} in ZnO [26, 27]. From our values of Γ and Γ_0 it is deduced that the impurity effects are the main contribution limiting the lifetime of this mode, which indicates that longer lifetimes can be obtained if sample quality is improved.

In fact, as the intrinsic phonon lifetime is related to the decay probability through the possible decay channels, the E_2^{low} phonon mode has a long intrinsic lifetime, because its only available decay channel is a low-probability up-conversion process. In contrast, the shortest lifetimes are those of the LO phonon modes, whose main decay channels are the decay into a pair

Table 5.2: *Phonon lifetimes of all the studied phonon modes of InN at 80 K and room temperature for both thin films and NWs The characteristic decay time associated with impurities τ_I is estimated from the background broadening parameter Γ_0 used to fit the FWHM temperature dependence.*

		$T = 80$ K		Room temperature			
	Phonon mode	Γ cm^{-1}	τ 10^{-12} s	Γ cm^{-1}	τ 10^{-12} s	Γ_0 cm^{-1}	τ_I 10^{-12} s
Thin films	E_2^{low}	0.6	8.8	0.69	7.7	0.5	10.6
	E_2^{high}	2.6	2.05	4.2	1.3	1.9	2.8
	A_1(LO)	4.5	1.18	8.0	0.66	1.1	4.8
	E_1(LO)	7.5	0.71	11.7	0.45	3.1	1.7
	A_1(TO)	4.2	1.3	6.4	0.83	4	1.3
	E_1(TO)	2.6	2.0	3.7	1.43	1.9	2.8
NWs	E_2^{low}	0.053	101	0.3	17.7	0.05	106
	E_2^{high}	1.13	4.69	2.5	2.1	0.35	15
	E_1(LO)	5.81	0.91	8.8	0.6	2.95	1.8

of phonons. These 3-phonon processes leading to decay into lower energy phonons have a higher probability and therefore are more efficient in limiting the phonon lifetime.

From Table 5.2, it can be seen that the phonon modes measured from the *m*-face layer have, on average, a shorter lifetime than those measured from the *c*-face thin film. Regarding the values of the impurity-related parameter Γ_0, the results shown in Table 5.2 indicate that phonon lifetime is limited by the crystalline quality of the sample, which is poorer in the *m*-face sample, as deduced from the electrical measurements presented in Sec. 5.2. Much longer lifetimes are measured from the NWs samples, which is a clear evidence of the improved crystalline quality achieved in these nanostructures.

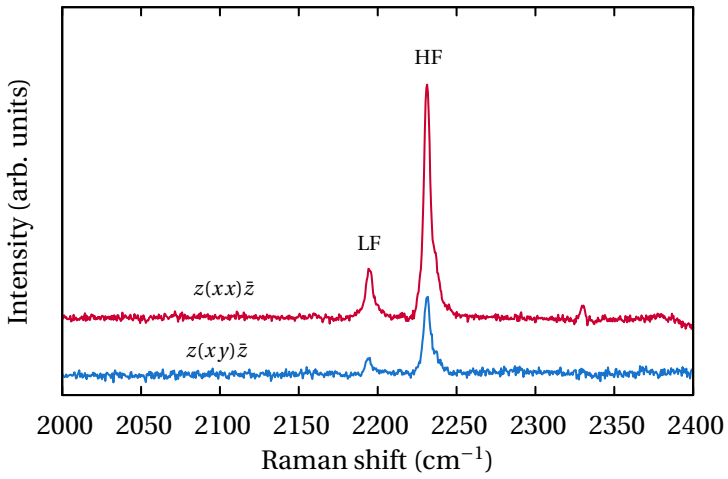

Figure 5.13: *Raman spectra of a heavily-doped InN:Mg in the spectral region of Mg-H complexes. Lower-frequency and higher-frequency peaks are labelled as LF and HF, respectively. and Spectra taken at $T = 80K$ and obtained with the standard spectrometer mode using parallel and crossed polarizations.*

5.5 Anharmonic broadening of LVMs in heavily-doped InN

Apart from lattice phonons, other vibrational excitations such as local vibrational modes (LVM) may exist in the material and also have their characteristic lifetimes. An introduction to the origin of the LVM was given in Sec. 4.2.3. Here we study the anharmonic broadening of LVMs involving H complexes in heavily-doped InN:Mg layers. These modes have frequencies much higher than the lattice phonons, and therefore anharmonic decay into lattice phonons is unlikely.

We study heavily-doped InN:Mg layers, which were grown by PAMBE on sapphire substrates with a GaN buffer layer. A thin undoped InN interlayer was grown at low temperature. After that, Mg-doped InN was grown under slightly In-rich conditions. Secondary ion mass spectometry measurements yield a Mg concentration in the doped layer of 2.3×10^{20} cm^{-3}. The Raman spectra obtained in backscattering geometry are shown in Fig. 5.13 for parallel and crossed polarizations, and in both spectra two peaks at 2194 cm^{-1} and 2231 cm^{-1} are detected.

By analogy with previous results and calculations on GaN:Mg [28], and assuming that the frequency of the H vibrations against interstitial impurities do not depend strongly on the host lattice, these peaks are attributed to Mg_iH_2 or Mg_{In}-N-In_i-H_2 defect complexes. As can be seen in Fig. 5.14, Mg_iH_2 consists in

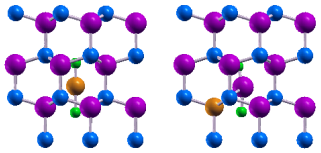

Mg_iH_2 Mg_{In}–N–In_iH_2

Figure 5.14: *Schematic representation of the acceptor-hydrogen complexes.*

a interstitial ion of magnesium with the two H atoms along the *c* axis, while the Mg_{In}-N-In_i-H_2 consist in a substitutional Mg-atom and a shorter In_i-H bond, which is slightly off *c* direction. As can be seen in the spectra plotted in Fig. 5.13, both peaks are still clearly detected in crossed polarization, albeit their intensity is lower. The observation of both LVM peaks in crossed polarization suggests that they may arise from the A' stretching modes of the substitutional-interstitial complex (C_s symmetry), which are allowed both in parallel and crossed polarizations, or from a misalignment of the Mg_iH_2 complex that would reduce its C_{3v} symmetry.

We have studied the temperature dependence of these LVMs in the 80-500 K range. The reproducibility of the measurements was checked by consecutively sweeping up and down the temperature to rule out the possibility of hydrogen desorption or thermal instability of the Mg-H complexes. The obtained spectra are displayed in Fig. 5.15. It can be seen that for temperatures higher than 520 K the signal is too poor to extract the frequency or linewidth of the peaks. We have analysed the temperature dependence of the frequency and the linewidth of both peaks, and the data obtained are plotted in Fig. 5.16. Both modes exhibit a significant linewidth broadening over the studied temperature range, which suggests that their lifetimes are limited by anharmonic interactions. However, as stated above, their decay into lattice phonons is unlikely because energy conservation would require a very high order decay channel. Therefore, other mechanisms must take part in the determination of the finite lifetime of these modes.

The higher frequency peak (HF) shows a progressive frequency downshift and broadening with increasing temperature. Since decay into lattice phonons is unlikely. We propose dephasing by quasi-elastic acoustic-phonon scattering to be the mechanism accounting for the anharmonic broadening of this mode [29]. This anharmonic broadening mechanism is based on the interaction of the LVMs with thermally-populated acoustic lattice phonons, which leads to the dephasing of the excited LVM. In the Debye approximation of the acoustic branches, the temperature-dependent corrections to the LVM linewidth and frequencies are described by [30, 31]

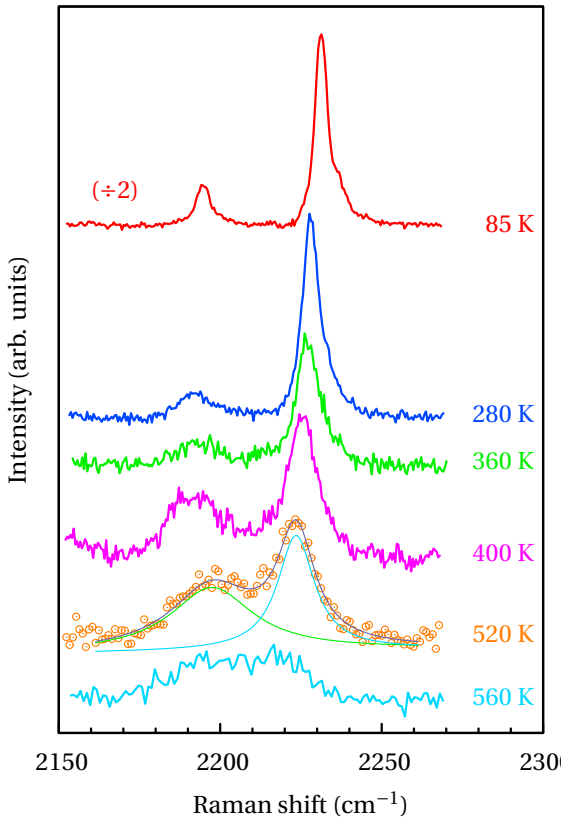

Figure 5.15: *Raman spectra of the Mg-H complexes in heavily-doped Mg:InN as a function of the temperature.*

$$\Gamma(T) = \Gamma_0 + A\left(\frac{T}{\Theta_C}\right)^7 \int_0^{\Theta_C/T} \frac{x^6 e^x}{(e^x-1)^2}\,dx, \tag{5.12}$$

$$\omega(T) = \omega_0 - B\left(\frac{T}{\Theta_C}\right)^4 \int_0^{\Theta_C/T} \frac{x^3}{(e^x-1)}\,dx. \tag{5.13}$$

In these equations $k_B\Theta_C$ is the Debye cutoff energy, which takes into account that only the low-energy acoustic branches interact with the LVM. The linewidth and frequency temperature dependences given by Eqs. (5.12) and (5.13) have been found to fit well the experimental data for $\Gamma_0 = 4.6$ cm^{-1}, $\Theta_C = 560$ K, $A = 64$ cm^{-1}. The calculated curves are plotted in Fig. 5.16 together with the experimental points obtained from the Raman measurements.

The temperature dependence of the frequency and FWHM of the lower frequency mode (LF) is plotted in Fig. 5.16. The frequency of this mode shows an unexpected temperature behaviour. For low temperatures it displays a frequency decrease, but for $T \gtrsim 350$ K the trend is reversed and its frequency increases with temperature. This behaviour cannot be accounted for by the quasi-elastic acoustic phonon scattering dephasing. Another mechanism should be

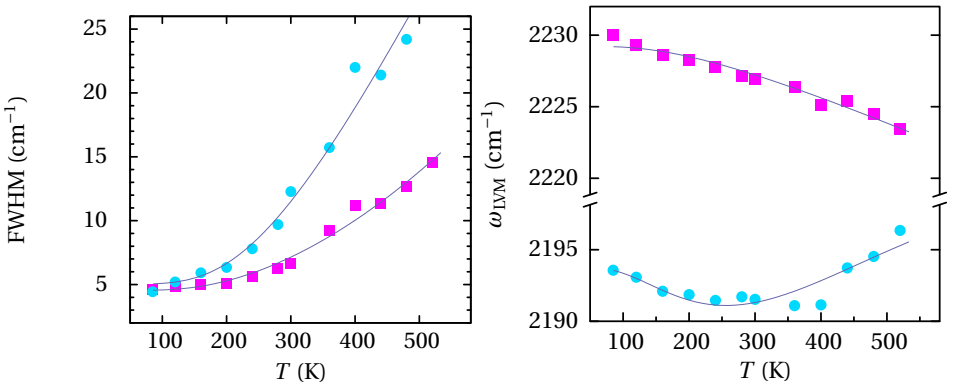

Figure 5.16: *Temperature dependence of the Mg-H local vibrational modes in heavily-doped Mg:InN. The upper and lower panel show the linewidth and frequency temperature dependence, respectively. In both panels, red squares correspond to data from the higher frequency LVM and green triangles to the lower frequancy LVM. Lines are the calculations described in the text.*

involved in the anharmonic behaviour of this mode. We propose that anharmonic exchange-coupling to a lower frequency mode (ω_0) of the whole impurity complex may yield the additional frequency shift [31]. This mechanism is based on the perturbation of the LVM vibration due to a lower-frequency mode (for instance, a frustrated rotation of the impurity molecular unit). As a consequence of such a perturbation, a further dephasing of the LVM takes place, which results in an additional contribution to the temperature dependence. In the framework of this exchange-coupling model, the contributions to the temperature dependence of the phonon frequency and linewidth are given by [32]

$$\Gamma(T) = \Gamma_0 + 2\eta \frac{\delta\omega^2}{\delta\omega^2 + \eta^2} e^{-\hbar\omega_0/k_B T}, \tag{5.14}$$

$$\omega(T) = \omega_0 + \delta\omega \frac{\eta^2}{\delta\omega^2 + \eta^2} e^{-\hbar\omega_0/k_B T}. \tag{5.15}$$

In these equations $\delta\omega$ is the coupling strength, and η is damping of the lower-frequency mode ω_0. The linewidth and frequency temperature dependence of the lower LVM have been found to fit well the experimental data by taking into account both the quasi-elastic acoustic-phonon scattering and the exchange-coupling model with a lower frequency mode ω_0. The parameters that fit the data are Γ_0 = cm^{-1}, Θ_C = 560 K, A = 26 cm^{-1}, B = 78 cm^{-1}, ω_0 = 629 cm^{-1}, $\delta\omega_0$ = 129 cm^{-1}, η = 224 cm^{-1}. In these calculations we have considered a frequency for the lower frequency mode ω_0 that is higher than the lattice phonon frequencies. This frequency could correspond to an hypothetical mode related

to frustrated rotations/translations of the whole impurity complex or to a wag mode of the H atom in these complexes. As can be seen in Fig. 5.16, both the frequency and linewidth of the observed LVMs as a function of temperature are well reproduced by the empirical model described, which is based on quasi-elastic acoustic-phonon scattering and contains an anharmonic exchange coupling contribution in the case of the lower frequency mode.

Throughout this chapter we have presented the temperature dependence of the InN phonon modes measured from thin films and NWs. We have been able to model the temperature dependence of the FWHH of all the vibrational modes using the anharmonic model proposed, and we have deduced the decay mechanisms for the lattice phonons and H related LVMs. The results presented in this chapter provide a comprehensive picture of the lattice dynamics and phonon interactions in the InN compound.

References

[1] J. Serrano, F. J. Manjón, A. H. Romero, F. Widulle, R. Lauck, and M. Cardona. *Phys. Rev. Lett.*, 90:055510, 2003.

[2] L. Bergman, D. Alexson, P. L. Murphy, R. J. Nemanich, M. Dutta, M. A. Stroscio, C. Balkas, H. Shin, and R. F. Davis. *Phys. Rev. B*, 59:12977, 1999.

[3] R. Cuscó, E. Alarcón-Lladó, J. Ibáñez, L. Artús, J. Jiménez, B. Wang, and M. J. Callahan. *Phys. Rev. B*, 75:165202, 2007.

[4] M. Kuball, J. M. Hayes, Ying Shi, and J. H. Edgar. *Appl. Phys. Lett.*, 77:1958, 2000.

[5] J. W. Pomeroy, M. Kuball, J. Schaff H. Lu, X. Wang, and A. Yoshikawa. *Appl. Phys. Lett.*, 86:233501, 2005.

[6] X. D. Pu, J. Chen, W. Z. Shen, H. Ogawa, and Q. X. Guo. *J. Appl. Phys.*, 98:033527, 2005.

[7] B. Song, J. K. Jian, G. Wang, H. Q. Bao, and X. L. Chen. *J. Appl. Phys.*, 101:124302, 2007.

[8] R. A. Cowley. *Rep. Prog. Phys*, 31:123, 1968.

[9] J. Menéndez and M. Cardona. *Phys. Rev. B*, 29:2051, 1984.

[10] M. Canonico, C. Poweleit, J. Menéndez, A. Debernardi, S. R. Johnson, and Y.-H. Zhang. *Phys. Rev. Lett.*, 88:215502, 2002.

[11] P. G. Klemens. *Phys. Rev.*, 148:845, 1966.

[12] M. Balkanski, R. F. Wallis, and E. Haro. *Phys. Rev. B*, 28:1928, 1983.

[13] M. S. Liu, L. A. Bursill, S. Prawer, and R. Beserman. *Phys. Rev. B*, 61:3391, 2000.

[14] J. W. Pomeroy, M Kuball, H. Lu, W. J. Schaff, X Wang, and A. Yoshikawa. *Appl. Phys. Lett.*, 86:223501, 2005.

[15] W. J. Borer, S. S. Mitra, and K. V. Namjoshi. *Solid State Commun.*, 9:1377, 1971.

[16] K. Wang and R. R. Reeber. *Appl. Phys. Lett.*, 79:1602, 2001.

[17] W. Paszkowicz. *Powder diffraction*, 14:258, 1999.

[18] M. Leszczynski, T. Suski, H. Teisseyre, P. Perlin, I. Grzegory, J. Jun, S. Porowski, and T. D. Moustakas. *J. Appl. Phys.*, 76:4909, 1994.

[19] M. M. C. Chow, H. Chun Huang, D.-S. Gan, and C. W. C. Hsu. *J. Cryst. Growth*, 291:485, 2006.

[20] H. Lu, W. J. Schaff, L. F. Eastman, and C. E. Stutz. *Appl. Phys. Lett.*, 82:1736, 2003.

[21] T. Stoica, R. J. Meijers, R. Calarco, T. Richter, E. Sutter, and H. Luth. *Nano Lett.*, 6:1541, 2006.

[22] X. Wang, Che S-B, Y. Ishitani, and Yoshikawa A. *Appl. Phys. Lett.*, 89:171907, 2006.

[23] J. Ibáñez, F. J. Manjón, A. Segura, R. Oliva, R. Cuscó, R. Vilaplana, T. Yamaguchi, Y. Nanishi, and L. Artús. *Appl. Phys. Lett.*, 99:011908, 2011.

[24] V. S. Harutyunyan, P. Specht, J. Ho, and E. R. Weber. *Defect Data, Solid State Data A. Defect Diffus. Forum*, 226:79, 2004.

[25] X. Wang, S. B. Che, Y. Ishitani, and A. Yoshikawa. *Appl. Phys. Lett.*, 89:171907, 2006.

[26] C. Aku-Leh, J. Zhao, R. Merlin, J. Menéndez, and M. Cardona. *Phys. Rev. B*, 71:205211, 2005.

[27] M. Millot, R. Tena-Zaera, V. Muñoz-Sanjosé, J.-M. Broto, and J. González. *Appl. Phys. Lett.*, 96:152103, 2010.

[28] F. A. Reboredo and S. T. Pantelides. *Phys. Rev. Lett.*, 82:1887, 1999.

[29] M. D. McCluskey, E. E. Haller, J. Walker, and N. M. Johnson. *Phys. Rev. B*, 52:11859–11864, 1995.

[30] A. S. Barker and A. J. Sievers. *Rev. Mod. Phys.*, 47:S1–S179, 1975.

[31] D. E. McCumber and M. D. Sturge. *J. Appl. Phys.*, 34(6):1682–1684, 1963.

[32] B. N. J. Persson and R. Ryberg. *Phys. Rev. B*, 32:3586–3596, 1985.

CHAPTER 6

Resonant Raman scattering in InN and InGaN

As has been introduced in Sec. 3.1.3, when the excitation energy is close to electronic resonances of the material, resonant mechanisms are involved in the Raman scattering process. This results in an intensity enhancement of the Raman spectra [1]. Resonant Raman scattering has been reported for a range of materials, such as GaAs [2] or ZnO [3], and the analysis of the Raman resonant profiles has been used to study the electronic structure of the material and the exciton-phonon interaction mechanisms. More recently, resonant Raman spectroscopy is being widely used for studying graphite and carbon nanotubes [4, 5]. In polar semiconductor compounds, one of the most salient consequences of the resonant Raman scattering is the further enhancement of the LO phonon intensity, which takes place via Fröhlich interaction [6]. This scattering mechanism is strongly enhanced when the excitation energy is close to electronic resonances, and it is intensified by the presence of charged impurities, as will be explained in this chapter.

For the III-nitrides, although the electron-phonon coupling strength is small, the measurement of the Raman spectra under resonant conditions results in an increase of the overall Raman signal that allows one to measure weak features of the spectra and also to study the electronic structure of the material. Several studies have been reported on Resonant Raman and Fröhlich interaction in GaN [7, 8] and InN [9]. In the case of InN, however, it was experimentally observed that the frequency of the LO modes change when the Raman spectrum is excited using different wavelengths, both in epilayers [10–12] and in NWs [13]. These frequency shifts cannot be explained by the standard two-band or three-band Fröhlich scattering mechanisms, which suggests that another mechanism is mediating the LO scattering. A systematic study of the excitation wavelength dependence performed by Davydov *et al.* on InN thin films showed that the frequency shift of the LO modes is due to the dominance of Martin's double resonance mechanism [11]. The occurrence of this mechanism relies on the electronic structure of InN and the presence of native defects. Since the NWs are grown with less defects and impurities than the layers, the role of the Raman double resonant mechanism needs to be assessed in InN NWs. In Sec. 6.2 we

present a study of the mechanisms accounting for the LO scattering in InN NWs, in comparison with the results obtained from thin films.

When the excitation energy is well above the electronic band-gap of the material, higher order multiphonon scattering is strongly enhanced by impurity-induced Fröhlich interaction [14]. This condition is met in InGaN alloys with increasing In composition. In Sec. 6.3, we study the multiphonon scattering in InGaN alloys with different compositions. Moreover, in order to investigate the role of the defects on the scattering efficiency, we carry out Raman measurements of the multiphonons in He^+-implanted samples. The study of the InGaN implanted samples is of great interest, since InGaN alloys have generated a growing attention because their band gap can be tuned to cover the full solar spectrum. Furthermore, and they show a remarkable resistance to irradiation, which makes them suitable for outer space solar cells. For this reason is especially interesting to study the Raman spectra of implanted InGaN alloys and to extract information about the crystallinity of the samples after implantation and their resistance to the irradiation.

6.1 Framework: Resonance effects on the Raman spectra

Following the description of the Raman scattering outlined in Sec. 3.1.3, when the excitation energy coincides with a direct electronic transition of the material, the term corresponding to the electron-photon interaction [Eq. (3.21)] increases dramatically and therefore the overall probability of the scattering process given by Eq. (3.18) is enhanced. This enhancement of the Raman cross section near electronic resonances is known as resonant Raman scattering. The key difference between non-resonant and resonant Raman scattering processes is that the electron-hole pairs that mediate the process are real in resonant Raman scattering [6].

As already presented in Sec. 3.1.3, the Fröhlich mechanism is an electron-phonon interaction mechanism that is based on the Coulomb interaction existing between the electron-hole pairs and the macroscopic electric field associated with the LO phonons in polar materials. The Raman tensor of the Fröhlich mechanism is diagonal, which implies that Fröhlich scattering by LO phonons takes place in backscattering configuration when the incident and the scattered photon polarization have the same direction. The enhancement of the Fröhlich cross section under resonant conditions may therefore allow the detection of the LO modes in parallel configuration, regardless whether they are dipole-allowed or dipole-forbidden.

In Fig. 6.1 GaN spectra obtained using visible excitation compared to spec-

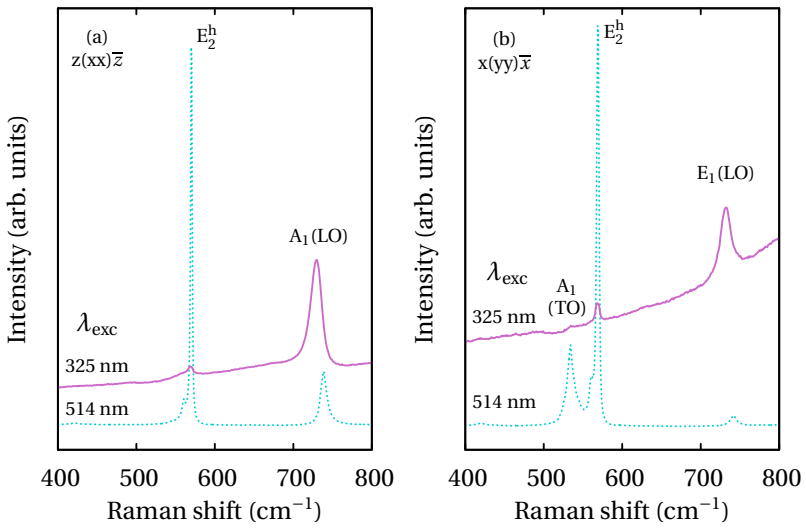

Figure 6.1: *GaN spectra obtained in the $z(xx)\overline{z}$ (a) and the $x(yy)\overline{x}$ (b) scattering configurations from a thick GaN sample. Dotted spectra were obtained with the 514-nm excitation wavelength, while the continuous lines are the spectra excited with the 325-nm wavelength. Vertical shift has been added for clarity.*

tra excited with UV light are shown. Two scattering configurations have been obtained by performing backscattering measurements on different faces of a thick GaN sample. The spectra obtained with the 514-nm excitation light show the peaks corresponding to dipole-allowed modes, according to the wurtzite selection rules given in Chapter 4. The spectra obtained with the UV excitation light from the same sample exhibit a more intense baseline due to the photoluminescence signal, which masks most of the signal arising from the Raman scattering of the E_2^{high} and A_1(TO) phonon modes. Moreover, for GaN the Raman signal is less intense under UV excitation because the UV light is under absorption regime of the GaN, and then the scattering volume is smaller. Despite these facts, in both scattering configurations a strong signal is detected from the A_1(LO) and E_1(LO) phonon modes in the $z(xx)\overline{z}$ and $x(yy)\overline{x}$ scattering configurations, respectively. These modes are detected via resonant Fröhlich mechanism, which leads to an intensity enhancement when excited with the UV excitation source because of the proximity to the GaN bandgap energy.

6.1.1 Impurity-induced Fröhlich mechanism

Figure 6.1 show resonant Raman spectra in which an enhancement of the first-order Fröhlich mechanism is observed by exciting with an energy close to the

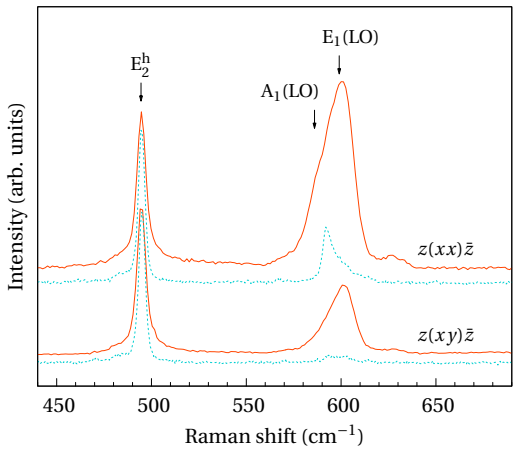

Figure 6.2: *Spectra of heavily Mg-doped InN layers (continuous line) compared to those of undoped InN layers (dotted lines), taken in the $z(xx)\overline{z}$ and $z(xy)\overline{z}$ as indicated in the figure. The spectra were excited using the 514-nm excitation line of an argon laser.*

direct band gap. Another interesting property of the intra-band Fröhlich interaction is that it is strongly enhanced by the interaction with charged impurities. This is the so-called *impurity-induced* Fröhlich mechanism.

The impurity-induced Fröhlich mechanism consists in a double scattering of the intermediate electron or hole. It is scattered by a charged impurity and also by a phonon or elementary excitation. The main consequence of this double scattering process is that it allows the scattering by non zone-center phonons, since the wave-vector transfer associated with the charged impurity scattering allows the wave-vector conservation rule to be fulfilled in the overall scattering process [15].

An example of the impurity-enhanced Fröhlich scattering is given in Fig. 6.2, in which the spectra of undoped InN layers are compared with those of heavily Mg-doped InN layers. It can be seen in this figure that the signal arising from the E_2^{high} phonon mode is similar in the spectra acquired from both samples, while the signal arising from the LO modes exhibits an strong enhancement and broadening in the spectra acquired from the heavily Mg-doped InN layer. As we will discuss throughout the following sections, the LO modes in InN are scattered through the Martin's double resonant mechanism, a second-order process that contains a Fröhlich interaction. The differences existing between the spectra of the as-grown and the heavily doped samples shown in Fig. 6.2 can be explained taking into account that the impurity-induced Fröhlich mechanism allows scattering by $q \neq 0$ phonons. This fact leads to wider Raman peaks and allows the

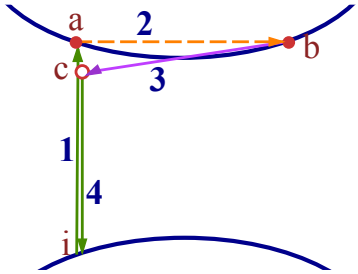

Figure 6.3: *Scheme of the mechanism:* ***1*** *For a particular excitation energy, a real electron-hole pair with a wave vector k is created (i→a)* ***2*** *The electron is elastically scattered due to impurities to another real state with wave vector −k (a→b)* ***3*** *An optical phonon with wave vector q = 2k scatters back the electron to a less energetic state (b→c)* ***4*** *The electron recombines emitting a photon (c→i)*

detection of phonons in *dipole-forbidden* scattering geometries [16].

6.1.2 Martin's double resonance

The Martin's double-resonance mechanism is a second-order transition which involves two real electronic states. For an specific excitation energy, a real electron-hole pair is created. The electron (hole) is elastically scattered to another real state by Coulomb interaction with ionized impurities. An optical phonon exists that scatters back the electron (hole) to a less energetic state by Fröhlich interaction, and finally the electron and the hole recombine emitting the scattered photon. An illustrative scheme of the complete mechanism is shown in Fig. 6.3. Even though this double-resonance mechanism is a second-order process, the resonant behaviour of Fröhlich and Coulomb intra-band transitions give rise to a substantial enhancement of the peak intensity.

This effect can occur in semiconductors which have a deep, isolated conduction band minimum at Γ, allowing direct transitions from valence to conduction band to take place for a wide energy range. Also, a significant density of charged impurity centres is needed, since they play a key role in the Coulomb interaction.

The Raman scattering from LO phonons due to double resonance mechanism can be described in fourth order in perturbation theory [11, 12]. The scattering probability contains two electromagnetic interactions (H_{eR}), the Coulomb interaction with the impurity (H_i) and the Fröhlich interaction (H^F_{ep}), and is given by

$$P^M_{ph}(\omega_s) \propto \Sigma_{n,n'} \frac{\langle i|H_{eR}(\omega_s)|n\rangle\langle n|H^F_{ep}|n'\rangle\langle n'|H_i|n''\rangle\langle n''|H_{eR}(\omega_i)|i\rangle}{[\hbar\omega_i-(E_n-E_i)][\hbar\omega_s-(E_{n'}-E_i)][\hbar\omega_s-(E_{n''}-E_i)]}, \tag{6.1}$$

where we have used the same notation as in Sec. 3.1.3 for denoting the incident, scattered and intermediate states and energies.

For excitation energies close to electronic interband transitions, the denominators of Eq. (6.1) can take zero value and therefore yield a resonant behaviour [11]. Following the results given in Ref. [12], the photon wave-vector magnitudes can be neglected. Then, by considering the energy conservation laws at electromagnetic transitions, the scattering probability can be written as

$$P_{ph}^{M}(q,\omega) \propto \left[\frac{2\mu v_c(m_e+m_h)}{4\pi^2\hbar^2 q}\right]\frac{2\mu}{\hbar\left(k_{eh}^{i}+k_{eh}^{s}\right)} \times\left\{\frac{k_{eh}^{i}}{\left(k_{eh}^{i}\right)^2-q^2/4-i\mu\gamma/\hbar}+\frac{k_{eh}^{s}}{\left(k_{eh}^{s}\right)^2-q^2/4-i\mu\gamma/\hbar}\right\}. \quad (6.2)$$

This corresponds to the scattering amplitude due to real absorption and emission. In this equation v_c is the volume of the primitive cell and $\mu=\frac{m_e^* m_h^*}{m_e^*+m_h^*}$ is the reduced effective mass. The uncertainty of these values is given by the broadening of the eh intermediate states $\gamma=1/\tau$, where τ is the relaxation time of these intermediate states. We have considered the exciton wave vectors k_{eh}^{i} and k_{eh}^{s} resulting from a real photon absorption or emission, which can be described as $k_{eh}^{i}=\sqrt{2\mu(\hbar\omega_i-E_g)/\hbar^2}$ and $k_{eh}^{s}=\sqrt{2\mu(\hbar\omega_s-E_g)/\hbar^2}$.

The probability given by Eq. (6.2) has maximum values for phonon wave vectors that are twice the value of the exciton wave vector, for which the denominators approach zero. Therefore, taking into account that the electron-hole pair wave vector k_{eh} is uniquelly determined by the electron dispersion curves and the excitation energy, and also that the dominant wave vector of the scattered phonon is $q=2k_{eh}$, the wave vector of the scattered phonon can be deduced from the excitation energy. This is an important result since it allows one to identify the wave vector of the scattered phonon and relates it to the frequency measured by Raman scattering [12, 17]. Therefore, by carring out Raman scattering measurements with different excitation wavelengths and analyzing the excitation wavelength dependence of the Raman peak frequency of the longitudinal modes, the wave-vector dispersion of these modes near zone-center can be obtained provided that Martin's double resonance plays a dominant role in the scattering process.

6.1.3 Cascade multiphonon scattering

High-order multiphonon scattering is in general an extremely weak process, since it involves the scattering of excitons by n phonons simultaneously or a sequential one-phonon scattering n times. Due to the usually small electron-phonon coupling strength, the probability of the high-order Raman processes

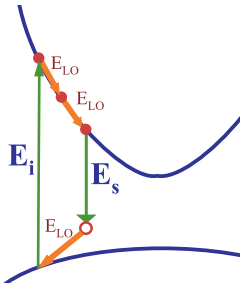

Figure 6.4: *Scheme of the cascade multiphonon scattering mechanism:* ***1*** *Incident photon is absorbed by an exciton* ***2*** *Exciton relaxes into lower energy states with successive emission of LO phonons* ***3*** *Electron-hole pair recombine radiatively and the scattered photon is emitted.*

is generally very small. Here we describe a resonant mechanism that allows the detection of high-order LO overtones, the so-called *cascade mechanism*.

The cascade model was first proposed by Martin in Ref. [18], and consists in the absorption of the incident photon by an exciton that relaxes into lower energy states with successive emission of LO phonons, and finally recombines radiatively with the emission of the scattered photon. A scheme of the mechanism is shown in Fig. 6.4.

The scattering probability for the nth-order LO multiphonon Raman scattering can be written as [19]

$$P_{ph}^{n} \propto \alpha \left(\frac{\tau_{\text{rel}}}{\Gamma_1(\mathbf{K}_1)}\right) \ldots \left(\frac{\tau_{\text{rel}}}{\Gamma_1(\mathbf{K}_{n-2})}\right) \left(\frac{\tau_{\text{rad}}}{\Gamma_1(\mathbf{K}_{n-1})}\right), \tag{6.3}$$

where α is the absorption coefficient for the LO-assisted creation of excitons, $\Gamma_1(\mathbf{K}_x)$ is the damping of the exciton state with wave vector $\mathbf{K}_x$, τ_{rel} and τ_{rad} are the exciton relaxation rate via the LO-emission or the LO-assisted radiative recombinations, respectively. This expression is independent of the usually small electron-phonon coupling strength. As a consequence, the intensity of the overtones decays gradually with the overtone order n, and allows one to detect overtones that otherwise would be very difficult to measure.

An important characteristic of the cascade-type successive emission of LO modes is that it is greatly enhanced in samples with a certain impurity density. This occurs mainly due to two mechanisms: (1) impurity enhanced Fröhlich interaction; and (2) contribution to the Raman scattering of excitons bound to defects and impurities [20–22].

Furthermore, the the cascade-like multiphonon scattering can only take place with above band-gap excitation, since the created electron-hole pairs have to be real in order to decay through successive LO emission [18, 22]. For excitation energies close to the band-gap edge, the photoluminescence signal may mask the signal arising from the multiphonon scattering.

6.2 Double resonance in InN thin films and NWs

In this section a study of the double resonance in InN is presented. To perform it, Raman spectra with different excitation wavelengths have been collected from both thin films and nanowires. As discussed in the previous section, the study of the frequency dependence on the excitation wavelength on the basis of the double resonance effects yields relevant information about the phononic structure of InN.

The studied undoped InN NWs were grown catalyst-free by plasma assisted molecular beam epitaxy under N-rich conditions on Si(111) substrate and they have been previously described in Sec. 5.2. The studied *c*-face InN epilayer (also described in Sec. 5.2) was grown at 500 °C by PAMBE on GaN/sapphire templates.

The spectra were recorded at room temperature in near-backscattering geometry. As excitation source we used the 488- and 514-nm lines of an Ar^+ laser, the 633-nm line of an He-Ne laser and 710-, 780- and 820-nm wavelength radiation of a Ti:sapphire laser.

6.2.1 Raman spectra with different excitation wavelengths

To study the double resonance effects on NWs in comparison with those existing in thin films, Raman measurements with different excitations wavelengths (from 488 nm to 820 nm) have been performed on InN NWs and thin films and are displayed in Fig. 6.5. The Raman spectra of the InN NWs show two features which are attributed to the E_2^{high} and E_1(LO) phonon modes, superimposed to a strong signal from the Si substrate. As discussed at length in Sec. 4.2, the effective scattering configuration is not well defined because the NWs exhibit a certain axis tilt, and therefore the measured Raman signal contains contributions from different scattering configurations.

As can be seen in Fig. 6.5(a) the Raman spectra of the NWs exhibit noticeable intensity changes when the excitation wavelength is changed. The E_2^{high} intensity shows a marked intensity decrease for longer excitation wavelengths, but it maintains the same frequency. The intensity of the E_1(LO) phonon mode also decreases for longer excitation wavelengths, but this decrease is less pronounced.

The collected spectra from the InN *c*-face thin film are shown in Fig. 6.5(b). In this case the LO phonon mode corresponds to an A_1(LO) mode, which has lower frequency than the E_1(LO) mode observed for NWs. These spectra collected from thin films also exhibit an overall intensity decrease for longer excitation wavelengths.

Apart from the changes in intensity, the Raman peak corresponding to the

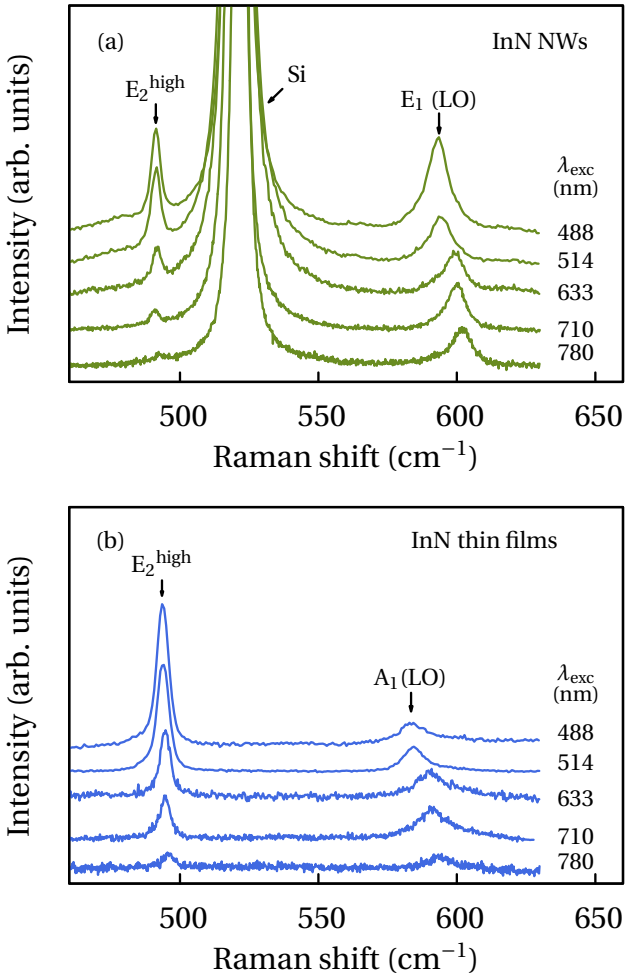

Figure 6.5: *Raman spectra obtained in backscattering geometry with different excitation wavelengths from the InN NWs (a) and the c-face InN thin films (b) described in the text.*

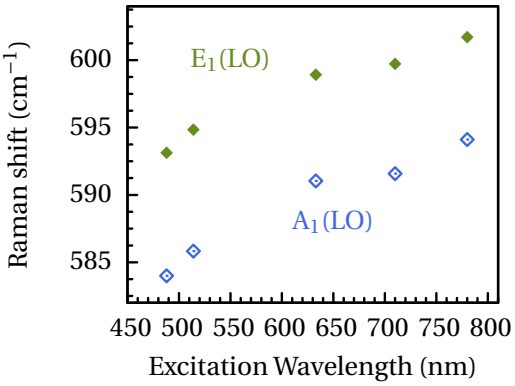

Figure 6.6: *Frequency of the LO phonon modes for the different excitation wavelengths. Filled diamonds are data obtained from InN NWs (corresponding to the E_1(LO) phonon mode), and empty diamonds are data obtained from InN c-face thin film (corresponding to the A_1(LO) phonon mode).*

LO phonon modes show a remarkable shift towards higher frequencies for longer excitation wavelengths both in NWs and thin films. The detected shift is much higher than that expected from the wave-vector conservation law [Eq. (3.2)] and the LO phonon dispersion. The wave-vector conservation law in the case of backscattering implies that the scattered phonon has a wave vector $q = 4\pi n/\lambda_{\text{exc}}$. Taking into account the used wavelengths and the corresponding changes in the InN refractive index n (it varies 6% over the range of excitations wavelengths used [23]), by considering the LO dispersion curves the estimated change in the phonon wave vector would correspond to a frequency shift of 0.1 cm^{-1}. This expected shift is much smaller than the ~ 8 cm^{-1} shift observed for the LO phonon modes (see Fig. 6.6). Therefore, a full account of the frequency shift requires taking into consideration other effects.

According to Davydov *et al.* the resonant behaviour of the LO modes in InN is due to the selective excitation of large-wave-vector phonons via Martin's double resonance [11, 12]. In the following sections we will carry out a detailed study of the LO frequency dependence on the excitation wavelength and we will analyse the results on the basis of the Martin's double resonance mechanism theory.

6.2.2 LO frequency dependence on the excitation wavelength

From the Raman spectra shown in Fig. 6.5, we have extracted the LO Raman shift as a function of the excitation wavelength for both InN thin films and NWs. The results are displayed in Fig. 6.6, and it can be seen that the behaviour of the E_1(LO) mode in NWs is similar to that of the A_1(LO) mode in thin films. As explained above, the frequency shift is much higher than that expected from the LO phonon dispersion, and we have attributed it to the selective excitation of large-wave-vector LO phonon via Martin's double resonance.

The basis of Martin's double resonance has been explained in Sec. 6.1. Basically, it consists on an impurity-mediated phonon scattering by a real electron-

hole pair. The key issue is that the electron-hole pair wave vector k_{eh} is univocally determined by the electron dispersion curves and the excitation energy. Moreover, the wave vector of the scattered phonon is in turn determined by the electron-hole pair wave vector ($q = 2k_{eh}$). Therefore, if the electron dispersion curves are known, the study of the resonant LO phonons excited with different wavelengths can yield the phonon dispersion curves of the LO phonon modes around the centre of the Brillouin Zone.

Electron and hole dispersion curves

In order to determine the wave vector of the excited electron-hole pairs for each excitation wavelength, we have to know the InN electron dispersion curves. We consider the expressions given in Ref. [12], which take into account the nonparabolicity of the bands. The expressions for the electron, the light-hole (lh) and the heavy-hole (hh) dispersion bands are, respectively:

$$\varepsilon_e(k) = E_g + E_e\sqrt{\frac{\hbar^2k^2}{2m_\Gamma^e E_e} + \frac{1}{4}} - \frac{1}{2}, \tag{6.4}$$

$$\varepsilon_{lh}(k) = -E_{lh}\sqrt{\frac{\hbar^2k^2}{2m_\Gamma^{lh} E_{lh}} + \frac{1}{4}} - \frac{1}{2}, \tag{6.5}$$

$$\varepsilon_{hh}(k) = \frac{\hbar^2k^2}{2m_\Gamma^{hh}}. \tag{6.6}$$

In these equations m_Γ are the effective masses at the center of the Brillouin zone and E_e and E_{lh} are the nonparabolicity parameters. The values used in the calculations are those given in Ref. [12] and the calculated curves are shown in Fig. 6.7. This Figure also displays the energy dispersion curves corresponding to e-lh and e-hh transitions. Dashed lines indicate excitation photon energies and their corresponding e-lh and e-hh exciton wave vectors. As can be seen in this figure, as a result of the different effective masses of heavy and light holes, the range of electron-hole pair wave vectors that may be involved in the scattering process is different for electron-light hole than for electron-heavy hole pairs. Following the arguments given in Ref. [12], the e-hh exciton mediates the scattering by the E_1(LO) phonon mode, while the scattering by the A_1(LO) mode via Martin's double resonance mechanism is only possible if e-lh excitons are considered.

Phonon dispersion curves

The LO mode wave-vector dispersion can be obtained from the study of the phonon frequency dependence on the excitation wavelength. For each excita-

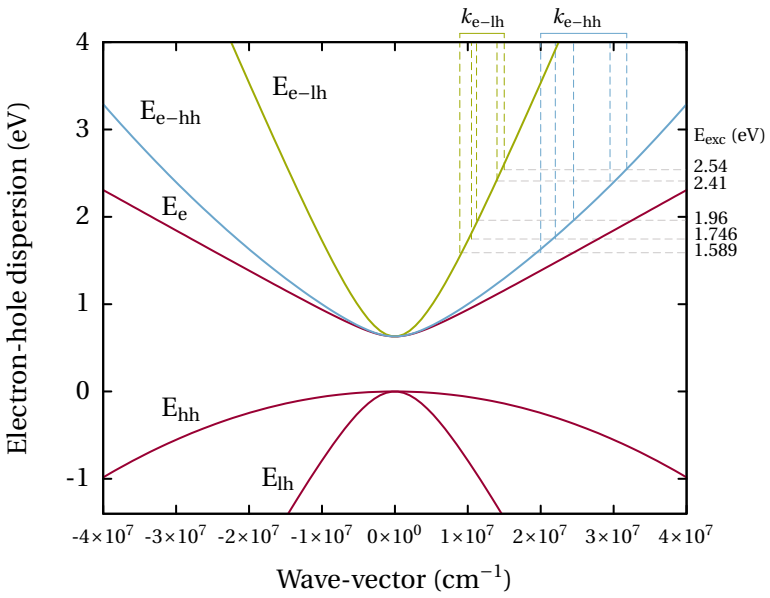

Figure 6.7: *Energy dispersion curves of the conduction and valence bands and electron-hole pairs of hexagonal InN (red lines). Blue lines correspond to energy dispersion curves of the e-lh and e-hh transitions. Dashed lines indicate excitation photon energies and the corresponding e-lh and e-hh exciton wave vectors.*

tion wavelength, we can extract the exciton wave vector (k_{eh}) from the analysis of the electronic energy dispersion curves. Since in Martin's double resonance the dominant wave vector of the scattered phonon is $q = 2k_{eh}$, we can relate the phonon frequency measured in the Raman spectra to the phonon wave vector. We have investigated the LO phonon dispersion of InN near the Brillouin zone center using this approach. The Raman scattering measurements excited with 488, 514, 633, 710 and 780-nm wavelength excitation (see Sec. 6.2.1) were analysed in the framework of Martin's double resonance, and the LO dispersion curves thus obtained are plotted in Fig. 6.8. In this figure we have also plotted the phonon dispersion curves given in Ref. [11], that were obtained by fitting experimental results obtained from thin films.

As can be seen in Fig. 6.8, the frequency dependence of the A_1(LO) mode measured on NWs follows a similar trend as that reported in thin films in Ref. [11]. The small discrepancies could be associated to differences in the strain state of the layers.

For the E_1(LO) mode, it can be seen that the frequencies that we have measured in NWs are in agreement with the curve fitted in Ref. [11] to the thin film data. This result indicates that, in spite of the fact that the defect density is significantly lower in NWs than in thin films, the scattering of longitudinal optical

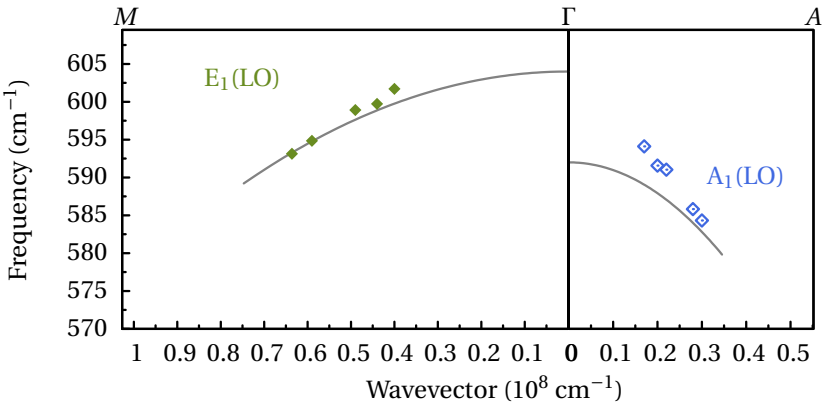

Figure 6.8: *InN longitudinal optical phonon frequencies vs. phonon wave vectors. Filled diamonds are data recorded from InN NWs (corresponding to the E_1(LO) phonon mode), and empty diamonds are data recorded from InN c-face thin film (corresponding to the A_1(LO) phonon mode). Solid lines are the empirical phonon dispersion curves obtained from fits to the Raman data given in Ref. [11].*

phonons in InN NWs is also dominated by Martin's double resonance mechanism.

The origin of the impurities that induce the double-resonance mechanism in our NW samples remains unclear. One of the more likely origins could be the Si diffusion from the silicon substrate. Ionized Si impurities in the InN NWs could therefore account for the observation of impurity induced resonant scattering. This hypothesis is supported by the fact that, as will be explained in the next chapter (Sec. 7.3), a significant free electron density has been found in these nominally-undoped InN NWs.

6.2.3 LO intensity resonance profile

In addition to the shift in the LO frequency discussed in the preceding section, the Raman spectra of InN excited with different wavelengths (see Fig. 6.5) also display significant changes in the relative intensity of the Raman peaks. The excitation wavelength dependence of the A_1(LO) mode intensity was previously reported by Kuball *et al.* [24] In that work the Raman spectra of InN thin films were studied for a range of excitation wavelengths and it was shown that the $A_1(\mathrm{LO})/E_2^{\mathrm{high}}$ intensity ratio increases monotonically for longer excitation wavelengths. A similar trend is observed in our Raman measurements performed on InN thin films and NWs.

From the measurements shown in Fig. 6.5, we have extracted the LO to E_2^{high}

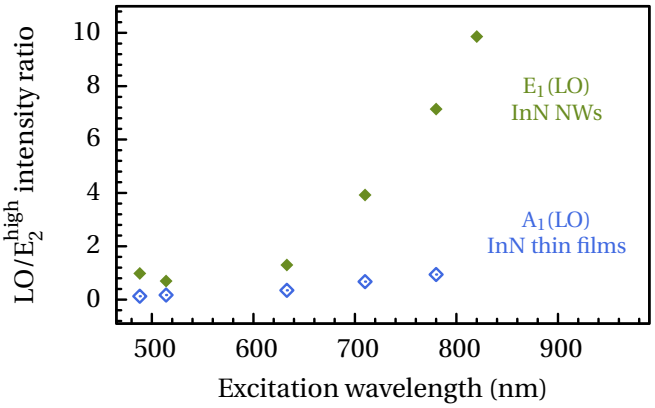

Figure 6.9: *Longitudinal optical (LO) to E_2^{high} Raman intensity ratio as a function of the excitation wavelength. Filled diamonds: data recorded from InN NWs, corresponding to the E_1(LO) phonon mode. Empty diamonds: data recorded from InN c-face thin film, corresponding to the A_1(LO) phonon mode.*

intensity ratio *vs* excitation wavelength. The results are plotted in Fig. 6.9, both in thin films and NWs we detect an increase of the LO/E_2^{high} intensity ratio for longer excitation wavelengths, following the trend reported in Ref. [24]. For the case of InN thin films, our results are comparable to those reported in Ref. [24]. For the InN NWs, however, the intensity ratio shows a much greater resonant enhancement for longer excitation wavelengths.

The analysis of these results is not straightforward since, as already pointed out, the NWs spectra are not taken in a pure scattering configuration and therefore they contain contributions of several scattering geometries. In fact, scattering through lateral faces can yield a significant contribution of the $x(zz)\bar{x}$ scattering configuration, in which the E_2^{high} mode is forbidden. Therefore, the intensity normalization to the E_2^{high} intensity may not provide a faithful representation of the resonance profile of the E_1(LO) mode.

The origin of the remarkable differences between both resonant intensity profiles can be: (1) effective scattering configuration favouring the detection of the E_1(LO) phonon mode in NWs; (2) enhancement of the LO modes in NWs due to its geometry and electric field distribution along the NW [25]; and (3) greater intrinsic scattering efficiency of the E_1(LO) mode in comparison of the A_1(LO) mode. We argue that probably all these reasons play a role in the detected resonance enhancement. However, to ascertain the specific contribution of each one, it would be necessary to perform a more extended Raman study of a single InN NW under controlled scattering configurations.

The study of the Raman spectra obtained from InN NWs with different exci-

tation wavelengths presented in this section allows us to conclude that, although these nanostructures have much less defect density than thin films, the presence of impurities is high enough to effectively mediate in the double resonant mechanism in NWs. The resulting resonant enhancement of the LO modes in NWs appears to be significantly higher than in thin films.

6.3 Multiphonons in He^+-implanted InGaN

This section presents a study of the multiphonon resonant Raman scattering in InGaN alloys with In content ranging from 17% to 42 % . Given the interest of III-nitrides for applications in devices resistant to high-energy particle radiation, we have also studied InGaN layers that have been implanted with He^+ ions. In general, as a consequence of the implantation the crystalline quality of the samples is reduced, which results in a quenching of the Raman peaks and in the emergence of disorder-activated features due to the relaxation of the wave-vector conservation selection-rules [26, 27]. However, the implantation also introduces charged impurities that can favour the impurity-induced Fröhlich scattering and can lead to an increase of the intensity of the LO Raman peaks. This was demonstrated in previous studies of the multiphonon resonance in GaN, in which multiphonons were observed in implanted GaN but not in undoped GaN [28–30]. Therefore, we measure Raman spectra of multiphonons in both unimplanted and implanted InGaN layers to study the damage effects on the Raman spectra.

As explained above, the observation of cascade-like phonons for a given excitation wavelength depends on the excitation energy relative to the sample band gap, and as a consequence, for a fixed excitation wavelength it depends on the In/Ga rate of each sample. Moreover, if the excitation line is close to the band gap resonance, a strong photoluminescence (PL) background signal is usually present, and this may prevent the observation of the Raman spectrum. Thus, to explore multiphonon scattering in InGaN, we perform Raman scattering measurements using both near-resonance visible excitation (514 nm) and above band-gap UV excitation (325 nm).

6.3.1 Ion implantation of the samples

The studied InGaN epilayers were grown by plasma-assisted MBE on sapphire substrates with a GaN buffer. The indium concentrations range from 17% to 42% and the thickness of the InGaN layers lies between 700 and 1000 nm.

Different specimens of each sample were implanted with He^+ ions. The displacement damage dose (D_d) is generally used to quantify the damage caused by the implantation. It is defined as the product of the non-ionizing energy loss (NIEL) and the particle fluency, and is commonly used to characterise solar cell degradation in space radiation environment [31, 32]. The NIEL is defined as the ion energy loss rate per length unit through non-ionizing collisions, and is given by

$$\mathrm{NIEL}(D) = \frac{M[\nu_i(D) + \nu_r(D)]}{\rho} \tag{6.7}$$

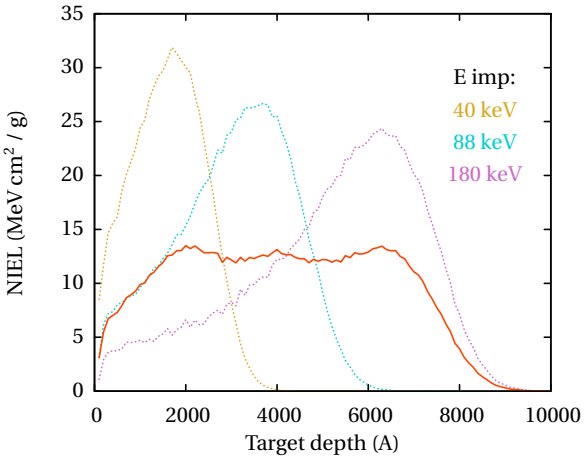

Figure 6.10: *Dotted lines show the NIEL profiles for He^+-ion implantation energies of 40, 88, and 180 KeV. The continous line shows the NIEL profile resulting of a combined implantation with a ion fluency proportion of 0.2:0.25:0.55 for the 40, 88 and 180 keV implantation energies, respectively*

where ρ is the material density, and $\nu_i(D)$ and $\nu_r(D)$ are the vacancies created by collisions with the incident and the backscattered ions, respectively. M is the energy needed to produce a vacancy, and is given by the Kinchin-Pease relation [33],

$$M = \frac{T_d}{0.4} + B, \tag{6.8}$$

where T_d is the threshold energy for the atomic displacement and B is the binding energy.

The NIEL is defined locally, because the energy that the ions lose in the material will vary as a function of the target depth. Therefore, since the most energetic ions have a bigger penetration depth, in general they will lead to lower NIEL values, because their energy is lost among a bigger volume. The ions with smaller energies will lose their energies in a smaller volume, in which the NIEL will be bigger. Since the value of the NIEL is local, for each sample we will give the mean value of the NIEL over the penetration depth of interest ($\overline{\text{NIEL}}$).

We have used the simulation program SRIM (Stopping and Range of Ions in Matter) to simulate the vacancies created by different implantation energies [34, 35], and to design a combination of the appropriate implantation energies and fluences to obtain a homogeneous damage profile in the InGaN layer. The program SRIM is based on Monte-Carlo simulations, and enables us to simulate the implanted ion distribution and to calculate the created vacancies and the ionized atoms as a function of the penetration depth. We found out that performing three implantations with He^+-ion energies of 40, 88 and 180 keV, respectively, is optimal to achieve a fairly homogeneous damage profile extending over the whole layer thickness. From the SRIM calculations we can obtain the NIEL for each one of the implantations, and the results are plotted in Figure 6.10.

Table 6.1: *Indium concentration, damage dose and corresponding He^+-ion implantation fluencies for each studied specimen.*

Sample name	[In] (%)	Specimen	D_d (MeV/g)	Φ_{40keV} (cm^{-2})	Φ_{88keV} (cm^{-2})	Φ_{180keV} (cm^{-2})
A	42	A	Unimp.			
		A'	3.2×10^{15}	6.01×10^{13}	7.51×10^{13}	1.65×10^{14}
		A"	2.0×10^{16}	3.76×10^{14}	4.7×10^{14}	1.03×10^{15}
B	34	B	Unimp.			
		B'	3.2×10^{15}	6.01×10^{13}	7.51×10^{13}	1.65×10^{14}
		B"	2.0×10^{16}	3.76×10^{14}	4.7×10^{14}	1.03×10^{15}
C	24	C	Unimp.			
		C'	3.2×10^{15}	6.01×10^{13}	7.51×10^{13}	1.65×10^{14}
		C"	2.0×10^{16}	3.76×10^{14}	4.7×10^{14}	1.03×10^{15}
D	17	D	Unimp.			
		D'	3.2×10^{15}	6.01×10^{13}	7.51×10^{13}	1.65×10^{14}
		D"	2.0×10^{16}	3.76×10^{14}	4.7×10^{14}	1.03×10^{15}

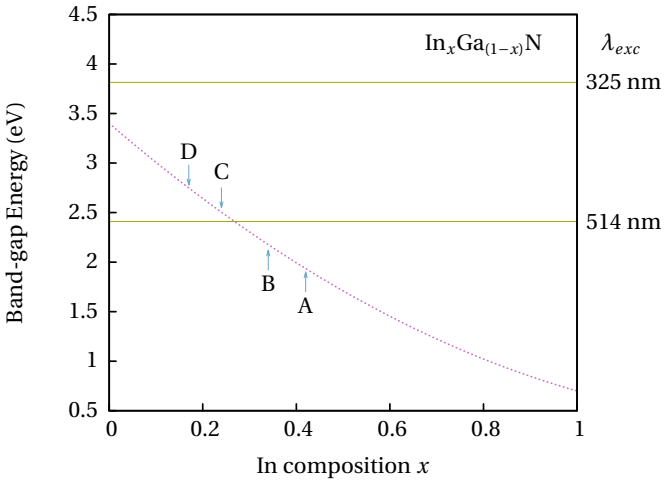

Figure 6.11: *Band-gap Energy of the $In_xGa_{1-x}N$ alloy as a function of the In concentration considering a bowing parameter of b = 1.36 eV (Ref. [36]). The In concentration of the studied samples and the laser excitation energies used in the experiments are indicated.*

The fluency proportions that lead to a nearly homogeneous profile were found to be 0.2:0.25:0.55 for the 40, 88 and 180 keV He^+ implantation energies, respectively. The NIEL resulting of these combined implantation is also plotted in Figure 6.10. Taking into account that the mean thickness of our layers is 850 nm, the mean value of the NIEL over this thickness will be $\overline{\text{NIEL}}$ = 10.66 MeV cm^2/g.

For each available sample, we have performed two different implantations by varying the total ion fluency in order to obtain a range of displacement

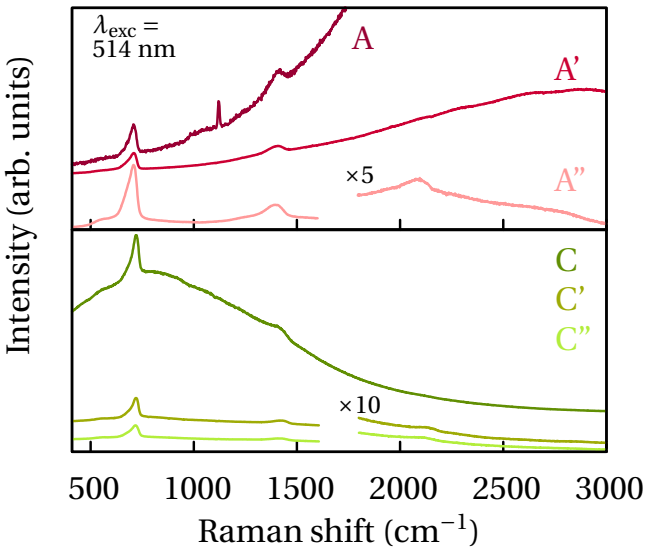

Figure 6.12: *Raman spectra of the $In_xGa_{1-x}N$ samples obtained with λ_{exc} =514 nm. Upper (bottom) panel shows spectra of unimplanted and implanted specimens of the sample with x =0.42 (x =0.24), as listed in Table 6.1.*

damage doses and study the effects of the implantation. The ion fluencies for each sample specimen are detailed in Table 6.1. As can be seen, the implanted specimens with the low displacement damage dose (3.2×10^{15} MeV/g) are labelled with an apostrophe and those with the high displacement damage dose (2.0×10^{16} MeV/g), with a double apostrophe.

6.3.2 Visible Raman spectra of the implanted InGaN thin films

We have started the study of the InGaN layers by performing Raman scattering measurements using an excitation wavelength of 514 nm. The band-gap energy of the studied samples is expected to be close to this excitation energy. Figure 6.11 shows the InGaN band-gap energy dependence on the In concentration, in comparison with the excitation energies used in this study. This dependence is only indicative, because the actual band-gap energy of each sample may be subject to slight modifications depending on its strain state and composition homogeneity. However, from this band-gap dependence, we see that the 514-nm excitation energy is well above the band gap of the samples A and B, and is very similar to that of samples C. Therefore, these samples may exhibit outgoing resonances and photoluminescence signal. The expected band gap of sample D is significantly higher than the excitation energy, and therefore this sample may be transparent to the 514-nm excitation light. The Raman spectra of the unimplanted samples excited with λ_{exc} =514 nm have already been presented in Chapter 4 (Fig. 4.6). Here we describe them in comparison with the spectra of the implanted samples.

The upper panel in Fig. 6.12 shows the spectra obtained from sample A. As

expected, the spectrum of the unimplanted sample (A) exhibits a strong photoluminescence peak, with maximum signal at 1.86 eV (not shown in the figure). The photoluminescence signal masks most of the Raman signal, but two peaks at 705 and 1409 cm^{-1} can be distinguished. These peaks correspond to the A_1(LO) phonon and to the 2LO, respectively, and are observed due to the resonant Fröhlich mechanism. In the spectrum of the implanted sample with lower D_d (A'), the PL peak up-shifts in energy and its intensity is reduced by more than one order of magnitude. The shift in the PL peak position is due to the increase of the free electron density caused by the He^+-implantation. As it has been explained in Sec. 2.3, in In-rich InGaN the damage created by the irradiation produces preferentially donor-like defects due to the location of the Fermi Stabilization Level high in the conduction band [37, 38]. Another consequence of the implantation is the reduction of the crystal quality which results in a PL intensity decrease. The photoluminescence signal is totally quenched in the spectrum obtained from the most heavily implanted sample (A") due to the non-radiative defects introduced in the sample by the implantation. In this spectrum, the intensity of the A_1(LO) and 2LO peaks are remarkably higher, and even some signal from the third order multiphonon scattering at 2091 cm^{-1} can be distinguished. The presence of a substantial concentration of charged defects in A' and A" implanted samples enhances the impurity-induced Fröhlich mechanism and explain the observed increase of the Raman signal. Sample B (x = 0.34) also has a band-gap smaller than the excitation energy and consequently the spectra obtained and the changes upon implantation are similar to these reported for sample A.

The spectrum obtained from the sample C (see lower panel of Fig. 6.12) is also dominated by the photoluminescence peak, which is superimposed to the A_1(LO) peak. The scattering of this phonon mode is under outgoing Fröhlich resonant conditions, which causes its remarkable intensity. Upon implantation (C' and C"), the PL intensity markedly decreases and the third order multiphonon is detected. For the alloy composition of sample D ($x = 0.17$) the band gap is well above the excitation energy, as can be seen in Fig. 6.11. As a consequence, Raman spectra of sample D exhibit two sharp peaks corresponding to the E_2^{high} and the A_1(LO) phonon modes (Fig. 4.6). Upon implantation, an overall reduction of the Raman signal is observed.

6.3.3 UV Raman study of the multiphonons in implanted InGaN

In order to study multiphonon scattering due to the cascade resonance mechanism, we have performed Raman scattering measurements with a more energetic excitation light, which allows us to have above band-gap excitation over the whole alloy composition range.

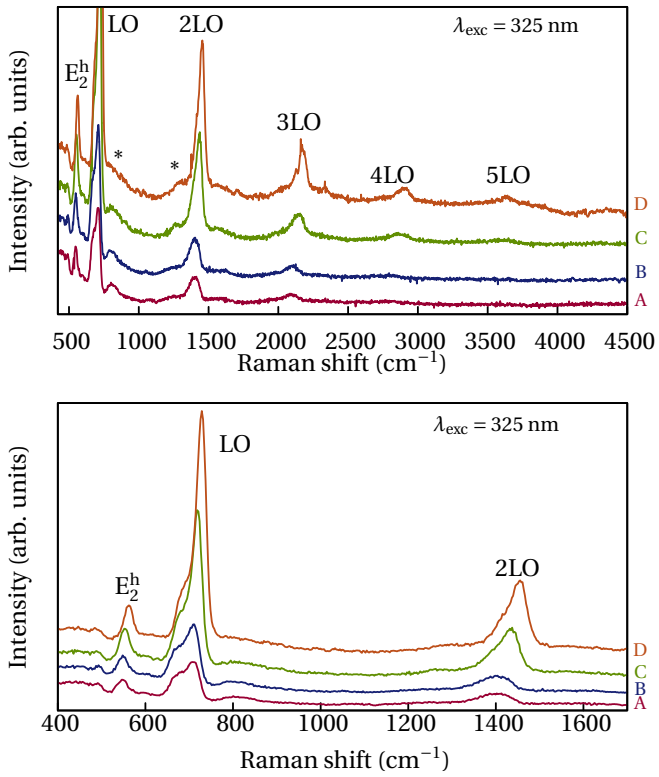

Figure 6.13: *UV Raman spectra of the $In_xGa_{1-x}N$ unimplanted samples A (x = 0.42), B (x = 0.34), C (x = 0.24), D (x = 0.17). Upper panel shows the full spectra and lower panel is an enlarged view of the 400-1700 cm^{-1} spectral region.*

The spectra collected from the unimplanted InGaN samples with λ_{exc} = 325 nm are shown in Fig. 6.13. All the spectra exhibit a very intense LO peak, followed by successive higher-order multiphonon peaks. The spectra also display a sharp E_2^{high} peak and weak signal from E_2^{high}+nLO combinations (marked with asterisks in Fig. 6.13). As the In content increases, both the intensity and the line shape of the LO peak and its multiphonons change. On one hand, the intensity of the LO and its higher order multiphonons is reduced (see upper panel in Fig. 6.13). On the other hand, the asymmetry of the A_1(LO) peak increases (see lower panel in Fig. 6.13). This effects can be explained by the higher defect density and crystalline disorder existing in the samples with higher In content, which reduces the intensity of the modes and allows the detection of $q \neq 0$ phonons, resulting in a broadening of the peaks.

We have performed similar UV Raman measurements in the implanted samples, and the obtained spectra are shown in Fig. 6.14. As previously discussed, the implanted samples have a higher defect density, which is reflected in weaker and broader Raman peaks. On the other hand, the charged impurities introduced by the implantation may lead to an increase of the intensity of the LO peak due to impurity-induced Fröhlich scattering. As we will discuss below, these competing effects may have a different importance in the first-order LO phonon and in the higher-order overtones.

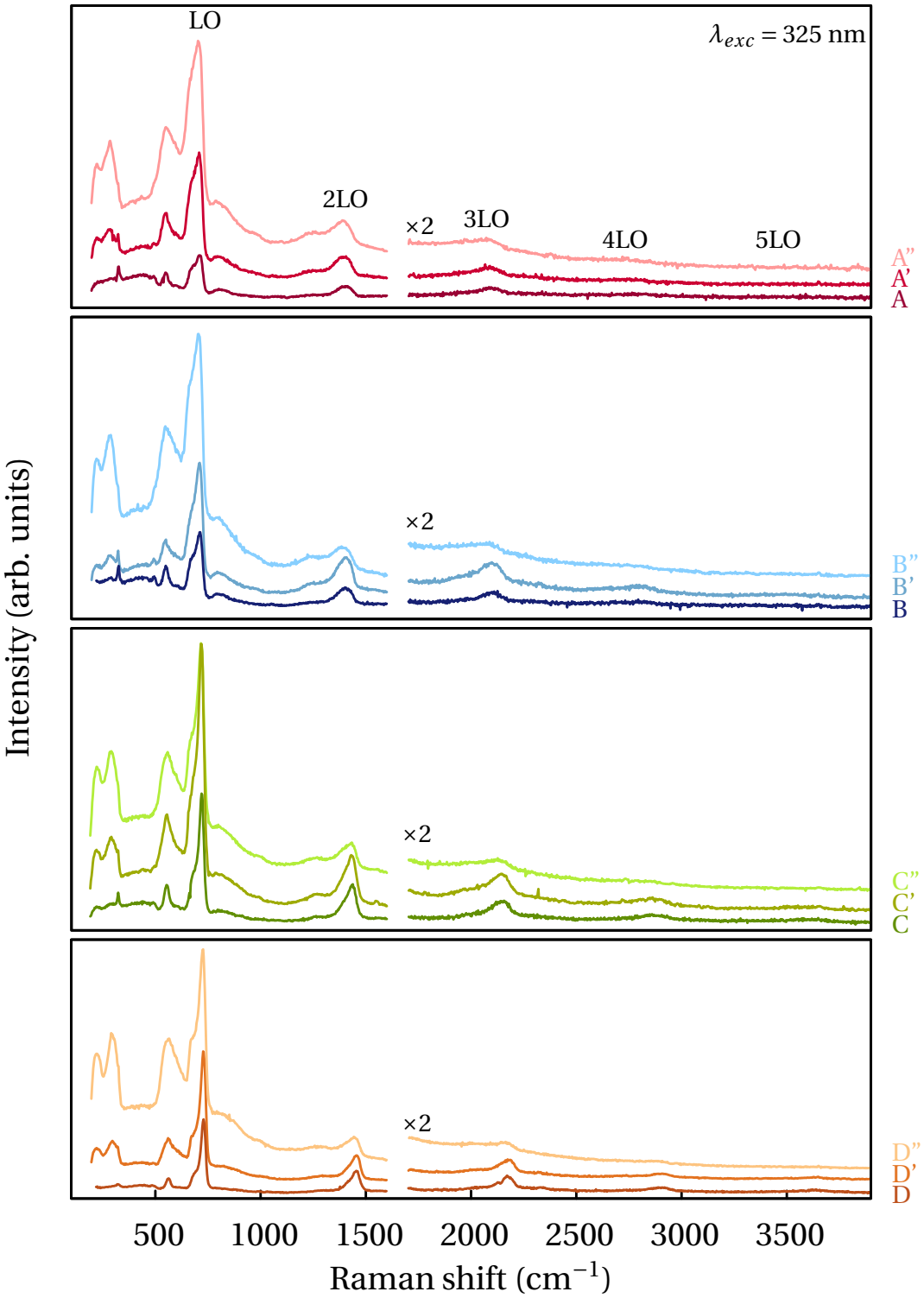

Figure 6.14: *UV Raman spectra of the $In_xGa_{1-x}N$ unimplanted and implanted samples listed in Table 6.1.*

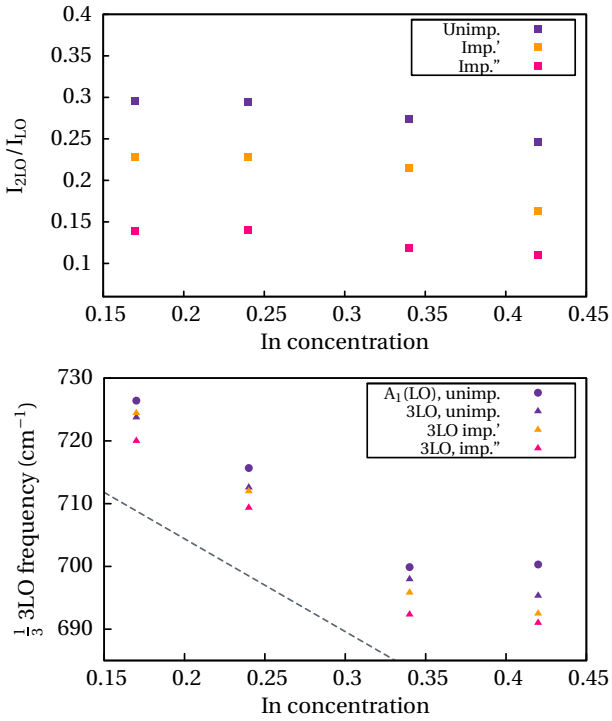

Figure 6.15: *Multiphonon frequencies and intensities for the different samples. Upper panel: 2LO/LO intensity ratio vs indium concentration. Lower panel: average LO frequency involved in 3LO scattering (1/3 ω(3LO)) vs indium composition. A_1(LO) frequencies of unimplanted samples (violet circles) and frequency values predicted by the MREI model (dashed line) are also shown.*

Actually, the spectra shown in Fig. 6.14 exhibit a broadening of the phonon peaks upon implantation, and also exhibit the emergence of features corresponding to disorder-activated structures (at 150-300 cm^{-1} and 600-700 cm^{-1}). The intensity of the first-order LO Raman peak increases as the implantation dose increases, indicating that the intensity enhancement of the LO scattering due to the impurity-induced mechanisms is stronger than the quenching resulting from the reduced crystalline quality. In the case of the second order 2LO, the intensity of the Raman peak remains similar in the implanted samples and in the unimplanted ones, indicating that the impurity-induced enhancement mechanisms are compensated by the reduced crystal quality. We expect the higher order overtones to be more sensitive to the crystal quality, and as a consequence the intensity of the higher order Raman peaks is substantially reduced as the implantation dose increases. This behaviour is qualitatively similar in all the studied samples.

To give a comparative picture of the intensity changes due to implantation, we plot the intensity ratio between the $2A_1$(LO) and the A_1(LO) phonon mode for all the measured samples in the upper panel of Fig. 6.15. The intensity ratios slightly decrease as the In concentration increases. The intensity ratio decreases with increasing implantation dose, showing a similar variation for the different compositions. This behaviour, depicted in the upper panel of Fig. 6.12, suggests that the $I_{2A_1(LO)}/I_{A_1(LO)}$ ratio can be used as an indicator of the implantation-

induced damage: higher value indicates higher crystalline quality. Since multiphonon Raman lines are observed in samples highly implanted in which the PL signal is totally quenched, this intensity ratio can provide a non-destructive assessment of the sample crystalline quality after implantation.

Frequency comparison between multiphonons of the same spectra shows that higher order overtones have frequencies which are slightly lower than the corresponding multiple of the first order A_1(LO) frequency. This can be explained by the participation of $q \neq 0$ phonons in higher order Raman processes which satisfy wave-vector conservation $\sum q = 0$. According to the A_1(LO) phonon dispersion curves, the contribution of such wave vectors is expected to yield an asymmetrically broadened band with a lower peak frequency.

Since lattice disorder and strain may lead to changes in phonon frequencies, we have also compared the frequencies of the multiphonons of samples with different implantation. The results are shown in the lower panel of Fig. 6.15, where we plot the average LO frequency involved in 3LO scattering ($\omega(3LO)/3$) for all compositions and implantation doses. We have seen that the frequencies of all the modes become lower as the implantation dose increases. Three different effects may be contributing to this shift: (1) the high density of defects relaxes the wave-vector conservation selection rule and allows non-zone-centre phonon scattering; (2) the defects created by the implantation damage (anti-sites, interstitials, etc) induce a tensile strain that results in a smaller phonon frequency; and (3) the interstitials and anti-sites created by the implantation result in a reduction of the TO-LO splitting, which also leads to a lower LO phonon frequency [28, 39].

In this study we have analysed Raman scattering measurements on InGaN layers that have been implanted with different He^+ doses. We conclude that the analysis of the Raman spectra can be useful to assess the disorder induced by the implantation, since the relative intensities and peak broadenings depend on the impurity and defect density.

Throughout this chapter we have shown the importance of considering the resonant mechanisms to interpret the III-nitrides Raman spectra. The proximity of their band-gaps with the visible light energies and the high defect density that still exist in the available layers, make the resonant mechanisms to play a key role in the Raman scattering of the InN and In-rich InGaN compounds.

References

[1] E. Smith and G. Dent. *Modern Raman Spectroscopy - A Practical Approach*. Wiley & Sons, 2005.

[2] R. Trommer and M. Cardona. *Phys. Rev. B*, 17:1865, 1978.

[3] J. M. Calleja and Manuel Cardona. *Phys. Rev. B*, 16:3753–3761, 1977.

[4] C. Thomsen and S. Reich. *Phys. Rev. Lett.*, 85:5214–5217, 2000.

[5] A. Jorio, R. Saito, J. H. Hafner, C. M. Lieber, M. Hunter, T. McClure, G. Dresselhaus, and M. S. Dresselhaus. *Phys. Rev. Lett.*, 86:1118–1121, 2001.

[6] J. Ibáñez and R. Cuscó. *Raman spectroscopy of compound semiconductors*. Semiconductor Research. Experimental Techniques. Editors: A. Patanè and N. Balkan. Springer-Verlag, 2012.

[7] D. Behr, J. Wagner, J. Schneider, H. Amano, and I. Akasaki. *Applied Physics Letters*, 68(17), 1996.

[8] H. Harima. *J. Phys. Condens. Matter*, 14:R967, 2002.

[9] M. Kuball, J. W. Pomeroy, M. Wintrebert-Fouquet, K. S. A. Butcher, H. Lu, W. J. Schaff, T. V. Shubina, S. V. Ivanov, A. Vasson, and J. Leymarie. *Phys. Status Solidi A*, 202(5):763–767, 2005.

[10] R. Cuscó, J. Ibáñez, E. Alarcón-Lladó, L. Artús, T. Yamaguchi, and Y. Nanishi. *Phys. Rev. B*, 79:155210, 2009.

[11] V. Yu. Davydov, A. A. Klochikhin, A. N. Smirnov, I. Yu. Strashkova, A. S. Krylov, Hai Lu, W. J. Schaff, H.-M. Lee, Y. L. Hong, and S. Gwo. *Phys. Rev. B*, 80:081204, 2009.

[12] V. Yu. Davydov, A. A. Klochikhin, A. N. Smirnov, I. Yu. Strashkova, A. S. Krylov, Hai Lu, W. J. Schaff, H.-M. Lee, Y.-L. Hong, and S. Gwo. *Semiconductors*, 44:161–170, 2010.

[13] E. O. Schäfer-Nolte, T. Stoica, T. Gotschke, F. A. Limbach, E. Sutter, P. Sutter, D. Grützmacher, and R. Calarco. *Nanotechnology*, 21:315702, 2010.

[14] D. Pastor, J. Ibáñez, R. Cuscó, L. Artús, G. González-Díaz, and E. Calleja. *Semicond. Sci. Technol.*, 22(2):70, 2007.

[15] M. Cardona. *Light scattering in Solids I.* Springer-Verlag, 1975.

[16] D. Olego and M. Cardona. *Phys. Rev. B*, 24:7217, 1981.

[17] R. M. Martin. *Phys. Rev. B*, 10:2620, 1974.

[18] R. M. Martin and C. M. Varma. *Phys. Rev. Lett.*, 26:1241, 1971.

[19] P. Y. Yu and M. Cardona. *Fundamentals of Semiconductors. Physics and materials properties.* Springer-Verlag, 1996.

[20] J. Menéndez and M. Cardona. *Phys. Rev. B*, 31:3696, 1985.

[21] J. Menéndez, M. Cardona, and L. K. Vodopyanov. *Phys. Rev. B*, 31:3705, 1985.

[22] W. Zhu, H. Wu, Z. Yuan, J. Kong, and W. Shen. *J. Raman Spectr.*, 40:2155–2161, 2009.

[23] A. B. Djurišić and E. H. Li. *J. Appl. Phys.*, 85:2848, 1999.

[24] M. Kuball, J. M. Pomeroy, M. Wintrebert-Fouquet, K. S. A. Butcher, Hai Lu, W. J. Schaff, T. V. Shubina, S. V. Ivanov, A. Vasson, and J. Leymarie. *Phys. Status Solidi A*, 202:765, 2005.

[25] G. Chen, J. Wu, Q. Lu, H. R. Gutierrez, Q. Xiong, M. E. Pellen, J. S. Petko, D. H. Werner, and P. C. Eklund. *Nano Lett.*, 8:1341–1346, 2008.

[26] N. Domènech-Amador, R. Cuscó, L. Artús, T. Yamaguchi, and Y. Nanishi. *Phys. Rev. B*, 83:245203, 2011.

[27] V. Yu Davydov, Yu E. Kitaev, I. N. Goncharuk, A. N. Smirnov, J. Graul, O. Semchinova, D. Uffmann, M. B. Smirnov, A. P. Mirgordsky, and R. A. Evarestov. *Phys. Rev. B*, 58:12899, 1998.

[28] D. Pastor, J. Ibáñez, R. Cuscó, L. Artús, G. González-Díaz, and E. Calleja. *Semicond. Sci. Technol.*, 22:70–33, 2007.

[29] D. Pastor, S. Hernández, R. Cuscó, L. Artús, R. W. Martin, K. P. O. O'Donnell, O. Briot, K. Lorenz, and E. Alves. *Superlattices and Microst.*, 40:440–444, 2006.

[30] W. H. Sun, S. J. Chua, L. S. Wang, and X. H. Zhang. *J. Appl. Phys.*, 91:4917, 2002.

[31] S. R. Messenger, G. P. Summers, E. A. Burke, R. J. Walters, and M. A. Xapsos. *Prog. Photovoltaics*, 9:103, 2001.

[32] J. Walters, E. M. Jackson, and B. D. Weaver. *IEEE Trans. Nucl. Sci.*, 46:1595, 1999.

[33] S. R. Messenger, E. A. Burke, G. P. Summers, M. A. Xapsos, R. J. Walters, E. M. Jackson, and B. D. Weaver. *IEEE Trans. Nucl. Sci.*, 46:1595, 1999.

[34] J. F. Ziegler, M. D. Ziegler, and J. P. Biersack. *SRIM*. Cadence Design Systems, 2008.

[35] J. F. Ziegler, M. D. Ziegler, and J. P. Biersack. *Nuclear Instruments and Methods in Physics Research Section B: Beam Interactions with Materials and Atoms*, 268:1818–1823, 2010.

[36] R. Oliva. *Optical emission and Raman scattering in InGaN thin films grown by molecular beam epitaxy*. Master Thesis, Universitat de Barcelona, 2010.

[37] S. X. Li, K. M. Yu, J. Wu, R. E. Jones, W. Walukiewicz, J. W. Ager III, E. E. Shan, W. ans Haller, H. Lu, and W. J. Schaff. *Phys. Rev. B*, 71:161201, 2005.

[38] J. W. Ager III, W. Walukiewicz, W. Shan, K. M. Yu, S. X. Li, E. E. Haller, H. Lu, and W. J. Schaff. *Phys. Rev. B*, 72:155204, 2005.

[39] G. Burns, F. H. Dacol, C. R. Wie, E. Burstein, and M. Cardona. *Solid State Commun.*, 62:449, 1987.

CHAPTER 7

LO-phonon plasmon coupled modes in InN and GaN

The control of the doping level and its homogeneity is essential for semiconductor device fabrication. To probe the free carrier density, doped samples are usually characterized by means of conventional Hall effect measurements, which provide an average value of the free charge density in the sample [1]. To carry out Hall measurements, it is necessary to process the sample and to make electrical contacts, which can be difficult in certain samples such as nanostructures. Moreover, Hall measurements can lead to misleading results in the case of semiconductors with surface electron accumulation layer as occurs for InN. In fact, it has been shown that *p*-doped InN layers exhibit a global *n*-type conductivity in Hall effect experiments [2].

In this chapter we use an alternative approach for studying the free charge density of III-nitrides, based on the analysis of the Raman spectra of the longitudinal optical phonon-plasmon coupled modes (LOPCMs). These coupled modes emerge as a consequence of the interaction of the macroscopic electric field produced by the free charge collective oscillations with the electric field caused by the longitudinal optical phonons. Since the frequency of the coupled modes depends on the free charge density, the detailed study of the Raman line shape of the coupled modes provides a reliable determination free carrier concentration in doped semiconductors [3, 4]. The behaviour of the coupled modes is different in *n*-type and *p*-type compounds, since the effective masses and mobilities of the electrons and holes are also significantly different. Typically, the heavy holes have an effective mass one order of magnitude higher than that of electrons, and as a consequence hole plasmas are over-damped.

Several works have used LOPCM Raman analysis as a tool for determing the free charge density in *n*-type polar semiconductors such as GaAs [5, 6], GaSb [7], SiC [8] or InP [9], among others. In those works two LOPCM were observed, and it was concluded that the analysis of their Raman line shape yields free electron density values similar to those obtained by Hall effect measurements. More scarce and controversial are the studies of LOPCMs in *p*-type semiconductors. Yuasa and Ishii (Ref. [10]) reported the observation of LOPCM lines in Be-doped, *p*-type GaAs, which they assigned to long-wavelength LOPCMs in contrast with a previous work by Olego and Cardona (Ref. [11]) on Zn-doped

GaAs which ascribed the LOPCM line to large-wave-vector L^- modes arising from wave-vector nonconservation. However, the analogy with LOPCMs in n-type material was disputed in later studies performed on a wider range of hole concentrations [5, 12].

There exist also some studies of the LOPCMs in materials of the (In,Ga)N system. In the case of GaN thin films, the LOPCM line shapes have been usually analysed using classical and semi-classical models [13–15]. More recently, LOPCMs have been studied also in GaN nanostructures on the basis of the classical models [16, 17]. The use of simple semi-classical models in GaN is justified by the fact that the conduction band nonparabolicity is relatively small in this wide-band-gap material. The accurate analysis of LOPCMs in InN presents more difficulties due to the presence of the surface electron accumulation layer and the strongly non-parabolic conduction band. Some controversy exists in the literature regarding the interpretation of LOPCMs in InN. Some authors have observed a feature close to the A_1(LO) frequency in n-InN and have attributed it to the high-frequency branch of the LOPCMs at large wave vector, invoking wave-vector nonconservation due to impurity-induced Fröhlich mechanism [18]. Others have assigned that peak to charge-density fluctuation mechanism [19]. Ref. [20] reports a comprehensive study on doped InN layers, which demonstrates that n-type doped InN samples exhibit long-wavelength LOPCMs. Remarkably, signal arising from the LOPCMs and from the unscreened A_1(LO) phonon-mode is detected simultaneously in the Raman spectra. The uncoupled A_1(LO) signal is detected in the spectra because the large wave vectors involved in Martin's double resonance mechanism are much larger than the Thomas-Fermi wave vector of the free carriers. Then, the free carriers cannot screen the electric fields of the LO phonons and these resonantly selected large-q modes are effectively decoupled from the free charge plasma. The Resonant Raman intensity of these modes is strongly enhanced by the high electric fields associated with the surface accumulation layer. It was argued that the confined electrons in the surface accumulation layer cannot sustain longitudinal oscillations and therefore the long-wavelength LOPCM Raman signal measured in InN arises from the bulk material underneath. In that work the analysis of the L^- coupled mode was used to probe the electron density of the samples.

Therefore, Raman scattering is a reliable alternative to determine bulk free electron density in InN without being affected by the electron accumulation layer. This technique has been used to probe the electron density in InN and the spectra have been modelled using either semi-classical models [21], or the more complete quantum-mechanical Lindhard-Mermin model [20, 22]. One of the main advantages of using Raman scattering of LOPCMs for probing the electron density is that it is able to provide a local determination of the free charge density. The aim of this chapter is to present a detailed model of the LOPCMs in

InN and GaN, and to apply it to determine the free electron density in specific cases where we can take advantage of the contactless and local probing characteristics of the Raman scattering technique. We begin by introducing the LOPCM behaviour in polar binary semiconductors and present both the classical and the Lindhard-Mermin models, discussing its adequacy for describing the LOPCMs in III-nitrides. Based on the Lindhard-Mermin approach, we present the results of two in-depth studies. First, we characterize the free charge distribution in an ammonothermally-grown GaN crystal. This growth technique is emerging as a candidate for bulk GaN growth of large crystals that can be used as substrates for homoepitaxial growth of GaN. Although this growth technique is promising for obtaining highly crystalline GaN, the homogeneity of the impurity and free charge distribution has not been studied yet. Second, we present an study of the free electron density in several InN nanowire samples with different doping, including *n*-type and *p*-type nominally doped samples.

7.1 Framework: LOPCMs modelling

The free electron plasma in a semiconductor material can be described as a delocalized Fermi gas (gas of free electrons) moving on a three-dimensional crystal of positive ions. The quantization of the collective oscillations of this Fermi gas results in quasi-particles called *plasmons* [3]. This collective oscillations generate an electric field that, in polar semiconductors, couples with that of the polar optical modes, giving rise to LO phonon-plasmon coupled modes (LOPCMs). These modes have a phonon/plasmon mixed nature and their line shape and frequency strongly depend on the free charge density of the sample and on its electronic properties.

Hole plasma oscillations can also couple with LO modes. The behaviour of the coupled modes is qualitatively different because hole plasmas are overdamped due to the large effective masses and low mobility of the holes. This results in a coupled mode with frequencies between the LO and TO, which in general is rather insensitive to the charge density and is difficult to detect. In contrast, in high-mobility electron plasmas a plasmon-like mode can often be detected, which strongly depends on the electron density.

Throughout this chapter we are mainly concerned with the study of LOPCMs in *n*-type binary semiconductor compounds. In the theoretical section, two approaches for the description of the LOPCMs are derived. First, we provide a classical description that gives an intuitive picture of the LOPCMs behaviour. Later, a more complete modelling from a quantum-mechanical approach (Lindhard-Mermin model) is developed. Finally, we address the main issues related to Raman scattering by these coupled modes in *n*-type semiconductors, as well as the

line-shape modelling procedure for extracting the free charge density.

7.1.1 Classical description of the LOPCMs

To give a first approach to the LOPCM behaviour, we start with the simplest description of the electron plasma, as given by the Drude model. Paul Drude developed his theory just three years after Thomson's discovery of the electron in 1897 [23]. The model describes the thermal and electrical conductivity of metals by applying the kinetic theory of gases to a metal. To do so, it considers the metal to be a gas of free electrons moving in a positive immobile background [24].

Drude model does not take into account the wave-vector dispersion of plasmons, the non-parabolicity effects of the bands, carrier statistics nor the possibility of energy transfer from the collective excitation of the electron gas to a single electron (single-particle excitation). Hence, it is an approximation that can be used in case of single-component plasmas in materials with parabolic electronic bands for plasma frequencies at which plasmon absorption by intra-band transitions is negligible.

An improvement on the Drude model is provided by the Hydrodynamical model (HD) [25]. The HD model is also a classical model, but it includes the wave-vector dispersion of the plasmons. This model can be extended by including the band non-parabolicity, the wave-vector dependence and the thermal distribution effects, giving rise to the so-called *extended hydro-dynamical model* (EHD) [26]. The EHD model improves significantly the accuracy of the LOPCMs description, but it is still valid only far from the single particle excitation regime. This regime is properly addressed in a quantum-mechanical model, that is presented in Section 7.1.2.

We present here a derivation of the Drude model equations, which provides a physical insight into the collective excitations of the free charge and their coupling with the LO modes. Within the classical framework, by considering the free charges to move harmonically and assuming the electrons to have an effective mass m^*, the frequency of the free carrier collective oscillations (i.e., the plasma frequency ω_p) is [24]

$$\omega_p^2 = \frac{4\pi e^2 N_{\mathrm{fc}}}{\varepsilon_\infty m^*}, \tag{7.1}$$

where ε_∞ is the high-frequency dielectric constant of the material. Eq. (7.1) shows that, within the classical description, the plasma frequency ω_p is proportional to the square root of the free charge density (N_{fc}).

In the case of LO-phonon-plasmon coupled modes, the frequency of oscillation can be deduced taking into account their mascropic electric field in the

form of plane waves, which must satisfy the Gauss equation $\nabla \cdot \mathbf{D} = 0$. Since for plane waves

$$\mathbf{D} = \varepsilon \mathbf{E} = \varepsilon \mathbf{E_0} e^{i(\mathbf{k}\cdot\mathbf{r} - \omega t)}, \tag{7.2}$$

the fulfilment of the Gauss equation leads to the condition

$$\nabla \cdot \mathbf{D} = \varepsilon \mathbf{k} \cdot \mathbf{E_0} = 0. \tag{7.3}$$

In longitudinal modes the electric field has the same direction than its propagation ($\mathbf{k} \cdot \mathbf{E_0} \neq 0$), and then to satisfy Eq. (7.3) the dielectric function $\varepsilon(\omega)$ must be zero at the frequency of the coupled modes [27]. Therefore, to find the frequency of the coupled modes that emerge as a result of the plasmon coupling with the LO-phonons, we require the frequency-dependent dielectric function of the system to be zero.

We consider here the dielectric function, that can be written in terms of the dielectric susceptibility of the ionic lattice (χ_I) and the free carrier plasma (χ_p) [3],

$$\varepsilon(\omega) = \varepsilon_\infty + 4\pi \left(\chi_I + \chi_p\right). \tag{7.4}$$

The dielectric susceptibility of the ionic lattice essentially depends on the LO- and TO-phonon frequencies and for binary semiconductors is given by [3]

$$\chi_I(\omega) = \frac{\varepsilon_\infty}{4\pi} \frac{\omega_{\mathrm{LO}}^2 - \omega_{\mathrm{TO}}^2}{\omega_{\mathrm{TO}}^2 - \omega^2 - i\Gamma_I \omega}, \tag{7.5}$$

where the ionic damping Γ_I takes into account the finite lifetime of the phonons. The dielectric susceptibility of the plasma can be described on the basis of the classical plasma oscillation as

$$\chi_p(\omega) = -\frac{\varepsilon_\infty}{4\pi} \frac{\omega_p^2}{\omega(\omega + i\Gamma_p)}. \tag{7.6}$$

In this expression Γ_p is a phenomenological plasma damping parameter that accounts for the finite lifetime of the charge density oscillations. In the relaxation-time approximation the electron mobility is related to the plasma damping via

$$\mu = \frac{e\tau}{m^*} = \frac{e}{m^* \Gamma_p}. \tag{7.7}$$

Samples with small electron mobility have high plasma damping. The value of plasma damping has a considerable impact on both the frequency and the line shape of the coupled modes.

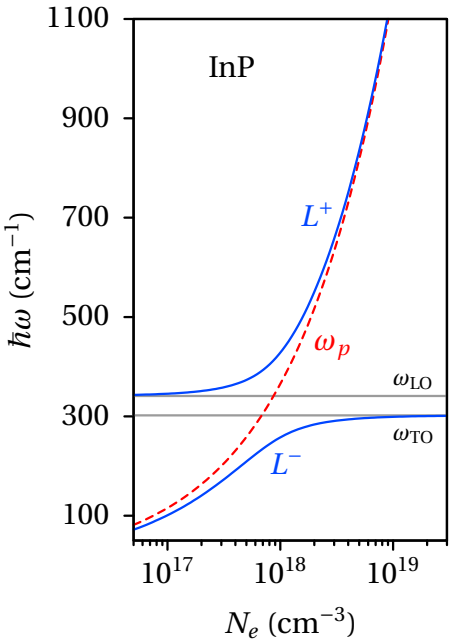

Figure 7.1: *Frequency of the LOPCMs L^+ and L^- in n-type InP as a function of the free electron densities, obtained from the classical approach without dampings [Eq. (7.8)]. The frequencies of the phonon modes (ω_{TO} and ω_{LO}) and the plasma frequency (ω_p) are also plotted.*

As a first approximation, if we assume negligible ionic and plasma damping, Eqs. (7.4), (7.5) and (7.6) lead to a simple analytical expression for the LOPCMs frequencies, which is

$$\omega_{\pm}^2 = \frac{1}{2}\left[\left(\omega_{LO}^2 + \omega_p^2\right) \pm \sqrt{\left(\omega_{LO}^2 + \omega_p^2\right)^2 - 4\omega_p^2\omega_{TO}^2}\right]. \tag{7.8}$$

The examination of this expression gives an approximate but intuitive picture of the LOPCMs behaviour. To illustrate the LOPCMs dependence on carrier density that results from the classical model, we have plotted in Fig. 7.1 the frequency values corresponding to the LOPCMs for indium phosphide (InP) obtained from the Eq. (7.8). As can be seen in Fig. 7.1, two coupled modes, labelled as L^- and L^+, appear as a consequence of the coupling between the free charge density oscillations and the polar optical phonons. For low free charge densities ($\omega_p \ll \omega_{TO}$), the L^- mode has a plasmon-like behaviour, and its frequency is close to that of the plasmon mode, while the L^+ mode has a frequency close to the longitudinal optical phonon. For high free charge densities ($\omega_p \gg \omega_{TO}$) the character of the coupled modes is reversed. Within this regime, the L^- is phonon-like and asymptotically approaches the TO frequency. The L^+ mode is plasmon-like, and its frequency increases linearly with the square root of the free charge density, asymptotically approaching the plasmon frequency.

The LOPCMs behaviour is illustrated by the Raman spectra shown in Figure 7.2, which correspond to Si-doped InP samples with different free electron densities (from Ref. [9]). These spectra exhibit Raman peaks at 304 cm^{-1} and 343.5 cm^{-1}, corresponding to the TO and LO modes, respectively, as well as three

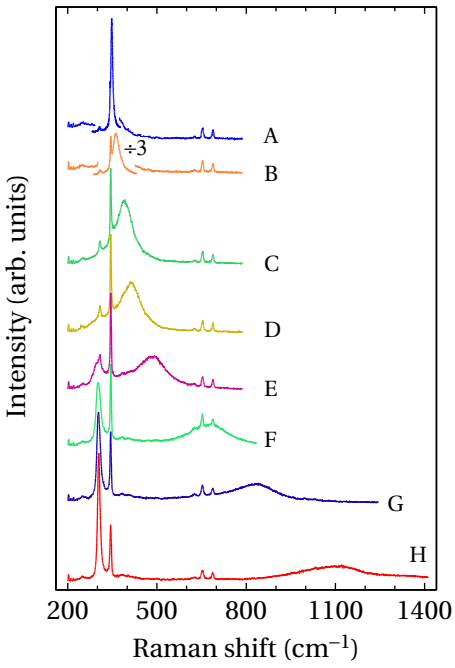

Figure 7.2: *Raman spectra of n-InP samples taken with the $x(yz)\bar{x}$ scattering configuration. Free electron density ranges from 7×10^{16} cm^{-3} in sample A to 1×10^{19} cm^{-3} in sample H, as obtained from Hall effect measurements. Figure extracted from Ref. [9].*

second-order modes in the 600-700 cm^{-1} region. A broader mode corresponding to the L^+ coupled mode is observed in all the spectra. The frequency of this mode strongly depends on the free electron density and shifts by more than 750 cm^{-1} in the studied electron density range. The phonon-like L^- coupled mode can also be seen in the Raman spectra of the samples with higher doping level (E-H). The behaviour of these L^- and L^+ coupled modes is in good agreement with that predicted by the Drude model, that was depicted in Fig. 7.1.

One of the limitations of the Drude model is that it considers a parabolic approximation of the electronic bands. This approximation leads to inaccurate results for semiconductors with a strong nonparabolicity of the conduction band, such as InN [2]. This drawback can be overcome by using an hydrodynamic model, as shown in Ref. [28]. Another limitation of the classical description is that it does not take into account the damping caused by single particle excitation (SPE). In the real coupled system, the coupled mode oscillations can be damped by their interactions with lattice phonons, defects, free charges, ionized impurities, etc. The damping of the plasma excitations due to interaction with SPE is known as Landau damping and may occur when the energy of the coupled mode is close to that of the carrier excitations. Under these conditons, if the thermal mean velocity of the electrons is slightly lower than the phase velocity of the plasmon oscillation, the electrons are able to follow the wave oscillations and increase their energy by reducing the collective excitation energy. The energy conservation in this process can be expressed in terms of the electron energy dispersion band $[E(\mathbf{k})]$ and the plasmon frequency and wave vector

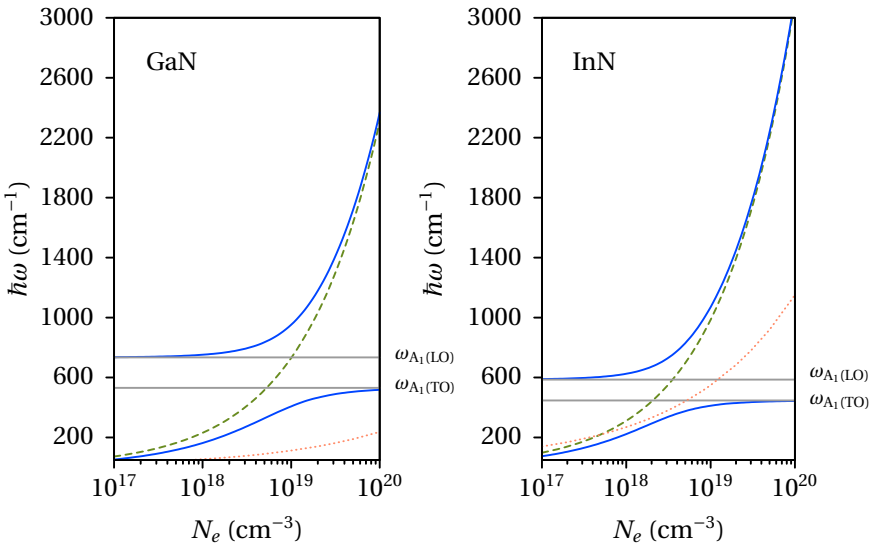

Figure 7.3: *Frequency of the LOPCMs (solid lines) and plasma frequency (dashed line) as a function of the free electron density, for GaN (left) and InN (right). The upper limit of the Landau damped region is also plotted (dotted line). These dependences have been calculated using the classical model described in Sec. 7.1.1 and the parameters are shown in Table 7.1 and Table 7.3 for the GaN and InN, respectively.*

$(\omega, \mathbf{q})$ as

$$E(\mathbf{k}) + \hbar\omega_p = E(\mathbf{k}+\mathbf{q}) \tag{7.9}$$

Within the parabolic approximation, the frequencies for which Landau damping takes place lie in the region [29]

$$\omega_{\text{SPE}} = \frac{\hbar}{2m^*} q^2 \pm q v_F, \tag{7.10}$$

where the Fermi velocity (v_F) is related to the free carrier density (N_{fc}) through $v_F = \frac{\hbar}{m^*}\sqrt[3]{3\pi^2 N_{\text{fc}}}$. The Landau damping can be an important damping channel for the coupled modes in semiconductors with small electron effective masses and small optical phonon frequencies.

Figure 7.3 shows the calculated frequencies for the LOPCMs in InN and GaN taking into account the given classical description. We have also plotted in this figure the upper limit of the Landau damping regime (dotted line), calculated with Eq. (7.10) and taking into account the electron effective masses given in Table 2.1. As can be seen in Fig. 7.3, the Landau damping has a negligible effect on the LOPCMs of GaN, but it affects the L^- branch of the LOPCMs of InN, whose electron effective mass is smaller than that of GaN. In addition to the fact that the

Drude model is a poor approximation for nonparabolic semiconductors, these simple calculations indicate that a more accurate model is needed to describe the LOPCMs coupling in InN-related materials.

7.1.2 Lindhard-Mermin model

In order to give a more accurate description of the LOPCMs behaviour, the plasma susceptibility can be described by a quantum mechanical approach, considering the Lindhard-Mermin model [30, 31]. The Lindhard model is derived from a linear treatment of the screening in which the free carrier intraband transitions are taken into account. In this section we present this model and the expressions used in this thesis for modelling the LOPCMs. For a more detailed description of the model, see Refs. [3, 9, 24, 30–32].

In order to describe the interaction between electric fields, we consider a charge density distribution denoted by $\rho^{\text{ext}}(\mathbf{r})$. The electrostatic potential induced by the charge distribution ($\phi^{\text{ext}}(\mathbf{r})$) satisfies the Poisson equation,

$$-\nabla^2\phi^{\text{ext}}(\mathbf{r}) = 4\pi\rho^{\text{ext}}(\mathbf{r}). \tag{7.11}$$

We define also $\rho^{\text{ind}}(\mathbf{r})$ as the free charge density induced in the electron gas by the presence of the external particle. Then, the full charge density and the full potential are

$$\rho(\mathbf{r}) = \rho^{\text{ext}}(\mathbf{r}) + \rho^{\text{ind}}(\mathbf{r}) \tag{7.12}$$

$$\phi(\mathbf{r}) = \phi^{\text{ext}}(\mathbf{r}) + \phi^{\text{ind}}(\mathbf{r}) \tag{7.13}$$

and they satisfy

$$-\nabla^2\phi(\mathbf{r}) = 4\pi\rho(\mathbf{r}). \tag{7.14}$$

We may also take into account the Fourier transforms of the Poisson's equations,

$$q^2\phi^{\text{ext}}(\mathbf{q}) = 4\pi\rho^{\text{ext}}(\mathbf{q}) \tag{7.15}$$

$$q^2\phi(\mathbf{q}) = 4\pi\rho(\mathbf{q}) \tag{7.16}$$

Following the derivation given in Ref. [24], by assuming a spatially uniform electron gas and that ϕ and ϕ^{ext} are linearly related, we find that

$$\phi(\mathbf{q}) = \frac{1}{\varepsilon(\mathbf{q})}\phi^{\text{ext}}(\mathbf{q}), \tag{7.17}$$

where $\varepsilon(\mathbf{q})$ is the wave-vector dependent dielectric function. Although the dielectric function is the variable with physical significance, to obtain it we first relate the susceptibility $\chi(\mathbf{q})$ with the induced charge density ρ^{ind} and the total potential ϕ. For small ϕ, the $\rho^{\text{ind}}(\mathbf{r})$ and $\phi(\mathbf{r})$ are linearly related, and then their Fourier transforms satisfy the relation

$$\rho^{\text{ind}}(\mathbf{q}) = \chi(\mathbf{q})\phi(\mathbf{q}). \tag{7.18}$$

By taking into account the expressions given above, we can express the Fourier transform of the dielectric function in terms of ρ^{ind} and ϕ as follows:

$$\varepsilon(\mathbf{q}) = 1 - \frac{4\pi}{q^2}\chi(\mathbf{q}) = 1 - \frac{4\pi}{q^2}\frac{\rho^{\text{ind}}(\mathbf{q})}{\phi(\mathbf{q})} \tag{7.19}$$

The electron gas susceptibility is calculated in the random phase approximation (RPA) using the Lindhard method. This method is a Hartree calculation, in which ρ^{ind} is only required to linear order in ϕ [24]. The one-electron Schrödinger equation describing the system is

$$-\frac{\hbar^2}{2m}\nabla^2\psi(\mathbf{r},t) - e\phi(\mathbf{r})\psi(\mathbf{r},t) = i\hbar\frac{\partial\psi(\mathbf{r},t)}{\partial t}, \tag{7.20}$$

where $\phi(\mathbf{r})$ is the total potential. This equation was solved by Lindhard in Ref. [30] using time-dependent perturbation theory, which lead to the Lindhard plasma susceptibility,

$$\chi_p^L(\mathbf{q},\omega) = \frac{e^2}{2\pi^3 q^2}\int f(E_F,T,k) \times \frac{E(\mathbf{q}+\mathbf{k}) - \mathbf{E}(\mathbf{k})}{\left[E(\mathbf{q}+\mathbf{k}) - \mathbf{E}(\mathbf{k})\right]^2 - (\hbar\omega)^2} d^3\mathbf{k}, \tag{7.21}$$

where $f(E_F,T,k)$ is the Fermi-Dirac distribution and $E(\mathbf{k})$ is the energy dispersion band of the carriers. This expression takes into account the interaction of the coupled mode collective excitations with single particle excitations that lead to the Landau damping, as can be deduced from its explicit dependence on electronic intra-band transitions. In contrast, the damping of the plasma due to interaction with ionized impurities and lattice vibrations is not considered in Eq. (7.21). These effects can be included in the plasma susceptibility by considering a complex frequency with an imaginary part $i\Gamma_p$, where Γ_p is a phenomenological damping constant in the RPA framework. Mermin showed in Ref. [31] that to enforce the conservation of the number of particles, the Lindhard susceptibility had to be modified according to the following prescription:

$$\chi_p^{LM}(\mathbf{q},\omega) = \frac{\left[1+\dfrac{i\Gamma_p}{\omega}\chi_p^L\left(\mathbf{q},\omega+i\Gamma_p\right)\right]}{1+\dfrac{i\Gamma_p\chi_p^L\left(\mathbf{q},\omega+i\Gamma_p\right)}{\left[\omega\chi_p^L(\mathbf{q},0)\right]}}. \tag{7.22}$$

The Lindhard-Mermin model gives a complete description of the plasma behaviour in polar semiconductors, although its mathematical complexity is considerably higher than the analytical classical approximations.

7.1.3 Raman scattering of LOPCMs in *n*-type semiconductors

In the previous sections we have presented the models that can be used to calculate the frequency of the phonon-plasmon coupled modes. Here we present the analytical expressions used to calculate Raman line shapes and give some examples of the results obtained using different approaches.

As in the case of LO phonons, three mechanisms are relevant for Raman scattering by LOPCMs. The deformation potential and the electro-optical mechanisms are both dipole-allowed mechanisms, and the Fröhlich mechanism is dipole-forbidden and allows the measurement of the coupled modes in parallel polarization and backscattering geometry. Depending on the scattering geometry, the measured LOPCMs signal arises from the coupling with A_1 or E_1 phonons. As described in Chapter 4, the A_1(LO) phonon propagates along the c axis, while the E_1(LO) propagates in directions perpendicular to the c axis. Therefore, the coupling with the plasmons occurs with A_1(LO) phonon for propagation along the (0001) direction (as excited in backscattering from a c face, $z(xx)\bar{z}$ configuration), and with the E_1(LO) phonon for propagation directions perpendicular to the c axis.

The differential Raman cross section for the dipole-allowed scattering by LOPCMs can be described by the fluctuation-dissipation formalism developed by Hon and Faust [33]. It can be expressed in terms of the total dielectric constant and the ionic and plasma susceptibilities, and reads

$$\frac{\partial^2\sigma}{\partial\omega\partial\Omega} \propto [n(\omega)+1]\times\Im\left\{\frac{-1}{\varepsilon(\omega,q)}\left[\frac{\varepsilon_\infty}{4\pi}+2C_{\mathrm{FH}}A\chi_{\mathrm{ion}}-C_{\mathrm{FH}}^2A^2\chi_{\mathrm{ion}}\left\{1+\frac{4\pi}{\varepsilon_\infty}\chi_e\right\}\right]\right\}, \tag{7.23}$$

where $n(\omega)$ is the Bose-Einstein distribution function. The parameter A can be written as

$$A = \frac{C_{\mathrm{FH}}\omega_{\mathrm{TO}}^2}{\omega_{\mathrm{LO}}^2-\omega_{\mathrm{TO}}^2}, \tag{7.24}$$

where C_{FH} is the Faust-Henry coefficient. The value of the Faust-Henry coefficient is related to the relative magnitude of the lattice and electro-optic contributions to the Raman tensor. Therefore, it can be determined by studying the relative intensities of the TO/LO modes as shown in Ref. [34].

In this chapter we use this formalism to calculate the line shapes of the coupled modes, taking into account the Lindhard-Mermin susceptibility [Eq. (7.22)]. We have only two free parameters in the model: the free charge density (N_{fc}) and the plasma damping (Γ_p). To give a general overview of the predictions of this model, we have calculated the Raman line shapes corresponding to several free electron concentrations and plasma dampings for InN (Fig. 7.4). Note that in this case we have considered coupling of the plasmons with the E_1(LO) phonons. The *ideal* behaviour of the LOPCMs is exhibited by the less damped line shapes (red line shapes in Fig. 7.4). However, in real samples a significant plasma damping often exists, and then the LOPCM line shapes are likely to be similar to those shown in Fig. 7.4 for $\Gamma_p = 250$ cm^{-1} or $\Gamma_p = 500$ cm^{-1} .

For the lowest free electron density in Fig. 7.4 ($N_e = 1\times10^{18}$ cm^{-3}), the line shape with the lowest damping exhibits a phonon-like L^+ coupled mode, and also weak signal arising from the plasmon-like L^- mode. For the more heavily damped line shapes, only the L^+ is still visible. This indicates that the L^- coupled mode is very sensitive to the damping in this regime, and therefore it can be difficult to detect experimentally. For higher free charge densities ($N_e = 3\times10^{18}$ cm^{-3}), the plasma frequency is similar to the LO phonon frequency ($\omega_p \sim \omega_{\mathrm{LO}}$); this is called the strong coupling regime. Within this regime the resulting coupled modes present a phonon-plasmon mixed behaviour. For the line shape with the lowest damping, both L^+ and L^- modes are clearly detected and resolved. When the value of the damping is increased, their frequencies become closer and the peaks broaden. For $N_e = 1\times10^{19}$ cm^{-3}, the L^- peak sharpens and asymptotically approaches the TO frequency (phonon-like behaviour), while the L^+ peak becomes plasmon-like. The line shapes with higher damping show a similar behaviour, but with weaker and broadened peaks. The spectra with $N_e = 3\times10^{19}$ cm^{-3} also follow this trend.

In order to compare the results of the Lindhard-Mermin calculations with the predictions of the Drude model, we have plotted the frequency values of the line-shape peaks, together with the Drude results in Fig. 7.5. Note that in this figure we show the frequencies of the coupled mode taking into account coupling with the E_1(LO) phonon mode, while in Fig. 7.3 the calculations were made taking into account coupling with the A_1(LO) phonon mode. In Fig. 7.5 it can be seen that, in general, the frequencies of the coupled modes follow qualitatively the behaviour described by the Drude theory. By comparing both models it can be seen that the use of the Drude model to calculate the free electron density will lead to an overestimated value if the L^- is analyses and to an underestimation if

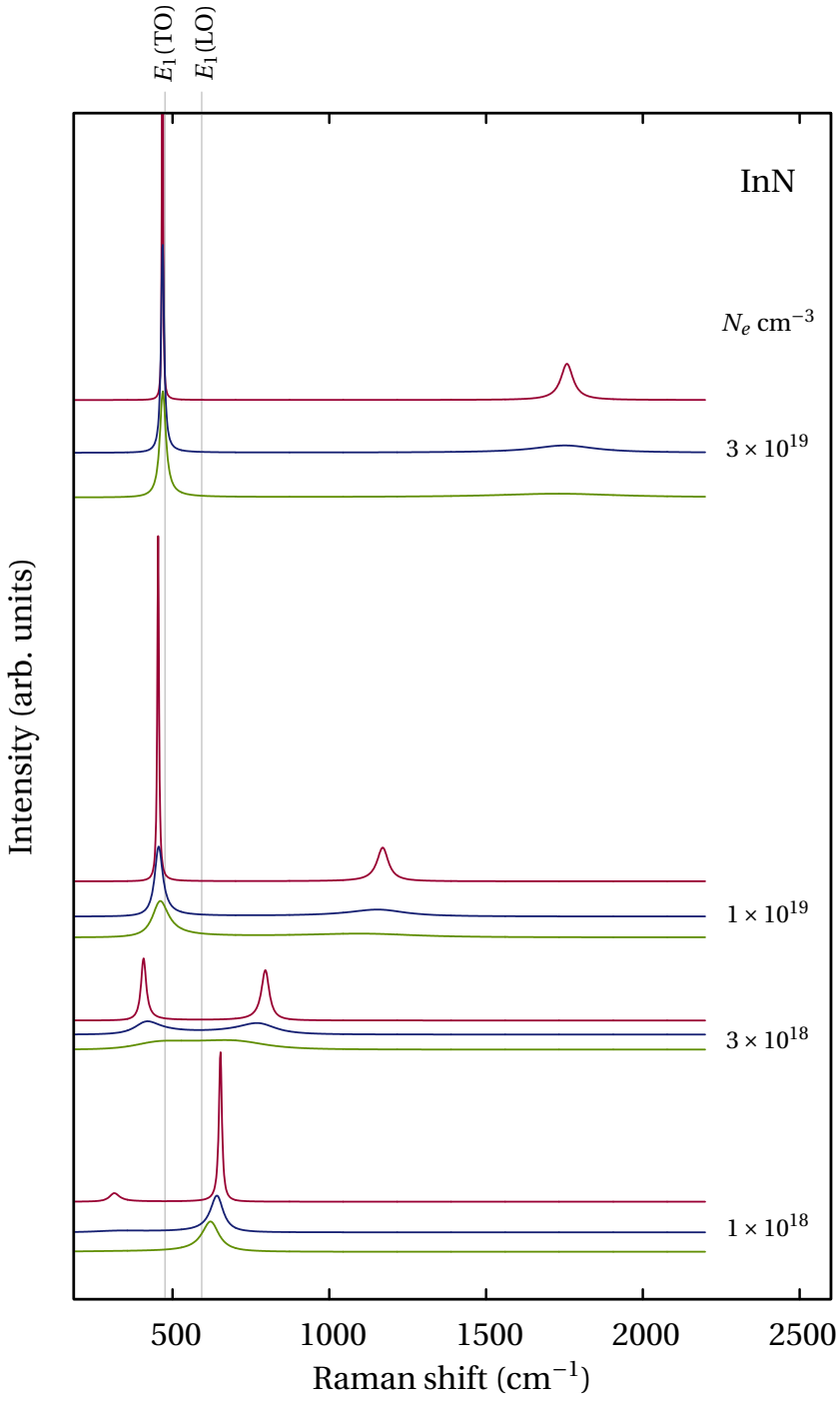

Figure 7.4: *LOPCM line shapes for different free electron densities for InN taking into account coupling with the E_1(LO) phonon mode. The line shapes have been calculated using the Lindhard-Mermin model, the Hon and Faust line-shape formalism and the parameters given in Table 7.3. For each N_e value, three line shapes are shown, corresponding to a plasma dampings of $\Gamma_p = 50\ cm^{-1}$ (red upper line shape), $\Gamma_p = 250\ cm^{-1}$ (blue middle line shape), and $\Gamma_p = 500\ cm^{-1}$ (green lower line shape).*

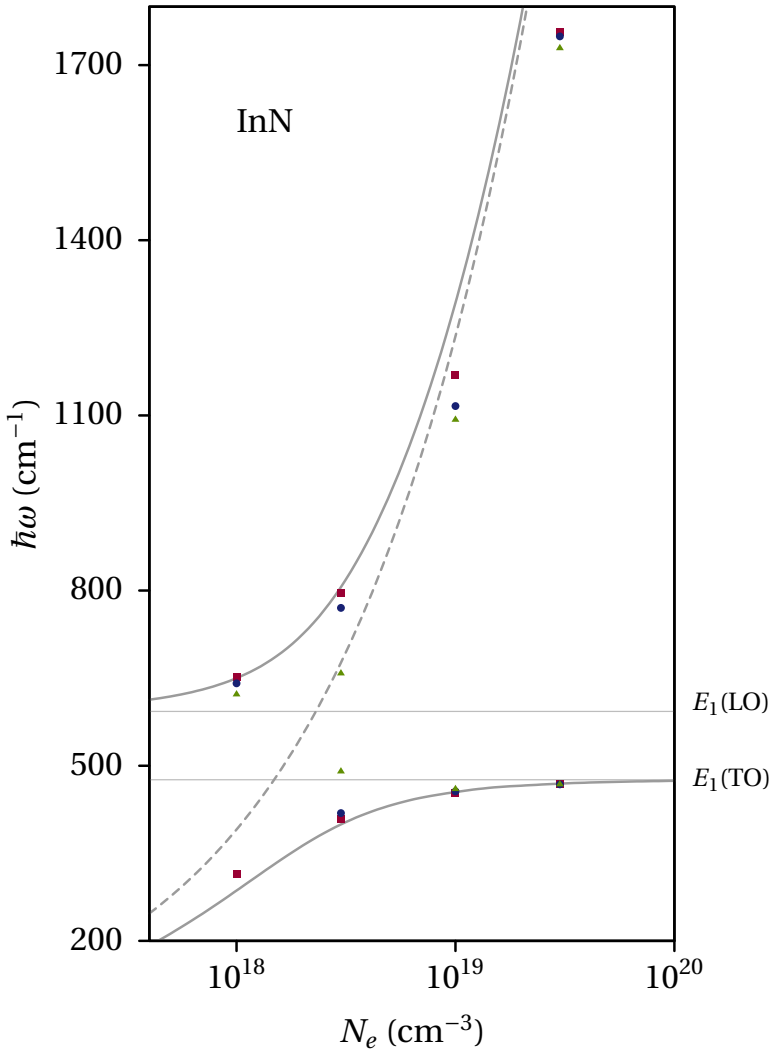

Figure 7.5: *Frequency of the LOPCMs in InN as a function of the free electron density taking into account coupling with the E_1 (LO) phonon mode. Grey lines show the frequency of the LOPCMs (solid lines) and plasma frequency (dashed line) as calculated from the Drude model. We have plotted the frequencies of the coupled modes calculated using the Lindhard-Mermin model taking into account a plasma damping of $\Gamma_p = 50$ cm^{-1} (red squares), $\Gamma_p = 250$ cm^{-1} (blue circles), and $\Gamma_p = 500$ cm^{-1} (green triangles), extracted from the line shapes shown in Fig.7.4.*

the studied mode is the L^+.

For high free electron densities, Fig. 7.5 shows that both models give similar frequencies for the phonon-like L^- mode, but remarkably different values are obtained for the plasmon-like L^+. This is a consequence of the non-parabolicity of the InN electronic bands, which is not accounted for in the Drude model. Since for high free-electron densities the L^+ coupled mode is the most sensitive to the carrier density, it is evident from Fig. 7.5 that Drude model cannot be a quantitative tool for extracting accurate values of the InN free electron density.

The most significant differences between both models are found in the strong coupling regime, in which the damping plays a fundamental role determining the frequency and shape of the coupled mode peaks. In fact, for even higher plasma dampings (i. e. $\Gamma_p > 700$ cm^{-1}), only one overdamped LOPCM is detected in this regime. This is the case of p-type semiconductors, in which the free charges are holes, described by effective masses much bigger than those of the electrons. The interaction of the hole plasma with the polar modes leads to results that are substantially different from those explained throughout this chapter for electrons. It has been observed that binary p-type compounds exhibit only one coupled mode, whose frequency varies only slightly from the frequency of the LO mode for low free charge densities and asymptotically approaches the frequency of the TO mode for high free hole densities [5]. This behaviour is a consequence of the overdamped nature of the hole plasma. Because of the high mass and low mobility of the holes, the coupling with the hole plasma yields a screened LO phonon-like coupled mode.

7.2 LOPCMs in bulk *n*-type GaN

One of the main advantages of studying the free-charge density through the analysis of the LOPCMs Raman spectra is that it provides a local probe, and therefore it can be used to analyse the homogeneity of the free charge density in doped samples. This is specially interesting in doped bulk samples in which the dopant distribution and activation can be inhomogeneous.

The interest in bulk growth of III-nitrides is very high because of the lack of native substrates. As described in Sec. 2.2, III-nitride thin films are often obtained by heteroepitaxial growth on foreign substrates such as Si, SiO_2 or SiC, leading to a high dislocation density. In spite of the significant improvement in the quality of thin film layers, they still contain a high density of dislocations. One of the most promising methods for bulk growth of III-nitrides is the ammonothermal technique. In the case of GaN, ammonothermal growth has been proven to be able to produce large-scale GaN crystals with the desired crystal quality and scaling-up characteristics [35]. In the ammonothermal method, the samples grow in both Ga- and N-polarity faces, which may contain different impurity and defect densities. Due to the interest of GaN for device applications it is specially relevant to control the homogeneity of the free electron density, since it can have an important impact on device performance [36].

In this section we use Raman scattering to perform a study of a high-quality ammonothermally-grown Si-doped GaN sample. The ammonothermally-grown samples present both Ga and N crystalline polarity faces. We study the phonon modes in both polarities, and also the signal arising from LOPCMs. The spectra have been taken using confocal micro-Raman in order to attain high spatial resolution of the Raman signal.

The ammonothermally-grown Si-doped GaN sample

The sample studied in this section is an ammonothermally-grown Si-doped GaN crystal. The ammonothermal growth is a solvothermal method to grow III-nitrides, similar to the hydrothermal processes used to grow α-quartz, but using an alkaline ammonia solution. In the solvothermal growth, the chemical species react and crystallize on a crystalline seed. The crystalline quality of the seed used to begin the growth plays a key role in determining the crystalline quality of the obtained crystal. All the process steps are described in detail in Refs. [35, 37].

For the growth of the sample studied in this thesis, a hydride vapor phase epitaxy (HVPE) template seed was used [35]. Figures 7.6(a) and (b) show optical microscope images of the cross section of the studied sample. The crystalline growth that proceeds on each side of the seed exhibits a different polarity. As it has been explained in Sec. 2.1, the kinetics of the growth is different in both

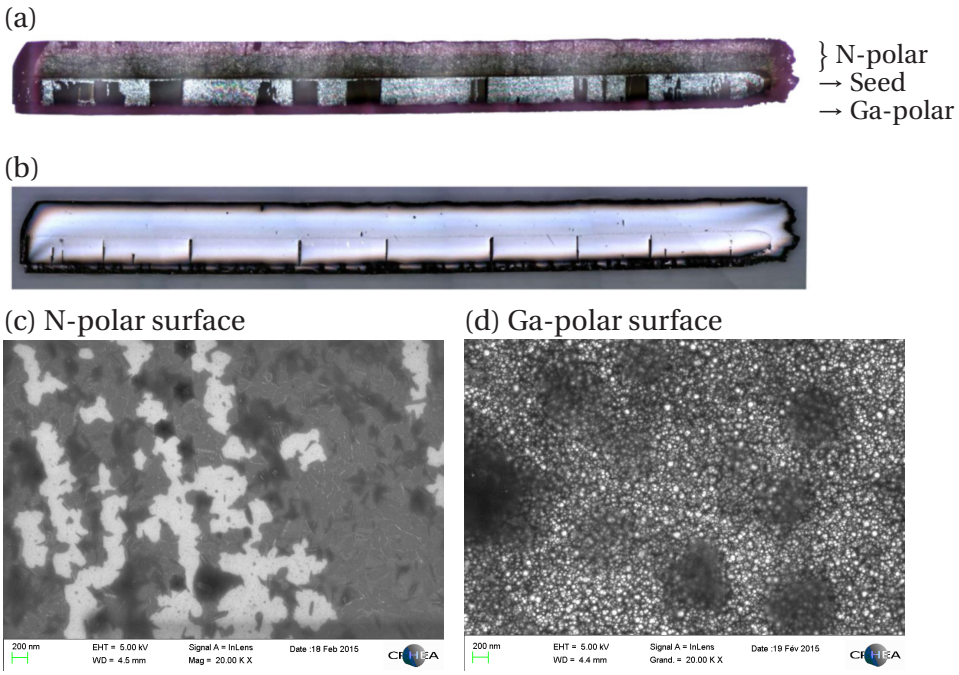

Figure 7.6: *Characterization of the ammonothermal GaN sample. Optical microscope images of the sample in cross section using transmission and reflected light (a) and only reflected light (b). SEM images of the N-polar surface (c) and Ga-polar surface (d).*

polarities, which results in a different growth rate and impurity incorporation. Figures 7.6(c) and (d) show SEM images of both surfaces of the sample, in which the higher quality of the N-polar surface can be noticed.

Mapping along the *z*-axis

To obtain spatially-resolved spectra, confocal micro-Raman measurements are carried out. The excitation wavelength used in this section is the 514-nm line of an argon laser. The Raman spectra are recorded through a 100× objective with a numerical aperture of 0.95, using the standard spectrometer mode. See Chapter 3 for a general description of the Raman set-up and Sec. 3.12 for the confocal micro-Raman details.

The possibility of obtaining local measurements of the Raman spectra has been exploited to perform mappings along the z-axis. Two scattering configurations are used: $z(xx)\bar{z}$ and $x(yy)\bar{x}$. The $z(xx)\bar{z}$ in-depth measurements have been performed using confocal micro-Raman, which allows us to select the depth of the measurement. In this chapter, we define the depth as the distance

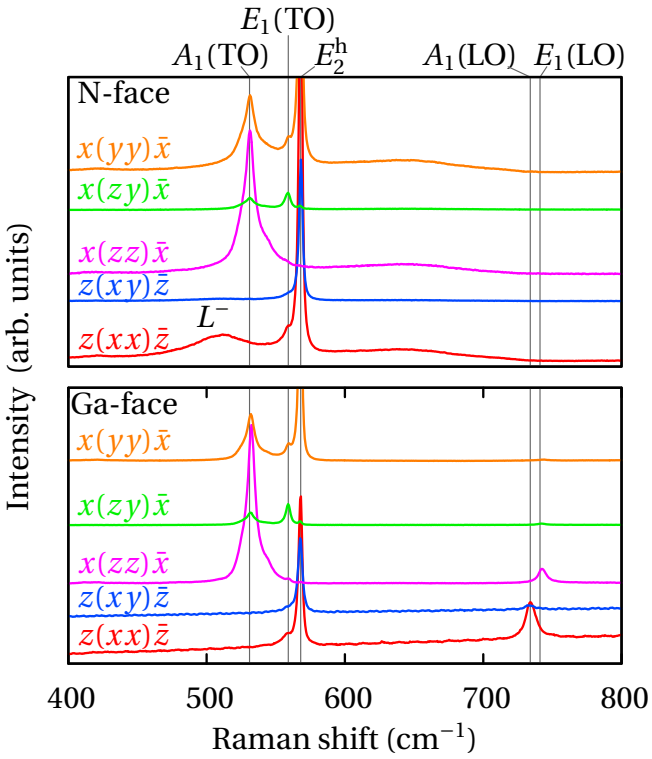

Figure 7.7: *Raman spectra of the ammonothermal GaN sample obtained in different scattering configurations on both the N- and Ga-polar surfaces.*

between the actual probed volume and the surface of the N-sector. A piezoelectric system attached to the objective has been used to change the depth of the measurement, which has been calculated taking into account the GaN refractive index. An added difficulty of measurements in this scattering configuration is that the intensity of the Raman signal gradually decreases as the depth increase, making it difficult to obtain an accurate evaluation of N_e for depths higher than 130 μm. As a further check of the free charge in-depth variation and to extend the probed region beyond 130 μm, $x(yy)\bar{x}$ Raman spectra have been recorded on a lateral $(1\bar{1}00)$ face. In this case, we have performed a scan at 30 μm steps from the surface to the seed using a motorized stage.

7.2.1 Raman spectra of the N- and Ga-polar surfaces

As a starting point of the homogeneity study, we have performed a detailed Raman study of both the N- and Ga-polar surfaces of the sample. The Raman spectra obtained for different scattering configurations are shown in Fig. 7.7. In general, in the spectra obtained from the Ga-polar surface the Raman selection rules for wurtzite materials strictly hold, except for the observation of the A_1(TO) mode in the $x(zy)\bar{x}$ spectrum and the observation of a weak E_1(LO) peak in the $x(zz)\bar{x}$ spectrum. As extensively discussed in Sec. 4.2, this mode is detected via Fröhlich intra-band interaction.

The spectra and the adherence to selection rules are quite similar for the N-polar surface except for the absence of the LO modes and the observation in the $z(xx)\bar{z}$ spectrum of a broad peak emerging below the A_1(TO). These are indicative that the free electron density is coupled with the LO-phonons in the N-polar surface. Therefore, the feature below the A_1(TO) in the $z(xx)\bar{z}$ spectrum can be assigned to the low-energy branch of the LOPCMs, L^-. Although the $x(zz)\bar{x}$ and $x(yy)\bar{x}$ spectra do not exhibit a clear L^- peak for reasons that are discussed below, the absence of the E_1(LO) signal in these spectra is an indirect evidence of free-charge coupling with the LO modes.

Crystal quality of the Ga- and N-polar sectors

The Raman spectra obtained from the N- and Ga-polar surfaces indicate that coupling between free electrons and polar phonons takes place in the N-polar sector, but not in the Ga-polar sector. Since crystal quality may play an important role in the dopant incorporation, we have checked it in both surfaces. To study the crystalline quality of both sample sectors, we have measured the linewidth of the E_2^{high} in the $z(xy)\bar{z}$ Raman spectrum, in which it is symmetry-allowed. After correcting for the spectrometer bandwidth, an E_2^{high} linewidth of 2.2 cm^{-1} was found for the N-polar surface. This value compares well with the E_2^{high} line width of 2.1 cm^{-1} reported for undoped GaN grown by hydride vapour phase epitaxy [38] and with the recently reported value of 2.6 cm^{-1} in undoped ammonothermal GaN [39]. This indicates that the crystalline quality of the studied ammonothermal sample is comparable to the state-of-the art epitaxial samples.

The linewidth of the E_2^{high} mode measured on the Ga-polar surface is 2.9 cm^{-1}, reflecting the higher defect incorporation and lower crystalline quality of this region with respect to the N-region. Previous studies on similar samples have also found that Ga-polar GaN has less crystalline quality than N-polar GaN, and attributed this to columnar growth in the Ga-polar region [40]. Other studies on ammonothermal undoped GaN crystals have found that the incorporation of heavy metal impurities such as Ni, Fe, and Co from the autoclave walls, which form deep levels and may act as compensating centres, is one order of magnitude higher in the Ga-polar face [41]. This is confirmed by the cathodoluminescence measurements reported in Ref. [42], which show that deep level emission is higher in the Ga-polar side than in the N-polar side. We argue that the lower crystalline quality and the higher defect density as well as the presence of acceptor-like grain boundaries may limit N_e in the Ga-polar sector.

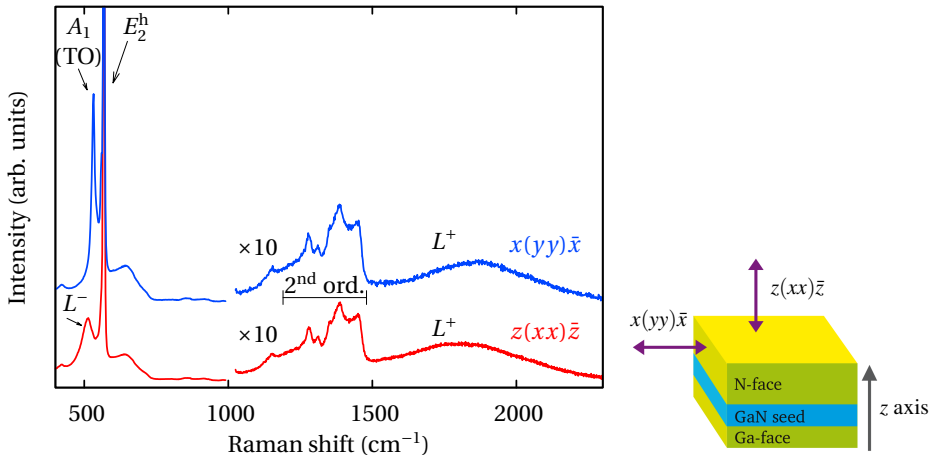

Figure 7.8: *Left: Raman spectra of the ammonothermal Si-doped GaN sample taken in the $z(xx)\bar{z}$ and $x(yy)\bar{x}$ scattering configurations on the N-polar surface. Right: scheme of the scattering configurations.*

LOPCMs in the N-polar surface

Taking into account the frequency of the L^- coupled mode detected, we expect the L^+ coupled mode to emerge around 1800 cm^{-1} and to have broad line shape. Therefore, to have a complete picture of the free charge coupling on the N-polar surface, we have performed Raman scattering measurements over an extended frequency range using the diffraction grating of 600 lines/mm (see Table 3.1). Raman measurements have been performed in the $z(xx)\bar{z}$ and $x(yy)\bar{x}$ scattering configurations in the spectral region of the L^+ coupled mode. The obtained Raman spectra are displayed in Fig. 7.8. These spectra reveal a broad band centred at the expected frequency of 1800 cm^{-1}, which is assigned to the long-wavelength L^+ coupled mode [14].

Although the phonon-like L^+ coupled mode exhibits a similar frequency in the spectra shown in Fig. 7.8, only in the $z(xx)\bar{z}$ spectrum the L^- coupled mode is clearly detected. As explained in Sec. 7.1.3, the plasmons are coupled with the E_1(LO) phonon in the measurements performed with the $x(yy)\bar{x}$ scattering configuration. Therefore, the phonon-like L^- coupled mode has a frequency close to the E_1(TO), becoming completely masked by the strong A_1(TO) signal, which is dipole-allowed in this configuration.

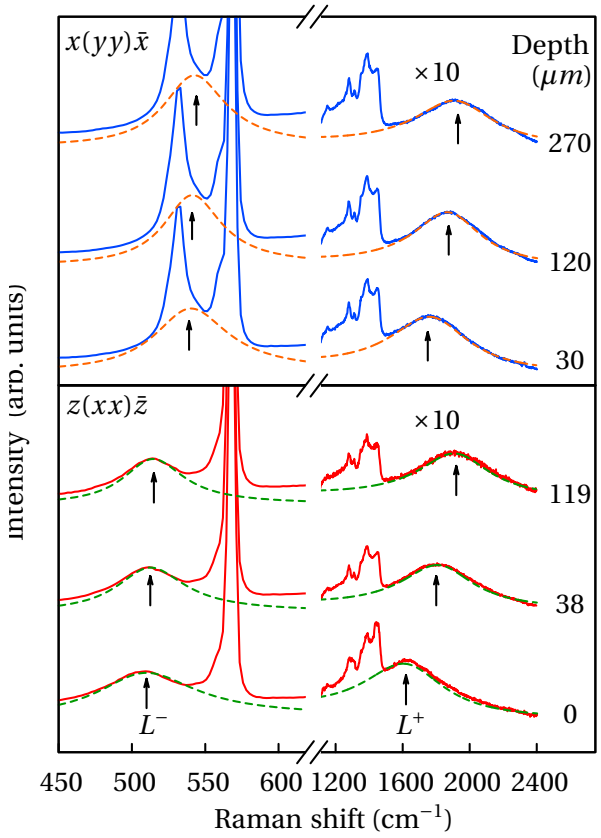

Figure 7.9: *Raman spectra obtained at different depths below the N-polar surface in $z(xx)\bar{z}$ and $x(yy)\bar{x}$ configurations. Dashed lines correspond to the line-shape calculations obtained by fitting the L^+ Raman peak. Note the expanded frequency scale used to display the L^- region.*

Table 7.1: Values of the parameters used for the LOPCM line-shape model in GaN

Symbol	Description	Value	Ref.
m^*	Electron effective mass	$0.227 m_e$	[43]
C_{FH}	Faust-Henry coefficient	-2.3	This thesis
$\varepsilon_{\infty\parallel}$	High-freq. parallel diel. const.	5.3	[43]
$\varepsilon_{\infty\perp}$	High-freq. perpendicular diel. const.	5.16	[43]
$\omega_{E_1(TO)}$	E_1(TO) phonon frequency	559 cm^{-1}	This thesis
$\omega_{E_1(LO)}$	E_1(LO) phonon frequency	741 cm^{-1}	This thesis
$\omega_{A_1(TO)}$	A_1(TO) phonon frequency	531 cm^{-1}	This thesis
$\omega_{A_1(LO)}$	A_1(LO) phonon frequency	734 cm^{-1}	This thesis
Γ_I	Ionic damping constant	5 cm^{-1}	This thesis
n	Refractive index	2.38	[44]
E_g	Band-gap energy	3.39 eV	[15]

7.2.2 Charge density gradient along the z-axis in the N-polar sector

In this section we present a study of the free charge density distribution along the z-axis obtained from the analysis of the Raman spectra recorded at different depths with respect to the N-polar surface. As the L^+ LOPCM is more sensitive to N_e variations than the L^-, the free electron density was obtained by fitting the L^+ mode. The fits were performed using the dielectric linear-response line-shape model presented in Sec. 7.1.2, which takes into account the Lindhard-Mermin electronic susceptibility, with N_e and the electronic damping parameter Γ_p as free parameters. The complete set of parameters used for the calculations are given in Table 7.1.

Faust-Henry constant determination

The Raman scattering cross section depends on the Faust-Henry constant C_{FH}, as shown in Eq. (7.23) and Eq. (7.24). The model line-shape simulations indicate that the L^+/L^- intensity ratio is highly sensitive to the actual value of C_{FH}. To determine the C_{FH} for GaN, we have varied its value in the line-shape calculations until we have been able to reproduce the L^+/L^- intensity ratio exhibited in the $z(xx)\bar{z}$ spectrum. The obtained value is $C_{FH} = -2.3$. Previous C_{FH} estimations made from the A_1(LO)/A_1(TO) intensity ratio [45, 46] are slightly higher in magnitude. In those works the intensity of the modes was extracted from measurements made in different scattering geometries, which may be differently af-

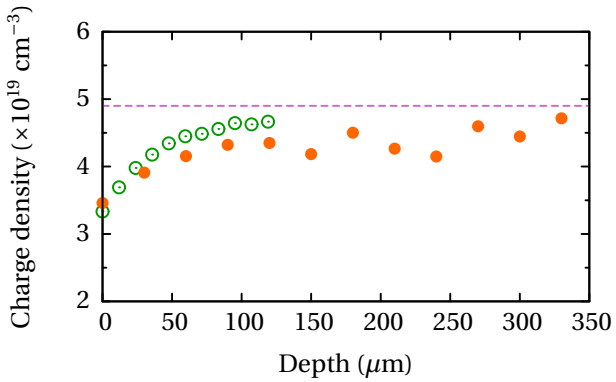

Figure 7.10: *Charge density versus depth in the N-sector of the ammonothermal Si-doped GaN sample as determined from line-shape fits to the L^+ coupled mode. Raman spectra have been obtained in $x(yy)\bar{x}$ (filled circles) and $z(xx)\bar{z}$ (empty circles) scattering configurations. Dashed line indicates the average N_e obtained from the Hall effect measurements.*

fected by the experimental errors in each measurement. In contrast, in our case we have extracted the L^+/L^- intensity ratio from the same spectra, which may lead to more reliable values.

Fits to the L^+ coupled mode

Representative spectra obtained from different depths are shown in Fig.7.9. As described, above two scattering configurations have been used to obtain the Raman spectra from probing volumes with different z-axis depth.

The spectra obtained in the $z(xx)\bar{z}$ exhibit both the L^+ and the L^- modes, and a frequency up-shift is detected as the focusing depth increases. The spectra and the model line-shape fits to the L^+ coupled mode are shown in Fig. 7.9. It can be seen that the model line-shape fitted to the L^+ mode also matches closely the L^- Raman peak for all the spectra. This validates the LOPCM assignment and the value of the Faust-Henry constant used in the calculations.

The upper panel in Fig.7.9 shows $x(yy)\bar{x}$ Raman measurements performed on a lateral $(1\bar{1}00)$ face at different distances from the (0001) surface. The plasmon-like L^+ mode exhibits a behaviour parallel to that observed in $z(xx)\bar{z}$ configuration. Although the relatively broad L^- peak cannot be resolved in the spectra, the increase in the baseline signal in this frequency region is consistent with the calculated line shape.

The model fits for both scattering configurations yield electron densities increasing from 3.3×10^{19} cm^{-3} at the surface to 4.6×10^{19} cm^{-3} at ≈ 120 μm depth, with Γ_e ranging from 560 to 620 cm^{-1}. These large damping constants indicate a

relatively low mobility of the electrons, in fair agreement with the collision time τ_{Hall} derived from the average Hall mobility measurements, $\tau_{\mathrm{Hall}}^{-1} = e/\mu_e m_{\mathrm{eff}}^* \approx$ 720 cm^{-1}. While these dampings are rather large, they are still well below the plasma frequency in these samples ($\omega_p \sim 1700$ cm^{-1}) making it possible to observe both branches of the long-wavelength LOPCMs.

Free-electron gradient along z-axis

In Fig. 7.10, the N_e values determined from the L^+ line-shape fits are plotted *vs.* depth for the full set of spatially-resolved Raman spectra obtained from the N-polarity sector. Empty circles represent the results derived from the confocal Raman measurements in the $z(xx)\bar{z}$ scattering geometry and full circles correspond to Raman spectra recorded on different points of a lateral $(1\bar{1}00)$ face in the $x(yy)\bar{x}$ scattering configuration. These results indicate that N_e steadily increases over the first 50 μm of the N-polarity sector and then tends to saturate to about 4.6 $\times 10^{19}$ cm^{-3} at depths of $\approx$ 100 μm, close to the average value obtained by Hall measurements. The somewhat larger scatter of N_e values obtained from the $x(yy)\bar{x}$ spectra may be partly due to irregularities in the cleaved lateral face.

7.3 LOPCMs in undoped, Si-doped and Mg-doped InN nanowires

As it has been shown along this chapter, Raman scattering is a powerful tool for locally probing the free charge density in III-nitrides. Carrier density can be determined in a nondestructive and contactless way, which is specially interesting for the case of nanostructures. The electrical characterization of the nanostructures presents the evident difficulty of making electrical contacts, which requires processing steps using focused ion beam (FIB) to make nano contacts [47, 48]. Although the results are rather impressive, this approach presents several drawbacks. On one hand, FIB is a high-cost technique and cannot be used as a routine characterization of nanostructures. On the other hand, measuring the free charge density by FIB requires selecting a single NW and separate it from the substrate, and therefore it destroys the sample and can lead to results that are not representative of the NW sample.

In this section we present a Raman scattering study of Si-doped, Mg-doped and undoped InN nanowires. From the Raman spectra, the LOPCMs are evaluated and their free charge densities are determined from the analysis. Since this is a non-contact technique, it allows one to probe the free electron density in a non-destructive way.

The undoped, Si-doped and Mg-doped InN nanowires

The studied InN NWs were grown by plasma-assisted MBE (PAMBE) under N-rich conditions on Si (111) substrates. Here, apart from the undoped sample described in Sec. 5.3, we study also doped samples grown using the same equipment. In the PAMBE set-up, the flux of the metal atoms is controlled by the temperature of each effusion cell. A measure of the atomic flux is given by the beam-equivalent pressure (BEP), which is the increase of the pressure in the chamber due to a certain atomic flux.

We study a set of six samples grown by using this growth technique. The set is composed of an undoped sample (labelled S0), three Si-doped samples (S1, S2 and S3) and two Mg-doped samples (M1 and M2). The range of diameters for each NW sample are listed in Table 7.2. A Si flux was used during the growth to obtain Si doped, *n*-type samples. The beam equivalent pressure (BEP) used for each sample are listed in Table 7.2. Similarly, Mg-doped, *p*-type samples were grown by supplying a Mg flux, also given in Table 7.2.

The grown nanowires are single crystalline, with the *c*-axis parallel to the wire. Nevertheless, they exhibit a small tilt relative to the normal of the substrate, as can be seen in the SEM image of the undoped NWs shown in Figure 7.11.

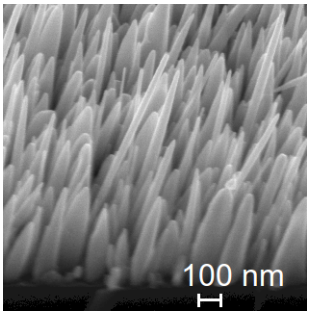

Figure 7.11: *SEM image of the studied InN NWs*

Experimental conditions

The Raman scattering measurements were performed in backscattering geometry and the light was analysed using the Jobin Yvon T-64000 spectrometer described in Section 3.2 in the standard mode. The excitation sources used were the 514-nm line of the Ar^+ laser and the 325-nm line of the He-Cd laser. In all the measurements, the macrocamera configuration was used to minimize the laser heating of the sample and to obtain an average measurement of the sample.

Although the measurements have been performed in backscattering geometry, the effective light scattering configuration is determined by the NWs tilt and refractive index, as has been discussed in Section 4.2. As a consequence, the resulting Raman spectra have contributions of several scattering configurations.

7.3.1 Visible and UV Raman spectra

Modes identification

The Raman spectra of the undoped, Si-doped and Mg-doped InN NWs obtained with an excitation light of 514 nm are displayed in Fig. 7.12. All the spectra are dominated by the strong signal of the silicon substrate (521 cm^{-1}). A Raman

Table 7.2: *Growth parameters of the InN NWs studied*

	Diameter (nm)	Sample	Si/Mg BEP (10^{-9} mbar)
Undoped	30-110	S0	-
Si-doped	60-180	S1	1
		S2	3
		S3	5.8
Mg-doped	80-120	M1	1
		M2	3

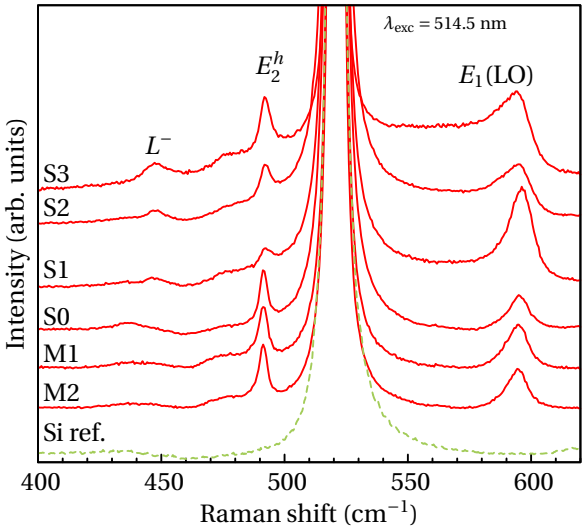

Figure 7.12: *Raman spectra of the undoped (S0), Si-doped (S1, S2, S3) and Mg-doped (M1, M2) InN NWs obtained using a visible excitation.*

spectra of a silicon reference sample is also shown in the figure for comparison. The spectra of the InN NWs also exhibit the Raman peaks corresponding to the E_2^{high} (488 cm^{-1}) and to the E_1(LO) ($\approx$ 593 cm^{-1}) InN phonon modes. A weaker feature is detected in the 430-450 cm^{-1} region, whose frequency slightly up-shifts as the doping increases. Since the E_2^{high} phonon exhibits the same frequency in all the samples, strain effects due to dopant incorporation can be ruled out. Therefore, we tentatively assign the weak feature at the 430-450 cm^{-1} region to the L^- branch of the E_1(LO)-phonon-plasmon coupled mode. As expected for a coupled mode, its frequency increases with the free electron density in the Si-doped samples. It is difficult to discern this feature in the Mg-doped samples due to the overlapping second-order band of the silicon substrate spectrum.

To confirm the coupled mode identification, UV Raman scattering measurements of the InN NWs samples have been made. Since the InN absorbance is higher in the UV region, the signal arising from the silicon substrate is strongly attenuated in the UV spectra, as can be seen in the UV spectra shown in Fig. 7.13. In all the spectra we can distinguish the signal of the E_2^{high}, and a weaker E_1(TO) is also resolved. The mode which was tentatively assigned to the L^- coupled mode in the visible excitation spectra, clearly exhibits here the typical coupled mode behaviour: as the free charge density increases, the L^- displays a frequency up-shift and sharpens due to its increasing phonon-like character. Therefore, the L^- nature of this mode is confirmed by the Raman spectra performed using UV excitation.

Another striking difference between the visible and the UV spectra of the NWs samples (figures 7.12 and 7.13, respectively) is that no LO signal is detected in the latter. We attribute the quenching of the LO intensity to the fact that

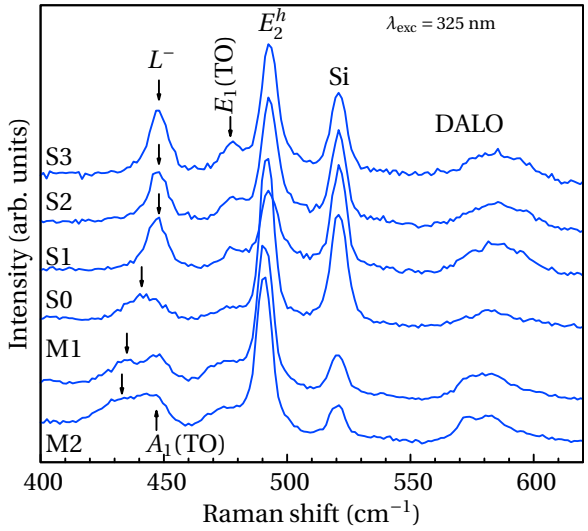

Figure 7.13: *Raman spectra of the undoped (S0), Si-doped (S1, S2, S3) and Mg-doped (M1, M2) InN NWs obtained using a ultraviolet excitation.*

the UV excitation energy is much further from the electronic resonance conditions which lead to a Fröhlich enhancement of the Raman signal. Therefore, the E_1(LO) phonon mode is not detected using UV excitation, and only a weak and broad band corresponding to the disorder-activated longitudinal-optical modes (DALO) is measured.

Crystal quality of the nanowires

The doping of crystals can result in a reduced crystalline quality and an additional lattice strain, since atomic radï of the dopant atoms is different from that of the host elements. Therefore, high dopant concentrations may induce an hydrostatic strain in the lattice [49]. From the analysis of the Raman spectra, information about the crystalline quality and the strain state of the InN NWs can be extracted. We have checked the frequency of the E_2^{high} of all the InN samples, and all of them exhibit the same frequency. This is an indication that the dopant incorporation is not high enough to result into a measurable hydrostatic strain.

The E_2^{high} peak linewidth of the different samples has been compared to check its crystalline quality. In the undoped sample, the FWHH of the E_2^{high} (3.7 cm^{-1}) compares favourably to that of a high-quality InN epilayer (5.1 cm^{-1} [20]), indicating better crystalline quality in the undoped NWs than in the thin film. This is due to the high dislocation density existing in most of the state-of-the-art InN thin films as a consequence of the lattice mismatch with the substrate.

Concerning the Si-doped InN NWs samples, their visible Raman spectra exhibit slightly broader E_2^{high} peaks compared to those of the InN high-quality epilayer. Moreover, in the UV spectra of the Si-doped samples the DALO signal is more intense than in the undoped samples. These are indications that that Si-

Table 7.3: Values of the parameters used for the LOPCM line-shape model in InN

Symbol	Description	Value	Ref.
m^*	Electron effective mass	$0.07m_e$	[19]
C_{FH}	Faust-Henry coefficient	-2.0	[19]
ε_∞	High-frequency dielectric constant	6.7	[50]
$\omega_{E_1(TO)}$	E_1(TO) phonon frequency	476 cm^{-1}	This thesis
$\omega_{E_1(LO)}$	E_1(LO) phonon frequency	593 cm^{-1}	This thesis
Γ_I	Ionic damping constant	5 cm^{-1}	[51]
n	Refractive index	2.5	[52]
E_g	Band-gap energy	650 meV	[50]

doping slightly degrades the crystal quality of the nanowires. A different situation occurs for the Mg-doped samples, in which E_2^{high} linewidth is comparable to that of the undoped sample, indicating that crystal quality of the studied NWs is essentially unaffected by the Mg doping achieved in our samples.

Free charge behaviour in InN NWs

As it has been extensively discussed in Sec. 7.1, from a classical point of view, the collective excitations of the high-mobility electron plasmas couple with the polar phonon modes and therefore the LO modes are expected to disappear from the Raman spectra while two LOPCMs are expected to emerge. Our Raman spectra of doped InN NWs (Fig. 7.12) present remarkable differences with respect to this simple picture.

On one hand, only the L^- coupled mode has been detected and no signal from the high-frequency L^+ coupled mode was found. This observation was also made for InN epilayers in Ref. [20]. The absence of L^+ peak may be caused by the strong background signal arising from the Si substrate, which may mask the coupled mode weak signal.

On the other hand, the E_1(LO) signal is detected in the same spectra than the coupled mode L^- (see Fig. 7.12). As reported for InN epilayers [20], the observation of the unscreened LO modes is enhanced by the electric-field induced resonant scattering mechanism in the surface accumulation layer of InN. In this accumulation layer, the electrons are confined and cannot sustain longitudinal collective oscillations, and therefore the LO-phonon-plasmon coupling does not occur. As a consequence, the long-wavelength LOPCM Raman signal measured arises from the bulk material underneath. Although the presence of the electron accumulation layer in nonpolar faces is still matter of debate, Calleja *et*

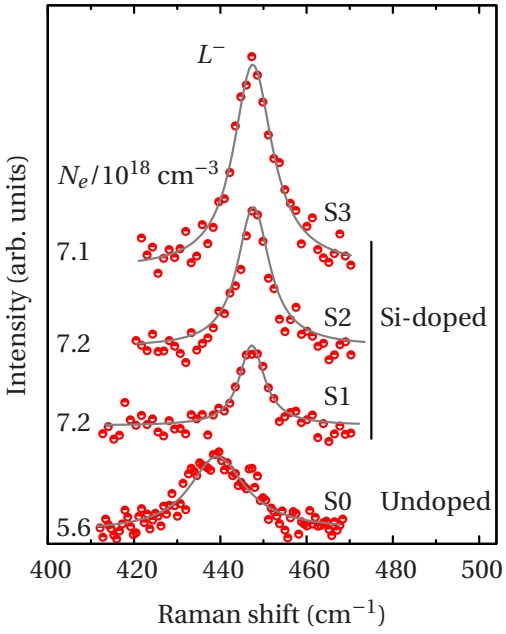

Figure 7.14: *Line-shape fits (solid lines) to the visible Raman spectra of the L^- phonon-plasmon coupled mode (open squares) for the undoped (S0) and the Si-doped InN nanowires (S1-S3).*

al. showed that nonpolar faces of InN nanocolumns exhibit this accumulation layer [53].

Our results also indicate that the nonpolar faces of the InN NWs present an electron accumulation layer. The higher intensity enhancement of the LO mode in NWs samples as compared to thin films can be caused by the higher surface/volume ratio of the NWs, which favours the enhancement of the resonantly-selected uncoupled E_1(LO) mode by the strong electric fields at the surface accumulation layer.

7.3.2 LOPCMs fits

The modelling of the detected LOPCMs allows us to extract the free electron density for each sample. This is accomplished by fitting the LOPCM model to the L^- Raman peak of the spectra obtained with the visible 514-nm excitation, in order to avoid the absorption effects present in the UV spectra. The model we used is the Lindhard-Mermin model described in Sec. 7.1.2. In our case, we have considered plasmon coupling with the E_1(LO) phonon mode because, as already discussed, the effective scattering configuration of the NWs make the Raman excitation light to propagate along directions perpendicular to the c-axis inside the NWs, and therefore the coupling of the plasmons with the E_1(LO) phonon is measured. The parameters used for the fits are listed in Table 7.3.

The line-shape fits to the L^- coupled modes and the extracted free electron densities are shown in figure 7.14 for the undoped and the Si-doped samples.

In the case of the undoped sample, we have determined a free electron density of 5.6×10^{18} cm^{-3}. This value agrees well with the free electron density obtained from the study of the PL peak [54]. A certain degree of Si diffusion from the substrate may be the cause of the presence of a significant free electron density in the undoped sample. The free charge densities obtained for the Si-doped samples are slightly higher ($\approx 7.2\times10^{18}$ cm^{-3}), but they do not present significant differences for increasing doping levels. This suggests a rapid saturation of the silicon incorporation process in InN NWs

Model fits have not been performed on the coupled modes of the Mg-doped nanowires because of the low intensity of the mode and its overlap with the Si-substrate second-order signal. Nevertheless, the spectra allow the identification of the L^- coupled mode in a frequency lower than that of the undoped sample. This indicates that the Mg-doping may partially compensate the Si incorporation from the substrate, and therefore the free electron density is lower in the Mg-doped samples than in the undoped one.

Throughout this chapter we have presented the study of LOPCMs by means of Raman spectroscopy. A complete LOPCM line-shape model has been developed and applied to obtain an accurate determination of the free electron density. With the presented results, we demonstrate that the proper analysis of the Raman spectra can be used to extract the free electron density in III-nitrides. Micro-Raman measurements allow the free carrier density to be determined in a local, contactless way, which is particularly relevant for the study of nanostructured material. The applicability of this technique has been demonstrated in Si-doped InN NWs.

References

[1] D. K. Schroeder. *Semiconductor Material and Device Characterization*. Wiley-Interscience, 2006.

[2] J. Wu. *J. Appl. Phys.*, 106:011101, 2009.

[3] M. Cardona and G. Güntherodt. *Light scattering in Solids IV*. Springer-Verlag, 1984.

[4] J. Ibáñez and R. Cuscó. *Raman spectroscopy of compound semiconductors*. Semiconductor Research. Experimental Techniques. Editors: A. Patanè and N. Balkan. Springer-Verlag, 2012.

[5] K. Wan and J. F. Young. *Phys. Rev. B*, 41:10772–10779, 1990.

[6] G. Abstreiter, R. Trommer, and M. Cardona. *Solid State Commun.*, 30:703, 1979.

[7] J. E. Maslar, W. S. Hurst, and C. A. Wang. *J. Appl. Phys.*, 103(1):013502, 2008.

[8] S. Nakashima, T. Kitamura, T. Kato, K. Kojima, R. Kosugi, H. Okumura, H. Tsuchida, and M. Ito. *Appl. Phys. Lett.*, 93(12), 2008.

[9] L. Artús, R. Cuscó, J. Ibáñez, N. Blanco, and G. González-Díaz. *Phys. Rev. B*, 60(8):5456, 1999.

[10] T. Yuasa and M. Ishii. *Phys. Rev. B*, 35:3962–3970, 1987.

[11] D. Olego and M. Cardona. *Phys. Rev. B*, 24:7217–7232, 1981.

[12] R. Fukasawa and S. Perkowitz. *Phys. Rev. B*, 50:14119–14124, 1994.

[13] T. Kozawa, T. Kachi, H. Kano, M. Hashimoto, N. Koide, and K. Manabe. *J. Appl. Phys.*, 75:1098, 1994.

[14] P. Perlin, J. Camassel, W. Knap, T. Taliercio, J. C. Chervin, T. Suski, I. Grzegory, and S. Porowski. *Appl. Phys. Lett.*, 67:2524, 1995.

[15] H. Harima. *J. Phys. Condens. Matter*, 14:R967, 2002.

[16] K. Jeganathan, R. K. Debnath, R. Meijers, T. Stoica, R. Calarco, D. Gruutzmacher, and H. Luth. *J. Appl. Phys.*, 105:123707, 2009.

[17] D. Wang, C.-C. Tin, J. R. Williams, M. Park, Y. S. Park, C. M. Park, T. W. Kang, and W.-C. Yang. *Appl. Phys. Lett.*, 87(24):242105, 2005.

[18] J. S. Thakur, D. Haddad, V. M. Naik, R. Naik, G. W. Auner, H. Lu, and W. J. Schaff. *Phys. Rev. B*, 71(11):115203, 2005.

[19] F. Demangeot, C. Pinquier, J. Frandon, M. Gaio, O. Briot, B. Maleyre, S. Ruffenach, and B. Gil. *Phys. Rev. B*, 71:104305, 2005.

[20] R. Cuscó, J. Ibáñez, E. Alarcón-Lladó, L. Artús, T. Yamaguchi, and Y. Nanishi. *Phys. Rev. B*, 79:155210, 2009.

[21] J. G. Kim, Y. Kamei, N. Hasuike, H. Harima, K. Kisoda, K. Sasamoto, and A. Yamamoto. *Phys. Status Solidi C*, 7(7-8):1887–1889, 2010.

[22] E. Tiras, M. Tanisli, N. Balkan, S. Ardali, E. Iliopoulos, and A. Georgakilas. *Phys. Status Solidi B*, 249(6):1235–1240, 2012.

[23] P. Drude. *Annalen der Physik*, 306(3):566–613, 1900.

[24] N. W. Ashcroft and N. D. Mermin. *Solid State Physics*. Harcourt College Publishers, 1976.

[25] U. Nowak, W. Richter, and G. Sachs. *Phys. Status Solidi B*, 108:131, 1981.

[26] J. Ibáñez, R. Cuscó, and L. Artús. *Phys. Status Solidi B*, 223:715–722, 2001.

[27] P. Y. Yu and M. Cardona. *Fundamentals of Semiconductors. Physics and materials properties.* Springer-Verlag, 1996.

[28] R. Cuscó, E. Alarcón-Lladó, J. Ibáñez, T. Yamaguchi, Y. Nanishi, and L. Artús. *J. Phys. Condens. Matter*, 21(41):415801, 2009.

[29] J. E. Maslar, J. F. Dorsten, P. W. Bohn, S. Agarwala, I. Adesida, C. Caneau, and R. Bhat. *Phys. Rev. B*, 50:17143–17150, 1994.

[30] J. Lindhard and A. Winther. *Matt. Fys. Medd. Dan. Vid. Selsk.*, 34, 1969.

[31] N. D. Mermin. *Phys. Rev. B*, 1:2362–2363, 1970.

[32] R. Cuscó, L. Artús, S. Hernández, J. Ibáñez, and M. Hopkinson. *Phys. Rev. B*, 65:035210, 2001.

[33] D. T. Hon and W. L. Faust. *Appl. Phys*, 1:241, 1973.

[34] J. Biellmann, B. Prevot, and C. Schwab. *Jour. of Phys. C: Solid State Phys.*, 16(6):1135, 1983.

[35] B. Wang, D. Bliss, M. Suscavage, S. Swider, R. Lancto, C. Lynch, D. Weyburne, T. Li, and F. A. Ponce. *J. Cryst. Growth*, 318:1030–1033, 2011.

[36] J. Lutz, H. Schlangenotto, U. Scheuermann, and R. D. Doncker. *Semiconductor Power Devices: Physics, Characteristics, Reliability*. Springer, 2011.

[37] B. Wang and M. J. Callahan. *Crystal Growth & Design*, 6(6):1227–1246, 2006.

[38] D. Y. Song, S. A. Nikishin, M. Holtz, V. Soukhoveev, A. Usikov, and V. Dmitriev. *J. Appl. Phys.*, 101:053535, 2007.

[39] D. Gogova, P. P. Petrov, M. Buegler, M. R Wagner, C. Nenstiel, G. Callsen, M. Schmidbauer, R. Kucharski, M. Zajac, R. Dwilinski, M. R. Phillips, A. Hoffmann, and R. Fornari. *J. Appl. Phys.*, 113:203513, 2013.

[40] B. Wang and M. J. Callahan. *Cryst. Growth and Des.*, 6:1227–1246, 2006.

[41] D. Bliss, B. Wang, M. Suscavage, R. Lancto, S. Swider, W. Eikenberry, and C. Lynch. *J. Cryst. Growth*, 312:1069–1073, 2010.

[42] V. Hortelano, O. Martínez, J. Jiménez, B. G. Wang, S. Swider, M. Suscavage, and D. Bliss. *Mater. Sci. Forum*, 725:63, 2012.

[43] M. Feneberg, K. Lange, C. Lidig, M. Wieneke, H Witte, J. Bläsing, A. Dadgar, A. Krost, and R Goldhahn. *Appl. Phys. Lett.*, 103:232104, 2013.

[44] G. Yu, G. Wang, H. Ishikawa, M. Umeno, T. Soga, T. Egawa, J. Watanabe, and T. Jimbo. *Appl. Phys. Lett.*, 70(24):3209, 1997.

[45] C. Wetzel, W. Walukiewicz, E. Haller, J. Ager, I. Grzegory, S. Porowski, and T. Suski. *Phys. Rev. B*, 53(3):1322–1326, January 1996.

[46] F. Demangeot, J. Frandon, M.A. Renucci, N. Grandjean, B. Beaumont, J. Massies, and P. Gibart. *Solid State Comm.*, 106:491–494, 1998.

[47] E. C. Garnett, Y.-C. Tseng, D. R. Khanal, J. Wu, J. Bokor, and P. Yang. *Nature Nanotechnology*, 4(5):311–314, 2009.

[48] K. Storm, F. Halvardsson, M. Heurlin, D. Lindgren, A. Gustafsson, P. M Wu, B. Monemar, and L. Samuelson. *Nature Nanotechnology*, 7(11):718–722, 2012.

[49] C. Kisielowski, J. Krüger, S. Ruvimov, T. Suski, J. W. Ager, E. Jones, Z. Liliental-Weber, M. Rubin, E. R. Weber, M. D. Bremser, and R. F. Davis. *Phys. Rev. B*, 54:17745–17753, 1996.

[50] A. Kasic, E. Valcheva, B. Monemar, H. Lu, and W. J. Schaff. *Phys. Rev. B*, 70:115217, 2004.

[51] J. Wu, W. Walukiewicz, W. Shan, K. M. Yu, J. W. Ager, E. E. Haller, Hai Lu, and William J. Schaff. *Phys. Rev. B*, 66:201403, 2002.

[52] Q. Guo, O. Kato, M. Fujisawa, and A. Yoshida. *Solid State Commun.*, 83(9):721 – 723, 1992.

[53] E. Calleja, J. Grandal, M. A. Sánchez-García, M. Niebelschütz, V. Cimalla, and O. Ambacher. *Appl. Phys. Lett.*, 90:262110, 2007.

[54] R. Calarco T. Richter E. Sutter T. Stoica, R. J. Meijers and H. Luth. *Nano Lett.*, 6:1541, 2006.

CHAPTER 8

Summary and conclusions

In this Thesis we have used Raman scattering to study the lattice dynamics of the (In,Ga)N system in order to gain insight into the phonons and their interactions. We have studied how phonons interact with other phonons (anharmonic interactions), with impurities (leading to resonances) and with free charge density (leading to coupling) in InN-related materials. First, we have discussed the Raman selection rules for wurtzite materials. We have presented the first-order Raman spectra of InN, GaN and InGaN alloys, in order to have a reference framework to perform the further in-depth studies of phonon dynamics and interactions.

We have studied the anharmonic decay channels of phonons in InN layers and nanostructures. The linewidth temperature dependence of all the phonon modes has been studied using an anharmonic model which considers the contribution of 3-phonon and 4-phonon processes to the anharmonic phonon decay. The results of *ab-initio* calculations of the phonon dispersion curves, phonon DOS and two-phonon DOS have been used for the implementation of the anharmonic model. We have calculated the anharmonic contribution to the frequency temperature-dependence of the phonon frequencies and linewidths, and we have discussed other possible contributions. By comparing the data from thin films and NWs, we have obtained information about the defect density and the strain state of the samples. We have also studied the anharmonic decay of high-frequency LVMs in Mg-doped InN through quasi-elastic acoustic phonon scattering.

We have discussed the relevant electronic resonances that affect Raman scattering in the (In,Ga)N system. We have shown that the optical excitation of the longitudinal optical modes in InN occurs through the Martin's double resonance both in InN layers and nanostructures, even though the defect density of the latter is significantly lower. We have also studied the mechanism underlying the high-order multiphonon scattering, which is the impurity-mediated cascade mechanism. To ascertain the role of the impurities we have studied as-grown InGaN layers in comparison with He^+-implanted InGaN layers.

We have also discussed the behaviour of the LO-Phonon-Plasmon Coupled Modes (LOPCMs) in InN and GaN. First, we have presented the classical and quantum mechanical descriptions of the electromagnetic coupling in semiconductors, as well as their limitations. We have used the Lindhard-Mermin model

to perform two detailed Raman scattering studies of the LOPCMs in an ammonothermal Si-doped GaN sample, and in a set of doped and undoped InN nanowires. In both cases, the study of the LOPCMs Raman signal has been proven to be useful for determining the free electron density in samples in which conventional Hall effect measurements would be difficult to perform. We have shown that Raman scattering technique is ideally suited for a local assessment of the free charge density.

The main conclusions of these studies on each type of sample are summarized below.

InN layers

The undoped InN *c*-face and *m*-face layers have been studied by Raman spectroscopy in several scattering configurations in order to measure all the phonon modes. The LO phonon modes have been analysed considering Martin's double resonance. By performing wavelength-dependent measurements on the *c*-face sample, the A_1(LO) resonance profile and the phonon dispersion close to centre-zone have been obtained. We have also performed Brillouin scattering measurements on these thin films. The angular dependence of the surface acoustic waves velocities has been analysed and a set of elastic constants for InN has been proposed.

In these samples we have performed a comprehensive study of the phonon anharmonic interactions. To this end, we have studied the Raman spectra of wurtzite InN thin films over a temperature range from 80 to 660 K and we have performed DFT lattice dynamical calculations to determine the phonon dispersion curves, which have allowed us to deduce the decay channels of all the phonon modes. We have found the E_2^{high} phonon mode to mainly decay through 4-phonon processes, whereas the extremely narrow E_2^{low} mode can decay only through up-conversion processes. The longitudinal optical modes, A_1(LO) and E_1(LO), mainly decay into a sum of two phonons, although the contribution of 4-phonon processes is also relevant at high temperatures. The transversal optical modes, A_1(TO) and E_1(TO) have been found to decay through 3-phonon and 4-phonon up-conversion interactions. The anharmonic contribution to the frequency downshift have been calculated in all cases from the anharmonic coupling parameters derived from the linewidth analysis. The measured frequency downshift in the case of the E_2 modes is reasonably accounted for by the anharmonic frequency renormalization. In the case of the LO and TO modes, the measured frequencies show a frequency downshift much higher than that predicted by the anharmonic calculation. This difference can be attributed to the differential thermal strain with respect to the substrate, which is higher for the *m*-face sample. For the LO phonon modes, the temperature dependence of the TO-

LO splitting was suggested as a further contribution to the frequency downshift. The lifetimes of the phonon modes at 80 K and at room temperature have been derived from the measured phonon linewidths. The long-lived E_2^{low} phonon exhibits the largest lifetime (8.8 ps at 80 K), which is mainly limited by impurity scattering. The impurity scattering contribution to the linewidth has been found to be greater in those modes measured from the *m*-face thin film, corroborating that this sample has higher defect density.

We have also studied heavily doped Mg:InN. The Raman spectra of these samples exhibit a more intense signal from the LO phonon modes, due to impurity-enhanced the Fröhlich interaction. Apart from the lattice phonon modes, we have detected signal arising from high frequency local vibrational modes, and we assigned them to Mg-H complexes. We have measured the temperature dependence of their frequency and linewidth. Due to their high frequencies, these modes cannot decay following the usual mechanisms. We show that their anharmonic decay can be explained by considering dephasing due to quasi-elastic acoustic phonon scattering.

InN nanowires

We have studied undoped, Si-doped and Mg-doped InN NWs grown by plasma-enhanced molecular beam epitaxy on silicon substrate. Due to the effective scattering configuration of the sample, backscattering Raman measurements allowed us to detect the E_2^{low}, E_2^{high} and $E_1(LO)$ phonon modes. We have studied the mechanism underlying the Raman scattering of the LO modes in NWs. Although the NWs have a reduced defect density in relation to thin films, we have found that Martin's double resonance also applies to Raman scattering by LO modes in NWs. By studying the Raman spectra obtained with different excitation wavelengths, we have obtained the $E_1(LO)$ wave-vector dispersion close to centre zone. The resonant intensity profile for this LO mode as a function of the excitation wavelength shows a much stronger intensity increase for longer excitation wavelengths than that observed for the $A_1(LO)$ in InN thin films. Although being governed by the same mechanism, the resonant intensity of LO modes appears to be more pronounced in NWs.

We have studied the anharmonic decay interactions of the detected phonon modes in the undoped InN NWs with the model used for the InN layers. The phonon linewidths display the same temperature dependence as in the InN layers, and therefore we assume that they decay through the same channels. However, the linewidths of the phonon modes measured in NWs are significantly reduced, indicating a higher crystalline quality. As a consequence, we observe an increase of the phonon lifetime in NWs. The most illustrative example is the E_2^{low} phonon lifetime, which is one order-of-magnitude higher in NWs than in

thin films. The increase in the phonon lifetime can contribute to slow the carrier cooling, which can be interesting for some applications such as hot carrier solar cells. The changes in the phonon frequencies allowed us to corroborate that the NWs lattice is relaxed as compared to thin films.

We have also studied the Raman spectra of doped InN NWs. The spectra exhibit LO signal, and also an L^- LOPCM that shifts to higher frequencies in the Si-doped NWs and to lower frequencies in the Mg-doped NWs. The line-shape analysis of the L^- LOPCM peak has allowed us to determine the free electron density, which is found to be residual in the undoped NWs and to slightly increase in the Si-doped samples, irrespective of the Si flux used during the growth. The electron density is reduced in Mg-doped samples, indicating that electrical activation of Mg occurs in Mg-doped nanowires.

InGaN layers

As grown and He^+-implanted $In_xGa_{1-x}N$ epilayers with $0.17< x <0.42$ have been studied by means of Raman scattering using visible and UV excitation sources, in order to analyse resonance effects and to probe their crystalline quality upon implantation. For samples with $x >0.24$, the Raman spectra obtained with the 514-nm line display an intense photoluminescence signal which prevents the observation of the lattice modes. These spectra only exhibit a broad LO mode which is excited through Fröhlich interaction. In the implanted samples, the photoluminescence signal is quenched and the 2LO and 3LO overtone scattering can also be observed.

UV Raman-scattering measurements on InGaN epilayers allow us to measure up to fifth order multiphonon scattering due to cascade mechanism. Their relative intensities depend on the indium concentration and implantation dose. The spectra of the implanted samples exhibit disorder-activated modes and broadened phonon and multiphonon peaks, and the A_1(LO) signal is strongly enhanced due to impurity-induced Fröhlich mechanism. The intensity ratio between A_1(LO) and $2A_1$(LO) phonon modes obtained under UV excitation is found to be a good indicator of the crystalline quality of highly implanted InGaN alloys.

GaN bulk

We have studied a bulk, ammonothermally-grown Si-doped GaN sample. This sample has two regions with different polarity, both of them exhibiting narrow phonon linewidths and adherence to the selection rules. No evidence of LOPCMs has been detected in the Ga-polar face, probably due to the higher defect density existing in this sample sector. In the N-polar surface, both branches

of the LOPCMs have been detected. By studying the line shape of the L^+ coupled mode using a Lindhard-Mermin dielectric model, accurate local determinations of the free electron density have been obtained. Confocal micro-Raman measurements allowed us to perform a depth profiling and to study the spatial dependence of the free charge density. A significant gradient in N_e is found over the first 50 μm from the top surface of the N-polarity side, where N_e increases by about 40% and reaches a value that keeps constant for greater depths.

APPENDIX A

Future works

Throughout this thesis we have studied the vibrational properties of wurtzite III-nitrides. These materials present some characteristics that limit the full development of the nitride-based optoelectronic applications. The most relevant is the efficiency decrease for wavelengths beyond 500 nm, corresponding to the green region. Both the LEDs and laser diodes still have lower quantum efficiencies for green emission than for shorter wavelengths. The causes of this efficiency decrease for InGaN with intermediate In concentrations are twofold. First, InGaN layers with intermediate In concentrations present composition fluctuations and unequal crystalline quality. Second, piezoelectric fields appear in the InGaN *c*-face due to the biaxial strain. These fields appear because of the different lattice constants between the InGaN active quantum wells and the surrounding (Al)GaN layers. The strong internal piezoelectric fields cause a local separation of electrons and holes in the InGaN quantum wells (due to QCSE) and result in a reduction of the device efficiency.

To overcome these limitations and progress towards the full development of the nitrides capability, several approaches are being investigated, such as the growth of wurtzite nitrides on semipolar crystalline orientations, the fabrication of zinc-blende cubic nitrides or the growth of nanostructures.

In the wurtzite structure, the electric field vanishes completely for crystal facets perpendicular to the *c*-plane (nonpolar planes) and are typically reduced for intermediate orientations (semipolar planes). Along this thesis we have already presented several measurements on the nonpolar *m*-plane of InN, and our aim is to continue with studies on other nonpolar and semipolar nitride planes. One of the approaches commonly used for the growth of semipolar nitrides is the epitaxial lateral overgrowth (ELO) on patterned substrates. Raman spectroscopy can be useful to study issues such as the strain distribution or the free electron density homogeneity on these samples.

Cubic nitrides are also attracting much interest as a promising candidates to overcome the built-in piezoelectric fields and spontaneous polarisation effects of polar wurtzite heterostructures. Due to the absence of built-in fields, cubic nitrides-based devices are expected to exhibit a higher efficiency. Moreover, as was shown in the Fig. 1.1 of this thesis, they have a band-gap range also very interesting. Since their band gaps are 0.2 eV lower than those of the wurtzite phase, less In concentration is required to reach the green emission. Moreover,

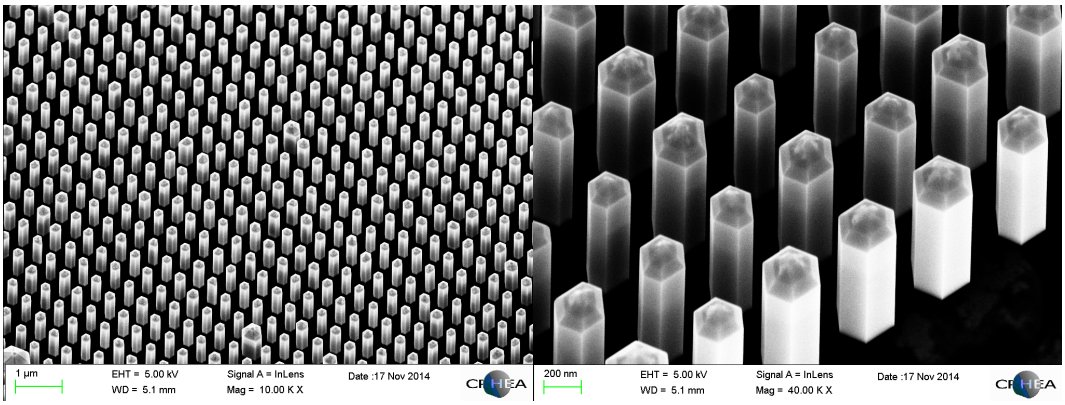

Figure A.1: *SEM images of GaN NWs grown by selective-area growth MOCVD. These samples have been grown at CRHEA-CNRS during a PhD stage.*

due to the absence of polarization fields, wider wells with lower carrier density can be used and hence the Auger non-radiative recombination rate is reduced.

Finally, the growth of nanostructured nitride materials is being the focus of huge research efforts and is leading to high-quality nitride NW samples, which exhibit impressive optical properties. Figure A.1 shows GaN NWs grown by selective-area growth MOCVD, which exhibit high homogeneity and reduced defect concentration. The further study of the vibrational properties of these nitride structures will allow to ascertain the behaviour of the nonpolar faces and the issues related to the possible free-electron gradients or defect distribution along the NWs, among others.

Therefore, the future perspectives of this thesis are the study of the Raman spectra of emerging nitride structures. The knowledge of their vibrational properties will contribute to the characterization of their lattice dynamics and to the development of their potential applications.

APPENDIX B

Attributions

The studies presented in this thesis have been performed on the basis of scientific collaborations and team work. My work has been devoted to the experimental measurements and their analysis in the basis of the presented theoretical models. To this purpose, I have studied samples that have been grown in other laboratories, and I have collaborated with other scientists and groups. This is why I would like to clarify here the attribution of specific results that have been included in the thesis.

Samples growth have been performed by different laboratories in collaboration. Undoped and doped InN layers have been grown by the group of Prof. Nanishi at the Ritsumeikan University. InN NWs have been grown by the group of Prof. Calarco at the Research Center Jülich. InGaN layers were fabricated at the University of Houston by the group of Prof. Bensaoula. Ammonothermal GaN samples were grown at the Air Force Research Laboratory by the group of Prof. Wang.

The Brillouin spectroscopy measurements have been performed by Prof. Jiménez-Riobóo at the ICMM-CSIC. The *ab-initio* calculations presented have been performed by Dr. Cuscó at ICTJA-CSIC. High energy particle irradiation have been performed by the group of Prof. González-Díaz in Univ. Complutense de Madrid.

APPENDIX C

List of publications

1. *"Raman scattering of cadmium oxide epilayers grown by metal-organic vapor phase epitaxy"*
   Cuscó, R; Ibáñez, J; Domènech-Amador, N; Artús, L; Zúñiga-Pérez, J; Muñoz-Sanjosé, V.
   Journal of Applied Physics 107, 063519 (2010)

2. *"Probing the electron density in undoped, Si-doped and Mg-doped InN nanowires by means of Raman scattering"*
   Cuscó, R; Domènech-Amador, N; Artús, L, Gotschke, T; Jeganathan, K; Stoica, T; Calarco, R.
   Applied Physiscs letters 97, 221906 (2010)

3. *"Raman scattering study of anharmonic phonon decay in InN"*
   Domènech-Amador, N.; Cuscó, R.; Artús, L.; Yamaguchi, T.; Nanishi, Y.
   Physical Review B 83, 245203 (2011)

4. *"Longer InN phonon lifetimes in nanowires"*
   Domènech-Amador, N.; Cuscó, R.; Artús, L.; Stoica, T.; Calarco, R.
   Nanotechnology 23, 085702 (2012)

5. *"Double resonance Raman effects in InN nanowires"*
   Domènech-Amador N.; Cuscó, R.; Calarco R.; Yamaguchi, T.; Nanishi, Y.; Artús, L.
   Physica Status Solidi − Rapid Research Letters 6, 160-162 (2012)

6. *"Surface acoustic waves and elastic constants of InN epilayers determined by Brillouin scattering"*
   Jiménez-Riobóo, R. J.; Cuscó, R.; Domènech-Amador, N.; Prieto, C.; Yamaguchi, T.; Nanishi, Y; Artús, L.
   Physica Status Solidi − Rapid Research Letters 6, 265-258 (2012)

7. *"Brillouin scattering determination of the surface acoustic wave velocity in $In_xGa_{1-x}N$: A probe into the elastic constants"*
   R. J. Jiménez-Riobóo, R. J.; Cuscó, R.; Oliva, R.; Domènech-Amador, N; Prieto, C.; Ibáñez, J.; Boney, C.; Bensaoula, A. and Artús, L.
   Applied Physics Letters 101, 062103 (2012)

8. *"Temperature dependence of Mg-H local vibrational modes in heavily doped InN:Mg"*
   Cuscó, R; Domènech-Amador, N.; Artús, L.; Wang, L.; Yamaguchi, T. and Nanishi, Y.
   Journal of Applied Physics 112, 053528 (2012)

9. *"Electron density gradients in ammonothermally-grown Si-Doped GaN"*
   Cuscó, R.; Domènech-Amador, N.; Jiménez, J.; Artús, L.
   Applied Physics Express 7, 021.001 (2014)

10. *"Multiphononon resonant Raman scattering in He^+ -implanted InGaN"*
    Domènech-Amador, N.; Cuscó, R.; García-Hernansanz, R.; González-Díaz, G.; Gandhi, J.; Bensaoula, A.; Artús, L.
    Seniconductor Science and technology 29, 045013 (2014)

11. *"Raman scattering study of LO phonon-plasmon coupled modes in p-type InGaAs"*
    Cuscó, R.; Domènech-Amador, N.; Hung, P. Y.; Loh, W.-Y.; Artús, L.
    Journal of Alloys and Compounds 634, 87-93. (2015)

12. *"Lattice dynamics of a mist-chemical vapor deposition-grown corundum-like $Ga_2 2O_3$ single crystal "*
    Cuscó, R.; Domènech-Amador, N.; Hatakeyama, T.; Yamaguchi, T.; Honda, T.; Artús, L.
    Journal of Applied physics 117, 185706. (2015)

13. *"Anharmonic phonon decay in cubic GaN"*
    Cuscó, R.; Domènech-Amador, N.; Novikov, S.; Foxon, C. T.; Artús, L.
    Submitted.

APPENDIX D

Resum en català

Introducció

La fabricació de díodes emissors de llum (LED) de nitrur de gal·li (GaN) amb nitrur d'indi-gal·li (InGaN) com a material actiu ha suposat en els darrers anys un impuls molt important per a la investigació de les propietats dels nitrurs del grup III. Malgrat que les propietats dels nitrurs del grup III havien estat destacades en diferents estudis teòrics, les dificultats en el creixement cristal·lí van suposar un enorme obstacle per a la fabricació de dispositius electrònics de GaN. L'obtenció de LEDs de GaN d'alta eficiència amb InGaN com a material actiu, emetent en longituds d'ona de 365 nm a 530 nm va representar un gran impuls per a la recerca entorn dels nitrurs. La combinació dels LEDs blaus amb fósfors va permetre la fabricació de LEDs de llum blanca, que avui dia estan reemplaçant les bombetes incandescents i han permès incrementar l'eficiència de la tecnologia d'il·luminació. Per les seves aportacions en el desenvolupament d'aquests LEDs de GaN, I. Akasaki, H. Amano i S. Nakamura han estat guardonats amb el Premi Nobel de Física de l'any 2014.

L'interès en els LEDs d'alta eficiència ha concentrat enormes esforços investigadors en el GaN en els últims anys. Sorprenentment, tot i que la capa activa dels LEDs és d'InGaN, hi havia escassos estudis bàsics i experimentals del nitrur d'indi (InN) en el moment en què es van obtenir aquests LEDs, principalment a causa de la falta de mostres InN d'alta qualitat. L'exemple més paradigmàtic del poc coneixement de les propietats del InN és que el valor acceptat per a la seva banda d'energies prohibida (*band gap*) va ser erroni fins al 2002. Això va ser degut a les dificultats per a fabricar InN d'alta qualitat, fet causat per la seva baixa temperatura de dissociació i l'alt valor de la pressió de vapor d'equilibri de nitrogen. Aquestes característiques van causar que durant molts anys les mostres de InN eren de mala qualitat cristal·lina i tenien altes concentracions d'electrons lliures. De les mesures d'absorció òptica realitzades amb aquestes mostres es deduïa un llindar d'absorció de 1.9 eV, i aquest va ser el valor acceptat per al *band gap* del InN fins al 2002. El creixement per epitàxia de feixos moleculars (MBE), va permetre fabricar capes primes de InN amb una concentració d'electrons lliures molt inferior. La realització de nous experiments d'absorció en aquestes capes va demostrar que el InN té un *band gap* menor, que és de 0.64 eV en condicions normals.

La revisió del *band gap* del InN va fer créixer l'interès en el conjunt del sistema de nitrurs del grup III, ja que aquest nou valor amplia el rang d'emissions del sistema des de l'ultravioleta (corresponent al *band gap* del nitrur d'alumini) fins a l'infraroig (corresponent al *band gap* del InN). A més, degut a la seva notable resistència a la irradiació amb partícules d'alta energia, l'InGaN és un material atractiu per a les cèl·lules solars dissenyades per a l'espai exterior. El InN també té propietats de transport ben interessants, com ara una massa efectiva d'electrons petita. Totes aquestes propietats contribueixen a ampliar les potencials aplicacions dels nitrurs del grup III, que van des de dispositius emissors de llum fins a cèl·lules solars i dispositius electrònics d'alta velocitat i d'alta freqüència.

En els darrers anys s'ha intensificat la recerca entorn de les tècniques de creixement per tal de millorar la qualitat de les mostres de nitrurs del grup III, reduir la densitat de defectes i avançar en el control de dopatge. A causa de la manca de substrats nadius, les capes primes de nitrurs del grup III són generalment fabricades mitjançant heteroepitàxia. Les capes primes són sintetitzades sobre substrats que tenen paràmetres de xarxa diferents i coeficients de dilatació tèrmica també diferents. Aquest fet genera tensions en les capes primes, així com a una densitat de defectes estructurals alta. Un altre enfocament per obtenir nitrurs del grup III de millor qualitat son les tècniques de creixement de cristalls volúmics a gran escala (creixement *bulk*), com ara la tècnica amonotermal. A més de la millora de les tècniques de creixement epitaxial i de material *bulk*, també existeix un interès creixent entron de la síntesi de nitrurs nanoestructurats, entre els que destaquen els nanofils (NWs, de l'anglès *nanowires*). Aquestes estructures són interessants tant per les seves propietats estructurals com per les seves prometedores aplicacions, com ara emissors d'infrarojos o sensors. Pel que fa a les seves propietats estructurals, les nanoestructures són molt interessants, ja que generalment tenen una xarxa cristal·lina relaxada i menys defectes que les capes primes.

Tot i que les aplicacions presents i futures dels materials del sistema (In,Ga)N són molt prometedores, es requereix una gran quantitat d'investigació per a un desenvolupament ple de les aplicacions potencials. Cal seguir treballant per adquirir una comprensió més profunda de les propietats físiques bàsiques d'aquests materials, per millorar-ne les tècniques de creixement i optimitzar el rendiment dels dispositius.

Les propietats vibracionals es compten entre les característiques més fonamentals dels materials. La dinàmica de xarxa i les vibracions fonons estan estretament relacionades amb altres propietats bàsiques dels materials com ara l'estructura electrònica. L'espectroscòpia Raman és una tècnica molt adequada per estudiar les propietats de vibració de compostos i estructures semiconduc-

tores. Els experiments de dispersió Raman són utilitzats principalment per a l'estudi de les vibracions de fonons en les estructures cristal·lines, i a partir de l'anàlisi de l'espectre Raman de fonons, s'obté informació sobre la qualitat de les mostres i l'estat de tensió de la xarxa cristal·lina. Així, els experiments de dispersió Raman es poden utilitzar per a millorar la comprensió de la dinàmica de xarxa, les vides de fonons i les seves interaccions anharmòniques. En les mostres amb una concentració significativa d'impureses, les mesures Raman poden detectar modes locals de vibració relacionats amb les impureses. A més, en les mostres dopades el camp elèctric de les oscil·lacions col·lectives de la densitat de càrrega lliure s'acobla amb el dels modes polars, tot donant lloc a modes acoblats que poden ser detectats per mitjà d'espectroscòpia de Raman i es poden utilitzar com una mesura òptica de propietats elèctriques.

Estat de la qüestió

Durant les últimes dècades, s'han realitzat importants esforços en l'estudi de les propietats vibracionals de nitrurs. No obstant això, els avenços s'han fet a ritmes diferents: s'han obtingut molts més resultats relacionats amb el GaN que amb el InN. Això es deu al fet que, a part de les esmentades dificultats per obtenir mostres d'alta qualitat, el InN té un senyal Raman feble. A més, la interpretació dels espectres Raman de InN ha generat diverses controvèrsies. D'una banda, l'origen i el comportament dels fonons òptics longitudinals mesurats en experiments de Raman, que es va atribuir a la doble ressonància de Martin. L'aparició d'aquest mecanisme es basa en l'estructura electrònica del InN i en la presència de defectes nadius.

A part de ser difícil de sintetitzar, el InN també és difícil de dopar amb acceptors. De fet, el InN té una densitat intrínseca d'electrons lliures molt alta i una forta propensió a ser de tipus n. L'origen d'aquesta conductivitat està relacionada amb la seva estructura de bandes electròniques, que afavoreix la creació de defectes de tipus donador. La ionització dels estats de superfície dóna lloc a una densitat d'electrons lliures extremadament alta prop de la superfície de la mostra, que es coneix com la capa d'acumulació d'electrons. L'existència d'aquesta capa d'acumulació d'electrons fa que l'avaluació de la densitat de càrrega lliure en capes de InN no es pugui realitzar mitjançant tècniques habituals com l'efecte Hall, i s'ha de tenir en compte en la interpretació dels espectres Raman de les mostres dopades.

Aquesta tesi

Aquesta tesi està dedicada a l'estudi de les interaccions dels fonons en nitrurs del grup III amb estructura wurtzita, fent especial èmfasi en aquells aspectes que

romanen menys estudiats. Atès que les propietats vibracionals de GaN han estat àmpliament estudiades, ens hem centrat bàsicament en l'encara controvertit InN. Per a aquest propòsit, presentem una sèrie d'estudis de dispersió Raman en diferents tipus de mostres (de capes primes a nanoestructures, dopades o sense dopar, de InN a InGaN o GaN) per tal de donar una visió global de la dinàmica de fonons en aquests materials. Hem estudiat com els fonons interactuen amb altres fonons a través d'interaccions anharmòniques, el que porta al seu decaïment. En general, les interaccions dels fonons polars amb impureses carregades juguen un paper clau en les mesures de dispersió de Raman mitjançant mecanismes de ressonància. Així, hem estudiat les ressonàncies en el sistema (In,Ga) N i la influència de la densitat d'impureses en l'eficiència de ressonància. Finalment, hem estudiat l'acoblament de fonons polars amb els plasmons en mostres dopades amb la finalitat d'investigar la densitat d'electrons lliures utilitzant espectroscòpia Raman.

L'espectroscòpia Raman

La principal tècnica experimental emprada en aquesta tesi és l'espectroscòpia Raman. Tant l'espectroscòpia Raman com l'espectroscòpia de Brillouin són tècniques que analitzen la dispersió inelàstica de la llum degut a la seva interacció amb els materials mitjançant la creació o l'anihilació d'excitacions elementals. En el cas de l'espectroscòpia de Brillouin, aquestes excitacions elementals corresponen als fonons acústics. Per als processos de dispersió Raman, aquests quantums d'energia poden correspondre a fonons òptics, plasmons d'electrons lliures, modes locals de vibració o ones de spin, entre d'altres. En aquesta tesi ens centrem principalment en la dispersió Raman deguda a la interacció amb els fonons del material.

Per obtenir espectres Raman, una font de llum monocromàtica incideix a la mostra i la llum dispersada és recollida i analitzada per un espectròmetre, que elimina el senyal degut a de la dispersió elàstica i separa els components de la llum dispersada inelàsticament. L'espectròmetre Raman utilitzat en aquesta tesi és un Jobin-Yvon T-64000, un espectròmetre d'alta resolució amb alta sensibilitat.

Resultats

Els fonons en el InN i el GaN amb estructura wurtzita

Els fonons d'una xarxa cristal·lina es poden deduir a partir de l'estudi de la simetria de la seva estructura. El InN i el GaN de tipus wurtzita pertanyen al grup es-

pacial C_{6v}^4 amb dues unitats de fórmula a la cel·la primitiva, i per tant existeixen dotze modes normals de vibració, alguns dels quals són degenerats. Segons l'anàlisi de teoria de grups, els modes amb activitat Raman són A_1(TO),A_1(LO), E_1(TO), E_1(LO), E_2^{low} i E_2^{high}.

Hem presentat els espectres Raman de primer ordre del GaN, el InN i el InGaN emprant diferents configuracions de dispersió, fet que ha permès identificar tots els fonons en aquests espectres. També hem presentat espectres de Brillouin de capes primes de InN, a partir dels quals hem extret informació de les constants elàstiques del material.

Decaïment anharmònic dels fonons del InN

En els cristalls reals, els fonons desapareixen degut a la interacció anharmònica amb altres fonons de la xarxa o amb impureses. Hem estudiat els canals de desintegració anharmònica dels fonons en capes primes i nanoestructures de InN. La dependència de l'amplada del pic Raman amb la temperatura de tots els modes fonònics s'ha estudiat utilitzant un model anharmònic que considera la contribució dels processos de tres i quatre fonons. S'han fet càlculs *ab-initio* de les corbes de dispersió de fonons i de la densitat d'estats de fonons, i aquests resultats s'han utilitzat en l'aplicació del model anharmònic. Hem calculat la contribució anharmònica a la dependència amb temperatura de la freqüència i l'amplada del pic Raman, i hem discutit altres contribucions possibles.

Per a estudiar les interaccions anharmòniques dels fonons en capes primes de InN, hem estudiat la dependència amb temperatura dels espectres Raman de InN de capes primes amb dues orientacions cristal·lines diferents, *c* i *m*. Hem analitzat la dependència de l'amplada del pic Raman amb la temperatura a través del model de Cowley, i això ha permès deduir els canals de desintegració dels fonons. Hem trobat que el mode E_2^{high} decau a través de processos de 4 fonons, mentre que el mode E_2^{low}, pot decaure només a través dels processos de conversió ascendent. Els modes òptics longitudinals, A_1(LO) i E_1(LO), principalment decauen en una suma de dos fonons, tot i que la contribució dels processos a quatre fonons també és rellevant a altes temperatures. Els modes òptics transversals, A_1(TO) i E_1(TO), decauen a través d'interaccions a tres i quatre fonons. La contribució del decaïment anharmònic a les variacions en freqüència ha estat calculades en tots els casos a partir dels paràmetres d'acoblament anharmònic derivats de l'anàlisi de l'amplada del pic Raman. La variació amb temperatura de la freqüència mesurada en el cas dels modes E_2 s'explica raonablement bé tenint en compte la contribució anharmònica a la renormalització de la freqüència. En el cas dels modes LO i TO, les freqüències mesurades a alta temperatura tenen valors molt inferiors que els predits pel càlcul anharmònic. Aquesta diferència pot atribuir-se a l'expansió tèrmica diferencial de la xarxa re-

specte el substrat, que és més alta per a la mostra d'orientació m. Per als modes LO, la dependència amb la temperatura de la separació TO-LO podria afegir una contribució adicional a la reducció de la freqüència. S'han obtingut els temps de vida dels fonons a 80 K i a temperatura ambient a partir de les amplades dels pics Raman mesurats. El mode E_2^{low} té el temps de vida més llarg (8.8 ps a 80 K), que està limitat principalment per la dispersió per impureses. La contribució de la dispersió per impureses en els modes mesurats en la capa prima amb orientació m és més gran que en els modes mesurats en la capa prima amb orientació c, corroborant que la capa prima amb orientació m té major densitat de defectes.

Hem estudiat també el decaïment anharmònic dels fonons en NWs. Les amplades dels pics de fonons mesurades en NWs mostren la mateixa dependència amb temperatura que les mesurades en les capes primes, i per tant deduïm que es desintegren a través dels mateixos canals. No obstant això, les amplades dels pics dels modes fonònics mesurats en NWs són significativament menors, el que indica una qualitat cristal·lina superior. Com a conseqüència d'això, s'observa un augment del temps de vida de fonons en NWs. L'exemple més il·lustratiu és el mode E_2^{low}, el temps de vida del qual és un ordre de magnitud major en NWs que en capes primes. Els canvis en les freqüències de fonons ens han permès corroborar que l'estructura cristal·lina dels NWs es troba relaxada en comparació amb l'estructura de les capes primes de InN.

També hem estudiat capes primes de InN amb un alt dopatge de magnesi. Els espectres Raman d'aquestes mostres exhibeixen un senyal les modes LO més intens que en les mostres no dopades, a causa de la interacció Fröhlich mediada per impureses. A part dels fonons propis de les vibracions atòmiques dels atoms del compost, hem detectat el senyal de modes locals de vibració, que hem assignat a complexos d'impureses Mg-H. Hem mesurat la dependència amb temperatura de les freqüències i amplades dels pics Raman per a estudiar-ne el decaïment anharmònic. A causa de les seves altes freqüències, aquests modes no poden decaure mitjançant els mecanismes habituals. Hem demostrat que el decaïment anharmònic d'aquests modes locals de vibració es pot explicar considerant un desfasament causat per una interacció quasi-elàstica amb els fonons acústics.

Efectes de ressonància en InN i InGaN

Quan l'energia d'excitació és propera ressonàncies electròniques dels materials, els mecanismes ressonants estan involucrats en el procés de dispersió Raman. Això causa un increment de la intensitat dels espectres Raman. En semiconductors polars, una de les conseqüències més evidents de la dispersió Raman ressonant és l'increment significatiu de la intensitat dels fonons LO, que dispersen la llum a través del mecanisme ressonant de Fröhlich. L'eficiència d'aquest

mecanisme incrementa quan l'energia d'excitació és propera a ressonàncies electròniques, i també a causa de la presència d'impureses carregades. En funció de l'estructura electrònica de cada material i de les condicions d'excitació, altres mecanismes ressonants poden ser rellevants en la dispersió Raman.

En aquesta tesi hem estudiat l'efecte de les ressonàncies electròniques rellevants que afecten la dispersió Raman en el sistema (In,Ga)N. Hem demostrat que l'excitació òptica dels modes longitudinals òptics (LO) en el InN es produeix a través de doble ressonància de Martin tant en capes primes com en nanoestructures, tot i que la densitat de defectes d'aquestes últimes és significativament menor. També hem estudiat el mecanisme subjacent a la dispersió multifonònica d'alt ordre, que és el mecanisme de cascada mediat per impureses. Per a determinar la importància de la concentració d'impureses en l'eficiència d'aquest mecanisme, hem estudiat capes primes de InGaN abans i després d'un procés d'implantació iònica amb ions d'heli.

Els modes LO del InN han estat analitzats tenint en compte el mecanisme de doble de ressonància de Martin. Mitjançant la realització de mesures amb diferents longituds d'ona d'excitació en una capa prima de InN, hem obtingut el perfil de ressonància i la dispersió del mode A_1(LO) prop del centre de la primera zona de Brillouin. Hem realitzat aquest estudi també en NWs de InN. Tot i que els NWs tenen una densitat de defectes molt menor que les capes primes, hem trobat que la doble ressonància de Martin és també el mecanisme a través del qual es dispersen els modes LO en els NWs de InN. Mitjançant l'estudi dels espectres Raman obtinguts amb diferents longituds d'ona d'excitació, hem obtingut la dispersió del mode E_1(LO) a prop del centre de la primera zona de Brillouin. El perfil d'intensitat de ressonància d'aquest mode en funció de la longitud d'ona d'excitació mostra un augment molt més fort per a longituds d'ona d'excitació llargues que l'observat per al mode A_1(LO) en capes primes.

Hem estudiat capes primes de InGaN amb diferent composició i diferent grau d'implantació iònica mitjançant la dispersió Raman, utilitzant excitació visible i UV, per tal d'analitzar els efectes de ressonància i estudiar la seva qualitat cristal·lina després de la implantació. Per a mostres amb [In]>0.24, els espectres Raman obtinguts amb la línia de 514 nm mostren un senyal de fotoluminiscència intensa que impedeix l'observació dels fonons. En aquests espectres només es detecta el senyal intens del mode LO, que és excitat a través del mecanisme Fröhlich. En les mostres implantades, el senyal de fotoluminiscència es redueix i aleshores també s'observen el segon i el tercer ordre del mode LO. Les mesures Raman excitades amb llum UV sobre aquestes mateixes mostres ens permeten mesurar fins al cinquè ordre de dispersió per multifonons a causa del mecanisme de cascada. Les intensitats relatives dels multifonons depenen de la concentració d'indi i de la dosi de la implantació. En els espectres de les mostres implantades hem detectat un eixamplament dels pics fonònics, així com senyal de

modes activats pel desordre. El més destacable, però, és l'increment d'intensitat del mode A_1(LO), que és mesurat mitjançant el mecanisme de Fröhlich mediat per impureses. S'ha trobat que la relació entre les intensitats dels modes A_1(LO) i $2A_1$(LO) mesurats amb excitació de llum UV és un bon indicador de la qualitat cristal·lina dels aliatges d'InGaN altament implantats.

Modes acoblats plasmó-fonó en InN i GaN

Hem estudiat el comportament dels modes acoblats entre els fonons LO i els plasmons (LOPCMs, de l'anglès *LO-phonon-plasmon coupled modes*) en InN i GaN. Aquests modes sorgeixen com a conseqüència de la interacció del camp elèctric macroscòpic produït per les oscil·lacions de la densitat de càrrega amb el camp elèctric causat pels fonons òptics longitudinals. La freqüència dels modes acoblats resultants depèn de la densitat de càrrega lliure, de manera que l'estudi detallat del pic Raman dels modes acoblats permet determinar aquesta densitat.

En primer lloc, hem presentat les descripcions clàssica i quàntica dels LOPCMs. Hem utilitzat la susceptibilitat quàntica de Lindhard-Mermin per a realitzar dos estudis detallats de l'espectre Raman dels LOPCMs: en una mostra de GaN fabricada pel mètode amonotermal i dopada amb Si; i en un conjunt de NWs de InN dopats i sense dopar. En tots dos casos, l'estudi del senyal Raman dels LOPCMs ha estat útil per determinar la densitat d'electrons lliures en mostres en les que és difícil de realitzar mesures d'efecte Hall, com és el cas dels NWs.

En el espectres Raman de NWs de InN sense dopar i dopats, el senyal corresponent als modes acoblats es desplaça a freqüències més altes en les mostres dopades amb Si, i a freqüències més baixes en els NWs dopats amb Mg. L'anàlisi del pic del mode acoblat de baixa freqüència (L^-) ens ha permès determinar la densitat d'electrons lliures, que és residual en els NWs sense dopar i augmenta lleugerament en les mostres dopades amb Si, independentment del flux de Si utilitzat durant el creixement. La densitat d'electrons es redueix en mostres dopades amb Mg, el que indica que l'activació elèctrica dels acceptors de Mg es produeix en aquests NWs.

Hem estudiat també una mostra *bulk* de GaN dopat amb Si crescuda mitjançant la tècnica amonotermal. Aquesta mostra té dues regions amb diferent polaritat, i en ambdues regions els espectres Raman acompleixen les regles de selecció i mostren pics estrets. A la cara de polaritat Ga, no hi ha evidència d'acoblament entre els modes LO i els plasmons, probablement a causa de la major densitat de defectes existent el cristall crescut amb aquesta polaritat. A la superfície de polaritat N, s'han detectat les dues branques dels LOPCMs. Mitjançant l'estudi del pic del mode acoblat d'alta freqüència (L^+), s'ha obtingut la densitat d'electrons lliures. S'ha realitzat un perfil de profunditat de la densitat

de càrrega mitjançant mesures de micro-Raman confocal. En la zona de polaritat N, s'ha trobat un gradient de la densitat de càrrega en els primers 50 μm de la superfície, en els quals la densitat de càrrega augmenta al voltant d'un 40 % i assoleix un valor que es manté per a profunditats majors.

Tesi finalitzada a Barcelona, juny de 2015.

Aquesta és la història d'un cristall
que somiava abraçar un bri de llum,
que no volia ser mai més mirall
ni veure els fotons marxar tan lluny.

Veia expectant com la llum venia,
tan coherent, d'un làser llunyà.
I li robava un poc d'energia,
i amb nou color la veia marxar.

Li restava una lleu tremolor,
precisa en energia i moment,
que dansava amb els àtoms suaument:
carícies en forma de fonó.